DYNAMICS OF MOLECULAR CRYSTALS AND ADSORBED MOLECULAR LAYERS

(including analytical potential expansions)

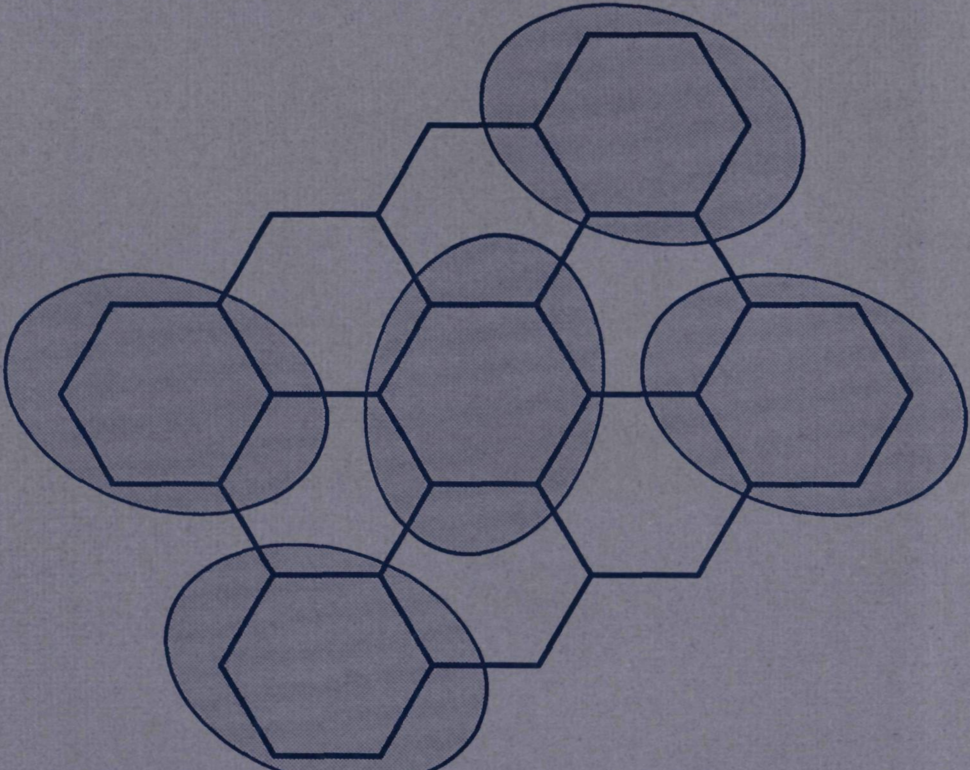

T. H. M. VAN DEN BERG

DYNAMICS OF MOLECULAR CRYSTALS AND ADSORBED MOLECULAR LAYERS

(including analytical potential expansions)

een wetenschappelijke proeve op het
gebied van de Natuurwetenschappen

PROEFSCHRIFT

ter verkrijging van de graad van doctor
aan de Katholieke Universiteit te Nijmegen
volgens besluit van het College van Decanen
in het openbaar te verdedigen
op woensdag 27 februari 1991
des namiddags te 1.30 uur precies

door

Thomas Hermanus Maria van den Berg

geboren op 18 april 1961 te Schijndel

Druk: Boek en Offsetdrukkerij Letru, Helmond, 04920-37797

Promotor: Prof. dr. ir. A. van der Avoird aan *Angelique*

Op deze plaats wil ik graag een ieder bedanken die geholpen heeft bij het tot stand komen van dit proefschrift. In het bijzonder wil ik noemen:

- Ad van der Avoird voor de enorme inzet en steun waarmee hij mij met name het laatste jaar terzijde heeft gestaan.
- Ad Jongenelis en Jan Schmidt voor de prettige en vruchtbare samenwerking tussen theorie en experiment.
- Wilfred Janssen, Thijs Bongers en Henri de Bekker voor hun hulp bij de berekeningen.
- John van Bladel voor het ontwerp van de omslag.
- Ine van Berkel voor het vele typewerk.
- Angelique voor haar liefdevolle zorg en het vele afzien.

This investigation is part of the research program of the 'Stichting Scheikundig Onderzoek Nederland' (SON), financially supported by the 'Nederlandse organisatie voor Wetenschappelijk Onderzoek' (NWO). Part of this work has been performed as an IBM/ACIS project.

Contents

PART A: DYNAMICS OF MOLECULAR CRYSTALS

PART B: DYNAMICS OF ADSORBED MOLECULAR LAYERS

General introduction

This thesis is concerned with the dynamics of molecular crystals and adsorbed molecular layers. The molecular entities in these systems are still clearly recognizable and in their motions one can distinguish the intramolecular vibrations and the so-called lattice vibrations. The latter are the center-of-mass or translational vibrations and the orientational oscillations or librations of the whole molecules. In a solid these vibrations become collective modes which are called translational phonons and librons, respectively. If the solid is periodic, they can be characterized by wave vectors $\boldsymbol{q}$ which lie in the first Brillouin zone of the reciprocal lattice. Also the intramolecular vibrations are coupled in the solid through the intermolecular interactions, however, and the corresponding modes are called vibrons. The frequencies of the translational phonons and librons are comparable and usually these modes are mixed, except in the points of the Brillouin zone where this is forbidden by symmetry. The frequencies of the vibrons are substantially higher, but especially in the case of large non-rigid molecules one finds also low-lying vibrons which can strongly mix with the lattice modes.

For the thermodynamic properties of molecular solids the dynamics is extremely important. The reason for this is that especially the lattice vibrations have low frequencies, *i.e.* low excitation energies, and thus they can be thermally excited under most circumstances of practical interest. For instance, in considerations about phase stability and phase transitions it is not sufficient to look only at the packing or energy effects. Even at low temperature the zero-point vibrations are essential, and at somewhat higher temperature one should really take into account the entropy effects and consider the Helmholtz or Gibbs free energies. If one knows the particulars of the vibrations, however, it is easy to calculate the quantum statistical partition function and to derive all other thermodynamic properties.

Experimental techniques to characterize the intramolecular and lattice vibrations are the optical methods, infrared and Raman spectroscopy, and the inelastic scattering of neutrons. By the optical methods one can study only $\boldsymbol{q} = 0$ excitations, by inelastic neutron scattering one can determine the vibrational excitations for arbitrary wave vectors. The dependence of the phonon/libron or vibron frequencies on the wave vector is called dispersion relation. A technique which is promising for the study of surface and adsorbed layer dynamics is the inelastic scattering of helium atoms. Also this method permits, in principle, the measurement of the complete two-dimensional phonon/libron dispersion relations.

As illustrated in this thesis, it is very useful to combine the spectroscopic or scattering experiments with lattice dynamics calculations. In the calculations of phonons and librons one starts from the anisotropic intermolecular potential. In vibron calculations one needs an intramolecular force field too. These potentials can be either empirically parametrized model potentials, of the atom-atom type for instance, or they can be obtained from *ab initio* quantum chemical computations for small molecules. The lattice dynamics calculations are usually performed by the standard harmonic method, but in this thesis we have developed and applied more advanced quantum mechanical methods (the Time-Dependent Hartree method, in particular) that hold also in the case of motions with larger amplitudes. Hindered rotations of N_2 molecules in the bulk solid or in adsorbed layers are an example of this category. In the case of quantum solids such as H_2 or D_2 the harmonic method is completely useless for the rotations (and bad for the translational vibrations) and one has to resort to quantum methods as applied in this thesis. Comparison with the spectroscopic and scattering data serves as a check on the potentials used and on the reliability of the lattice dynamics method. It is possible to improve parametrized model potentials in this manner. As illustrated in Chapters 1, 2, 3, 7 and 8, the calculations are also helpful in the interpretation of the measurements. An additional advantage is, however, that they go all the way from the intermolecular potentials via the dynamics to the macroscopic thermodynamic properties of the system, so that one gains useful insight in the molecular origin of these properties.

Before one can use an intermolecular potential in lattice dynamics calculations one has to derive explicitly the dependence of this potential on the molecular displacements. In the harmonic approximation these displacements are the center-of-mass translations, the linearized (infinitesimal) rotations and, for intramolecular vibrations, also the linearized atomic displacements within the molecules. One needs only the first and second order terms in the Taylor expansion of the potential about the equilibrium positions and the calculation of the required derivatives is relatively easy. Still, for intermolecular potentials which are not expressed by the atom-atom model we had to derive some new formulas (see Chapter 4). In the quantum mechanical TDH method, the orientational displacements are expressed in free rotor functions (spherical harmonics). For the translational displacements we have included the anharmonic (cubic and quartic) terms. The expansion of the intermolecular potential becomes much more complicated then (see Appendix A in Chapter 7).

In the first three chapters of this thesis we study crystals with somewhat larger molecules, in direct relation with problems in the interpretation of experimental data. The method used is the standard harmonic lattice dynamics technique, with the inclusion of the intramolecular vibrations. Both the intramolecular force fields and the intermolecular atom-atom potentials are of empirical origin. By a special technique it was possible to obtain information about $q \neq 0$ vibrons in chlorinated benzene crystals from optical measurements. In order to interpret the spectra and to understand the basic phenomena the calculations described in Chapters 1 and 2 proved to be very valuable. In tetracyano-ethene there appears to be a strong mixing between the intra- and intermolecular vibrations. Complete phonon/libron/vibron dispersion relations were measured by inelastic neutron scattering. The calculations described in Chapter 3 were undertaken in order to explain the anomalous dispersion observed in one of the vibron branches. Chapter 4 is a methodological study. On the well-known ordered α and γ phases of solid nitrogen we compare the different lattice dynamics methods used in the remainder of this thesis, as well as the different forms to express the anisotropy of *ab initio* intermolecular potentials.

The second part of this thesis is concerned with the dynamics of molecular layers, physically adsorbed on graphite. It might be thought that these layers behave as two-dimensional crystals. It turns out, however, that the interaction of the layers with the underlying substrate is very important for their stability and dynamics. One finds a rich variety of phases, both commensurate and incommensurate with the periodicity of the graphite layers. The last few years there is a strong interest in the experimental and theoretical study of these phases. In principle, one can apply the same lattice dynamics methods to these layers as applied to bulk solids. In practice, however, a considerable amount of analytical work had to be performed first, in order to expand the molecule-substrate interaction potential in such a form that it can be used in lattice dynamics calculations. This work involves the displacement expansions used in bulk solids, as well as two-dimensional Fourier and displacement expansions of the substrate potential (see Chapters 5 and 6). The resulting formulas have been implemented in the computer programs applied to the calculations for N_2, H_2 and D_2 layers on graphite described in Chapters 7 and 8.

PART A

DYNAMICS OF MOLECULAR CRYSTALS

1. Vibron band structure in chlorinated benzene crystals; lattice dynamics calculations and Raman spectra of 1,2,4,5-tetrachlorobenzene

A.P.J.M. Jongenelis[a], T.H.M. van den Berg[b], A.P.J. Jansen[b], J. Schmidt[a] and A. van der Avoird[b]

a) *Center for the Study of Excited States of Molecules, Huygens Laboratory, Leiden University, P.O. Box 9504, Leiden, The Netherlands*
b) *Institute of Theoretical Chemistry, University of Nijmegen, Toernooiveld, Nijmegen, The Netherlands*

(Published in J.Chem. Phys. 89, 4023 (1988))

Abstract. From a combined theoretical and experimental study of 1,2,4,5-tetrachlorobenzene (TCB) we conclude that this crystal shows many interesting effects. In agreement with earlier optical measurements, which probe the complete vibron band structure of TCB, we calculate that several of the vibron modes have the dispersion of a one-dimensional crystal with stacks of molecules along the a axis. The inclusion of fractional atomic charges in the atom-atom potential used in the calculations is absolutely necessary to obtain the correct vibron band widths. Also the sign of the vibrational coupling matrix elements, which is given correctly by the calculations, is determined by these charges. For other properties, such as the crystal stability, the phonon frequencies, the site splitting in the vibron bands, and also the dispersion of the lower frequency vibrations, the interactions between the "one-dimensional" stacks are essential, however. The calculations predict further, in qualitative agreement with the Raman spectra, that the splitting between the pairs of inequivalent vibron bands in α-TCB (the site splitting) is significantly larger than the factor group splitting in β-TCB. Finally we have found that, for those vibrations where the conditions are shown by the calculations to be favorable, the ^{35}Cl / ^{37}Cl isotope effects are clearly visible in the Raman spectra.

1.1. Introduction

In a recent paper [1] an optical technique has been described to measure the frequencies of vibrational excitons in the molecular crystal of 1,2,4,5-tetrachlorobenzene (TCB). In contrast with the usual infrared and Raman spectroscopy, this technique yields not only the frequencies of vibrons with wave vector $\boldsymbol{k} = 0$, but it gives information on the complete vibron band structure. In the experiment the crystal is optically excited to the lowest electronic triplet exciton state and the phosphorescence spectrum to the vibrationally excited levels of the electronic ground state is inspected. The optical excitation and emission obey the selection rule $\Delta\boldsymbol{k} = 0$, so that originally only the $\boldsymbol{k} = 0$ triplet exciton state is populated. This state relaxes to all other $\boldsymbol{k}$ states in a time short compared with its decay time, and the population distribution of the triplet exciton band becomes thermalized. By controlling the temperature (in the range from 0.4 to 4.2 K), or the time interval between excitation and detection of the phosphorescent emission, the relative population of the different k states can be affected, and the dispersion of the electronic triplet exciton band and of the vibron bands can be probed. Because the triplet exciton band structure is known (one-dimensional, with a band width of 1.36 cm^{-1} and with the $k = 0$ states at the top of the band [2]), information about the vibron band structure can be directly obtained.

The interesting result obtained from these measurements is that the vibron bands can be interpreted by a simple one-dimensional band model, analogous to that for the electronic triplet excitation. In other words, it could be concluded that the couplings between the vibrational excitations are significant only *within* the stacks of TCB molecules that lie along the crystallographic a axis. This conclusion applies to the three different (gerade) vibrational modes that have been studied in detail, but it is striking that the actual size of the coupling parameters that determine the band widths is very different for the various modes and also that their signs are different.

In the present paper we describe lattice dynamics calculations on TCB which have been undertaken in order to understand the origin of the observed phenomena. In particular, it is interesting to investigate the one-dimensional character of the vibron bands and the relationship between their dispersion and the intermolecular interactions. Further, since TCB crystallizes in two different phases, it might be possible to reveal the effect of the crystal structure on the vibronic dispersion. These phases are the triclinic α phase, with two molecules in the unit cell that are not related by any space group operation [3,4], and the monoclinic β phase with two molecules in the unit cell that are related by a glide-plane [5]. The α phase is stable below 188 K, the β phase above this temperature.

Lattice dynamics calculations on chlorinated benzene crystals have been reported earlier [4,6-10]. Especially Bonadeo *et al* [4,6-8] have investigated the structure and stability of the α and β phases of TCB and the lattice modes (phonons). The internal vibrations were not considered because it was expected that the vibron band structure in chlorinated benzenes would be completely obscured by the broadening effects due to the occurrence of various ^{35}Cl and ^{37}Cl isotope combinations [7]. In the present paper we have explicitly calculated the chlorine isotope effects and we find that, rather than obscuring the vibron band structure, they yield interesting phenomena for some of the vibrational modes in TCB.

In addition, we have measured Raman spectra for both phases of TCB. By comparing the phonon frequencies for these phases with those previously reported [7], the Raman spectra ascertained that the experiments described in [1] were indeed performed on α-TCB. The Raman measurements on the internal vibrations, yielding vibron frequencies for $k = 0$, can be compared with the results of the lattice dynamics calculations on α- and β-TCB.

1.2. Lattice dynamics method

1.2.1. Theory

The lattice dynamics calculations which yield the vibron and phonon frequencies have been made by the standard harmonic method, as extended by Taddei and Califano *et al* [11,12] in order to include vibrons and their coupling with the phonons. This extended method can be written very compactly as follows. The harmonic crystal hamiltonian

$$H = \frac{1}{2} \sum_{P} \boldsymbol{P}_P{}^{\dagger} \boldsymbol{G}_P \boldsymbol{P}_P + \frac{1}{2} \sum_{P,P'} \boldsymbol{Q}_P{}^{\dagger} \boldsymbol{F}_{PP'} \boldsymbol{Q}_{P'} \quad , \tag{1}$$

with the generalized inverse inertia tensor $\boldsymbol{G}_P$ and force constant matrix $\boldsymbol{F}_{PP'}$ (defined below) is expanded in the normal coordinates $\boldsymbol{Q}_P = \{Q_P^\lambda \mid \lambda = 1, \ldots, 3N\}$ of the free molecules and their conjugate momenta $\boldsymbol{P}_P$. The column vectors $\boldsymbol{Q}_P$ are defined as

$$Q_P^\lambda = \begin{cases} u_P^\lambda & \text{for } \lambda = 1,2,3 \\ \theta_P^\lambda & \text{for } \lambda = 4,5,6 \\ q_P^\lambda & \text{for } \lambda = 7,\ldots,3N \end{cases} \quad , \tag{2}$$

where N is the number of atoms in each molecule P. The "external" molecular coordinates u_P^λ and θ_P^λ describe the center of mass translations and the rigid body rotations of the molecules, respectively, relative to the lattice-fixed frame. The "internal" molecular coordinates q_P^λ are the normal coordinates of the free molecule vibrations. The latter can be calculated by means of Wilson's $\boldsymbol{FG}$-matrix method [13] if the intramolecular force field is known. Thus they are obtained with respect to a molecule-fixed frame of reference, but they can be easily rotated to the lattice frame.

Each of the (orthogonal) normal coordinates $\{Q_P^\lambda \mid \lambda = 1, \ldots, 3N\}$ is a function of the cartesian displacements $\boldsymbol{x}_P = \{x_P^i \mid i = 1, \ldots, 3N\}$ of the individual atoms. Conversely, the atomic displacements can be expressed in terms of the molecular normal coordinates as follows:

$$\boldsymbol{x}_P = \boldsymbol{A}_P \boldsymbol{Q}_P + \frac{1}{2} \boldsymbol{B}_P [\boldsymbol{Q}_P \otimes \boldsymbol{Q}_P] + \ldots \; . \tag{3}$$

The blocks of the linear transformation matrices $\boldsymbol{A}_P$ associated with the molecular translations u_P^λ and rigid body rotations θ_P^λ follow directly from the Eckart conditions [13]. The blocks associated with the vibrational normal coordinates q_P^λ are the (rotated) $\boldsymbol{FG}$-matrix eigenvectors of the free molecules. The non-linear terms in Eq. (3), which are required in order to ensure the correct invariance conditions (see below), with the cross product denoting the dyadic product of the two column vectors $\boldsymbol{Q}_P$, arise from the use of curvilinear rotational coordinates θ_P^λ. The coefficients $\boldsymbol{B}_P$ of the rotational-rotational blocks have been given by Neto *et al* [14,15]. Further non-zero coefficients $\boldsymbol{B}_P$ occur for the mixed rotational-vibrational blocks; these can be derived similarly.

The general force constant matrix $\boldsymbol{F}_{PP'}$ is given by

$$\boldsymbol{F}_{PP'} = \boldsymbol{A}_P{}^\dagger \boldsymbol{\Phi}^{(2)}_{PP'} \boldsymbol{A}_{P'} + \delta_{PP'} \boldsymbol{\Phi}^{(1)}_P \boldsymbol{B}_P + \delta_{PP'} \boldsymbol{\omega}^2_P \quad , \tag{4}$$

where $\boldsymbol{\Phi}^{(1)}_P$ and $\boldsymbol{\Phi}^{(2)}_{PP'}$ are matrices comprising the first and second derivatives of the intermolecular crystal potential with respect to the cartesian atomic displacements in the molecules P and P', and $\boldsymbol{\omega}^2_P$ is a diagonal matrix containing the squares of the vibrational frequencies of the free molecules, i.e. the $\boldsymbol{FG}$-matrix eigenvalues. If the intermolecular potential is approximated by a sum of analytical atom-atom potentials, of exp-6-1 type for instance, then the derivatives $\boldsymbol{\Phi}^{(1)}_P$ and $\boldsymbol{\Phi}^{(2)}_{PP'}$ can be easily found, using the formulas given in Ref. [11].

In the original paper by Taddei *et al* [11], the rotational coordinates θ^λ_P have been linearized or, in other words, the matrices $\boldsymbol{B}_P$ occurring in Eq. (3) and in the self term $\boldsymbol{F}_{PP}$ of Eq. (4) have been set to zero. In that case, the crystal hamiltonian is not invariant under overall rotations of the crystal, however. Later it has been shown [15] that the inclusion of the second term of Eq. (4) in the self term $\boldsymbol{F}_{PP}$ leads to the correct rotational invariance conditions [12] (if one starts from a crystal with the molecules adopting their equilibrium positions and orientations). The translational invariance conditions are satisfied in any case.

The generalized inertia tensor $\boldsymbol{G}^{-1}_P$ can be written as

$$\boldsymbol{G}^{-1}_P = \boldsymbol{A}_P{}^\dagger \boldsymbol{g}^{-1}_P \boldsymbol{A}_P \tag{5}$$

with the mass tensor $\boldsymbol{g}^{-1}_P$ associated with the cartesian atomic coordinates $\boldsymbol{x}_P$ containing the atomic masses on the diagonal. Fourier transformation of the crystal hamiltonian (1) and diagonalization of each block corresponding with a given wave vector $\boldsymbol{k}$ yields the lattice vibrations which, in general, can be (mixed) translational phonons, librational phonons and vibrons.

1.2.2. Test calculations on benzene

The computer program in which we have implemented this method has been tested via calculations on solid benzene, using the same intra- and intermolecular potential as Taddei *et al* [11] and Neto *et al* [14]. Both ways of writing the self term $\boldsymbol{F}_{PP}$ in Eq. (4) have been investigated. The linearized transformation between the atomic and the molecular displacements, i.e. setting $\boldsymbol{B}_P = 0$, gave results which are practically identical to those of Taddei *et al* [11]. Inclusion of the full self term from Eq. (4), which we have derived by using the rotational invariance conditions [12], gave results identical to those of Neto *et al* [14]. The translational phonon modes do not depend on the way of writing the rotational and rotational-vibrational self terms; the effect on the vibron frequencies is practically zero. Only the libron frequencies increase, by about 10%, when the rotational displacement coordinates are linearized. In the calculations on TCB described in the sequel of this paper we have included the full self term as given by Eq. (4).

Further, we may reiterate the conclusion of Taddei *et al* [11] that there is very little mixing between the lattice modes (translational phonons and librons) and the vibrons. In separate calculations the frequencies of the lattice modes in benzene differ only by about 1 cm^{-1} and the vibron frequencies by less than 0.2 cm^{-1} from the results of the complete calculation. In the case of TCB which is discussed below, the situation is similar. Although the lowest vibron modes have frequencies in the same range as the lattice modes, they hardly mix with the latter. Even the frequency of the lowest internal vibration, the 80 cm^{-1} ($\mathrm{A_u}$) mode, is shifted by less than 2 cm^{-1} because of its mixing with the phonons.

1.3. Intra- and intermolecular potential and the molecular vibrations of TCB; isotope effects

The intramolecular potential which we have used to calculate the vibrations of the free TCB molecule is Scherer's force field for chlorinated benzenes [16,17]. This harmonic force field contains the force constants with respect to the internal coordinates: stretch, bending, torsion and out-of-plane wagging, and it includes also mixed terms. Using the well-known formulas [13] for the transformation from such internal coordinates to the cartesian atomic displacements, we have written the $\boldsymbol{FG}$-matrix problem in terms of the latter coordinates. Solution of this problem yields 6 zero eigenvalues which correspond with the 3 center-of-mass translations u_{p}^{λ} and the 3 rotations $\theta_{\mathrm{p}}^{\lambda}$, and 30 eigenvalues and eigenvectors which represent the vibrational normal modes q_{p}^{λ} of the free TCB molecule, cf. Eq. (2). The vibrational eigenvectors have been directly used as input for the lattice dynamics calculations, cf. Sec. 1.2; instead of the eigenvalues we have substituted the squares of the *experimental* frequencies [16,17] into Eq.(4), however. The experimental frequencies are close to the values calculated from Scherer's force field but, according to the reasoning of Taddei *et al* [11], they probably yield slightly better results.

We have explicitly studied the effect of isotopic substitution on our calculated vibrational frequencies by considering the seven possible distributions of $^{35}\mathrm{Cl}$ and $^{37}\mathrm{Cl}$ isotopes over the TCB molecule. For each of the seven different molecular species, with different atomic mass distributions, we have calculated the vibrational frequencies using Scherer's force field. If we weight each species with a factor that can be derived from the natural isotope abundance, $^{35}\mathrm{Cl}/^{37}\mathrm{Cl} = 0.7553/0.2447$, we obtain the root mean square amplitude of the vibrational frequency distribution, relative to the (isotopically weighted) average frequency. The size of the isotope effect so defined, for each particular mode in TCB, is indicated in Table I. The average frequency for a given mode is almost the same as the frequency calculated for that mode with all chlorine atoms

Table I. The frequencies of the internal vibrations of TCB in cm^{-1} calculated with the force field given by Scherer [16,17]. The calculations have been performed for all 7 different TCB species which can be formed with ^{35}Cl and ^{37}Cl atoms (natural abundance 3:1). The column "Average" lists the (abundance weighted) average frequencies and the column "rmsd" the (weighted) root mean square deviation of the frequency distribution. The experimental frequencies with the symmetry assignments are also from Ref. [16,17].

Experimental	Calculation			
(symmetry)	$(^{35}Cl)_4$	$(^{37}Cl)_4$	Average	rmsd
80 (A_u)	81.5	79.3	81.0	0.47
140 (B_{3u})	132.5	131.3	132.3	0.26
190 (A_g)	197.8	192.4	196.4	1.24
209 (B_{2u})	210.1	204.6	208.7	1.29
218 (B_{1u})	210.2	205.8	209.5	0.81
225 (B_{2g})	227.5	226.3	227.3	0.26
312 (B_{3g})	313.0	305.6	311.2	1.62
348 (B_{1g})	352.1	351.5	352.0	0.13
352 (A_g)	347.4	338.7	345.5	1.82
442 (B_{3u})	446.7	446.7	446.7	0.01
510 (B_{1u})	502.7	494.9	500.9	1.66
511 (B_{3g})	509.4	507.7	509.0	0.34
600 (A_u)	600.4	600.3	600.4	0.03
645 (B_{2u})	656.8	650.2	655.3	1.41
681 (B_{2g})	681.6	681.6	681.6	0.00
684 (A_g)	685.8	684.8	685.5	0.21
860 (B_{2g})	867.1	867.1	867.1	0.00
868 (B_{3g})	858.2	855.2	857.6	0.65
878 (B_{3u})	870.3	870.2	870.3	0.01
1063 (B_{1u})	1073.2	1072.5	1073.0	0.16
1118 (B_{2u})	1106.8	1106.4	1106.7	0.09
1165 (A_g)	1162.5	1161.3	1162.2	0.25
1226 (B_{2u})	1235.0	1235.0	1235.0	0.01
1240 (B_{3g})	1241.3	1241.3	1241.3	0.00
1327 (B_{1u})	1327.3	1327.2	1327.3	0.03
1448 (B_{2u})	1455.3	1455.2	1455.3	0.02
1549 (A_g)	1529.0	1528.8	1529.0	0.00
1566 (B_{3g})	1573.2	1573.2	1573.2	0.00
3070 (A_g)	3069.7	3069.7	3069.7	0.00
3094 (B_{1u})	3070.2	3070.2	3070.2	0.00

given their average nuclear mass, 35.453 a.m.u.. If we use the nuclear mass of ^{35}Cl for all chlorine atoms in TCB our calculated vibrational frequencies are practically the same as Scherer's [16,17]. How these isotope splittings of the vibrational frequencies can manifest themselves in the solid will be discussed in Sec. 1.4.

Intermolecular potentials for chlorinated benzenes are available from Bonadeo *et al* [6] and from Reynolds *et al* [10]. Both these potentials are based on the empirical atom-atom exp-6 interaction model. Reynolds *et al* have supplemented their potential by Coulomb interactions, by introducing polarized C-Cl bonds with negative charges of $-0.25e$ on the Cl atoms. In our lattice dynamics studies of TCB we have used both these intermolecular potentials; the relevant parameters are given in Table II. The use of polarized bonds appeared to be essential (see Sec. 1.4); we have introduced also polarized C-H bonds with a positive charge of $+0.10e$ or $+0.15e$ on the H-atoms.

Table II. Potential parameter sets according to Bonadeo *et al* [6] and Reynolds *et al* [10] for the exp-6(-1) atom-atom potential $V(r_{ij}) = B\exp[-Cr_{ij}] - Ar_{ij}^{-6} + Dr_{ij}^{-1}$. The electrostatic parameter D in the Reynolds parameter set corresponds to the following fractional atomic charges: $C_1 = -0.10e$, $C_2 = +0.25e$, $H = +0.10e$ and $Cl = -0.25e$ where C_1 denotes the C atoms of the C—H bonds and C_2 the C atoms of the C—Cl bonds.

Bonadeo potential set [6]

Interaction	A (kcal mol^{-1} Å^6)	B (kcal mol^{-1})	C (Å^{-1})	D (kcal mol^{-1} Å)
C — C	568	83630	3.600	—
C — H	125	8766	3.670	—
C — Cl	−631	44200	3.653	—
H — H	27.3	2654	3.740	—
H — Cl	1005	33300	3.623	—
Cl — Cl	3650	263000	3.510	—

Reynolds potential set [6]

Interaction	A (kcal mol^{-1} Å^6)	B (kcal mol^{-1})	C (Å^{-1})	D (kcal mol^{-1} Å)
C_1 — C_1	568	83630	3.60	3.32
C_1 — C_2	568	83630	3.60	−8.30
C_1 — H	125	8766	3.67	−3.32
C_1 — Cl	1140	180000	3.62	8.30
C_2 — C_2	568	83630	3.60	20.75
C_2 — H	125	8766	3.67	8.30
C_2 — Cl	1140	180000	3.62	−20.75
H — H	27.3	2654	3.74	3.32
H — Cl	250	18000	3.70	−8.30
Cl — Cl	2300	426000	3.65	20.75

1.4. Lattice dynamics calculations on α- and β-TCB

1.4.1. Crystal structure and phonons

From x-ray diffraction [3] it is known that the crystal structure of α-TCB is triclinic with two molecules in the unit cell. The positions and orientations of these molecules in the cell and the space group of the crystal, $P1$ or $P\bar{1}$, could not be uniquely inferred from the x-ray data, however. Bonadeo *et al* [4] have solved this problem by using spectroscopic evidence, in combination with packing and lattice dynamics calculations based on the available empirical atom-atom potentials [6,10]. They found that the crystal space group of α-TCB is $P\bar{1}$ and that the centers of mass of both molecules coincide with inversion centers of the crystal. The orientations of the two primitive molecules are not related by any symmetry operation; they have been found by minimization of the calculated lattice energy.

We have started our calculations by repeating the structure optimization of Bonadeo *et al* [4], using the same empirical atom-atom potentials [6,10]. However, we have chosen a more regular molecular geometry than these authors, who used the strongly distorted nonplanar geometry derived from the x-ray data on β-TCB. Our choice is justified by the observation that the older x-ray measurements on p-dichlorobenzene [18] seem to imply a strongly distorted geometry as well, whereas the more recent x-ray data [19] lead to a much more regular geometry. The structure and cohesion energy that we calculate agree fairly well with the results in Ref.[4], but we could not compare the molecular orientation angles to better than a few degrees because of the differences in the molecular geometries. We have also tried to relax the unit cell parameters in our structure optimization. Using the experimental triclinic unit cell as a starting point, we obtained a monoclinic lattice, however, with the two molecules in the unit cell being symmetry related as in β-TCB. So we conclude that the empirical atom-atom potentials [6,10] are not sufficiently accurate to reproduce the experimental structure of α-TCB in a full structure optimization. In our further calculations on α-TCB we have fixed the unit cell parameters at the experimental values [3] determined at $T = 150$ K (see Table III) and we have optimized the orientations of both molecules in the unit cell independently (see Table IV), for each potential used, before we started the lattice dynamics calculations.

Table III. Unit cell parameters for the two phases of 1,2,4,5-TCB from Refs. [3] and [5].

	Unit cell parameters of TCB	
	Triclinic α phase at 150 K	Monoclinic β phase at ~ 300 K
a	3.76 Å	3.86 Å
b	10.59 Å	10.63 Å
c	9.60 Å	9.73 Å
α	92.5°	90°
β	102.5°	103.5°
γ	95°	90°

The crystal structure of β-TCB is completely known from x-ray diffraction and Nuclear Quadrupole Resonance [5] (although the matrix of direction cosines given in Ref.[5] contains a mistake). This phase is monoclinic, space group $P2_1/c$, with two molecules in the unit cell. These molecules are located at inversion centers and their

Table IV. Calculated fractional atomic coordinates given by Bonadeo *et al* [4] for the optimum crystal structure of α-TCB and x-ray data for β-TCB [5], compared with our results using Bonadeo's atom-atom potential parameter set. In our calculations we used as bond lengths C—H = 1.08 Å, C—C = 1.39 Å and C—Cl = 1.74 Å, bond angles ∠ C—C—C = ∠ C—C—H = ∠ C—C—Cl = 120° and masses $m_H = 1.008$ a.m.u., $m_C = 12.011$ a.m.u. and $m_{Cl} = 35.453$ a.m.u. Calculations using Reynolds' parameter set with or without fractional atomic charges yield about the same crystal structure.

α-TCB	Bonadeo *et al* [4]			This work		
Molecule 1	*x*	*y*	*z*	*x*	*y*	*z*
C(1)	0.0201	0.1267	0.0425	0.0255	0.1272	0.0469
C(2)	0.1761	0.0322	0.1407	0.1548	0.0379	0.1423
C(3)	0.1710	−0.0906	0.0882	0.1293	−0.0893	0.0954
Cl(1)	0.0011	0.2848	0.0993	0.0575	0.2864	0.1055
Cl(2)	0.4070	0.0763	0.3187	0.3485	0.0854	0.3203
H(3)	0.2976	−0.1571	0.1606	0.2297	−0.1587	0.1695
Molecule 2						
C(1)	−0.0460	0.6240	0.4593	−0.0085	0.6246	0.4606
C(2)	−0.1824	0.5242	0.3661	−0.1651	0.5249	0.3612
C(3)	−0.1497	0.4042	0.4175	−0.1566	0.4003	0.4006
Cl(1)	−0.0637	0.7792	0.4030	−0.0191	0.7807	0.4112
Cl(2)	−0.4212	0.5580	0.1972	−0.3718	0.5562	0.1874
H(3)	−0.2614	0.3336	0.3492	−0.2783	0.3228	0.3234
β-TCB	Experiment [5]			This work		
Molecule 1	*x*	*y*	*z*	*x*	*y*	*z*
C(1)	0.0193	0.1252	0.0425	0.0315	0.1254	0.0417
C(2)	0.1817	0.0322	0.1362	0.1714	0.0312	0.1378
C(3)	0.1623	−0.0929	0.0937	0.1399	−0.0941	0.0961
Cl(1)	0.0434	0.2818	0.0957	0.0708	0.2823	0.0939
Cl(2)	0.4090	0.0727	0.3067	0.3859	0.0703	0.3104
H(3)	0.2885	−0.1650	0.1666	0.2486	−0.1672	0.1709

orientations are related by reflection with respect to the *ac* plane. In our calculations on β-TCB we have always used the experimental structure at T = 300 K (given in Table III) as a starting point, but we have optimized the molecular orientations (see Table IV), while maintaining the reflection symmetry.

Phonon frequencies of α-TCB calculated with the atom-atom potentials of Bonadeo *et al* [6] and Reynolds *et al* [10], with and without addition of fractional atomic charges (see Table II), are listed in Table V. In the lattice sums for each of the two primitive molecules we have included all molecules lying within a center-of-mass distance of 12 Å, which is amply sufficient to converge the results. The results deviate substantially from those of Bonadeo *et al* [4,8] even though we used the same atom-atom potential, because of the differences in the molecular geometries used. We have checked that changes in

Table V. Observed and calculated frequencies in cm^{-1} of the lattice vibrations in α-TCB. Our values are obtained from complete calculations including the vibrons; values from rigid body calculations are given in parentheses. The cohesion energy for the optimum crystal packing is also given.

			This work		
Experiment [7]		Bonadeo *et al* [4]	Bonadeo pot.	Reynolds pot.	Reynolds pot. with charges
(u)	—	47	46 (48)	51 (53)	47 (49)
(u)	—	63	76 (89)	77 (87)	78 (85)
(u)	—	90	90 (99)	108 (107)	94 (104)
(g)	33	33	21 (23)	26 (29)	25 (28)
(g)	43	38	44 (45)	42 (44)	43 (46)
(g)	48	46	50 (52)	55 (57)	56 (58)
(g)	55	62	66 (68)	69 (71)	73 (74)
(g)	68	68	70 (72)	73 (76)	76 (79)
(g)	—	88	95 (102)	94 (98)	94 (98)
Cohesion energy in kcal mol^{-1}					
		−18.82	−17.67	−22.05	−19.81

the molecular orientation angles of the size that corresponds with the differences in the molecular geometries alter the phonon frequencies by substantial amounts. The differences between the results obtained from the different atom-atom potentials are not very large; the addition of the Coulomb interactions by putting fractional charges on the atoms does not have a very significant effect on the phonon frequencies. Moreover, part of these differences are caused by the changes in the equilibrium orientations of the molecules that result from the optimization procedures with the different potentials. The agreement with experimental data is reasonably good. We have not tried to minimize the remaining deviations, as it is sometimes done, by adjusting the parameters in the atom-atom potentials.

In order to verify whether α-TCB is really an effective one-dimensional crystal as the experimental data [1] suggest, we have also made lattice dynamics calculations on a single stack of TCB molecules lying along the crystallographic a axis. If we use the molecular orientations found in the optimization of the three-dimensional crystal structure, some phonon frequencies become imaginary, however, which indicates the instability of this one-dimensional crystal. On the other hand, if we relax the molecular orientations in the one-dimensional stack, the optimized structure becomes very different from the actual structure of the stacks in α- and β-TCB. Moreover, we have found that the phonon frequencies show considerable dispersion in the directions orthogonal to the stacks. So we conclude that both for the crystal packing and for the lattice modes (and, as we shall see below, also for the dispersion of the lower frequency vibrons and for the splitting of all $\boldsymbol{k} = 0$ vibrons) the interactions *between* the stacks in TCB are essential.

1.4.2. Vibron frequencies for $\boldsymbol{k} = 0$

Before we discuss the complete dispersion in the vibron bands, we consider the splitting in the $\boldsymbol{k} = 0$ vibron frequencies, since this splitting can be directly obtained from the Raman spectra given in Sec. 1.5 and it also plays a role in the interpretation of the experimental data of paper [1]. The splittings obtained from the lattice dynamics calculations are listed in Table VI and they can be understood as follows. Both in α- and β-TCB there are two molecules in the unit cell and the molecular centers of inversion coincide with the inversion centers of the whole crystal. So we can expect [4] that all (gerade) Raman active vibrational modes of the free TCB molecule will remain Raman active in the crystal, and that all (ungerade) infrared active modes of the molecule will also be infrared active in the solid. For $\boldsymbol{k} = 0$ each of these modes will split into two peaks with frequencies that are different (in principle). In β-TCB the two molecules in the unit cell are equivalent and the splitting of the $\boldsymbol{k} = 0$ vibron frequencies is caused only by off-diagonal terms $\boldsymbol{F}_{PP'}$ in the dynamical matrix of Eq. (4). In α-TCB the two primitive molecules are not related by symmetry, however, so that also the single-molecule or crystal-field terms $\boldsymbol{F}_{PP}$ may be different. So in α-TCB the splitting of the $\boldsymbol{k} = 0$ vibrons is caused both by the off-diagonal terms $\boldsymbol{F}_{PP'}$ and by the differences in the crystal-field terms $\boldsymbol{F}_{PP}$ for the two inequivalent molecules. In Table VI we observe that, indeed, the frequency splittings between most of the $\boldsymbol{k} = 0$ vibrons in α-TCB are considerably larger than the splittings in β-TCB. The differences in the crystal field terms appear to be dominant in determining the splitting. Since these differences in the single-molecule terms $\boldsymbol{F}_{PP}$ are larger than the off-diagonal terms $\boldsymbol{F}_{PP'}$ we find that most of the vibrons are localized on either one of the two sublattices in α-TCB.

In our calculations we have further analyzed the origin of the crystal-field splittings in α-TCB and their dependence on the intermolecular potential. We have found that they are not so much caused by the interactions between molecules within the stacks along the $\boldsymbol{a}$ axis, but mainly by the interactions between molecules lying in adjacent stacks. So, as far as these splittings are concerned, α-TCB is not an effective one-dimensional crystal. It is the repulsive exponential terms in the atom-atom potential that account for most of the splittings. Their effect is partly compensated by an opposite but smaller effect from the attractive r^{-6} interactions. The Coulomb interactions between fractionally charged atoms have practically no effect on the crystal-field splittings. We have also found that these splittings depend very sensitively on the molecular orientations. Changing the atom-atom potential changes the splittings too, but mainly through the change in the equilibrium orientations of the molecules. The strong dependence of the vibron splittings on the molecular orientations might indicate a rather

Table VI. Calculated splittings for $k = 0$ vibron frequencies and vibron band widths in the a^* directions for α- and β-TCB in cm^{-1}.

	α-TCB				β-TCB	
	Reynolds pot.		Reynolds pot. with charges		Reynolds pot. with charges	
Symmetry	Splitting	Dispersion[a]	Splitting	Dispersion[a]	Splitting	Dispersion[a]
190 (A_g)[b]	6.5	−2.3 / 0.7	4.8	−1.0 / 1.8	3.6	−4.4 / −1.2
209 (B_{2u})[b]	4.7	−12.8 / −3.1	3.7	−8.1 / 0.5	0.0	−2.0 / 0.5
218 (B_{1u})[b]	6.7	7.4 / 3.9	4.2	8.5 / 4.0	1.0	3.4 / 2.0
225 (B_{2g})[b]	12.1	−3.5 / −3.4	12.0	−2.1 / −1.9	3.5	−1.6 / −1.4
312 (B_{3g})	7.1	0.5 / 0.2	6.0	0.4 / 0.3	0.6	−0.3 / 0.7
348 (B_{1g})	6.9	−9.1 / −6.1	11.5	−15.3 / −8.7	0.4	−9.5 / −9.4
352 (A_g)	6.8	0.7 / 0.0	5.4	1.0 / 0.0	0.2	−0.5 / 1.2
442 (B_{3u})	8.4	−1.8 / 0.8	7.9	−3.0 / 1.5	0.1	−1.0 / −0.7
510 (B_{1u})	3.7	−1.2 / −0.2	2.6	−0.6 / 0.6	0.3	0.1 / 0.1
511 (B_{3g})	3.0	0.0 / 0.0	3.2	0.0 / 0.0	0.8	−0.1 / 0.1
600 (A_u)	3.2	1.4 / 1.3	4.4	2.5 / 2.4	0.0	1.6 / 1.5
645 (B_{2u})	1.2	−1.0 / 0.5	1.4	1.7 / 0.2	0.8	0.9 / 0.8
681 (B_{2g})	3.1	0.4 / 0.0	3.5	1.0 / 0.9	0.3	0.6 / 0.6
684 (A_g)	6.4	0.6 / 0.6	5.8	1.2 / 1.1	0.4	0.9 / 0.8
860 (B_{2g})	4.9	0.0 / 0.0	1.8	−2.5 / −2.5	0.4	−2.5 / −2.3
868 (B_{3g})	0.6	0.0 / 0.0	0.3	0.4 / 0.1	0.5	0.3 / 0.2
878 (B_{3u})	4.9	−0.1 / 0.3	2.5	−4.0 / −4.0	1.2	−3.8 / −3.5
1063 (B_{1u})	1.5	0.0 / 0.0	1.7	0.3 / 0.3	0.2	0.3 / 0.3
1118 (B_{2u})	7.4	0.0 / 0.0	6.1	0.4 / 0.1	0.1	0.2 / 0.2
1165 (A_g)	0.8	0.0 / 0.0	0.9	1.1 / 1.1	0.5	1.0 / 0.6
1226 (B_{2u})	0.2	−0.2 / −0.2	0.2	0.1 / 0.1	0.1	0.1 / 0.1
1240 (B_{3g})	9.1	0.0 / 0.0	7.5	0.9 / 0.9	1.3	1.5 / 0.2
1327 (B_{1u})	1.1	−0.1 / −0.1	1.3	0.1 / 0.1	0.0	0.2 / 0.2
1448 (B_{2u})	3.2	0.0 / 0.0	2.6	1.1 / 1.1	0.0	1.0 / 1.0
1549 (A_g)	0.6	−0.2 / −0.2	0.7	−0.3 / −0.3	0.1	−0.2 / −0.2
1566 (B_{3g})	0.8	0.0 / 0.0	0.7	0.1 / 0.1	0.3	0.3 / 0.0
3070 (A_g)	10.1	0.0 / 0.0	12.8	0.3 / 0.3	0.5	0.5 / 0.1
3094 (B_{1u})	10.0	0.0 / 0.0	12.7	0.3 / 0.3	0.1	0.2 / 0.1

[a] The two columns refer to the widths of the two bands.

[b] Band widths in the b^* and c^* directions of the Brillouin zone are smaller than 0.5 cm^{-1}, except for these modes.

important vibration-rotation coupling. Although this coupling is indeed visible, for instance in the differences between the non-rigid and rigid molecule (gerade) lattice mode frequencies in Table V, it does not lead to substantial vibron-phonon mixing. Even the lowest vibron frequencies shift by less than 2 cm^{-1} through mixing with the phonons (see the end of Sec. 1.2). We return to the splittings of the $k = 0$ vibron frequencies in α- and β-TCB after the presentation of the Raman spectra in Sec. 1.5.

1.4.3. Vibron band structure

The dispersion calculated for some typical vibrons, along various directions in the Brillouin zone, is illustrated in Fig. 1 and the band widths for most of the vibrons in α- and β-TCB are tabulated in Table VI. These results have been obtained with the atom-atom potential of Reynolds with and without fractional atomic charges. As can be seen in Table VI the vibron band widths in the two phases of TCB are about the same. Since the crystal structure of α-TCB is so similar to that of β-TCB and since we found from our calculations that the band width of the vibrons is hardly affected by small changes in the molecular orientations, this behavior can be understood. It is in marked contrast with the variation of the lattice mode frequencies and with the splittings of the $\boldsymbol{k} = 0$ vibron frequencies, however, which depend sensitively on the molecular orientations and are significantly different in the two phases of solid TCB. The lattice dynamics calculations show further that in most cases there is almost no interaction between vibrons that correspond with different molecular vibrations, and that also the vibron-phonon mixing is practically negligible. So we could have obtained the vibron band structure from separate calculations in which only a specific molecular vibration is excited and we can discuss the results for each vibration separately. An exception with interesting consequences (discussed below) is the Fermi resonance between the 352 cm^{-1} (A_g) vibration and the 348 cm^{-1} (B_{1g}) mode. The mixing of these modes by the intermolecular interactions is symmetry allowed in the solid for all wave vectors $\boldsymbol{k}$. In the remainder of this section we concentrate on the calculations for α-TCB.

It appears from Fig. 1 that several vibrons show dispersion, mainly in the $\boldsymbol{a}^*$ direction of the Brillouin zone, and that the frequencies display a cosine dependence on the wave vector $\boldsymbol{k}$ in this direction. So the intermolecular interactions responsible for most of the dispersion in the vibrons occur within the stacks of molecules along the $\boldsymbol{a}$ axis, mainly between nearest neighbors. Therefore, the conclusion of a one-dimensional vibron band structure in paper [1] seems justified. Exceptions are the low frequency internal vibrations (80 (A_g), 190 (A_g), 209 (B_{2u}), 218 (B_{1u}) and 225 cm^{-1} (B_{2g})), which show significant dispersion in all directions of the Brillouin zone, indicating important interactions between molecules in different stacks.

An interesting observation is that without the fractional charges on the atoms the vibrational bands in the higher frequency region (above 600 cm^{-1}) are practically flat. So in order to obtain the correct experimentally observed dispersion of these bands (see below), it is absolutely necessary to add electrostatic interactions to the exp-6 atom-atom potential. For the lower frequency vibrons it appears that, in addition to the fractional atomic charges, also the repulsive exponential terms contribute to the dispersion. Since the amount of charge on the atoms is the dominating factor in determining the widths of the vibron bands, it is not surprising that calculations either with the potential sets of Reynolds *et al* or with the sets of Bonadeo *et al* yield practically the same vibron band structure if the same charges are used.

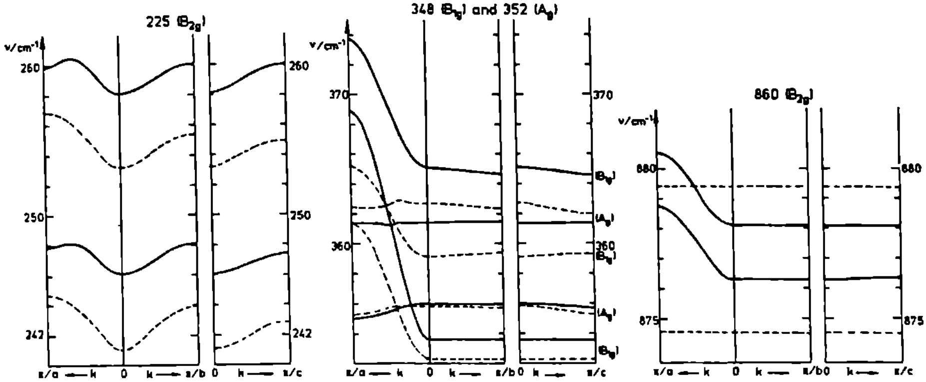

Fig. 1. Calculated dispersion along the a^* and b^* and c^* directions in the Brillouin zone of four different internal vibrational modes of α-TCBin cm^{-1}, using the potential set of Reynolds with (–) and without (– –) fractional charges.

The sign of the dispersion, which determines whether the $\boldsymbol{k} = 0$ states lie at the top of the vibron band or at the bottom, appears to be related to the charges on the atoms. If the Cl atoms, which carry a negative charge, are involved in the vibration, the sign is positive in most cases. The dispersion is negative if the H atoms, with a positive charge, are involved. One exception is the 348 cm^{-1} (B_{1g}) vibration, a pure C-Cl out-of-plane vibration, with a negative dispersion. As we discuss next, the calculated signs of the dispersion agree with the experimental results reported in Ref. [1].

The results of the calculations will now be compared in detail with the experimentally reported vibron band widths in Ref. [1]. A nice example of a one-dimensional vibron band with significant dispersion is the 860 cm^{-1} (B_{2g}) C-H out-of-plane vibration (see Fig. 1). This mode is reported in [1] as the 864 cm^{-1} (B_{2g}) vibration with a dispersion of -4.4 cm^{-1}. If we calculate the dispersion with a positive charge of $+0.10e$ on the H atoms we obtain -2.5 cm^{-1}. Increase of this charge to $+0.15e$ increases the dispersion to -5.5 cm^{-1}. Without the charges on the H atoms the band width would be smaller than 0.1 cm^{-1}.

Another example of a one-dimensional vibron band structure is the 684 cm^{-1} (A_g) vibration, an in-plane C-H bending. Experimentally no dispersion could be observed (less than 2 cm^{-1}). The calculations indeed show only a small dispersion of 1 cm^{-1} in the a^* direction, while the frequency in the other two directions of the Brillouin zone does not vary. Addition of charges does not alter these results.

An interesting case is the 352 cm^{-1} (A_g) vibration (see Fig. 1). This mode is reported as 355 cm^{-1} (A_g) with the largest experimental dispersion of about -15 cm^{-1}. In our calculations we observe a very small band width for this vibration, even with the charges on the atoms. In paper [1] it is already suggested that the (A_g) vibration is in resonance with the nearby lying 348 cm^{-1} (B_{1g}). In the calculations we observe that this (B_{1g}) C-Cl out-of-plane vibration has a large negative dispersion of -15 cm^{-1} (-10 cm^{-1} without charges on the Cl atoms), but this vibration should be very weak in the phosphorescence spectrum [20]. However, as we can read from Table I, the frequency of the strong 352 cm^{-1} (A_g) vibration is very sensitive to the mass of the Cl atoms and in the crystal this vibration will not lead to a single sharp peak, but to several peaks or to a broad structure of several cm^{-1} (see the remarks on isotope effects below). Further, we calculate that the (A_g) and (B_{1g}) modes mix for those wave vectors $\boldsymbol{k}$ for which their frequencies nearly coincide. Hence the 348 cm^{-1} (B_{1g}) vibration can steal intensity from the (A_g) mode over a wide frequency range, and the large dispersion of the (B_{1g}) mode can become visible in the spectrum. It can now be understood why it was impossible to fit the observed lineshape to a simple model [1].

For the 1165 cm^{-1} (A_g) breathing vibration, which is reported in paper [1] as 1159 cm^{-1} (A_g), the experimental dispersion of +7.4 cm^{-1} cannot be reproduced quantitatively. The addition of the charges on the Cl atoms gives a dispersion of only +1.0 cm^{-1} in the a^* direction. Increase of these charges from $-0.25e$ to $-0.40e$ increases the dispersion to +2 cm^{-1}, but with these large charges the optimization yields a crystal structure which is no longer stable. So, the correct size of the dispersion in this vibration cannot be obtained from the atom-atom potential; the sign is given correctly by the calculations.

Finally for the 225 cm^{-1} (B_{2g}) C-Cl out-of-plane vibration, which has been reported as 233 cm^{-1} (B_{2g}) with a dispersion of less than 2 cm^{-1}, we calculate a dispersion of about 3 cm^{-1} in all three directions of the Brillouin zone, caused mainly by the short range exponential terms in the atom-atom potential (see Fig. 1). The charges on the atoms change the absolute frequency, but the splitting at $\boldsymbol{k} = 0$ and the dispersion are hardly affected. We conclude that this vibration is not a simple one-dimensional vibrational exciton.

1.4.4. Isotope effects

The differences in the vibrational frequencies of TCB due to the occurrence of different ^{35}Cl and ^{37}Cl mass distributions can manifest themselves in different ways in the crystal. It should be realized that the 7 different molecular isotopic species, for which we have calculated the vibrational spectra in Sec. 1.3, occur randomly in the crystal. So TCB is a solid with random (isotopic) disorder, for which interesting effects can occur [21,22]. The nature of the spectrum is determined by the size of the isotope *shifts* in the *intra*molecular vibrational frequencies relative to the size of the *inter*molecular coupling elements in the dynamical matrix. The latter coupling elements also determine the size of the dispersion in the vibron bands given in Table VI.

One extreme situation occurs when the intramolecular shifts are large compared with the intermolecular couplings. In that case the vibrational exciton may become

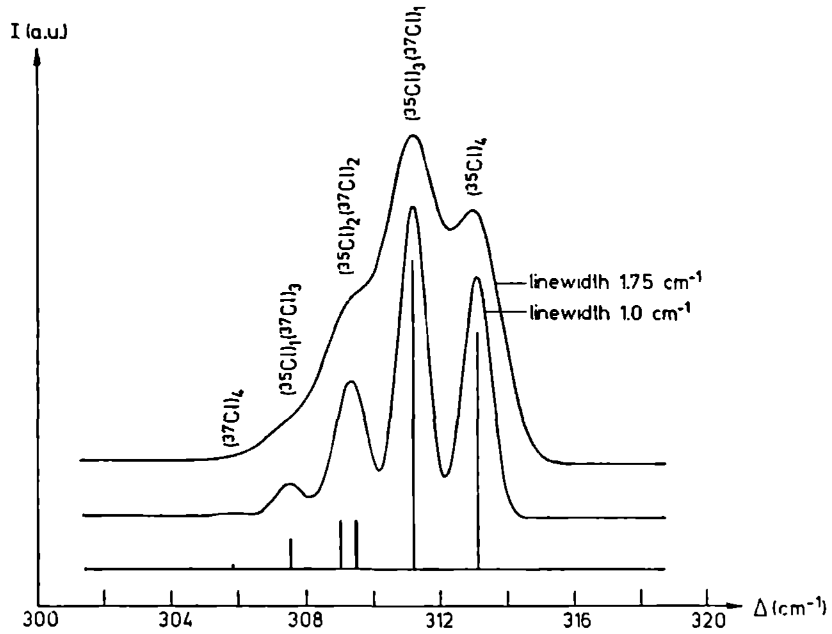

Fig. 2. Calculated frequencies of the 312 cm^{-1} (B_{3g}) mode for the 7 different Cl atomic mass distributions in TCB. The intensities are proportional to the natural abundance of each species. In the two curves the lines of the stick spectrum are broadened by Gaussian line shape functions with a width of 1.0 cm^{-1} and 1.75 cm^{-1}, respectively.

localized in clusters of isotopically identical molecules. Such clusters occur with random sizes in the crystal. The spectrum of the solid will then show the vibrational peaks of each of the 7 molecular species, broadened by the intermolecular interactions within these clusters. A clear example of this case is the 312 cm^{-1} (B_{3g}) vibration which has an intramolecular rms isotope shift of 1.62 cm^{-1} (see Table I) and intermolecular coupling matrix elements smaller than 0.15 cm^{-1} (i.e. a vibron dispersion less than 0.5 cm^{-1} (see Table VI)). In Fig. 2 we have constructed a theoretical spectrum for the 312 cm^{-1} (B_{3g}) mode in the solid by taking the frequencies and weights of the stick spectrum for the 7 molecular isotopic species, and simulating the cluster broadening, as well as temperature broadening and experimental resolution, by adding Gaussian line broadening to the stick spectrum of the molecular vibrations. We will see in Sec. 1.5 that this theoretical spectrum agrees very well with the experimentally observed Raman spectrum of this mode.

The other extreme occurs when the intramolecular isotope shifts are much smaller than the intermolecular couplings. In that case, the vibrational excitation will move very fast between the different isotopic species and the crystal spectrum will resemble the spectrum calculated for a homogeneous solid with the various isotopic masses replaced by the average mass (the so-called virtual crystal model). In the intermediate case, when the intramolecular shifts are comparable with the intermolecular couplings, the spectrum of the solid becomes very complex [21,22].

Another important effect due to the occurrence of the random isotope distributions concerns the selection rules. In general, random disorder lowers the symmetry and, thereby, weakens the selection rules. In the particular case of TCB, the most frequently occurring (42%) isotopic species contains three atoms of ^{35}Cl and one atom of ^{37}Cl. This species has no inversion symmetry, and neither have several other of the 7 possible species. Therefore, vibrational modes which are only Raman active in the homogeneous crystal will be infrared active as well, in the "natural" crystal. And, similarly, the infrared active modes will become Raman active too. This breaking of the selection rules will be most visible for those vibrational modes which involve particularly the chlorine atoms.

1.5. Raman experiments

1.5.1. *Experimental procedure*

Raman spectra were obtained by exciting the crystal with 1 Watt of the 488.0 nm line of a Spectra-Physics Ar-ion laser (model 171). The scattered light was inspected with a Spex model 1402 double monochromator with two 1200 ℓ/mm ruled gratings blazed at 1000 nm, which was operated at a resolution of about 1 cm^{-1}. The output was collected by a cooled photomultiplier (EMI 9658B) and processed by a photon counting system (EG&G 1182 amplifier/discriminator and Ortec 449 log/rate meter). The positions of the lines were measured relative to the laser line and were reproducible to 1 cm^{-1}. For the spectra at 210 K, just above the phase transition, and at 90 K, the sample was cooled in a stream of nitrogen vapor. The temperature of the sample was monitored via a resistor. Due to differences in location and heating of the sample the estimated accuracy of the temperature during the recording of these spectra is 5 K to 10 K. For the spectra between 4.2 K and 1.2 K the sample was immersed in liquid ^{4}He.

1,2,4,5-Tetrachlorobenzene was obtained from Aldrich Chemical Company and zone refined for 140 passes. Crystals were grown from the melt by the Bridgeman technique and annealed for 3 days at 2 °C below the melting point to reduce structural imperfections. Analysis by gas chromatography and mass spectroscopy established the presence of 20 ppm 1-bromo,2,4,5-trichlorobenzene and less than 1 ppm 1,2,3,5-TCB in the final product. The sample, a single crystal with a thickness of less than 0.5 mm, was selected using a polarization microscope.

1.5.2. Results and discussion

The Raman experiments have been performed for several purposes. First, the experiments yield the phonon frequencies, which makes it possible to distinguish between the α phase and the β phase crystal structure. In this way we were able to ascertain that the earlier experiments [1] were indeed performed on TCB crystals in the low temperature α phase since the observed frequencies are in agreement with those previously reported [7] . At 300 K and at 210 K the β phase lattice mode frequencies were observed. Upon cooling the crystal structure changed, giving the frequencies of the α phase. Either by quick or slow cooling it proved impossible to maintain β phase crystals at liquid helium temperatures.

Further, we wanted to see whether the site splittings calculated for $\boldsymbol{k} = 0$ in α-TCB and the ^{35}Cl/^{37}Cl isotope effects could be observed in the Raman spectrum. In Fig. 3 the Raman signals of six internal vibrations at different temperatures are shown. These vibrations have been selected because there are no nearby lying gerade vibrations, which facilitates the assignment of the lines. The assignments are based on the analysis of Scherer [16,17]. The β phase spectra show lines much broader than the resolution limit of the monochromator. Most lines are structureless at the high temperatures, but the 312 cm^{-1} (B_{3g}) line and the 352 cm^{-1} (A_g) line (not shown) have shoulders. In the region of the 225 cm^{-1} (B_{2g}) vibration three overlapping lines appear in the spectrum, with their peaks about 8 cm^{-1} apart. Upon cooling from 300 K to 210 K a decrease of all line widths is observed, which continues below the phase transition at 188 K. At 90 K the 511 cm^{-1} (B_{3g}) and the 3070 cm^{-1} (A_g) vibration are beginning to show a double peak structure, with a splitting of 1 and 2 cm^{-1}, respectively. The obvious conclusion is that the change from the monoclinic β phase, with two equivalent molecules in the unit cell, to the triclinic α phase with two inequivalent molecules, is responsible for these splittings. As can be seen in these spectra the splitting of the $\boldsymbol{k} = 0$ vibron frequencies in α-TCB is indeed significantly larger than in β-TCB, in agreement with the calculations (see Sec. 1.4).

Although the calculated $\boldsymbol{k} = 0$ vibron splittings, small in β-TCB and substantially larger in α-TCB, are qualitatively confirmed by the Raman measurements, the quantitative agreement between calculations and experiments is poor. The calculated splittings (see Table VI) are much larger than the observed values. Since the calculations show that the splittings depend very sensitively on the molecular orientations and since it is unlikely that the empirical atom-atom potentials reproduce the experimental crystal packing really accurately, the discrepancy might be explained by the inaccuracy in the calculated orientations of the molecules in the crystal.

The effect of the different Cl isotope masses on the vibrational frequencies is relatively large in modes with in-plane Cl vibrations such as the 190 (A_g), 312 (B_{3g}), 352 (A_g), 209 (B_{2u}), 218 (B_{1u}), 510 (B_{1u}) and the 645 cm^{-1} (B_{2u}), see Table I. Let us first discuss the gerade modes, which are Raman active in the homogeneous crystal.

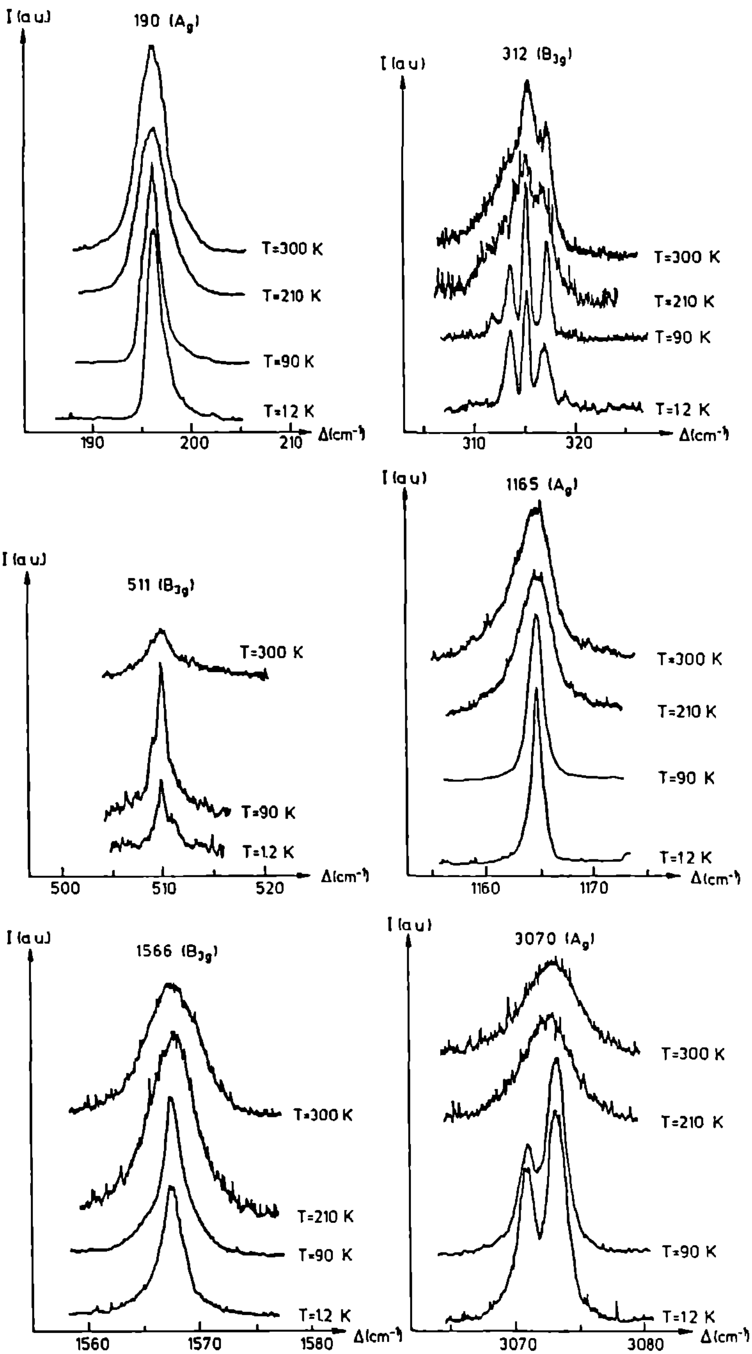

Fig. 3. Raman spectra at four different temperatures of six internal vibrations of TCB. The energy scale gives the difference in cm^{-1} with the 4880 Å laser line which was used for excitation.

Especially in the 312 cm^{-1} (B_{3g}) mode, where the ratio between the intramolecular isotope splitting and the vibron dispersion (see Tables I and VI) is very favorable, the isotope splitting should be visible (see Sec. 1.4). The Raman spectrum of this mode given in Fig. 3 shows that this is indeed the case. The β phase spectrum taken at 300 K is strikingly similar to the theoretically simulated spectrum in Fig. 2 with a line width of 1.75 cm^{-1} and the α phase spectrum at 90 K perfectly resembles the theoretical spectrum with a line width of 1.0 cm^{-1}. The α phase spectrum at 1.2 K is slightly different, which is probably caused by a more marked site splitting at this temperature. A similar isotope splitting has been observed for the 328 cm^{-1} (A_g) mode in the Raman spectrum of p-dichlorobenzene by Bellows *et al* [23]. These authors have not performed any lattice dynamics calculations, but they conclude on the basis of the experiments that the vibron band width for this 328 cm^{-1} mode should be less than 4 cm^{-1}.

For the other gerade vibrations that are candidates for displaying visible isotope effects, the situation is more complicated. The 190 cm^{-1} (A_g) mode has a considerably larger dispersion (see Table VI), i.e. larger intermolecular coupling matrix elements. The experimental Raman spectrum only shows a single peak which remains broader than the experimental resolution even at the lowest temperature, but which displays no clear structure. The dispersion of the 352 cm^{-1}(A_g) mode is smaller but this mode is engaged in a Fermi resonance with the much more dispersed 348 cm^{-1} (B_{1g}) mode. We have observed three peaks in this region in the higher temperature spectra and five peaks at the lower temperatures, but the precise assignments of these peaks is difficult because of the various effects occurring (isotope splitting, site splitting, Fermi resonance). We expect that at least part of the structure in this region is due to isotope effects, however.

The ungerade modes are infrared active in the homogeneous solid, but in the isotopically disordered crystal these modes may become Raman active as well. Especially those isotopically mixed molecular species which lack an inversion center will contribute to the Raman scattering. In the region around 230 cm^{-1} we observe three peaks which sharpen at lower temperatures. We attribute the peak at 235 cm^{-1} to the 225 cm^{-1}(B_{2g}) vibration, in agreement with the phosphorescence spectrum [1] where this vibration is observed at 233 cm^{-1}. In view of the small isotope splitting calculated for this vibration (see Table I) it is very unlikely that the other two peaks at 228 cm^{-1} and 221 cm^{-1} are caused by different isotopic species of this (B_{2g}) vibration. We assign the peak at 228 cm^{-1} to the 218 cm^{-1} (B_{1u}) and the peak at 221 cm^{-1} to the 209 cm^{-1} (B_{2u}) vibration. Both these vibrations have a rather strong intermolecular coupling so it could be expected that no simple isotope splitting of these peaks is visible. So, both these peaks demonstrate the breaking of the selection rules due to the isotopic disorder. Another peak, which splits into two components in the α phase, is visible around 510 cm^{-1} but it is not clear whether, besides the 511 cm^{-1} (B_{3g}) mode, the 510 cm^{-1} (B_{1u}) contributes anything to the Raman scattering.

It is remarkable that no isotope or site splittings are observed in the low temperature $T_0 \rightarrow S_0$ phosphorescence spectrum of α-TCB in paper [1]. This can now be understood, however, since the overall resolution in Ref. [1] was about 2 cm^{-1} and all splittings observed in the Raman spectra are smaller than a few cm^{-1}.

All Raman lines show a temperature dependent line width. The narrowest lines are obtained at 1.2 K, where the width of the 1165 cm^{-1} (A_g) vibration is almost equal to the resolution limit of the monochromator, whereas, for instance, the 1560 cm^{-1} (B_{3g}) vibration shows a width of 2.7 cm^{-1} which is constant below 90 K. It is known that the observed line width of Raman transitions can be affected by inhomogeneities (like impurities and crystal defects) or by relaxation. Keeping in mind that a lifetime in the order of a few ps can account for a line width of a few cm^{-1} the narrowing observed in our spectra upon cooling might be explained by an increase of the vibron lifetime. This narrowing even continues for some vibrations (190 cm^{-1} (A_g) and 1165 cm^{-1} (A_g)) between 90 K and 1.2 K, in contrast with the benzene crystal [24] where no decrease in the Raman line width is observed between liquid N_2 and liquid He temperatures. It has been pointed out that inhomogeneities have a negligible effect on the line broadening at low temperatures [25,26], so the observed narrowing in the low temperature region indicates an increase of the relaxation time.

1.6. Conclusions

From the lattice dynamics calculations and the Raman spectra of the low temperature α phase and the high temperature β phase of TCB presented in this paper, and from the optical spectra of α-TCB given in Ref. [1], we can draw the following conclusions.

The calculations, based on empirical atom-atom potentials, show that the structure of the vibrational exciton bands, especially those above 600 cm^{-1}, is one-dimensional, in agreement with the interpretation of the phosphorescence spectra in Ref. [1]. Significant dispersion occurs only in the $\boldsymbol{a}^*$ direction of the Brillouin zone, due to the importance of the (nearest neighbor) interactions between the molecules lying in the stacks along the $\boldsymbol{a}$ axis. The signs of the nearest-neighbor vibrational coupling elements in the dynamical matrix, which determine whether the $\boldsymbol{k} = 0$ states lie at the top of the band or at the bottom, are correctly reproduced by the lattice dynamics calculations. It is striking that the electrostatic interactions between the molecules, which are modelled in the atom-atom potential by the inclusion of fractional atomic charges, are absolutely essential to obtain the correct vibron band widths. An exception is the 1165 cm^{-1} (A_g) vibrational band which remains considerably too narrow in the calculations, even when the atomic charges are included. This vibration involves mainly the breathing motion of the Cl atoms, so we conclude, in agreement with previous experience [27-29], that for the interactions between Cl atoms the use of an isotropic atom-atom potential is insufficient. From the calculations it follows further that the widths of the vibron bands are not extremely sensitive to the crystal structure. So the vibrational band structure in β-TCB will not be very different from that observed [1] in α-TCB. The Raman spectra have confirmed that the optical experiments in Ref. [1], which were carried out at temperatures below 4.2 K, refer to the α phase of TCB.

The calculations also predict, in agreement with the Raman spectra for several vibrations, that the splitting of the $k = 0$ vibron frequencies is significantly larger in α-TCB than in β-TCB. This appears to be caused by the crystal-field terms, i.e. the self terms in the dynamical matrix, of the solid. In α-TCB the two molecules in the unit cell are not equivalent and they experience a different crystal field, whereas in β-TCB these molecules are equivalent. However, the splittings observed in the Raman spectra are considerably overestimated by the calculations. Since these $k = 0$ site splittings appear to depend very sensitively on the molecular orientations, this discrepancy is probably due to the approximate nature of the atom-atom potential model, which leads to inaccuracies in the orientations of the molecules in α-TCB (remember that these have not yet been determined experimentally).

The conclusion that the band structure, especially for the vibrations at higher frequencies, is one-dimensional does not imply that the interactions between the stacks of TCB molecules are negligible. It becomes clearly evident from the calculations that for the overall crystal stability, for the dispersion of the phonon bands and also the lower frequency vibron bands, and for the site splitting of the $k = 0$ vibron frequencies in α-TCB, the interstack interactions are essential.

Another interesting phenomenon, which emerges from the Raman spectra of both α- and β-TCB, is the observation of isotope splittings. The statistical occurrence of ^{35}Cl and ^{37}Cl atoms in the ratio 3:1 leads to 7 different TCB species, which are randomly distributed over the crystal. The calculations show that particularly for the 312 cm^{-1} (B_{3g}) mode, which has large molecular isotope shifts and small intermolecular coupling matrix elements, the isotope splitting should be visible. The perfect resemblance between the theoretically simulated spectrum for this mode and the observed Raman spectrum confirms this conclusion. This mode demonstrates one of the effects that can occur in crystals with random disorder: the (vibrational) excitations may lose their Bloch wave character and become localized in clusters of (isotopically) similar species. Also for other vibrations we have observed effects of random disorder, such as peak broadening and the detection of transitions that would be forbidden in homogeneous crystals (i.e. the breaking of selection rules). Summarizing, we conclude that the vibron band structure in TCB is not masked by chlorine isotope effects. For most of the vibron bands the dispersion appears to be significantly larger than the isotope shifts. For one vibration where the isotope shifts are larger, the peaks from the 7 different molecular species are clearly separated, and for the vibrations where the two quantities are comparable, the spectra show interesting structures.

Acknowledgement

We thank dr. H. Bonadeo for a very useful correspondence about his calculations and mr. J.H.M.T. Timmermans for valuable assistance with the Raman experiments. This investigation is part of the research programs of the "Stichting voor Fundamenteel Onderzoek der Materie (F.O.M.)" and the "Stichting Scheikundig Onderzoek in Nederland (S.O.N.)", financially supported by the "Nederlandse Organisatie voor Wetenschappelijk Onderzoek (N.W.O.)".

Note

This chapter is also included in the Ph.D. thesis of A.P.J.M. Jongenelis (University of Leiden, 1988).

References

[1] E.H. Abramson, A.P.J.M. Jongenelis and J. Schmidt, J. Chem. Phys. **87**, 3719 (1987).
[2] A.J. van Strien and J. Schmidt, Mol. Phys. **46**, 151 (1982).
[3] F.H. Herbstein, Acta Cryst. **18**, 997 (1965).
[4] E.B. Halac, E.M. Burgos, H. Bonadeo and E.A. D'Alessio, Acta Cryst. **A33**, 86 (1977).
[5] C. Dean, M. Pollak, B.M. Craven and G.A. Jeffrey, Acta Cryst. **11**, 710 (1958).
[6] H. Bonadeo and E. D'Alessio, Chem. Phys. Letters **19**, 117 (1973).
[7] E.A. D'Alessio and H. Bonadeo, Chem. Phys. Letters **22**, 559 (1973).
[8] H. Bonadeo, E. D'Alessio E. Halac and E Burgos, J. Chem. Phys. **68**, 4714 (1978).
[9] P.A. Reynolds, J.K. Kjems and J.W. White, J. Chem. Phys. **56**, 2928 (1972).
[10] P.A. Reynolds, J.K. Kjems and J.W. White, J. Chem. Phys. **60**, 824 (1974).
[11] G. Taddei, H. Bonadeo M.P. Marzocchi and S. Califano, J. Chem. Phys. **58**, 966 (1973).
[12] S. Califano, V. Schettino and N. Neto, *Lattice dynamics of molecular crystals*, Springer, Berlin (1981).
[13] E.B. Wilson, J.C. Decius and P.C. Cross, *Molecular vibrations*, McGraw Hill, New York (1955).
[14] N. Neto, G. Taddei, S. Califano and S.H. Walmsley, Mol. Phys. **31**, 457 (1976).
[15] N. Neto and D. Kirin, Chem. Phys. **44**, 245 (1979).
[16] J.R. Scherer, Spectrochim. Acta **20**, 345 (1964).
[17] J.R. Scherer, Spectrochim. Acta **23A**, 1489 (1967).

[18] E. Frasson, C. Garbuglio and S. Bezzi, Acta Cryst. **12**, 126 (1959).

[19] G.L. Wheeler and S.D. Colson, J. Chem. Phys. **65**, 1227 (1976).

[20] A.H. Francis and C.B. Harris, J. Chem. Phys. **57**, 1050 (1972).

[21] A.A. Maradudin, E.W. Montroll and G.H. Weiss, *Theory of lattice dynamics in the harmonic approximation*, Academic Press, New York (1963), Ch. 5.

[22] E.N. Economou, *Green's functions in quantum physics*, 2nd ed., Springer, Berlin (1983), Ch. 7.

[23] J.C. Bellows, P.N. Prasad, E.M. Monberg and R. Kopelman, Chem. Phys. Letters **54**, 439 (1978).

[24] A.R. Gee and G.W. Robinson, J. Chem. Phys. **46**, 4847 (1967).

[25] F. Ho, W.S. Tsay, J. Trout and R.M. Hochstrasser, Chem. Phys. Letters **83**, 5 (1982).

[26] B.H. Hesp and D.A. Wiersma, Chem. Phys. Letters **75**, 423 (1980).

[27] M.G. Munowitz, G.L. Wheeler and S.D. Colson, Mol. Phys. **34**, 1727 (1977).

[28] S.L. Price and A.J. Stone, Mol. Phys. **47**, 1457 (1982).

[29] S.C. Nyburg and C.H. Faerman, Acta Cryst. **B41**, 274 (1985).

2. Vibron band structure in chlorinated benzene crystals; lattice dynamics calculations and Raman spectra of 1,4-dichlorobenzene

A.P.J.M. Jongenelis[a], T.H.M. van den Berg[b], J. Schmidt[a]
and A. van der Avoird[b]

a) *Center for the Study of Excited States of Molecules, Huygens Laboratory, Leiden University, P.O. Box 9504, Leiden, The Netherlands*
b) *Institute of Theoretical Chemistry, University of Nijmegen, Toernooiveld, Nijmegen, The Netherlands*

(Published in J. Phys.: Condens. Matter **1**, 5051 (1989))

Abstract. Lattice dynamics calculations of the lattice modes (phonons) and the internal modes (vibrons) and Raman spectra at liquid helium temperatures are presented for the β, α and γ phase of 1,4-dichlorobenzene (DCB). It follows from the calculations and it is confirmed by the Raman spectra that these three phases are characteristically different with respect to the following properties: vibron band dispersion, Davydov splitting, ^{35}Cl/^{37}Cl isotopic effects on the bandstructure and vibron-phonon mixing. Only the low temperature γ phase shows a nice one-dimensional band structure for some vibrations. The vibron band dispersion in all phases of DCB is caused by the repulsive exponential terms in the intermolecular potential. This is in contrast to 1,2,4,5-tetrachlorobenzene, where the electrostatic interactions are responsible for the dispersion. Some of the ungerade vibron modes become visible in the Raman spectra of DCB due to the (random) occurrence of molecules with different distributions of ^{35}Cl/^{37}Cl isotopes. A few of the Raman lines observed could not be uniquely assigned; they are probably caused by Fermi resonances.

2.1. Introduction

Lattice dynamics calculations on 1,2,4,5-tetrachlorobenzene (TCB) have been described in a previous paper [1]. They were performed to obtain the dispersion and the splittings at $k = 0$ of the coupled internal vibrations in the two phases of TCB. The intermolecular potentials used were based on the empirical atom-atom model [2-4]. It turned out to be essential to introduce polarized bonds, i.e. to add the electrostatic interaction to the atom-atom potential, in order to reproduce the experimentally observed [5] vibron band widths in α-TCB. The calculations showed that some of the vibrons are one-dimensional in the direction of the molecular stacks (the crystallographic a axis). The lattice modes and the lower vibron modes, however, did not show a one-dimensional behaviour and also for the overall crystal stability the interactions between the stacks were important. It was further found that the splittings at $k = 0$ in β-TCB are much smaller than in α-TCB. This finding was confirmed by Raman spectra. Moreover, the internal modes of the free TCB molecule were calculated for molecules with different $^{35}Cl/^{37}Cl$ isotopic mass distributions and the isotope shifts were compared with the calculated vibron band widths. The calculated isotope splittings of the vibron bands were in very good agreement with the splittings observed in some of the Raman lines.

In this contribution we present similar calculations of the dispersion of the coupled internal vibrations in the β, α and γ phase of 1,4-dichlorobenzene (DCB). This crystal was chosen because it also exhibits a one-dimensional stacked crystal structure [6–11] and because investigations on the triplet electronic excitation by von Borczyskowski *et al* [12,13] show that the interaction between equivalent molecules in the stacks ($J_{||}$) is about two orders of magnitude larger than the interaction between inequivalent molecules. Calculations of the lattice modes (phonons) of α- and β-DCB have been reported earlier and in particular the frequencies at $\boldsymbol{k} = 0$ and the dispersion of the phonons have been investigated [2-4,14,15]. In addition, we calculate the effects of the different $^{35}Cl/^{37}Cl$ mass distributions on the vibron band structure. Raman experiments of the three phases at liquid helium temperatures are presented and confirm several aspects of the calculations.

2.2. Theory

The calculations are based on the standard harmonic lattice dynamics method, as extended to internal vibrations by Califano *et al* [16,17] and summarized in the previous paper [1]. We include the full self term [18,19] (Eq. (4) in Ref. [1]).

For the calculation of the vibrations of the free DCB molecule Scherer's generalized valence force field for chlorinated benzenes is used [20,21]. Transformation from the stretch, bending, torsion and wagging coordinates to cartesian atomic displacements and solution of the $\boldsymbol{FG}$-matrix problem in terms of the latter coordinates [22] yields six zero eigenvalues, which correspond with the three translations and the three rotations of the molecule, and 30 eigenvalues and eigenvectors which represent the normal modes of the free molecule.

The intermolecular potential is represented by an atom-atom potential of exp-6-1 type: $V(r_{ij}) = B\exp[-Cr_{ij}] - Ar_{ij}^{-6} + Dr_{ij}^{-1}$. Parameter sets for this potential, without the electrostatic parameter D, are given by Bonadeo *et al* [2] and by Reynolds *et al* [4]. In order to obtain the correct vibron band widths for TCB, it was necessary to introduce polarized C–Cl and C–H bonds by including fractional atomic charges in both potential sets (charges of $-0.25e$ on Cl and $+0.25e$ on the corresponding C, and charges of $+0.10e$ on H and $-0.10e$ on the corresponding C) [1]. In this paper we have used four potential parameter sets: the parameters given by Bonadeo or by Reynolds, either with or without fractional atomic charges.

2.3. Molecular vibrations; isotope effects

The vibrational normal modes of the free DCB molecule with D_{2h} symmetry were calculated and the resulting eigenvectors have been directly used in the lattice dynamics calculations. The calculated frequencies were replaced by the experimental values [20,21] (as was also done for TCB [1]) although the calculated values are not very different.

The effect of chlorine isotope substitution on the molecular frequencies is investigated by calculations on the three molecular species which can be formed with ^{35}Cl and ^{37}Cl atoms (natural abundance 3:1). We define the isotope shift of a specific vibration as the (average) shift of the frequency of this vibration caused by the substitution of one ^{37}Cl atom by one ^{35}Cl atom. It is observed that the C—Cl stretch vibrations (328 cm^{-1} (A_g) and 550 cm^{-1} (B_{1u})) in particular are very sensitive to the chlorine mass, as is illustrated by their strong isotope shifts (4.0 cm^{-1} and 3.7 cm^{-1}). The (in-plane) C—Cl bend vibrations (226 cm^{-1} (B_{2u}) and 350 cm^{-1} (B_{3g})) show smaller shifts (1.6 cm^{-1} and 1.0 cm^{-1}). The out-of-plane vibrations show shifts which are very small, except for the 115 cm^{-1} (B_{3u}) vibration (0.8 cm^{-1}). The same behaviour was observed in the case of TCB where also the C—Cl stretch vibrations were most sensitive to the chlorine masses. In the lattice dynamics calculations the average chlorine mass of 35.453 a.m.u. is used. We return to the chlorine isotope effects after the presentation of the Raman spectra in Sec. 2.5.

2.4. Lattice dynamics calculations on β-, α- and γ-DCB

2.4.1. Crystal structure and phonons

It is known that DCB can exist in three different phases. Under normal conditions DCB crystallizes from the melt at 55 ° C in the triclinic β phase (space group $P\bar{1}$) with 1 molecule in the unit cell ($Z = 1$) [6], and transforms at 30.8 ° C to the monoclinic α phase ($P2_1/a$; $Z = 2$) [7,8]. Below 0 ° C a second monoclinic phase, the γ phase, can exist with space group $P2_1/c$ and $Z = 2$ [9,10]. In all phases the molecules are located at inversion centers and in α- and γ-DCB the orientations of the two molecules in the unit cell are related by reflection with respect to the *ac* plane. The positions and orientations of the molecules in the α and β phase have been determined in the late 1950's [6-8] and the DCB molecules seemed to be heavily distorted in the crystal. Later more accurate and detailed x-ray studies of the three phases at different temperatures became available [10,11] and these new results showed that actually the DCB molecule in the crystal is almost regular and planar.

We have started the calculations by a structure optimization of all three DCB phases, using planar DCB molecules with D_{2h} symmetry. The unit cell parameters for the three phases used in the calculations are given in Table I, and were fixed in

Table I. Unit cell parameters for the three phases of DCB used in the lattice dynamics calculations and taken from Ref. [11]. The volume V of and the number of molecules Z in the unit cell are also given.

	Unit cell parameters of DCB		
	β phase at 300 K	α phase at 100 K	γ phase at 100 K
a	7.361 Å	14.664 Å	8.624 Å
b	5.963 Å	5.740 Å	6.021 Å
c	3.959 Å	3.925 Å	7.414 Å
V	159.4 Å^3	306.8 Å^3	305.4 Å^3
α	92.13°	90°	90°
β	113.24°	111.77°	127.51°
γ	91.42°	90°	90°
Z	1	2	2

the optimization procedure. The optimized molecular orientations for all three phases calculated with the atom-atom potential sets given by Bonadeo *et al* [2] and by Reynolds *et al* [4] are in good agreement with the results of the x-ray diffraction measurements [11]. The various potential sets give only small differences. Addition of fractional atomic charges hardly influences the optimized structure.

In Table II we present the optical phonon frequencies of the three DCB phases obtained in a complete calculation and in a rigid body calculation with the potential set given by Bonadeo including fractional atomic charges. In addition we list the frequencies obtained in a Raman experiment at 1.2 K. Firstly, we discuss the phonon frequencies of β-DCB. From Raman experiments it is known that these frequencies are temperature dependent. Colson *et al* [11] report at 300 K frequencies of 46 cm^{-1}, 56 cm^{-1} and 90 cm^{-1}, in agreement with 45 cm^{-1}, 56 cm^{-1} and 84 cm^{-1} of Bonadeo *et al* [3], and at 100 K frequencies of 54 cm^{-1}, 64 cm^{-1} and 99 cm^{-1}, compared with 56 cm^{-1}, 67 cm^{-1} and 102 cm^{-1} reported by Reynolds *et al* [4]. In our calculation with the potential of Bonadeo with fractional charges we obtain lattice frequencies in reasonable agreement with the experimental frequencies reported at 300 K and with the calculated frequencies reported in Refs. [2,3]. This agrees with the fact that we used the unit cell parameters obtained at this temperature. When the parameters of the 100 K crystal structure are used all three calculated lattice frequencies increase in agreement with experiment [11]. From our calculations we see that the lattice frequencies, as in the case of TCB [1], are very sensitive to small deviations from the optimized crystal structure. Calculations with the other potential sets (see Sec. 2.2) yield about the same results; the deviations are mainly caused by the small changes in the equilibrium orientation of the molecules. When the internal vibrations are included in the calculations the lattice frequencies change by less than 2 cm^{-1}, indicating a very small vibron-phonon mixing. The lattice modes show almost equal dispersion in all three directions of the

Table II. The optical lattice mode frequencies of the three phases of DCB in cm^{-1}. The experimental values are from our Raman experiments performed at 1.2 K. The calculated values are obtained from a complete calculation including the vibrons using the Bonadeo potential set with the fractional atomic charges (see text). Values from the rigid body calculations are given in parentheses. The relatively large discrepancy between experiment and calculation for β-DCB is related to the fact that in the calculation the unit cell parameters for a crystal at room temperature are used. The frequencies calculated for β-DCB with the unit cell parameters at 100 K are 34, 50 and 102 cm^{-1}.

	Phonon frequencies (cm^{-1}) at $k = 0$								
	β phase			α phase			γ phase		
Symmetry	Experiment	Calculation		Experiment	Calculation		Experiment	Calculation	
(u)	—	—	—	—	31	(31)	—	44	(44)
(u)	—	—	—	—	37	(37)	—	49	(48)
(u)	—	—	—	—	52	(52)	—	91	(88)
(g)	56	32	(32)	—	51	(51)	52	48	(48)
(g)	65	40	(40)	59	55	(55)	67	61	(59)
(g)	103	88	(89)	109	104	(107)	143	122	(127)
(g)	—	—	—	33	30	(30)	76	62	(60)
(g)	—	—	—	66	61	(61)	86	78	(82)
(g)	—	—	—	117	110	(112)	133	115	(121)

Brillouin zone, leading to the conclusion that in this phase the interactions in all three crystallographic directions are important.

The lattice mode frequencies of α-DCB have been calculated using various potential sets. The results from different potentials differ by 5 cm^{-1} at most and the overall agreement with the experimentally observed and other calculated values [3] is good. In the complete calculation including the internal modes the lattice mode frequencies for this phase also change by less than 2 cm^{-1}. The dispersion of the phonon frequencies calculated either with the Bonadeo or with the Reynolds potential set is considerably smaller along a^* than along b^* and c^*, indicating that the interactions in two crystallographic directions are more important than in the third (a) direction. This is not surprising since the distance between the molecules along the a axis is much larger than along the other two directions in the crystal. It will be seen that the calculated dispersion of the internal modes shows a similar behaviour.

The calculated lattice frequencies of γ-DCB show considerable differences (up to 14 cm^{-1}) when the Bonadeo or the Reynolds potential parameters are used. We have checked that in this case the difference in optimized crystal structure does not account for the difference in phonon frequencies, but that it is really caused by the differences between the potentials. Addition of charges hardly alters the frequencies. When performing a complete calculation the lowest phonon frequencies change by less than 2 cm^{-1}

but the highest lattice modes, with frequencies close to those of the lowest internal vibrations, change considerably (up to 5 cm^{-1}). Also in the eigenvectors we observe (weak) mixing between the highest lattice modes and the lowest internal modes. In agreement with the experimental observations we see that the calculated lattice mode frequencies of γ-DCB are considerably higher than the frequencies of α-DCB. As in the α phase the calculated dispersion is smallest in the $\boldsymbol{a}^*$ direction, in agreement with the fact that the distance between the molecules in the $\boldsymbol{a}$ direction is the largest. From these results it can be concluded that the dispersion, and thus the interaction, in both other directions is the most significant.

2.4.2. Davydov splittings of the vibrons

The internal modes in α- and γ-DCB are expected to be split into two components as a result of the presence of two symmetry related molecules in the unit cell (Davydov splitting). The splittings at $\boldsymbol{k} = 0$ calculated in α-DCB, given in Table III, are small ($\leq$ 1 cm^{-1}) except for the 115 cm^{-1} (B_{3u}), 226 cm^{-1} (B_{2g}) and 819 cm^{-1} (B_{3g}) internal vibrations where we find splittings up to 7 cm^{-1}. A small deviation from the optimized crystal structure has hardly any effect on the frequencies except for the lowest two internal vibrations. In the high frequency region the splittings are mainly caused by the fractional charges. Omitting these charges decreases the splittings at $\boldsymbol{k} = 0$, for the 819 cm^{-1}(B_{3u}) vibration from 3.5 cm^{-1} to a few tenths of a wavenumber. In the low frequency region either the r^{-6} term or the exponential term in the atom-atom potential gives the largest contribution to the Davydov splitting, but the effect caused by the dominant term is always partly compensated by an opposite contribution from the other part of the potential. The observation that either of these two terms of the potential can dominate the calculated Davydov splitting contrasts with the case of β-TCB where the splitting in the low frequency region was mainly caused by the repulsive short-range interactions.

The calculated vibron frequencies at $\boldsymbol{k} = 0$ for γ-DCB, given in Table IV, are similar to those in α-DCB, but since the phonon frequencies in γ-DCB are higher than in α-DCB mixing with internal vibrations is more significant. This explains the considerable splitting of 7.7 cm^{-1} for the 298 cm^{-1} (B_{2g}) vibration. Compared with α-DCB the overall splitting of the modes in γ-DCB is somewhat larger. The same decrease of the splittings as in α-DCB is observed in the 819 cm^{-1} region when the charges are omitted. Analysis of the origin of the splittings in the low frequency region shows that in γ-DCB the exponential terms of the potential give the largest contribution which is partly compensated by an opposite effect from the r^{-6} term. This situation resembles that in β-TCB.

Table III. Calculated splittings for $k = 0$ vibron frequencies and vibron band widths in cm^{-1} in all three directions of the Brillouin zone for α-DCB. The two columns in every direction refer to the width of the two bands. The Bonadeo potential set with charges is used. The Reynolds potential set gives similar results. Calculations without fractional atomic charges hardly alter these numbers.

	α-DCB			
		Band width (cm^{-1})		
Vibration (cm^{-1})	Splitting (cm^{-1})	a^*	b^*	c^*
115 (B_{3u})	6.8	−4.0 / 2.9	7.1 / 0.3	−15.0 / −8.7
226 (B_{2u})	2.6	−1.3 / 1.3	8.6 / 6.0	5.3 / 3.8
298 (B_{2g})	0.9	−0.5 / 0.4	3.1 / 2.2	−2.9 / −2.1
328 (A_g)	0.9	−0.4 / 0.4	−0.9 / 0.0	−0.8 / 0.0
350 (B_{3g})	0.7	−0.3 / 0.3	−1.3 / −0.6	−0.8 / −0.5
407 (A_u)	0.1	0.0 / 0.0	−4.6 / −4.6	−0.2 / −0.2
485 (B_{3u})	0.1	0.0 / 0.0	−0.5 / −0.5	0.1 / 0.1
550 (B_{1u})	1.0	−0.5 / 0.5	−1.2 / −0.2	−0.5 / −0.1
626 (B_{3g})	0.1	0.0 / 0.0	1.6 / 1.6	0.6 / 0.6
687 (B_{2g})	0.0	0.0 / 0.0	0.5 / 0.5	0.5 / 0.5
747 (A_g)	0.6	−0.3 / 0.3	0.8 / 0.2	0.7 / 0.1
815 (B_{1g})	0.5	−0.5 / 0.0	−1.8 / −1.3	−4.0 / −2.2
819 (B_{3u})	3.5	−1.4 / 2.1	−1.1 / 1.4	−6.0 / −4.1
934 (B_{2g})	0.2	−0.1 / 0.1	3.2 / 3.0	−1.1 / −1.1
951 (A_u)	0.2	−0.1 / 0.1	−2.5 / −2.5	−0.7 / −0.7
1015 (B_{1u})	0.5	−0.2 / 0.2	0.5 / 0.0	0.8 / 0.5
1090 (B_{1u})	0.1	0.0 / 0.0	−1.6 / −1.6	−1.3 / −1.3
1096 (A_g)	0.4	−0.2 / 0.2	−0.4 / 0.1	−0.4 / 0.0
1107 (B_{2u})	0.2	−0.1 / 0.1	−3.2 / −3.2	−2.4 / −2.1
1169 (A_g)	1.4	−0.5 / 0.5	2.8 / 1.8	2.8 / 2.8
1221 (B_{2u})	0.5	−0.2 / 0.2	−0.2 / 0.2	0.7 / 0.2
1290 (B_{3g})	0.5	−0.2 / 0.2	3.4 / 2.9	2.8 / 2.6
1394 (B_{2u})	0.4	−0.2 / 0.2	−0.6 / −0.1	−0.1 / −0.1
1477 (B_{1u})	1.5	−0.7 / 0.7	−1.8 / −0.3	−0.7 / 0.5
1574 (B_{3g})	0.0	0.0 / 0.0	0.1 / 0.1	0.4 / 0.4
1574 (A_g)	0.1	−0.1 / 0.0	−0.5 / −0.4	−0.2 / −0.1
3065 (B_{3g})	0.4	−0.2 / 0.2	1.0 / 0.6	1.4 / 1.0
3070 (A_g)	0.1	0.0 / 0.0	0.1 / 0.0	1.3 / 1.2
3090 (B_{2u})	0.4	−0.2 / 0.2	−0.8/ −0.4	−0.2 / 0.2
3090 (B_{1u})	0.4	−0.1 / 0.0	−0.3 / −0.2	−0.2 / 0.0

2.4.3. Vibron band structure

The computed vibron band widths for β-DCB are given in Table V and clearly show that the dispersion in this system is not one-dimensional. Most vibrations have a band width which is smaller than 1 cm^{-1}, but some have a larger dispersion in one or in two directions. In contrast to TCB [1] addition of charges barely affects the widths of the vibron bands. The results hardly vary when using the Bonadeo or Reynolds potential

Table IV. Calculated splittings for $k = 0$ vibron frequencies and vibron band widths in cm^{-1} in all three directions of the Brillouin zone for γ-DCB, using the Bonadeo potential set with charges. The Reynolds potential set gives similar results. A calculation without charges hardly alters these numbers.

		γ-DCB		
		Band width (cm^{-1})		
Vibration (cm^{-1})	Splitting (cm^{-1})	a^*	b^*	c^*
115 (B_{3u})	7.4	−3.1 / 5.4	−6.6 / 0.8	−3.6 / 3.8
226 (B_{2u})	2.8	4.4 / 1.7	4.4 / 1.7	4.2 / 1.5
298 (B_{2g})	7.7	−0.9 / 0.5	7.2 / −0.5	−3.4 / 4.3
328 (A_g)	0.6	0.0 / 0.0	0.6 / 0.0	0.5 / 0.0
350 (B_{3g})	0.0	−0.4 / −0.4	−0.4 / −0.4	−0.4 / −0.4
407 (A_u)	0.2	0.3 / 0.3	−8.2 / −8.0	0.2 / 0.0
485 (B_{3u})	2.1	0.0 / 0.0	−8.2 / −6.1	−1.0 / 1.1
550 (B_{1u})	1.3	−0.7 / 0.0	−1.7 / −0.4	−0.8 / 0.4
626 (B_{3g})	0.1	0.4 / 0.4	1.5 / 1.4	0.4 / 0.3
687 (B_{2g})	0.0	0.0 / 0.0	2.8 / 2.8	0.0 / 0.0
747 (A_g)	0.2	0.3 / 0.3	0.4 / 0.2	0.5 / 0.4
815 (B_{1g})	3.0	−1.7 / −0.6	−3.3 / −0.3	−2.7 / 0.3
819 (B_{3u})	3.6	4.0 / 1.8	6.0 / 2.4	−0.4 / 3.2
934 (B_{2g})	1.3	−0.4 / −0.4	11.2 / 9.8	−1.1 / 0.2
951 (A_u)	0.2	0.4 / 0.4	−9.0 / −8.8	−0.1 / 0.1
1015 (B_{1u})	0.4	−0.5 / 0.3	−0.2 / 0.2	−0.1 / 0.3
1090 (B_{1u})	0.3	−0.6 / −0.6	−1.3 / −1.1	−0.7 / −0.6
1096 (A_g)	0.7	−0.2 / 0.2	0.7 / 0.0	−0.3 / 0.3
1107 (B_{2u})	1.5	−2.0 / −1.9	−3.0 / −1.5	−2.7 / −1.2
1169 (A_g)	0.6	1.6 / 1.6	1.7 / 1.4	1.7 / 1.4
1221 (B_{2u})	0.1	0.0 / 0.0	0.1 / 0.0	0.0 / 0.0
1290 (B_{3g})	0.4	1.5 / 1.4	1.5 / 1.1	1.7 / 1.3
1394 (B_{2u})	0.1	−0.2 / −0.2	−0.1 / 0.0	−0.1 / 0.0
1477 (B_{1u})	0.5	−2.3 / −0.3	−0.9 / −0.4	−0.9 / −0.4
1574 (B_{3g})	0.0	0.2 / 0.2	0.0 / 0.0	0.2 / 0.2
1574 (A_g)	0.2	0.0 / 0.0	−0.3 / −0.1	−0.1 / 0.1
3065 (B_{3g})	0.1	0.4 / 0.4	−0.8 / −0.7	0.5 / 0.4
3070 (A_g)	0.3	0.8 / 0.5	−0.8 / −0.5	0.8 / 0.5
3090 (B_{2u})	0.2	−1.1 / −0.8	0.6 / 0.4	−1.0 / −0.8
3090 (B_{1u})	0.3	−0.2 / −0.1	0.8 / 0.5	−0.3 / 0.0

sets and, moreover, they are insensitive to small variations of the optimized crystal structure. The conclusion is that, just as for the lattice modes, the interactions responsible for the dispersion in β-DCB are of about the same size in all three crystallographic directions. We find that in all cases the repulsive exponential term gives the largest contribution to the dispersion, with some compensation from the attractive r^{-6} term. The large dispersion (≈ 10 cm^{-1} along a^* and b^*) of the 328 cm^{-1} (A_g) vibration is remarkable. As mentioned in Sec. 2.3 this vibration is also very sensitive to the chlorine

Table V. Calculated vibron band widths in cm^{-1} in all three directions of the Brillouin zone for β-DCB. The Bonadeo potential set with charges is used. The Reynolds potential set gives similar results. Calculations without fractional atomic charges hardly alter these numbers.

	β-DCB		
	Band width (cm^{-1})		
Vibration (cm^{-1})	a^*	b^*	c^*
115 (B_{3u})	5.7	0.7	−5.4
226 (B_{2u})	3.9	3.7	3.7
298 (B_{2g})	−0.5	2.5	−1.0
328 (A_g)	10.0	10.3	−0.6
350 (B_{3g})	−0.5	−0.4	−0.4
407 (A_u)	−1.1	−6.2	−1.1
485 (B_{3u})	−1.1	−3.6	−2.1
550 (B_{1u})	−3.1	−4.0	0.0
626 (B_{3g})	0.2	1.0	0.5
687 (B_{2g})	0.4	1.8	0.6
747 (A_g)	1.0	1.0	0.6
815 (B_{1g})	1.7	0.2	−1.2
819 (B_{3u})	2.4	2.4	−5.5
934 (B_{2g})	1.0	5.2	0.3
951 (A_u)	−1.2	−4.8	−1.9
1015 (B_{1u})	−0.3	0.2	0.6
1090 (B_{1u})	−0.6	−1.2	−1.5
1096 (A_g)	0.0	0.2	0.2
1107 (B_{2u})	−1.8	−2.5	−2.3
1169 (A_g)	1.4	1.7	2.7
1221 (B_{2u})	−0.2	−0.2	0.4
1290 (B_{3g})	1.1	1.6	2.8
1394 (B_{2u})	−0.3	−0.1	−0.1
1477 (B_{1u})	−1.2	−0.7	−0.2
1574 (B_{3g})	0.1	0.1	0.3
1574 (A_g)	0.0	−0.3	−0.1
3065 (B_{3g})	0.0	0.0	1.0
3070 (A_g)	−0.1	−0.2	1.0
3090 (B_{2u})	−0.6	0.1	0.0
3090 (B_{1u})	0.4	−0.3	−0.8

mass (isotope shifts of about 4 cm^{-1}). In Sec. 2.5 we will discuss the Raman spectrum of this vibration in relation to the calculated results.

From the calculations on α-DCB (see Table III) we find that the dispersion of the internal vibrations is very small along a^* (except for the lowest vibrations) and large for some particular vibrations along b^* or along b^* and c^*. A calculation without the charges in the potential yields similar results. We have observed that the exponential terms in the atom-atom potential give the largest contribution to the band widths in the α phase. The dispersion of some low frequency vibrations shows a considerable dependence on the molecular orientations. This effect may be caused by the weak mixing with the lattice modes, which we have found to be sensitive to changes of the crystal structure. We therefore conclude that α-DCB, which was believed to represent a nice one-dimensional crystal [12,23,24] with respect to the delocalization of the internal vibrations, is not one-dimensional at all.

When examining the band widths for γ-DCB, which are given in Table IV, a striking difference with the two other phases is observed. Like in α- and β-DCB (and like in the one-dimensional system TCB [1]) the lowest vibrations exhibit dispersion in all three directions. Some higher modes, however, such as 407 cm^{-1} (A_u), 485 cm^{-1} (B_{3u}), 687 cm^{-1} (B_{2g}), 934 cm^{-1} (B_{2g}) and 951 cm^{-1} (A_u), show a clear one-dimensional dispersion up to 11 cm^{-1} along b^*. As in the other two phases the main contribution originates from the exponential term in the potential and the charges hardly alter the results. Since there are no experimental data on the dispersion of the vibrations in γ-DCB it is impossible as yet to verify these results. Our calculations suggest that the low temperature phase is an attractive candidate for a quasi one-dimensional model system.

2.5. Raman experiments

2.5.1. Experimental procedure

In the Raman experiments we have studied β-, α- and γ-DCB at liquid helium temperatures. The experimental arrangement used in the Raman experiments has been described in detail in the previous paper [1]. DCB single crystals were obtained in the following way. 1,4-Dichlorobenzene purchased from BDH (The British Drug Housed Ltd.) was zone-refined for 100 passes. The resulting product was analyzed by gas chromatography and contained less than 500 ppm of DCB isomers or other impurities. Neat crystals of β-DCB were grown from the melt by the Bridgman technique and subsequently annealed to reduce structural imperfections. To maintain DCB in the β phase the crystal was cooled down quickly to liquid nitrogen temperatures. To obtain α-DCB a β phase crystal was cooled down very slowly, especially around the phase transition at 30.8 ° C. These crystals were then stored at 10 °C where the α phase is known to be most stable. By quick cooling of this sample it was possible to maintain the α phase at liquid helium temperatures. As discussed in Ref. [9] the γ phase is created by storing an undercooled β phase crystal for some time at −10 °C.

2.5.2. Results and discussion

In Fig. 1 we present the Raman spectra of the lattice modes of all three phases of DCB obtained at 1.2 K. Since the linewidths at this temperature are small (about 0.8 cm^{-1}) the peaks in these spectra are well resolved, in contrast to previously reported spectra which were taken at about 100 K [9]. The frequencies of the lattice modes are all in good agreement with previously reported values and are given in Table II.

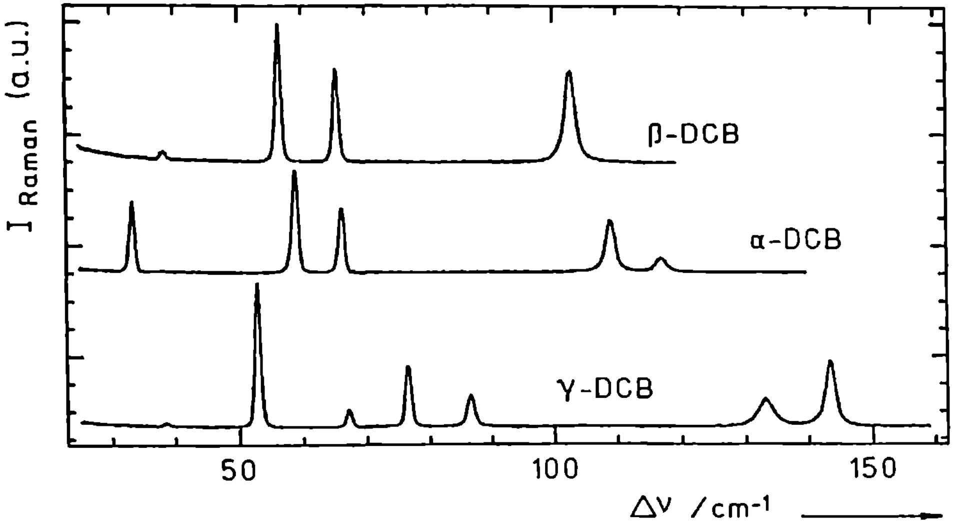

Fig. 1. Raman spectra of the lattice modes of β-, α- and γ-DCB taken at a temperature of 1.2 K with a resolution of 0.8 cm^{-1}. The energy scale gives the difference in cm^{-1} with the 4880 Å laser line which was used for excitation.

It is interesting to investigate whether the effects observed in the Raman spectra of TCB (isotope effects, site splitting and the observation of ungerade vibrations) can also be detected in the Raman spectra of DCB. Since both α- and γ-DCB have two molecules in the unit cell which are related by crystal symmetry we cannot observe site splittings in these spectra. However, it should be possible to observe a Davydov splitting of the lines.

A beautiful example of such a Davydov splitting is presented in Fig. 2 where we show the Raman spectra of the 298 cm^{-1} (B_{2g}) vibration. The β phase spectrum shows a single line, consistent with the fact that β-DCB has only one molecule in the unit cell. However, both α- and γ-DCB show a doublet. From the calculations summarized in Sec. 2.3 we conclude that a splitting of this mode as a result of the different chlorine isotopes should be small and probably not detectable with our resolution. Bellows *et al* [25] concluded, on the basis of the merging of the two lines in an isotopically mixed α-DCB crystal, that this splitting is a Davydov splitting. Comparison of our experimentally observed splittings with the calculated ones (see Tables III and IV) shows a good

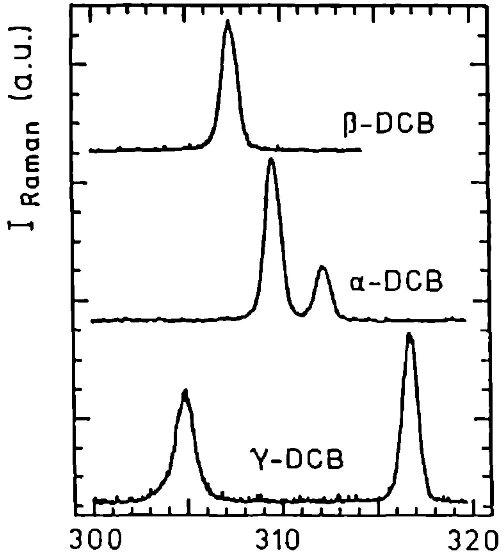

Fig. 2. Raman spectra of the 298 cm^{-1} (B_{2g}) C–Cl out-of-plane vibration. Conditions are as detailed in Fig. 1.

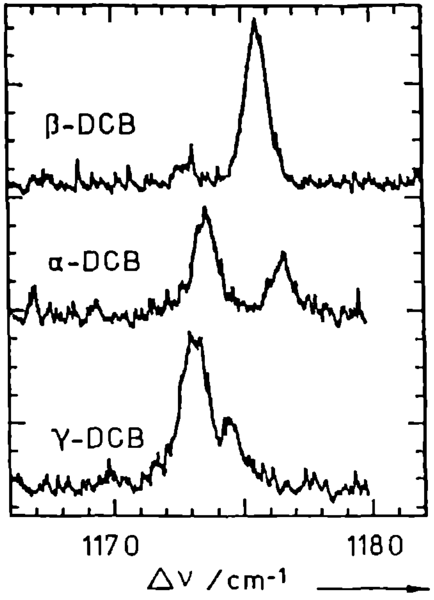

Fig. 3. Raman spectra of the 1169 cm^{-1} (A_g) in-plane C–H bend vibration. Conditions are as detailed in Fig. 1.

qualitative agreement. For α-DCB we measure a splitting of 2.6 cm^{-1} and calculate 0.9 cm^{-1} and for γ-DCB we measure about 12 cm^{-1} and calculate 7.7 cm^{-1}. So, even though γ-DCB seems a more one-dimensional system than α-DCB (if we consider the higher frequency internal vibrations) the Davydov splitting for this low frequency vibration in the γ phase is considerably larger owing to its mixing with the higher frequency lattice modes.

The vibronic line in the $T_0 \longrightarrow S_0$ phosphorescence spectrum of α-DCB, related to this 298 cm^{-1} C—Cl out-of-plane vibration also shows a double peak spectrum, which was previously attributed to a transition from the one-dimensional triplet exciton to a one-dimensional vibrational exciton [23]. With this assumption a triplet exciton band width of about 1 cm^{-1} was obtained from phosphorescence spectra at various temperatures. Since in the 298 cm^{-1} vibron mode the Raman spectrum exhibits a Davydov splitting of 2.6 cm^{-1} and more accurate measurements show no variation of the phosphorescence lineshape with the temperature, it is clear that the structure in the phosphorescence spectrum is due to a Davydov splitting and that this observation cannot be used for determination of the triplet exciton band width.

Another Davydov splitting, shown in Fig. 3, is observed for the 1169 cm^{-1} (A_g) vibration. In the β phase spectrum a single line is observed at 1176 cm^{-1} which is

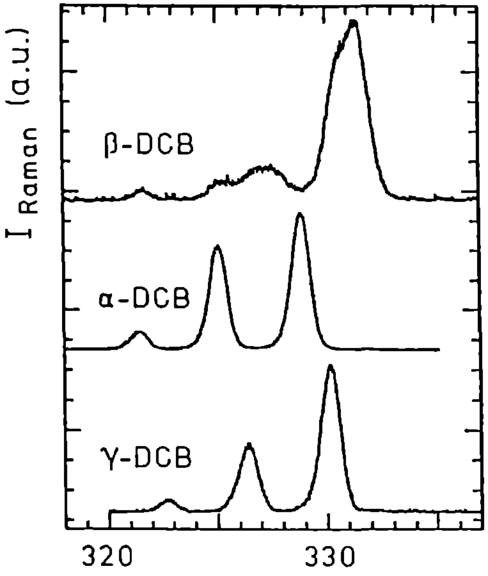

Fig. 4. Raman spectra of the 328 cm^{-1} (A$_g$) C–Cl stretch vibration. Conditions are as detailed in Fig. 1.

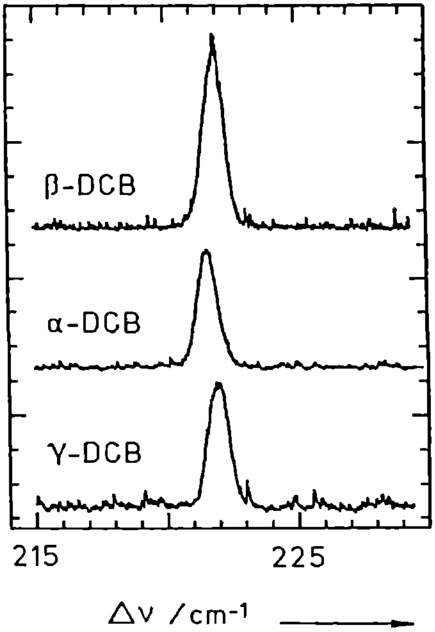

Fig. 5. Raman spectra of the 220 cm^{-1} region. The signal is attributed to the 226 cm^{-1} (B$_{2u}$) C–Cl bend vibration. Conditions are as detailed in Fig. 1.

attributed to this vibration. In both α- and γ-DCB this line is split by about 3.5 cm^{-1} and 2 cm^{-1}, respectively, probably due to a Davydov splitting. The calculations predict a splitting of about 1.4 cm^{-1} for the α phase and a splitting of about 0.6 cm^{-1} for the γ phase. When a potential set without the Coulomb term is used, the calculated Davydov splittings in both phases are smaller than 0.1 cm^{-1}.

In Fig. 4 we present the Raman line corresponding to the 328 cm^{-1} (A$_g$) vibration. Both for the α- and for the γ phase we observe three lines separated by about 4 cm^{-1}, with an intensity ratio of about 1:6:9 and linewidths of $\approx$ 1.0 cm^{-1}. From this ratio Bellows *et al* [25], who studied α-DCB, concluded that all three lines belong to the 328 cm^{-1} (A$_g$) vibration and that they are caused by the different isotopic DCB species. This is confirmed by our calculation of the free molecule frequencies where it is seen that this vibration is very sensitive to the chlorine mass and that the three peaks should indeed be separated by 4 cm^{-1} (see Sec. 2.3). The fact that the three different isotopic species can actually be observed separately in the Raman spectra agrees with the lattice dynamics calculations on α- and γ-DCB from which we see that the dispersion of this vibration ($\leq$ 1 cm^{-1}) is much smaller than the frequency shift caused by the isotopes. As

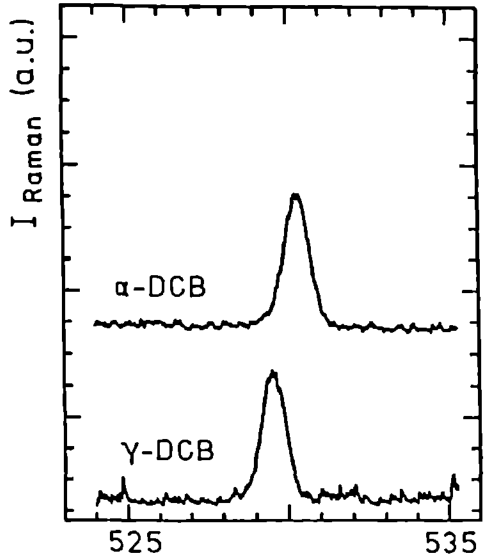

Fig. 6. Raman spectra of the 530 cm^{-1} region of α- and γ-DCB. This signal is attributed to the 550 cm^{-1} (B_{1u}) C–Cl stretch vibration. Conditions are as detailed in Fig. 1.

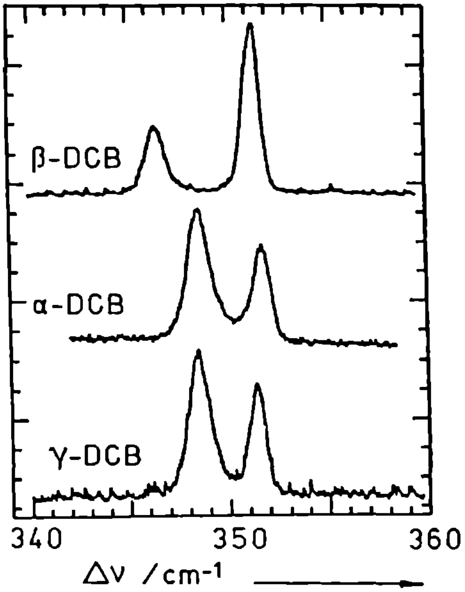

Fig. 7. Raman spectra of the 350 cm^{-1} (B_{3g}) in-plane C–Cl bend vibration. Conditions are as detailed in Fig. 1.

discussed in [1] this corresponds to a situation where a vibrational excitation is localized on clusters of molecules of the same isotopic species (the separated band limit). In β-DCB the situation is different. We calculate a band width of about 10 cm^{-1} for this vibration. The intermolecular coupling is therefore comparable with the intramolecular isotope shift, which implies that the different isotopic DCB species are more or less amalgamated in the vibron band. We expect to observe one line in the Raman spectrum which may have a complicated structure. As can be seen in Fig. 4 the β phase spectrum differs considerably from the other two spectra and the peak structure is very complex indeed. Since the calculations show that the isotope effects are small for all gerade vibrations, except the for 328 cm^{-1} (A_g) vibration, it is not surprising that in the Raman spectra of the other vibrations no effects of the different chlorine masses can be detected.

The breaking of the selection rules due to isotopic disorder, which caused some of the ungerade modes in TCB to become visible in the Raman spectrum (see Ref. [1]), is also observed in DCB. The ungerade vibrations in the Raman spectrum will be most intense for the DCB molecules with the lowest symmetry: molecules with one ^{35}Cl and one ^{37}Cl. This means that instead of the three lines originating from all isotopic species

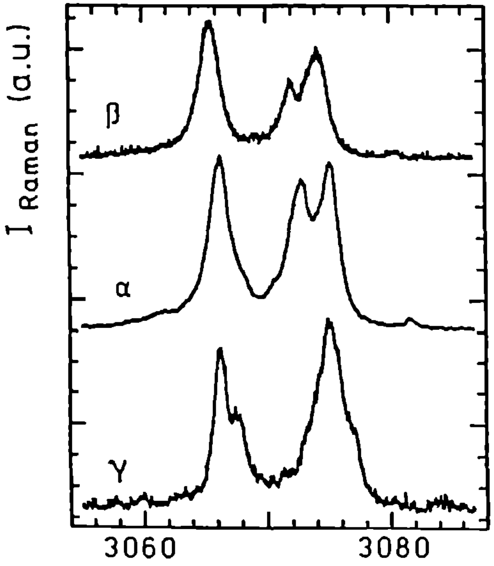

Fig. 8. Raman spectra of the 3065 cm^{-1} (B_{3g}) C–H stretch and the 3070 cm^{-1} (A_g) C–H stretch vibration. Conditions are as detailed in Fig. 1.

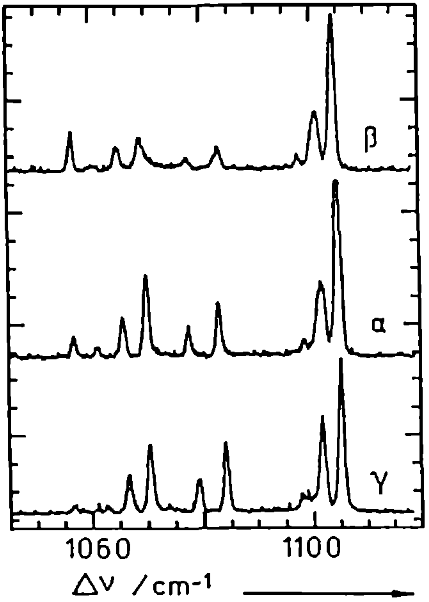

Fig. 9. Raman spectra from 1050 cm^{-1} to 1110 cm^{-1}. Conditions are the same as in Fig. 1.

we observe only a single line. In Fig. 5 it can be seen that in the spectra of all three DCB phases we indeed observe a single line at about 222 cm^{-1} which we attribute to the 226 cm^{-1} (B_{2u}) vibration. The same effect is illustrated in Fig. 6 where in the region around 530 cm^{-1} a single line is also observed which we attribute to the 550 cm^{-1} (B_{1u}) vibration. These two ungerade vibrations are indeed most sensitive to the chlorine mass (see Sec. 2.3).

Besides the observations mentioned above some intriguing phenomena are observed in the Raman spectra. For instance, in Fig. 7 we show the spectra of the 350 cm^{-1} region. Bellows *et al* [25] observed a splitting in the Raman spectrum of α-DCB in this region and concluded, using the same arguments as for the 298 cm^{-1} vibration, that this splitting is a Davydov splitting. However, β-DCB contains only one molecule in the unit cell which eliminates the possibility of a Davydov splitting in this phase. An explanation of the doublet observed in all three spectra in Fig. 7 might be a Fermi resonance of the 350 cm^{-1} (B_{3g}) vibration with the combination band of the 115 cm^{-1} (B_{3u}) and the 226 cm^{-1} (B_{2u}) vibrations. Because of the symmetry in the crystal this resonance is possible. We cannot ascertain that the doublets in our α and γ phase spectra derive from a Fermi resonance as well, but the Davydov splitting calculated for both phases is much too small to account for the observed separation of the two peaks.

In the 3070 cm^{-1} region, shown in Fig. 8, we observe in the spectra of all three phases two main lines that are structured. These lines are attributed to the 3065 cm^{-1} (B_{3g}) and the 3070 cm^{-1} (A_g) vibrations. Since the structure is also observed in the β phase spectrum, we again think that it might be caused by a Fermi resonance with close-lying overtones or combination bands.

A number of Raman lines are observed between 1050 cm^{-1} and 1110 cm^{-1} as shown in Fig. 9. The spectra are very similar for all three phases of DCB. We observe two strong lines, one at about 1102 cm^{-1} and one at 1106 cm^{-1}. These two strong lines are also reported by Gash *et al* [26] who studied the phosphorescence of α- and γ-DCB at low temperatures. The splitting was previously interpreted as a Davydov splitting [26]; this cannot be true because we also observe it in β-DCB. It might be due to a Fermi resonance between the strong 1096 cm^{-1} (A_g) vibration and various overtone or combination bands. Gash *et al* also report the observation of two lines at 1068 cm^{-1} and at 1072 cm^{-1} which they assign to the $0 \rightarrow 2$ 550 cm^{-1} (B_{1u}) vibration, in Fermi resonance with the (A_g) vibration. All other bands in Fig. 9 may also be caused by Fermi resonances but the assignment is difficult.

Spectra at 77 K, not shown here, exhibit lines which are almost a factor of 2 broader than those at 1.2 K. The most likely explanation is that the increase of linewidths at higher temperatures is caused by a decrease of the vibron lifetime. The same effects are also observed in the Raman spectra of TCB [1].

2.6. Conclusions

From the lattice dynamics calculations on β- and α-DCB it is clear that these two phases are not quasi one-dimensional, neither with respect to the lattice modes nor with respect to the propagation of the internal vibrations. However, to our surprise the low temperature γ phase shows a nice one-dimensional behaviour of some internal vibrations, although the phonon frequencies vary in all three directions of the Brillouin zone.

In contrast to TCB, where the calculated dispersion of the internal modes could only match the experimentally observed values when fractional atomic charges were added to the potential, the dispersion in the three phases of DCB is mainly caused by the exponential (exchange) terms and partly compensated by the attractive r^{-6} terms. Addition of charges in DCB hardly influences the results. So it is striking that in all three phases of DCB a mechanism different from that in TCB accounts for the vibron band width.

Not only the one-dimensional vibron band structure but also the (weak) mixing between vibrons and phonons makes it interesting to study γ-DCB by phosphorescence and Raman experiments. This vibron-phonon mixing is absent in the other two phases of DCB and, as we saw, also in TCB [1].

Calculation of the Davydov splitting for α- and γ-DCB yields small values (≤ 1 cm^{-1}), except for some low frequency internal modes. Addition of charges increases these splittings especially in the high frequency region. In the Raman spectra of DCB Davydov splittings are indeed observed for the 298 cm^{-1} (B_{2g}) and for the 1169 cm^{-1} (A_g) vibrations. The observed splittings are in qualitative agreement with the computed values, especially when charges are included in the potential. Some other modes also show splittings which have previously been assigned as Davydov splittings, but which we find also to be present in the β phase spectrum. These splittings might be explained by Fermi resonances with close-lying overtones and combination bands.

The isotope splitting in the Raman spectrum of the 328 cm^{-1} (A_g) vibration observed in α- and γ-DCB is in quantitative agreement with our calculation of the internal modes of DCB for different chlorine isotopes. In these two phases the splitting is visible because the vibron band width appears to be small compared with the isotope shifts (the separated band limit). Because of the much larger vibron band width of the same vibration in β-DCB (calculated to be in the order of 10 cm^{-1}) the β phase Raman spectrum does not show the separated bands but instead shows a complicated band structure. So there is beautiful agreement between calculation and experiment also in this respect.

Because of the breaking of the selection rules due to isotopic disorder we observe in the Raman spectrum the two ungerade vibrations (226 cm^{-1} (B_{2u}) and 550 cm^{-1} (B_{1u})) which the calculations have predicted to be most sensitive to the chlorine mass. Isotope effects for gerade vibrations other than the 328 cm^{-1} (A_g) vibration could not be detected, again in agreement with the calculations.

The lines observed in the Raman spectrum of all three DCB phases between 1050 cm^{-1} and 1110 cm^{-1} are difficult to assign, but they are most probably due to Fermi resonances of the strong fundamental (A_g) transition with overtones and combination bands.

Acknowledgement

We thank A.M. Frens for valuable assistance with the Raman experiments. This investigation is part of the research programs of the "Stichting voor Fundamenteel Onderzoek der Materie (FOM)" and the "Stichting Scheikundig Onderzoek in Nederland (SON)", financially supported by the "Nederlandse Organisatie voor Wetenschappelijk Onderzoek (NWO)".

Note

This chapter is also included in the Ph.D. thesis of A.P.J.M. Jongenelis (University of Leiden, 1988).

References

[1] A.P.J.M. Jongenelis, T.H.M. van den Berg, A.P.J. Jansen, J. Schmidt and A. van der Avoird, J. Chem. Phys. **89**, 4023 (1988).

[2] H. Bonadeo and E.A. D'Alessio, Chem. Phys. Letters **19**, 117 (1973).

[3] H. Bonadeo, E. D'Alessio E. Halac and E. Burgos, J. Chem. Phys. **68**, 4714 (1978).

[4] P.A. Reynolds, J.K. Kjems and J.W. White, J. Chem. Phys. **60**, 824 (1974).

[5] E.H. Abramson, A.P.J.M. Jongenelis and J. Schmidt, J. Chem. Phys. **87**, 3719 (1987).

[6] J. Housty and J. Clastre, Acta Cryst. **10**, 695 (1957).

[7] U. Croatto, S. Bezzi and E. Bua, Acta Cryst. **5**, 825 (1952).

[8] E. Frasson, C. Garbuglio and S. Bezzi, Acta Cryst. **12**, 126 (1959).

[9] M. Gehlfenstein and H. Szwarc, Mol. Cryst. Liq. Cryst. **14**, 283 (1971).

[10] G.L. Wheeler and S.D. Colson, Acta Cryst. **B31**, 911 (1975).

[11] G.L. Wheeler and S.D. Colson, J. Chem. Phys. **65**, 1227 (1976).

[12] C. von Borczyskowski and T. Kirski, J. of Luminescence **38**, 295 (1987).

[13] J. Grimm and C. von Borczyskowski, J. of Luminescence **40,41**, 645 (1988).

[14] P.A. Reynolds, J.K. Kjems and J.W. White, J. Chem. Phys. **56**, 2928 (1972).

[15] E. Burgos, H. Bonadeo and E. D'Alessio, J. Chem. Phys. **63**, 38 (1975).

[16] G. Taddei, H. Bonadeo M.P. Marzocchi and S. Califano, J. Chem. Phys. **58**, 966 (1973).

[17] S. Califano, V. Schettino and N. Neto, *Lattice dynamics of molecular crystals*, Springer, Berlin (1981).

[18] N. Neto, G. Taddei, S. Califano and S.H. Walmsley, Mol. Phys. **31**, 457 (1976).

[19] N. Neto and D. Kirin, Chem. Phys. **44**, 245 (1979).

[20] J.R. Scherer, Spectrochim. Acta **20**, 345 (1964).

[21] J.R. Scherer, Spectrochim. Acta **23A**, 1489 (1967).

[22] E.B. Wilson, J.C. Decius and P.C. Cross, *Molecular vibrations*, McGraw Hill, New York (1955).

[23] J.F.C. van Kooten and J. Schmidt, Chem. Phys. Letters **117**, 77 (1985).

[24] S.M. Janes and H.C. Brenner, Chem. Phys. **101**, 429 (1986).

[25] J.C. Bellows, P.N. Prasad, E.M. Monberg and R. Kopelman, Chem. Phys. Letters **54**, 439 (1978).

[26] B.W. Gash, D.B. Hellmann and S.D. Colson, Chem. Phys. **1**, 191 (1972).

3. On the anomalous vibron/phonon dispersion in solid tetracyanoethene, $C_2(CN)_4$

T.H.M. van den Berg and A. van der Avoird

Institute of Theoretical Chemistry, University of Nijmegen, Toernooiveld, Nijmegen, The Netherlands

(Published in J. Phys.: Condens. Matter 1, 4047 (1989))

Abstract. The anomalous dispersion found by inelastic neutron scattering in one of the vibron bands in solid tetracyano-ethene appears to be due to the electrostatic interactions that couple the infrared-active intramolecular vibrations via the transition dipole resonance mechanism. This is demonstrated by way of both numerical lattice dynamics calculations and a simple mathematical analysis, which relates the Fourier components of the dispersion curves in specific directions of the wave vector $\boldsymbol{k}$ to two-dimensional lattice sums over the dipole-dipole interactions between layers perpendicular to $\boldsymbol{k}$. Only for specific orientations of the molecular transition dipole moments in a solid and for specific directions of $\boldsymbol{k}$ will this lead to a dispersion curve of an irregular shape.

3.1. Introduction

Tetracyanoethene (TCNE), being one of the strongest π-electron acceptors commonly used in electron donor/acceptor complexes, has been studied extensively. Several of these studies address the vibrational spectrum of TCNE [1-7], both in solution and in the crystalline state. A wide-ranging experimental and theoretical study of the lattice vibrations (phonons) and the coupled internal vibrations (vibrons) in solid TCNE has been made by Chaplot *et al* [8]. These authors have measured phonon and vibron dispersion relations by inelastic neutron scattering and they have calculated the corresponding dispersion curves by lattice dynamics methods, using a simplified force field for the lowest intramolecular vibrations and an empirical atom-atom potential for the intermolecular interactions. Generally, the calculated dispersion relations agree well with experiment, provided that the mixing between the lowest internal vibrations and the lattice vibrations is taken into account.

One of the branches showed an unusually strong dispersion, however, which has been determined both by constant wave vector scans and by constant energy scans with the triple-axis neutron spectrometer, but which is not reproduced in any way by the calculations. The calculations gave a smooth and rather flat energy dependence for this branch with no sign of the observed anomalous dispersion, even when phonon-vibron mixing and the mixing between the vibron-modes associated with different internal vibrations were included. Chaplot *et al* [8] speculated that the electrostatic interactions, which had not been included in the lattice dynamics calculations, might be responsible for this anomalous dispersion. In the present paper we shall show explicitly the effects of including the electrostatic interactions and of the use of a more realistic intramolecular force field. We shall demonstrate the physical explanation for the anomalous dispersion and discuss the conditions for which this phenomenon can occur, in TCNE as well as in other systems.

Table I. Free molecular vibrations of TCNE.

	Frequency (cm^{-1})†			
Symmetry (D_{2h})	VFF	Rigid C—C≡N model	Observed IR/Raman spectra	Character of normal mode
b_{2u}	81	74		(NC)—C—(CN) rocking
a_u	88	74		C=C torsion
a_g	133	102	130	(NC)—C—(CN) scissoring
b_{3u}	146	152	180	(NC)—C—(CN) wag
b_{1u}	182	154	165	(NC)—C—(CN) scissoring
b_{3g}	239	250	254	(NC)—C—(CN) rocking
b_{2g}	260	353	251	(NC)—C—(CN) wag
b_{1g}	375	-	360	C—C≡N bend (out-of-plane)
a_u	425	-	410	C—C≡N bend (out-of-plane)
b_{2u}	440	-	443	C—C≡N bend (in plane)
b_{3g}	452	-		C—C≡N bend (in plane)
a_g	489	-	490	C—C stretch / C—C≡N bend
b_{3u}	524	-	555	C—C≡N bend (out-of-plane)
b_{1u}	559	-	579	C—C≡N bend (in plane)
a_g	559	-	535	C—C stretch / C—C≡N bend
b_{2g}	682	-	674	C—C≡N bend (out-of-plane)
b_{1u}	956	-	958	C—C stretch
b_{2u}	1152	-	1155	C—C stretch
b_{3g}	1278	-	1282	C—C stretch
a_g	1571	-	1569	C=C stretch
b_{1u}	2231	-	2230	C≡N stretch
a_g	2235	-	2235	C≡N stretch
b_{2u}	2253	-	2263	C≡N stretch
b_{3g}	2256	-	2247	C≡N stretch

† 1000 cm^{-1} = 29.98 THz.

3.2. Internal vibrations

Empirical Valence Force Fields (VFF) [5,7] and Urey-Bradley Force Fields [2,3,6] for the free molecular vibrations in TCNE have been determined from the experimental infrared and Raman spectra. In our calculations we have used the VFF parameters of Hinkel and Devlin [5] for the in-plane vibrations and those of Michaelian *et al* [7] for the out-of-plane motions. The molecular vibrational frequencies and the corresponding normal mode eigenvectors have been determined by the standard $\boldsymbol{GF}$-matrix method [9]. We observe (see Table I) that the 7 lowest frequency vibrations do indeed correspond to the scissoring, rocking, wagging and torsional motions of the (NC)—C—(CN) groups, but also that the C—C≡N bending motions admix to a considerable extent. For instance, in the b_{3u} wagging mode discussed in Sec. 3.4 the C—C bonds bend out of the molecular plane by 1.5° ($\mathrm{C{=}(C{<}^{C}_{C})}$ wagging angle 3.0°), but the C—C≡N groups also bend by 1.5°. In other words, the C—C≡N groups do not really behave as rigid units in these low frequency vibrations. We have also simulated the rigid C—C≡N model of Chaplot *et al* [8] by making all stretch force constants and the C—C≡N bending force constant infinitely high and adapting the remaining VFF constants to obtain practically the same frequencies as Chaplot *et al* [8]. The eigenvectors are completely determined by symmetry in this model, but some of the frequencies differ considerably from those obtained in the complete VFF model (see Table I). This confirms the non-rigid nature of the C—C≡N groups in the low frequency modes.

3.3. Lattice dynamics calculations

The calculations of the phonon and vibron dispersion relations are based on the standard harmonic lattice dynamics method, as extended to internal vibrations by Taddei *et al* [10] and Califano *et al* [11]. We include the full self term [12,13], in order to ensure complete translational and rotational invariance of the harmonic lattice hamiltonian. For the internal vibrations we use the normal mode eigenvectors from the free molecule calculations (described in Sec. 3.2), transformed from a molecular system of axes to the crystal frame. The calculated free molecule frequencies are replaced by the experimental values, as far as available (see Table I).

The intermolecular potential is represented by an atom-atom potential $V(r) = B_{ij}\exp(-C_{ij}r) - A_{ij}r^{-6} + q_i q_j r^{-1}$ with the same parameters A_{ij}, B_{ij} and C_{ij} as used by Chaplot *et al* [8]. The electrostatic interactions have been added, however, and the fractional atomic charges q_i have been determined by the following procedure. Given the charge neutrality of the TCNE molecule as a whole and its D_{2h} symmetry, only two parameters q_i can be determined independently. These parameters can be obtained from the quadrupole moment tensor of the molecule which has also two independent components. Calculating the quadrupole moment of TCNE by means of *ab initio* LCAO-SCF calculations in one of the standard AO basis sets with the program GAMESS [14] yields $q_C = -0.190e$ for the C=C carbon atoms, $q'_C = +0.489e$ for the C≡N carbon atoms and $q_N = -0.394e$, if the split-valence 3-21G basis is used (and not very different values for the minimal STO-3G basis). Since later in this paper we shall concentrate on the b_{3u} out-of-plane (NC)—C—(CN) wagging mode, we have also made *ab initio* calculations for TCNE deformed along the normal coordinate of this mode. Thus, we could calculate numerically the dipole moment derivative along the b_{3u} wagging mode and compare the *ab initio* value with the value derived from the point charges obtained previously. The agreement is reasonably good: the point charge model adapted to the static quadrupole tensor yields a dipole derivative which is 20% too large (or 20% too small if we use the normal coordinate of the simplified wagging model with rigid C—C≡N groups). Furthermore, we have found that even the changes in the quadrupole moment upon deformation are reasonably well represented by the point-charge model. So we use these point charges[†] to represent the electrostatic interactions between the molecules and their dependence on the internal vibrations. Before performing the actual lattice dynamics calculations we optimized the unit cell parameters and the molecular orientations. Addition of the electrostatic interactions to the intermolecular potential did not significantly change the optimized crystal geometry already calculated by Chaplot *et al* [8], except that the unit cell becomes slightly too compact. We would have to reoptimize the empirical parameters A_{ij}, B_{ij} and C_{ij} in the atom-atom potential, after the addition of the electrostatic interactions, in order to recover the correct unit cell volume.

3.4. Vibron and phonon dispersion relations

The neutron scattering experiments [8] were performed on TCNE in the monoclinic phase, space group $P2_1/n$, supercooled to $T = 5$K. The two molecules in the unit cell are centered at (0,0,0) and $(a/2, b/2, c/2)$, respectively, and they are related by a screw axis 2_1 along the b direction and a glide plane parallel to the ac plane. We use the same convention as Chaplot *et al* [8] for displaying the phonon and vibron dispersion curves along the a^*, b^* and c^* directions of the Brillouin zone and defining the symmetry of the normal modes with respect to the screw axis and the glide plane.

When we omit the electrostatic interactions from our calculations, we obtain practically the same dispersion curves as Chaplot *et al* [8] (1983) for the lowest 26 modes, which originate from the three translational vibrations, three librations and the lowest seven internal vibrations of the two molecules in the unit cell. So the use of non-rigid

---

[†] Another way to obtain fractional atomic charges from *ab initio* LCAO-SCF calculations proceeds via a Mulliken population analysis. It is well known among quantum chemists, however, that the Mulliken atomic charges form a poor representation of the electrostatic interactions. We have also reached this conclusion in the present case.

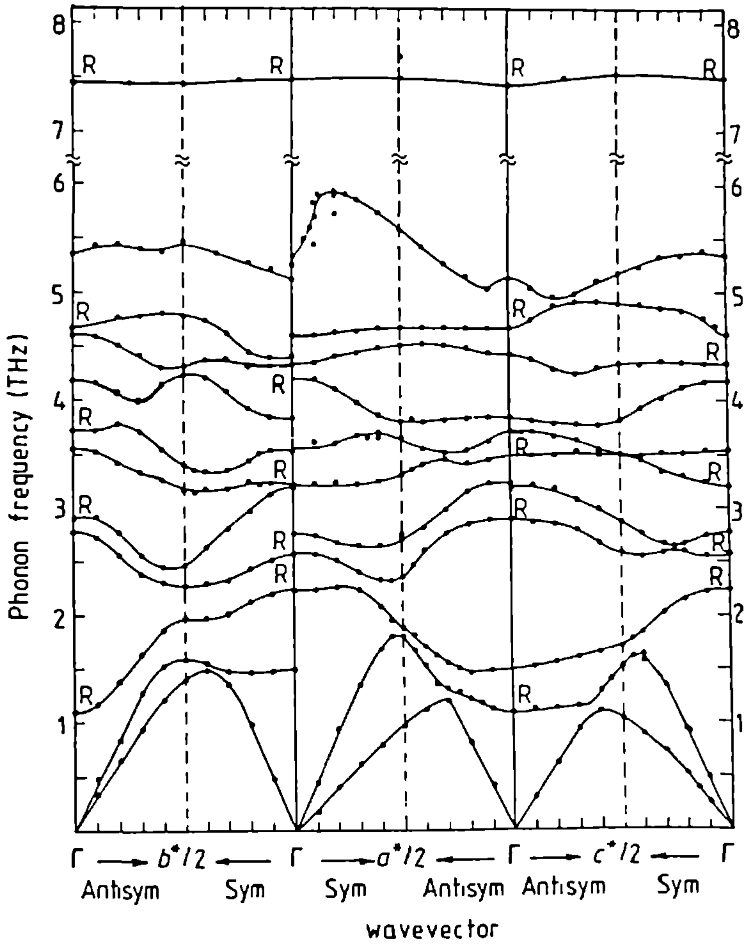

Fig. 1. Experimental phonon/vibron dispersion relations in the monoclinic phase of TCNE, obtained from coherent inelastic neutron scattering by Chaplot *et al* [8].

C—C≡N groups in the intramolecular force field practically does not influence the dispersion relations at this level. (We shall later observe that it does when the electrostatic interactions are included.) Apart from the anomalous dispersion along the a^* direction observed in the mode around 5.5 THz, the agreement with the experimental dispersion curves shown in Fig. 1 is rather good and we obtain substantial mixing between the highest lattice modes and the lowest internal modes, just as found by Chaplot *et al* [8].

The addition of electrostatic interactions via the point charge model discussed in Sec. 3.3 yields the dispersion curves shown in Fig. 2. Although most of the phonon/vibron dispersion curves are not much affected, their resemblance to the experimental picture (Fig. 1) becomes slightly better in general. All the frequencies are too high,

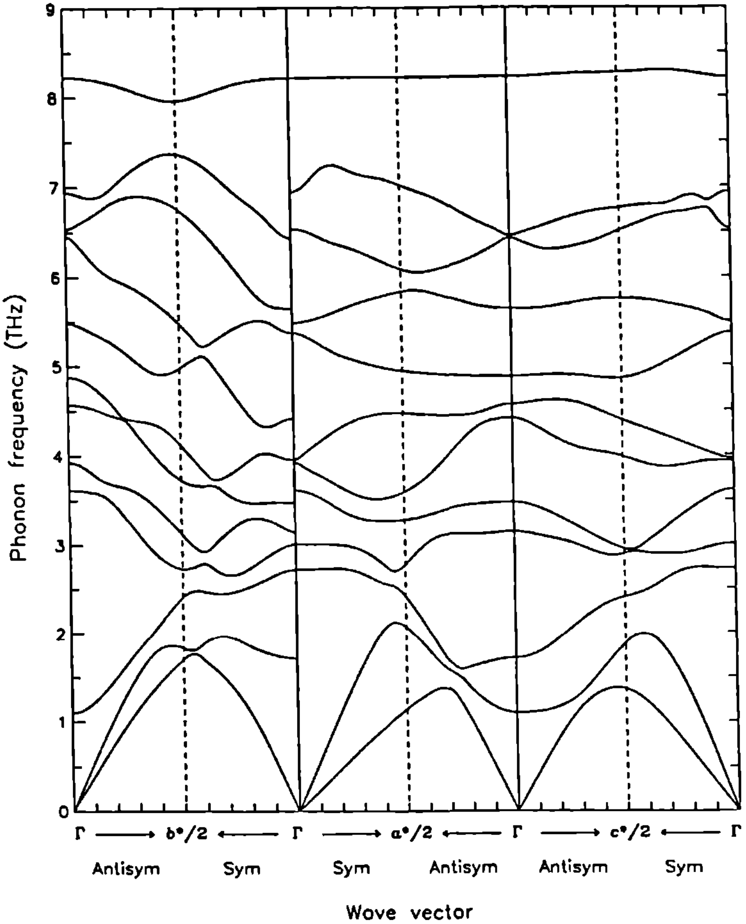

Fig. 2. Phonon/vibron dispersion relations in monoclinic TCNE from lattice dynamics calculations, using an atom-atom potential supplemented by electrostatic interactions between fractional atomic charges (see text). Lattice sums over the intermolecular interactions have been taken up to $R = 30$ Å.

however, which is due to the compactness of the unit cell calculated with the point charges without reoptimizing the remainder of the atom-atom potential. Also we find a too strong dispersion of some of the higher modes in Fig. 2 along the b^* direction which is due to artificial mixing between these modes, some of which are raised more than others.

Let us now concentrate on the mode around 5.5 THz in the Fig. 1 (experimental) which displays the anomalous dispersion in the a^* direction. In Fig. 2 (calculated) this mode lies around 7 THz and we clearly observe an irregular shape of its dispersion curve along the a^* direction which resembles the shape of the experimental curve. Since the

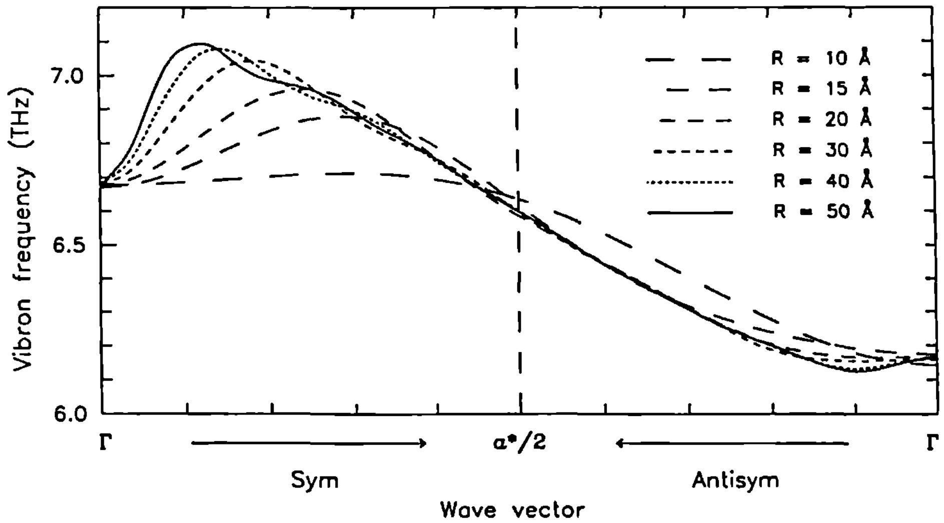

Fig. 3. Vibron dispersion of the b_{3u} out-of-plane wagging mode from lattice dynamics calculations, using the atom-atom potential with the fractional atomic charges. The dispersion curves for wave vectors k along the a^* direction in the Brillouin zone of the vibron modes that are symmetric/antisymmetric with respect to the crystal glide plane are shown for an increasing radius R of truncation of the lattice sums.

corresponding curve calculated without the addition of point charges to the atom-atom potential is completely structureless, as in Ref. [8], we conclude that the anomalous dispersion of this branch is indeed caused by the electrostatic interactions between the molecules. In Sec. 3.5, we shall investigate its shape and its physical origin more in detail. First we establish, by inspecting the eigenvector of the mode which displays the anomalous dispersion, that this mode is purely the b_{3u} out-of-plane wagging mode of the TCNE molecules. Inclusion of just this mode in the lattice dynamics model yields the dispersion curve, shown in Fig. 3, which is practically identical to the curve from the complete calculation, if we take the same radius of truncation (R = 30 Å) of the lattice sum over the intermolecular interactions. So the effects of phonon-vibron mixing or mixing between different internal vibrations which, via avoided crossings, are known to yield rather typical dispersion behavior in many instances, are not relevant in this case. On the other hand, we observe that the shape of the unusual dispersion curve is very sensitive to changes of the fractional atomic charges and to an increase of the radius of truncation of the lattice sum. The dispersion curve in Fig. 3 calculated with the largest radius, R = 50 Å, shows a striking similarity in shape to the experimental curve, shown in detail in Fig. 4. This shape is altered also by replacement of the intramolecular wagging eigenvector from the complete VFF calculation by the eigenvector from the simplified model with rigid C—C≡N groups. By means of a further analysis of the

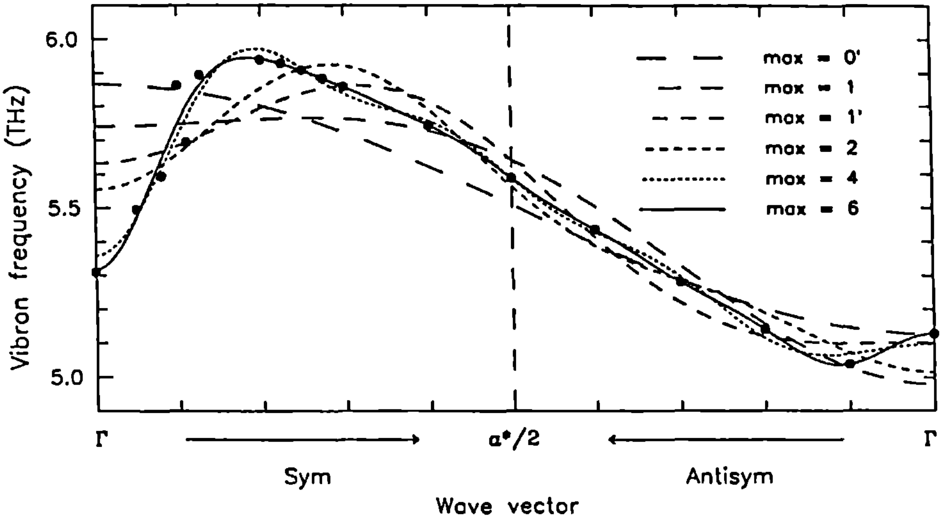

Fig. 4. Fourier analysis of the experimental vibron branch in Fig. 1 which shows the anomalous dispersion. The curves marked in the legend include higher and higher Fourier components $\cos(mkd/2)$. As explained in the text, these Fourier components correspond to the intermolecular couplings between crystal layers perpendicular to the a^* axis with increasing distances $md/2$, where $m = 1, 2, 3, 4, 8$ and 12 (e.g. max = 1' corresponds to a maximum value $m = 3$).

calculated and experimental dispersion curves in Sec. 3.5, we conclude that the coupling between the intramolecular wagging vibrations which leads to the unusual dispersion of the corresponding vibron band in the a^* direction is due to transition dipole-dipole interactions. As is shown by its strong infrared activity [8], the transition dipole moment associated with the b_{3u} out-of-plane wagging vibration is indeed large. We next discuss the conditions under which such a large transition dipole moment can cause unusual dispersion relations.

3.5. Anomalous vibron dispersion from transition dipole-dipole coupling

From the observation that vibron dispersion curves are mostly rather smooth and flat, except near avoided crossings, it may be concluded that the mere occurrence of relatively large vibrational transition dipole moments is not sufficient to cause such a strong dispersion as found in solid TCNE, in one particular vibron band. Here we investigate which are the additional conditions required.

A quantum mechanical system of molecules that vibrate in a single normal mode with (unperturbed) frequency ω_0, which are coupled via transition dipole-dipole interactions, may be replaced (in the sense that it has the same dispersion relations) by a model of oscillating dipoles with eigenfrequency ω_0 that interact via classical dipole-dipole interactions. Let us take a lattice of such dipoles with two equivalent sublattices, as is the case in solid TCNE. The transition dipole moment for the b_{3u} out-of-plane wagging mode in TCNE lies perpendicular to the molecular plane. So the molecular orientations in the solid fix the directions (ϑ, φ) and (ϑ', φ') of the oscillating dipole moments in the two sublattices. The dipole moments are written as $\boldsymbol{\mu} = \frac{\partial \boldsymbol{\mu}}{\partial Q} Q$, where Q is the normal coordinate of the free molecule vibration. This yields the following dispersion relations

$$\omega_{\pm}^2(\boldsymbol{k}) = \omega_0^2 + A(\boldsymbol{k}) \pm A'(\boldsymbol{k}), \tag{1}$$

where $A(\boldsymbol{k})$ and $A'(\boldsymbol{k})$ are the intra- and inter-sublattice couplings between Bloch waves of oscillating dipoles with wave vector $\boldsymbol{k}$. For a given direction of $\boldsymbol{k}$ in the Brillouin zone (for instance, either one of the $\boldsymbol{a}^*$, $\boldsymbol{b}^*$ and $\boldsymbol{c}^*$ directions shown in Figs. 1 and 2), we can write

$$\begin{aligned} A(\boldsymbol{k}) &= F_{00} + 2 \sum_{n=1}^{\infty} F_{0n} \cos knd \\ A'(\boldsymbol{k}) &= 2 \sum_{n'=0}^{\infty} F_{0n'} \cos k(n'd + d'), \end{aligned} \tag{2}$$

where k is the length of the vector $\boldsymbol{k}$. The labels n and n' run over layers perpendicular to the wave vector $\boldsymbol{k}$. The layers n are of the same sublattice as the layer $n = 0$, the layers n' belong to the other sublattice; d is the distance between subsequent layers of the same sublattice and d' is the distance between layer $n = 0$ and the nearest layer of the other sublattice. The quantities F_{0n} and $F_{0n'}$ are two-dimensional lattice sums over layers perpendicular to $\boldsymbol{k}$, which can be expanded in a two-dimensional Fourier series [15]

$$F_{0n} = \sum_{g} v_n(g) \ \exp(i\boldsymbol{g} \cdot \boldsymbol{\tau}_n) \tag{3}$$

and idem for n'. For a lattice of interacting dipoles the Fourier coefficients can be evaluated analytically [16]

$$\begin{aligned} v_n(g) &= \frac{2\pi \left| \frac{\partial \mu}{\partial Q} \right|^2}{\sigma_c} B(\vartheta, \varphi, \vartheta, \varphi, \varphi_g) \ g \exp(-gnd) \\ v_{n'}(g) &= \frac{2\pi \left| \frac{\partial \mu}{\partial Q} \right|^2}{\sigma_c} B(\vartheta, \varphi, \vartheta', \varphi', \varphi_g) \ g \exp[-g(n'd + d')]. \end{aligned} \tag{4}$$

The vectors $\boldsymbol{\tau}_n$ and $\boldsymbol{\tau}_{n'}$ describe the parallel displacements of the layers relative to the layer $n = 0$. The vector $\boldsymbol{g}$ is a two-dimensional reciprocal lattice vector perpendicular to $\boldsymbol{k}$, g is the length of this vector, φ_g its direction and σ_c the area of the two-dimensional unit cell. The function B equals -1 in the special case treated by Nijboer and De Wette [16]. In general, it depends on the polar angles (ϑ, φ) and (ϑ', φ'), which describe the orientations of the dipole moments in the two sublattices, relative to a frame which has its z axis parallel to the wave vector $\boldsymbol{k}$:

$$B(\vartheta_1,\varphi_1,\vartheta_2,\varphi_2,\varphi_g) = [\sin\vartheta_1\cos(\varphi_g-\varphi_1)+i\cos\vartheta_1] \\ \times[\sin\vartheta_2\cos(\varphi_g-\varphi_2)+i\cos\vartheta_2]\,. \tag{5}$$

For specific directions of the wave vector $\boldsymbol{k}$ the crystal symmetry, i.e. the screw axis or the glide plane, will induce special relations between (ϑ,φ) and (ϑ',φ').

According to Eqs. (1) and (2), the intra- and inter-sublattice coupling constants F_{0n} and $F_{0n'}$, which are given by Eqs. (3) to (5), are the Fourier components of the dispersion curves $\omega_+(k)$ and $\omega_-(k)$, considered along specific directions of the wave vector $\boldsymbol{k}$. In Fig. 4 we show a Fourier analysis of the experimental dispersion curve for $\boldsymbol{k}$ along the $\boldsymbol{a}^*$ direction, which displays the anomalous dispersion. We observe that rather high Fourier components contribute to this curve, which is not surprising given its irregular shape. The same effect is shown by the calculated results in Fig. 3: the dispersion curve associated with the b_{3u} wagging mode becomes more and more irregular when it is calculated with an increasing radius of summation of the intermolecular interactions. The increase of this radius implies, of course, that more and more interlayer couplings F_{0n} and $F_{0n'}$ and, therefore, higher Fourier components are taken into account. The shape of the curve calculated with the largest radius of summation is strikingly similar to that of the experimental curve. In order to obtain the exact result we have to invoke the Ewald method [17].

3.6. Conclusions

Through *ab initio* calculations we have obtained a fractional atomic charge model for TCNE which yields a good representation of the electrostatic intermolecular interactions, as well as a fairly good transition dipole moment for the b_{3u} out-of-plane wagging vibration in which we are especially interested. We have refined the lattice dynamics calculations of Chaplot *et al* [8] on solid TCNE, by addition of the interaction between these charges to the usual atom-atom potential and by the use of a more realistic force field for the internal molecular vibrations. The latter refinement did not prove very essential for the shape of the vibron dispersion curves (although it changes the vibrational frequencies considerably), but the addition of the electrostatic interactions shows clearly that the anomalous vibron dispersion found by inelastic neutron scattering for the b_{3u} wagging mode is due to strong transition dipole-dipole coupling. In a further analysis we have established that this coupling will only lead to such an irregular shape of the vibron dispersion curve for specific orientations of the molecular transition dipole moments in the two sublattices of TCNE and for specific directions of the wave vector $\boldsymbol{k}$. The observed hump in the dispersion curve is due to the relative importance of high

Fourier coefficients, which are given as two-dimensional lattice sums for the dipole-dipole interactions between different crystal layers perpendicular to the wave vector $\boldsymbol{k}$.

Acknowledgement

We thank dr. A. Mierzejewski for suggesting this problem and prof. T. Luty for useful discussions. This investigation was supported partly by the Netherlands Foundation for Chemical Research (SON) with financial aid from the Netherlands Organization for Scientific Research (NWO).

References

[1] F.A. Miller, O. Sala, P. Devlin, J. Overend, E. Lippert, W. Luder, W. Moser and J. Varchmin, Spectrochim. Acta **20**, 1233 (1964).

[2] T. Takenaka and S. Hayashi, Bull. Chem. Soc. Jpn. **37**, 1216 (1964).

[3] A. Rosenberg and P.J. Devlin, Spectrochim. Acta **21**, 1613 (1965).

[4] E.M. Popov, I.P. Yakovlev, G.A. Kogan and V.V. Zhogina, Teor. Eksp. Khim. **2**, 464 (1966).

[5] J.J. Hinkel and J.P. Devlin, J. Chem. Phys. **58**, 4750 (1973).

[6] K. Yokoyama and S. Maeda, Bull. Chem. Soc. Jpn. **53**, 1949 (1980)

[7] K.H. Michaelian, K.E. Rieckhoff and E.M. Voigt, J. Mol. Spectr. **95**, 1 (1982).

[8] S.L. Chaplot, A. Mierzejewski, G.S. Pawley, J. Lefebvre and T. Luty, J. Phys. C: Solid State Phys. **16**, 625 (1983).

[9] E.B. Wilson, J.C. Decius and P.C. Cross, *Molecular Vibrations*, McGraw Hill, New York (1955).

[10] G. Taddei, H. Bonadeo, M.P. Marzocchi and S. Califano, J. Chem. Phys. **58**, 966 (1973).

[11] S. Califano, V. Schettino and N. Neto, *Lattice Dynamics of Molecular Crystals*, Springer, Berlin (1981).

[12] N. Neto, G. Taddei, S. Califano and S. H. Walmsley, Mol. Phys. **31**, 457 (1976).

[13] N. Neto and D. Kirin, Chem. Phys. **44**, 245 (1979).

[14] M. Dupuis, D. Spangler and J.J. Wendoloski, NRCC program QG01 (1980).

[15] W.A. Steele, Surf. Sci. **36**, 317 (1973).

[16] B.R.A. Nijboer and F.W. de Wette, Physica **24**, 422 (1958).

[17] M. Born and K. Huang, *Dynamical Theory of Crystal Lattices*, Clarendon Press, Oxford (1954).

4. Modelling the anisotropy of the potential in the dynamics of solid nitrogen

T.H.M. van den Berg, M.M.G. Bongers and A. van der Avoird

Institute of Theoretical Chemistry, University of Nijmegen, Toernooiveld,
6525 ED Nijmegen, The Netherlands

(Published in J. Phys.: Condens. Matter **2**, 8015, (1990))

Abstract. Using a spherical expansion of an *ab initio* N_2-N_2 potential, we have calculated harmonic lattice vibration frequencies for solid α- and γ-nitrogen, in good agreement with experiment and Time Dependent Hartree calculations. Previous dynamics calculations with an (isotropic) atom-atom model fitted to the same *ab initio* potential yielded considerably too high libron frequencies. We conclude, therefore, that the atom-atom model does not do justice to the accurate anisotropy of intermolecular potentials found by *ab initio* calculations. The upward shifts of the lattice frequencies caused by the anharmonicity in the potential agree well with the results from Green's function calculations based on model potentials.

4.1. Introduction

Solid nitrogen, as one of the simplest molecular crystals, is used as a testing ground for modelling intermolecular potentials [1] and for lattice dynamics methods [2]. Much experimental data has been collected [3] and many calculations have been performed [1] especially on the low temperature α phase and the higher pressure γ phase. In these ordered solids the molecules perform oscillations around their equilibrium positions and orientations. The angular oscillations are determined by the anisotropy of the intermolecular potential. This anisotropy can be modelled in different ways: implicitly, by the use of an atom-atom potential, or explicitly, by a spherical expansion of the potential, which is a generalization of the electrostatic multipole expansion [4]. In practice [5], atom-atom potentials are mostly understood to imply isotropic interactions between atoms. This restriction leads to an approximation of the anisotropy in the intermolecular potential. Some authors [6-10] have proposed anisotropic atom-atom interactions. If these are chosen sufficiently flexible, they may reproduce the exact anisotropy of the intermolecular potential in a rather fast converging form [8-10]. The use of such isotropic or anisotropic atom-atom potentials is especially attractive for larger molecules.

Standard harmonic lattice dynamics calculations on α- and γ-nitrogen have been performed using either *ab initio* [11] or semi-empirical N_2-N_2 potentials [1]. An *ab initio* potential, obtained from quantum chemical calculations [12], has not been fitted to experimental (solid state) data and, therefore, is not dependent on the approximations made in the dynamics model. Such a potential can also be used to calculate gas state [13] or liquid state [14] properties of nitrogen and it yields satisfactory results, in general. Harmonic lattice dynamics calculations, using the *ab initio* N_2-N_2 potential of Berns and Van der Avoird [15], resulted in translational phonon frequencies in good agreement with experiment [11]. The calculated libron frequencies, corresponding with collective angular oscillations, came out about 30% too high, but this was believed to be due mainly to the failure of the dynamical model. Inclusion of potential anharmonicities and zero-point motion effects via the Self Consistent Phonon method [16] did not improve the libron frequencies significantly [11].

In order to describe strongly anharmonic motions, Briels, Jansen and Van der Avoird [17,18] developed a quantummechanical lattice dynamics method, based on the Time Dependent Hartree (TDH) formalism, in which the rotational molecular wave functions are expanded in a basis of free rotor functions. Also anharmonic potential terms up to fourth order inclusive in the translational displacements are taken into account. Mean Field calculations showed that the single particle rotational states are rather localized and that the corresponding set of energy levels resembles the spectrum of a two-dimensional harmonic oscillator [17]. Surprisingly, the TDH calculations yielded libron frequencies in good agreement with experiment, whereas the (quasi) harmonic models failed.

The discrepancy between the two lattice dynamics methods described above might be caused by the use of different analytical representations of the intermolecular potential. In the harmonic model, the force constants were calculated as second derivatives of an exp-6-1 isotropic atom-atom potential model [11], which was fitted to the *ab initio* N_2-N_2 potential surface. The inaccuracies in the fits of the individual exchange, dispersion and electrostatic contributions are less than 10% [15]. The resulting inaccuracy in the overall potential, for instance, in the Van der Waals depth is larger, however. The TDH calculations, on the other hand, used a spherical expansion [17] of the potential, which represents its anisotropy exactly.

In the following, we present analytical formulas required for the evaluation of the force constants of a spherical potential expansion. Using these force constants, harmonic lattice vibration frequencies are calculated for α- and γ-nitrogen, which will be compared with atom-atom results, TDH and experiment. Thus, we can explicitly separate the effects of approximations made in the anisotropy of the intermolecular potential and the effects of anharmonicity on the calculated phonon and libron frequencies.

4.2. Force constants from a spherically expanded potential

The anisotropy in the interaction between two linear molecules p and p' is represented explicitly by the following spherical expansion [12]

$$V_{pp'}(\boldsymbol{\omega}_p,\boldsymbol{\omega}_{p'},\boldsymbol{R}_{pp'}) = \sum_{\boldsymbol{l}} \Phi_{\boldsymbol{l}}(R_{pp'}) \sum_{\boldsymbol{m}} \begin{pmatrix} l_1 & l_2 & l \\ m_1 & m_2 & m \end{pmatrix} C^{(l_1)}_{m_1}(\boldsymbol{\omega}_p) C^{(l_2)}_{m_2}(\boldsymbol{\omega}_{p'}) C^{(l)}_{m}(\boldsymbol{\Omega}_{pp'}) \,, \tag{1}$$

which contains a summation over $\boldsymbol{l} = (l_1, l_2, l)$ and $\boldsymbol{m} = (m_1, m_2, m)$. The vector $\boldsymbol{R}_{pp'} = \boldsymbol{R}_{p'} - \boldsymbol{R}_p$ connects the centers of mass of the molecules at positions $\boldsymbol{R}_p$ and $\boldsymbol{R}_{p'}$; $\boldsymbol{\Omega}_{pp'} = (\vartheta_{pp'}, \varphi_{pp'})$ denotes the polar angles of $\boldsymbol{R}_{pp'}$ with respect to the global crystal frame. Further, $\boldsymbol{\omega}_p = (\vartheta_p, \varphi_p)$ describes the orientation of the molecular axis also with respect to the global frame. In Eq. (1), $C^{(l)}_m$ is a Racah spherical harmonic function [19] and the symbol following the second summation sign is a Wigner $3j$ coefficient. The distance dependent expansion coefficients $\Phi_{\boldsymbol{l}}(R_{pp'})$ can be obtained from *ab initio* calculations [15,20]. They contain electrostatic $(R_{pp'}^{-l_1-l_2-1})$, dispersion $(R_{pp'}^{-n}, n = 6, 8, 10)$ and (exponential) exchange contributions.

In harmonic lattice dynamics calculations, one needs the second derivatives of the total crystal potential with respect to the external molecular coordinates

$$Q_{p\lambda} = \begin{cases} R_{p\tau} & (\tau = x, y, z) \\ \omega_{p\rho} & (\rho = \vartheta, \varphi) \,. \end{cases} \tag{2}$$

If the crystal potential is assumed to be a sum of pairwise interactions the force constants are given by

$$\begin{aligned} F^{\lambda\lambda'}_{pp'} &= \frac{\partial^2 V_{pp'}}{\partial Q_{p\lambda} \partial Q_{p'\lambda'}} \quad (p' \neq p) \\ F^{\lambda\lambda'}_{pp} &= \sum_{p' \neq p} \frac{\partial^2 V_{pp'}}{\partial Q_{p\lambda} \partial Q_{p\lambda'}} . \end{aligned} \tag{3}$$

The self-term $F^{\lambda\lambda'}_{pp}$ contains a lattice sum that can be replaced, using translational and rotational invariance conditions [21-23], by an alternative expression in terms of intermolecular couplings $F^{\lambda\lambda'}_{pp'}$ with $p' \neq p$.

The rotational force constants contain derivatives of Racah harmonic functions $C^{(l)}_m$ with respect to molecular angles φ that can be easily evaluated using [19]

$$\frac{\partial^n}{\partial \varphi^n} C^{(l)}_m(\vartheta, \varphi) = (im)^n C^{(l)}_m(\vartheta, \varphi). \tag{4}$$

The first derivative of a Racah harmonic with respect to ϑ is also fairly standard and obeys [24]

$$\begin{aligned} \sin\vartheta \frac{\partial}{\partial \vartheta} C^{(l)}_m(\vartheta, \varphi) = &- (l+1) \cos\vartheta \, C^{(l)}_m(\vartheta, \varphi) \\ &+ \left[(l+1)^2 - m^2\right]^{1/2} C^{(l+1)}_m(\vartheta, \varphi). \end{aligned} \tag{5}$$

Applying Eq. (5) twice and using recurrence relations for the Racah harmonics [24] we find

$$\begin{aligned}\sin^2\vartheta\frac{\partial^2}{\partial\vartheta^2}C^{(l)}_m(\vartheta,\varphi) = {} & \left[(l+1)\cos^2\vartheta + m^2 - l(l+1)\sin^2\vartheta\right]C^{(l)}_m(\vartheta,\varphi) \\ & - \left[(l+1)^2 - m^2\right]^{1/2}\cos\vartheta C^{(l+1)}_m(\vartheta,\varphi).\end{aligned} \tag{6}$$

One has to be careful, however, if $\vartheta = 0$ or π because [24]

$$\lim_{\vartheta\to n\pi}\frac{\partial}{\partial\vartheta}C^{(l)}_m(\vartheta,\varphi) = \tfrac{1}{2}(-1)^{nl}\left[\delta_{m-1}e^{-i\varphi} - \delta_{m1}e^{i\varphi}\right]\left[l(l+1)\right]^{1/2} \quad (n = 0, 1), \tag{7}$$

which is not uniquely defined. A similar problem occurs for the second derivative with respect to ϑ if $m = -2, 0$ or 2. Therefore, one should avoid, by a convenient choice of the global frame, that at equilibrium the molecules are oriented parallel to the z axis.

In order to evaluate the translational force constants it is convenient to use spherical tensor coordinates R_μ defined by [19]

$$\begin{aligned}R_{+1} &= -\frac{1}{\sqrt{2}}\left(R_x + iR_y\right) \\ R_0 &= R_z \\ R_{-1} &= \frac{1}{\sqrt{2}}\left(R_x - iR_y\right).\end{aligned} \tag{8}$$

The position dependent part of the spherical expansion of Eq. (1) is a function of the intermolecular vector $\boldsymbol{R}_{pp'}$. Therefore, all derivatives with respect to individual molecular coordinates $R_{p\mu}$ and $R_{p'\mu}$ can be expressed in derivatives with respect to intermolecular components $R_{pp'\mu}$ according to

$$\frac{\partial}{\partial R_{p\mu}} = -\frac{\partial}{\partial R_{p'\mu}} = -\frac{\partial}{\partial R_{pp'\mu}}. \tag{9}$$

Using the spherical gradient formula of Refs. [18] and [19], it follows that

$$\frac{\partial}{\partial R_\mu}\Phi_l(R)C^{(l)}_m(\Omega) = (-1)^m\sum_k \hat{A}_{lk}\Phi_l(R)\begin{pmatrix} k & 1 & l \\ m-\mu & \mu & -m\end{pmatrix}C^{(k)}_{m-\mu}(\Omega) \tag{10}$$

and

$$\begin{aligned}\frac{\partial^2}{\partial R_\mu\partial R_{\mu'}}\Phi_l(R)C^{(l)}_m(\Omega) = {} & (-1)^\mu\sum_{k'}\sum_k \hat{A}_{kk'}\hat{A}_{lk}\Phi_l(R)\begin{pmatrix} k' & 1 & k \\ m-\mu-\mu' & \mu' & -m+\mu\end{pmatrix} \\ & \times\begin{pmatrix} k & 1 & l \\ m-\mu & \mu & -m\end{pmatrix}C^{(k')}_{m-\mu-\mu'}(\Omega),\end{aligned} \tag{11}$$

where the operator $\hat{A}_{lk}$ is defined as

$$\begin{aligned}\hat{A}_{lk} =&(-1)^l \left\{ \delta_{k,l-1} \left[\frac{l(2l-1)}{2l+1}\right]^{1/2} \left[\frac{\mathrm{d}}{\mathrm{d}R} + \frac{l+1}{R}\right] \right. \\ &\left. -\delta_{k,l+1} \left[\frac{(l+1)(2l+3)}{2l+1}\right]^{1/2} \left[\frac{\mathrm{d}}{\mathrm{d}R} - \frac{l}{R}\right] \right\}.\end{aligned} \tag{12}$$

The derivatives with respect to spherical tensor components $R_{p\mu}$ and $R_{p'\mu}$ have to be transformed into cartesian derivatives. By the use of Eq. (8) together with the property that the pair potential $V_{pp'}$ is a real function, it is easily shown that the cartesian translation-rotation force constants $F^{\tau\rho}_{pp'}$ ($\tau = x, y, z$; $\rho = \vartheta, \varphi$) are related to the spherical tensor components $F^{\mu\rho}_{pp'}$ ($\mu = -1, 0, 1$) via

$$\begin{aligned} F^{x\rho}_{pp'} =& -\sqrt{2}\,\mathrm{Re}\left[F^{1\rho}_{pp'}\right] \\ F^{y\rho}_{pp'} =& \sqrt{2}\,\mathrm{Im}\left[F^{1\rho}_{pp'}\right] \\ F^{z\rho}_{pp'} =& F^{0\rho}_{pp'}. \end{aligned} \tag{13}$$

The cartesian translation second derivatives $F^{\tau\tau'}_{pp'}$ can be obtained from the spherical tensor components $F^{\mu\mu'}_{pp'}$ using the relations

$$\begin{aligned} F^{xx}_{pp'} &= -F^{-11}_{pp'} + \mathrm{Re}\left[F^{11}_{pp'}\right] \\ F^{yy}_{pp'} &= -F^{-11}_{pp'} - \mathrm{Re}\left[F^{11}_{pp'}\right] \\ F^{zz}_{pp'} &= F^{00}_{pp'} \\ F^{xy}_{pp'} &= F^{yx}_{pp'} = -\mathrm{Im}\left[F^{11}_{pp'}\right] \\ F^{xz}_{pp'} &= F^{zx}_{pp'} = -\sqrt{2}\,\mathrm{Re}\left[F^{10}_{pp'}\right] \\ F^{yz}_{pp'} &= F^{zy}_{pp'} = \sqrt{2}\,\mathrm{Im}\left[F^{10}_{pp'}\right]. \end{aligned} \tag{14}$$

Herewith, we have given some basic analytical formulas that can be combined in order to evaluate the force constants corresponding with a spherically expanded intermolecular pair potential. These formulas will also be useful in applications of anisotropic atom-atom potentials [8-10]. The force constants have been implemented in a harmonic lattice dynamics program in which they are used to construct the wave vector dependent dynamical matrix [21]. Diagonalization of this matrix yields the desired lattice vibration frequencies.

4.3. Results and Discussion

We have performed harmonic lattice dynamics calculations on α- and γ-nitrogen using a spherical expansion of the intermolecular potential as described in Sec. 4.2. The self-term has been evaluated either as a lattice sum of second derivatives, see Eq. (3), or with translational and rotational invariance conditions [21-23], which yields identical results. Further test calculations have been performed with the exp-6-1 atom-atom model B of Ref. [15], which we have transformed into a spherical expansion using analytical formulas for the long range dispersion [25] and electrostatic interactions [4] and a fit procedure for the short range exponential terms. The resulting lattice vibration frequencies differ at most by 0.2 cm^{-1} from standard harmonic calculations, in which the force constants are evaluated via direct analytical derivatives of atom-atom potentials. These minor differences are probably due to fit inaccuracies.

In Table I experimental and calculated phonon frequencies are presented for α-N_2. It is observed that in particular the harmonic libron frequencies, obtained with the atom-atom model fitted to the *ab initio* potential, are too high compared with experiment (rms deviation 12.7 cm^{-1}). A similar deviation of the libron frequencies was obtained with the best empirical atom-atom potential from Ref. [1], whereas the translational phonon frequencies agreed well with experiment (see Table I; note that the parameters in this empirical atom-atom potential have been fitted [1] to the lattice frequencies). As mentioned in Sec. 4.1, this discrepancy was believed to be due mainly to the failure of the harmonic model, because of large amplitude angular motions. Now we find, however, that the harmonic calculations which use the direct spherical expansion of the *ab initio* potential of Ref. [15], i.e. without intervention of an atom-atom model, are in excellent agreement with experiment, even for the angular modes with an rms deviation of 5.4 cm^{-1}. Apparently, the direct spherical expansion provides a substantially better description of the potential anisotropy than the atom-atom potential. This plays an important role in the rotational dynamics. In addition, the translational lattice vibrations are also better described (1.3 cm^{-1} rms deviation). Optimization of the crystal structure, within the cubic $Pa3$ symmetry, increases the deviations slightly.

It is interesting to compare the harmonic lattice vibration frequencies with TDH results [18], also included in Table I, which are obtained with the same spherical expansion of Ref. [15]. This comparison yields directly the anharmonic shifts in the lattice frequencies. The TDH libron frequencies are higher, by 1.8 up to 5.2 cm^{-1}, than the corresponding harmonic values, which increases the discrepancy with experiment from 5.4 to 7.5 cm^{-1} if the experimental lattice constant is used ($a = 5.644$ Å). Further, the translational rms deviation is increased from 1.3 to 6.5 cm^{-1}, which appears to be mainly due to third and fourth order anharmonic terms in the potential expansion with respect to molecular displacements [18]. The upward anharmonic shifts of the lattice frequencies are in good agreement with the shifts obtained from Green's function calculations [27-29]. Optimization of the crystal structure lowers the TDH frequencies. The

Table I. Lattice vibration frequencies in α-N_2 (in cm^{-1}).

		Experiment	Semi-empirical	*Ab initio*					
				Atom-atom		Spherical expansion			
		(Ref. [26])	(Ref. [1])	Harmonic		Harmonic		TDH [18]	
Lattice constant a(Å)		5.644	5.644	5.644	5.611*	5.644	5.588*	5.644	5.699*
$\Gamma(0,0,0)$									
Librations	E_g	32.3	37.5	40.7	42.4	27.6	29.7	32.8	31.0
	T_g	36.3	47.7	50.9	52.8	41.6	44.3	43.4	41.0
	T_g	59.7	75.2	75.2	77.6	67.9	71.6	71.5	68.0
Translational vibrations	A_u	46.8	45.9	50.2	52.7	44.2	47.8	50.6	47.2
	T_u	48.4	47.7	49.8	52.6	46.8	51.1	52.7	48.8
	E_u	54.0	54.0	55.8	58.9	54.8	59.8	60.2	55.6
	T_u	69.4	69.5	74.3	78.8	70.4	77.5	79.4	73.1
$M(\frac{\pi}{a},\frac{\pi}{a},0)$									
Mixed	M_{12}	27.8	29.6	33.4	34.9	24.2	25.0	28.8	27.6
	M_{12}	37.9	40.6	44.3	46.3	36.2	39.0	41.5	39.1
	M_{12}	46.8	51.8	56.6	59.0	49.8	53.2	53.3	50.2
	M_{12}	54.9	59.0	61.3	64.4	58.5	63.8	63.7	59.1
	M_{12}	62.5	66.4	68.6	72.2	65.6	71.6	72.0	66.5
$R(\frac{\pi}{a},\frac{\pi}{a},\frac{\pi}{a})$									
Translational vibrations	R_1^-	33.9	34.4	35.3	37.1	33.5	36.4	37.0	34.4
	R_{23}^-	34.7	35.7	37.3	39.2	34.6	37.4	38.4	35.8
	R_{23}^-	68.6	68.3	73.0	77.6	69.4	76.6	78.4	72.3
Librations	R_1^+	43.6	50.7	55.9	58.0	48.6	51.7	50.7	47.9
	R_{23}^+	47.2	57.8	58.8	60.9	49.5	52.3	53.6	50.8
rms deviation of librational frequencies			10.6	12.7	14.9	5.4	7.6	7.5	5.0
rms deviation of translational frequencies			0.6	3.1	6.3	1.3	5.6	6.5	2.1
rms deviation of all lattice frequencies			6.1	8.1	10.4	3.1	6.5	6.7	3.4

* obtained via minimization of the lattice energy.

resulting overall deviation is 3.4 cm^{-1}, which is almost equal to the harmonic deviation of 3.5 cm^{-1} (at the experimental structure).

In addition, we have performed TDH calculations with the atom-atom potential model B of Ref. [15], via the spherical expansion used in the test calculations described above. This shows a similar deviation from experiment as the harmonic atom-atom results; in particular the TDH libron frequencies in α-nitrogen calculated with the

Table II. Lattice vibration frequencies in γ-N_2 (in cm^{-1}).

		Experiment	Semi-empirical	*Ab initio*					
				Atom-atom		Spherical expansion			
		(Ref. [26])	(Ref. [1])	Harmonic		Harmonic		TDH [18]	
Lattice constant a(Å)		3.957	3.940	3.957	4.181*	3.957	4.039*	3.957	3.961*
Lattice constant c(Å)		5.109	5.086	5.109	5.126*	5.109	5.246*	5.109	5.104*
Γ (0,0,0)									
Librations	E_g	55.0	50.5	56.0	48.6	65.7	54.4	67.5	67.6
	B_{1g}	98.1	74.8	101.8	70.6	102.1	89.1	104.2	103.3
	A_{2g}	–	105.1	122.5	92.4	118.3	103.2	125.1	124.4
Translational vibrations	E_u	65.0	58.3	68.6	55.7	58.1	47.9	65.0	65.2
	B_{1u}	–	103.1	112.2	83.2	106.0	86.0	115.8	114.9
rms deviation			14.2	3.0	17.2	7.7	11.2	8.0	7.9

* obtained via minimization of the lattice energy.

atom-atom potential came out about 30% too high. So, we conclude that the substantial differences between harmonic and TDH results found earlier [17,18] are mostly due to the different modellings of the *ab initio* potential, especially of its anisotropy. Lattice dynamics calculations on the γ phase, where the librational motions are more strongly localized, yield a similar conclusion (see Table II). Apparently, the specific strength of TDH lies not so much in the low temperature dynamics of ordered molecular crystals, but rather in the description of disordered phases (β-nitrogen [30], for example), quantum crystals (solid hydrogen [31]) and the combination of lattice dynamics with spin waves (in solid oxygen [2]).

Acknowledgement

This investigation was supported partly by the Netherlands Foundation for Chemical Research (SON) with financial aid from the Netherlands Organization for Scientific Research (NWO).

References

[1] J.C. Raich and N.S. Gillis, J. Chem. Phys. **66**, 846 (1977).

[2] W.J. Briels, A.P.J. Jansen and A. van der Avoird, Adv. Quant. Chem. **18**, 131 (1986).

[3] T.A. Scott, Phys. Rep. **27**, 89 (1976).

[4] M.E. Rose, J. Math. Phys. **37**, 215 (1958).

[5] A.J. Pertsin and A.I. Kitaigorodski, *The atom-atom potential method for organic molecular solids*, Springer, Berlin (1987).

[6] G. Filippini, C.M. Grammacioli, M. Simonetta and G.B. Suffritti, Mol. Phys. **35**, 1659 (1978).

[7] E. Burgos, C.S. Murthy and R. Righini, Mol. Phys. **47**, 1391 (1982).

[8] S.L. Price and A.J. Stone, Mol. Phys. **47**, 1457 (1982).

[9] P.M. Rodger, A.J. Stone and D.J. Tildesley, J. Chem. Soc. Faraday 2, **83**, 1689 (1987).

[10] A.J. Stone and S.L. Price, J. Phys. Chem. **92**, 3325 (1988).

[11] T. Luty, A. van der Avoird and R.M. Berns, J. Chem. Phys. **73**, 5305 (1980).

[12] A. van der Avoird, P.E.S. Wormer, F. Mulder and R. Berns, Topics Curr. Chem. **93**, 1 (1980).

[13] C. Nyeland, L.L. Poulsen and G.D. Billing, J. Phys. Chem. **88**, 1216 (1984).

[14] N. Corbin, W.J. Meath and A.R. Allnatt, Mol. Phys. **53**, 225 (1984).

[15] R.M. Berns and A. van der Avoird, J. Chem. Phys. **72**, 6107 (1980).

[16] N.R. Werthamer, in *Rare Gas Solids*, edited by M.L. Klein and J. Venables, Academic Press, London (1976).

[17] A.P.J. Jansen, W.J. Briels and A. van der Avoird, J. Chem. Phys. **81**, 3648 (1984).

[18] W.J. Briels, A.P.J. Jansen and A. van der Avoird, J. Chem. Phys. **81**, 4118 (1984).

[13] A.R. Edmonds, *Angular momentum in Quantum Mechanics*, Princeton University Press, Princeton, New Jersey (1957).

[20] A. van der Avoird, P.E.S. Wormer and A.P.J. Jansen, J. Chem. Phys. **84**, 1629 (1986).

[21] S. Califano. V. Schettino and N. Neto, *Lattice dynamics of molecular crystals*, Springer, Berlin (1981).

[22] N. Neto, G. Taddei, S. Califano and S.H. Walmsley, Mol. Phys. **31**, 457 (1976).

[23] N. Neto and D. Kirin, Chem. Phys. **44**, 245 (1979).

[24] D.A. Varshalovich, A.N. Moskalev and V.K. Chersonskij, *Quantum Theory of Angular Momentum*, Nauka, Leningrad (1975).

[25] H. Yasuda and T. Yamamoto, Progr. Theor. Phys. **45**, 1458 (1971).

[26] J.K. Kjems and G. Dolling, Phys. Rev. B **11**, 1639 (1975).

[27] K. Kobashi, Mol. Phys. **36**, 225 (1978).

[28] G.F. Signorini, P.F. Fracassi, R. Righini and R.G. Della Valle, Chem. Phys. **100**, 315 (1985).

[29] S. Gonçalves and H. Bonadeo, J. Chem. Phys. **84**, 4106 (1986).
[30] A. van der Avoird, W.J. Briels and A.P.J. Jansen, J. Chem. Phys. **81**, 3658 (1984).
[31] W.B.J.M. Janssen and A. van der Avoird, Phys. Rev. B **42**, 838, (1990).

PART B

DYNAMICS OF ADSORBED MOLECULAR LAYERS

5. Analytical two- and three-dimensional lattice sums for general multipole interactions

T.H.M. van den Berg and A. van der Avoird

Institute of Theoretical Chemistry, University of Nijmegen, Toernooiveld, Nijmegen, The Netherlands

(Published in Chem. Phys. Lett. **160**, 223 (1989))

Abstract. We present a rapidly convergent analytical Fourier expansion of the interaction between an electrostatic multipole moment and a two-dimensional lattice of multipoles, which is a generalisation of two-dimensional monopole-monopole and dipole-dipole lattice sums. Three-dimensional lattice sums can be obtained via analytical planewise summation.

5.1. Introduction

Lattice sums of pairwise interactions occur in many branches of solid state physics. A textbook example is the calculation of the cohesion energy of an ionic crystal [1]. Because of the crystal symmetry, it is sufficient to consider only the total interaction between an ion at a specific lattice site and the ions at all other lattice sites. Thus, the electrostatic cohesion energy can be written as a three-dimensional lattice sum of pairwise Coulomb potentials. In lattice dynamics calculations on ionic crystals, the Coulomb potential is expanded with respect to charge displacements, which, within the harmonic approximation, results in lattice sums of electrostatic dipole-dipole interactions for the force constants. Similar dipole-dipole sums occur in the dielectric theory of solids, for example, in calculations of the macroscopic polarisation of a dielectric material. Lattice sums of higher order multipole-multipole interactions are important for anharmonic lattice dynamics calculations, where the Coulomb potential is expanded beyond the harmonic approximation. They are also needed in lattice energy and dynamics calculations of molecular crystals with intrinsic higher order molecular multipole moments.

Often, special techniques are used to evaluate lattice sums of electrostatic multipole-multipole interactions, because the direct summation is either slowly or conditionally convergent [2-5]. Two classic examples are the treatment of Madelung [6] (for the Madelung constant) and the Ewald method [1,7], which can be applied to three-dimensional lattice sums of pairwise dipole-dipole interactions. Nijboer and De Wette [2] have developed an elegant and efficient method of evaluating three-dimensional lattice sums of general multipole-multipole interactions, which decay faster than the dipole-

dipole interaction with increasing distance. It was first used in connection with the theory of neutron scattering in dense systems [8].

Nijboer and De Wette [3] have also derived an expansion for the interaction between a dipole and a two-dimensional lattice of parallel dipoles, which are oriented perpendicular to the lattice plane. Because of the two-dimensional translation symmetry, the sum over pairwise dipole-dipole potentials can be replaced by a rapidly convergent Fourier series. They have used this expansion to evaluate the electric field within a slab of dielectric material via planewise summation. Steele [9] has derived a similar Fourier expansion for the interaction between an atom and a two-dimensional lattice of substrate atoms, adopting a Lennard-Jones 12-6 atom-atom potential model. This expansion has proved to be valuable in various dynamics calculations of molecules adsorbed or scattered on a surface. Steele has also given an explicit formula for the Fourier transform in the case of a Coulomb potential. This result was first derived, via direct solution of the Poisson equation, by Lennard-Jones and Dent [10]. Moreover, Steele has analytically evaluated, via planewise summation, the interaction of a charge with a semi-infinite three-dimensional ionic substrate.

In the present paper, we show that for general multipole-multipole interactions the occurring two- and three-dimensional lattice sums can also be evaluated analytically. Thus we extend the electrostatic monopole-monopole expansion of Steele [9] and the dipole-dipole expansion of Nijboer and De Wette [3] to a general multipole-multipole Fourier series which, to our knowledge, has not been derived before.

5.2. Derivation of the lattice sums

The electrostatic multipole moments $Q^{(l_A)}$ of a charge cloud A are defined as spherical tensors with components [11,12]

$$Q^{(l_A)}_{m_A} = \sum_{i_A=1}^{N_A} Z_{i_A}\, u_{i_A}^{l_A}\, C^{(l_A)}_{m_A}(\vartheta_{i_A}, \varphi_{i_A}). \tag{1}$$

The polar coordinates u_{i_A}, ϑ_{i_A} and φ_{i_A} denote the positions of the charges Z_{i_A} with respect to a local coordinate system, which is centered at position $\boldsymbol{r}_A$ and which is chosen to be parallel to a global frame. The function $C^{(l_A)}_{m_A}$ is a Racah spherical harmonic [13].

Consider the interaction of these multipole moments localised at $\boldsymbol{r}_A$ with a two-dimensional lattice of multipole moments $Q^{(l_B)}$ at positions

$$\boldsymbol{r}_B = k_1\boldsymbol{a}_1 + k_2\boldsymbol{a}_2 \tag{2}$$

in the xy plane of the global reference frame. Here, $\boldsymbol{a}_1$ and $\boldsymbol{a}_2$ are two-dimensional lattice vectors, k_1 and k_2 are integers. The pair interaction between the multipoles $Q^{(l_A)}$ and

$Q^{(l_B)}$, at positions $\boldsymbol{r}_A$ and $\boldsymbol{r}_B$, is written in the well-known spherical expansion [11,12]

$$V\left(Q^{(l_A)}, Q^{(l_B)}, \boldsymbol{r}_A, \boldsymbol{r}_B\right) = \sum_{m_A=-l_A}^{l_A} \sum_{m_B=-l_B}^{l_B} c_{m_A m_B}^{(l_A l_B)} \, Q_{m_A}^{(l_A)} \, Q_{m_B}^{(l_B)} \, \Upsilon_{-m_A-m_B}^{(l_A+l_B)}(\boldsymbol{r}_A - \boldsymbol{r}_B) \tag{3}$$

with coefficients

$$c_{m_A m_B}^{(l_A l_B)} = (-1)^{l_B} \left[\frac{(2l_A + 2l_B + 1)!}{(2l_A)!(2l_B)!}\right]^{\frac{1}{2}} \begin{pmatrix} l_A & l_B & l_A + l_B \\ m_A & m_B & -m_A - m_B \end{pmatrix} \tag{4}$$

which comprise a Wigner $3j$-symbol. The function $\Upsilon_m^{(l)}$, occurring in Eq. (3), represents an irregular solid Racah harmonic [13]

$$\Upsilon_m^{(l)}(\boldsymbol{r}) = r^{-l-1} \, C_m^{(l)}(\vartheta, \varphi) \tag{5}$$

where ϑ and φ denote the polar angles of the vector $\boldsymbol{r}$. From Eqs. (2) and (3) it follows directly that the total interaction between a single multipole $Q^{(l_A)}$ and a two-dimensional lattice of identical multipoles $Q^{(l_B)}$ contains a lattice sum

$$S_m^{(l)}(\boldsymbol{r}_A) = \sum_{k_1=-\infty}^{+\infty} \sum_{k_2=-\infty}^{+\infty} \Upsilon_m^{(l)}(\boldsymbol{r}_A - k_1\boldsymbol{a}_1 - k_2\boldsymbol{a}_2) \tag{6}$$

of pairwise irregular solid harmonics.

Because of the two-dimensional periodicity this lattice sum can be Fourier expanded as follows [9]

$$S_m^{(l)}(\boldsymbol{r}) = \sum_{\boldsymbol{g}} \widetilde{S}_m^{(l)}(g|z) \exp(i\boldsymbol{g} \cdot \boldsymbol{\tau}) \tag{7}$$

with reciprocal lattice vectors

$$\boldsymbol{g} = n_1\boldsymbol{b}_1 + n_2\boldsymbol{b}_2 \qquad (\boldsymbol{a}_i \cdot \boldsymbol{b}_j = 2\pi\delta_{ij}). \tag{8}$$

In Eq. (7), the vector $\boldsymbol{r} = \boldsymbol{r}_A$ is decomposed into its projection $\boldsymbol{\tau}$ on the xy plane and its component $z\boldsymbol{e}_z$ along the z-axis. The Fourier coefficients are given by the Fourier transform [9]

$$\widetilde{S}_m^{(l)}(g|z) = \frac{1}{\sigma_c} \int_{xy} \Upsilon_m^{(l)}(\boldsymbol{\tau} + z\boldsymbol{e}_z) \exp(-i\boldsymbol{g} \cdot \boldsymbol{\tau}) d\boldsymbol{\tau} \qquad (z \neq 0) \tag{9}$$

where σ_c is the area of the two-dimensional unit cell and the integration has to be performed over the entire xy plane. We will derive an analytical expression for the two-dimensional integral of Eq. (9). To this end, we use the following cylindrical expansion of a two-dimensional plane wave

$$\exp(-i\boldsymbol{g} \cdot \boldsymbol{\tau}) = \sum_{n=-\infty}^{+\infty} i^{-n} J_n(g\tau) \exp(in\varphi_g) \exp(-in\varphi_\tau) \tag{10}$$

which comprises Bessel functions J_n of the first kind [14]. The symbols φ_g and φ_τ denote the angles of the vectors $\boldsymbol{g}$ and $\boldsymbol{\tau}$ with respect to the x-axis, g and τ are the lengths of these vectors. The irregular solid harmonic is written in terms of associated Legendre functions P_l^m as [13]

$$\Upsilon_m^{(l)}(\boldsymbol{\tau}+z\boldsymbol{e}_z) = (-1)^m \left[\frac{(l-m)!}{(l+m)!}\right]^{\frac{1}{2}} \left(\frac{1}{\sqrt{z^2+\tau^2}}\right)^{l+1} P_l^m\left(\frac{z}{\sqrt{z^2+\tau^2}}\right) \exp(im\varphi_\tau). \tag{11}$$

After substitution of Eqs. (10) and (11) into Eq. (9) and performing the integration over φ_τ we obtain

$$\tilde{S}_m^{(l)}(g|z) = \frac{2\pi}{\sigma_o} \left[\frac{(l-m)!}{(l+m)!}\right]^{\frac{1}{2}} i^m \, f_m^{(l)}(g|z) \, \exp(im\varphi_g) \tag{12}$$

with radial integrals

$$f_m^{(l)}(g|z) = \int_0^\infty \left(\frac{1}{\sqrt{z^2+\tau^2}}\right)^{l+1} P_l^m\left(\frac{z}{\sqrt{z^2+\tau^2}}\right) J_m(g\tau)\, \tau d\tau. \tag{13}$$

The integrals of Eq. (13) are relatively simple in the case $g = 0$. Because of the property [14]

$$J_m(0) = \delta_{m0} \tag{14}$$

they reduce to

$$f_m^{(l)}(0|z) = \delta_{m0}\, z^{-l+1} \int_0^1 \rho^{l-2} P_l(\rho)\, d\rho = \delta_{l1}\, \delta_{m0} \qquad (l \geq 1) \tag{15}$$

with $\rho = z/\sqrt{z^2+\tau^2}$. We observe that the integral of Eq. (15) does not exist for the monopole-monopole interaction ($l = 0$).

Although the radial Fourier integrals of Eq. (13) are much more complicated for $g > 0$, an analytical solution is also possible in this case. These integrals are closely connected to specific Hankel transforms which are tabulated in Ref. [15]. Alternatively, they can all be derived from the well-known isotropic ($l = 0$) integral

$$f_0^{(0)}(g|z) = \frac{1}{g} \exp(-gz) \tag{16}$$

given in Ref. [9], with the aid of the relation

$$f_m^{(l)}(g|z) = g^m \, (-1)^{l-m} \, \frac{1}{(l-m)!} \, \frac{\partial^{l-m}}{\partial z^{l-m}} f_0^{(0)}(g|z). \qquad (m \geq 0) \tag{17}$$

This relation is derived in two steps. First, it can be proved, using partial integration and some properties of the associated Legendre and Bessel functions [14], that the indices l and m of $f_m^{(l)}$ can be raised simultaneously for $l = m$ using

$$f_m^{(m)}(g|z) = g \, f_{m-1}^{(m-1)}(g|z). \qquad (m \geq 1) \tag{18}$$

Secondly, from the derivative of Eq. (13) with respect to z, it follows that

$$f_m^{(l)}(g|z) = -\frac{1}{l-m}\,\frac{\partial}{\partial z} f_m^{(l-1)}(g|z) \qquad (l \geq 1) \qquad (19)$$

which can be used to raise the index l for fixed m. After successive application of Eqs. (18) and (19) to the monopole integral we arrive at Eq. (17), which is not directly applicable for negative values of the index m. In that case, however, the symmetry property

$$f_{-m}^{(l)}(g|z) = \frac{(l-m)!}{(l+m)!}\, f_m^{(l)}(g|z) \qquad (20)$$

can be used as an intermediate step. The combination of Eqs. (16), (17) and (20) results in the desired analytical expression

$$f_m^{(l)}(g|z) = \frac{1}{(l-m)!}\, g^{l-1}\, \exp(-gz) \qquad (g > 0) \qquad (21)$$

which is surprisingly simple. This expression, which is also given in Ref. [15], is valid for all relevant m-values. After substitution of Eqs. (15) and (21) into (12) we obtain the final result

$$\widetilde{S}_m^{(l)}(g|z) = \begin{cases} \frac{2\pi}{\sigma_c}\,\delta_{l1}\,\delta_{m0} & (g = 0,\ l \geq 1) \\ \frac{2\pi}{\sigma_a}\,[(l-m)!(l+m)!]^{-\frac{1}{2}}\ i^m g^{l-1} \exp(-gz)\ \exp(im\varphi_g) & (g > 0). \end{cases} \qquad (22)$$

We have now transformed the sum over pair interactions, occurring in Eq. (6), into a two-dimensional Fourier series (7) with coefficients that can be calculated with the aid of Eq. (22). Thus, the two-dimensional lattice sum has been written analytically. Eq. (22) is not valid if $z = 0$, i.e. if the single multipole lies in the lattice plane. A method of evaluating the two-dimensional lattice sum for that case can be found in Ref. [2].

The analytical two-dimensional Fourier series derived above is also convenient to evaluate three-dimensional lattice sums of general multipole-multipole interactions for semi-infinite and infinite crystals, via planewise summation. For a semi-infinite three-dimensional lattice we replace Eq. (2) by

$$\boldsymbol{r}_B = k_1\boldsymbol{a}_1 + k_2\boldsymbol{a}_2 - k_3\boldsymbol{a}_3 \qquad (k_3 \geq 0) \qquad (23)$$

and substitute this into Eq. (6). If we then write the interlayer translation $\boldsymbol{a}_3$ as $\Delta\boldsymbol{r} = \Delta\boldsymbol{\tau} + \Delta z\boldsymbol{e}_z$ the summation over the layers can be performed analytically with the aid of the rapidly converging series

$$\sum_{k_3=0}^{\infty} \exp\left[k_3(-g\Delta z + i\boldsymbol{g}\cdot\Delta\boldsymbol{\tau})\right] = \frac{1}{1 - \exp\left[-g\Delta z + i\boldsymbol{g}\cdot\Delta\boldsymbol{\tau}\right]} \qquad (24)$$

which yields

$$\sum_{k_3=0}^{\infty} S_m^{(l)}(\boldsymbol{r}+k_3\Delta\boldsymbol{r}) = \frac{2\pi}{\sigma_c}\left[(l-m)!(l+m)!\right]^{-\frac{1}{2}}\ i^m \sum_{\boldsymbol{g}} \frac{g^{l-1}\exp\left[-gz+im\varphi_g+i\boldsymbol{g}\cdot\boldsymbol{\tau}\right]}{1-\exp\left[-g\Delta z+i\boldsymbol{g}\cdot\Delta\boldsymbol{\tau}\right]}. \tag{25}$$

The combination of two of these semi-infinite lattice sums with the two-dimensional lattice sum for $z = 0$ [2] gives the three-dimensional lattice sum for an infinite crystal. One has to be careful, however, if $l \leq 2$, because in that case the original three-dimensional lattice sum of irregular solid harmonics is conditionally convergent, i.e. the result depends on the order of summation which is prescribed by the macroscopic shape of the crystal [2-5]. As pointed out by Nijboer and De Wette [3] this implies that for $l \leq 2$ the layerwise summation is only correct for slablike materials. For $l \geq 3$ the lattice sum is absolutely convergent, i.e. independent of the crystal shape, so that a planewise summation may always be applied.

Acknowledgement

This investigation was supported partly by the Netherlands Foundation for Chemical Research (SON) with financial aid from the Netherlands Organization for Scientific Research (NWO).

Note

After this paper was published, it came to our knowledge that our results are in agreement with results of V. Massida and J.A. Hernando (Physica **101B**, 159 (1980)).

References

[1] M. Born and K. Huang, *Dynamical Theory of Crystal Lattices*, Clarendon, Oxford (1954).
[2] B.R.A. Nijboer and F.W. de Wette, Physica **23**, 309 (1957).
[3] B.R.A. Nijboer and F.W. de Wette, Physica **24**, 422 (1958).
[4] J.H.P. Colpa, Physica **56**, 185 (1971).
[5] J.H.P. Colpa, Physica **56**, 205 (1971).
[6] E. Madelung, Phys. Z. **19**, 524 (1918).
[7] P.P. Ewald, Ann. Physik **64**, 253 (1921).
[8] G. Placzek, B.R.A. Nijboer and L. van Hove, Phys. Rev. **82**, 392 (1951).
[9] W.A. Steele, Surf. Sci. **36**, 317 (1973).

[10] J.E. Lennard-Jones and B.M. Dent, Trans. Faraday Soc. **24**, 92 (1928).

[11] M.E. Rose, J. Math. Phys. **5**, 215 (1958).

[12] A. van der Avoird, P.E.S. Wormer, F. Mulder and R. Berns, Topics Curr. Chem. **93**, 1 (1980).

[13] A.R. Edmonds, *Angular momentum in Quantum Mechanics*, Princeton University Press, Princeton, New Jersey (1957).

[14] M. Abramowitz and I.A. Stegun, *Handbook of Mathematical Functions*, National Bureau of Standards, Washington D.C. (1964).

[15] A. Erdélyi, W. Magnus, F. Oberhettinger and F.G. Tricomi, *Tables of Integral Transforms* (McGraw-Hill, New York, 1954).

6. Potential expansion for molecules adsorbed or scattered on a surface

T.H.M. van den Berg and A. van der Avoird

Institute of Theoretical Chemistry, University of Nijmegen, Toernooiveld, Nijmegen, The Netherlands

(Published in Phys. Rev. B 40, 1932 (1989))

Abstract. We present an analytical potential expansion for a molecule interacting with a two-dimensional lattice of atoms which is convenient in quantummechanical scattering and lattice dynamics calculations. It combines the following three ingredients: a spherical expansion in symmetry adapted free rotor functions of the molecule which represents the anisotropy of the potential explicitly, a translational displacement expansion that goes beyond the harmonic approximation, and a two-dimensional Fourier expansion, which reflects the translational symmetry parallel to the substrate. As an example, we show some numerical results for N_2 on graphite which illustrate the convergence of the various expansions. The potential anisotropy is visualized explicitly. At an adsorption site, the in-plane anisotropy appears to be negligible with respect to the out-of-plane anisotropy. The anharmonic terms in the molecular displacement expansion are so important that they will influence the out-of-plane translational vibrations.

6.1. Introduction

The interaction between molecules and substrates plays an important role in many interesting physical phenomena. It can be probed by molecular beam surface scattering experiments [1,2]. Furthermore, it leads to the adsorption of molecules or molecular layers on the surface, which can take part in many interesting processes. Adsorbed layers are (quasi) two-dimensional systems which occur in a rich variety of phases [3] that can differ strongly from the ordinary bulk phases. Of course, in an adsorbed layer the admolecule-admolecule and the substrate mediated interactions [4,5] must also be taken in account. The competition between all types of interactions determines, for instance, whether an adsorbed molecular layer is commensurate or incommensurate with the underlying crystal [6,7]. However, in this paper we concentrate on the molecule-substrate interactions.

In order to calculate the dynamics of adsorbed or surface scattered molecules, one needs expansions of the total molecule-substrate potential. First we summarize what is available in the literature. Steele [8] has derived a powerful expansion for the interaction between an atom and a two-dimensional lattice of substrate atoms, adopting an atom-atom pair potential model. Because of the two-dimensional translation symmetry, the sum over pair potentials can be replaced by a rapidly convergent Fourier series. Steele has given explicit formulas for the Fourier transforms in the case of a Lennard-Jones 12-6 atom-atom potential. The extension to exponential potentials has been made by Belak [9]. Both types of Fourier series have proved to be valuable in various classical molecular dynamics and harmonic lattice dynamics calculations on adsorbed molecular layers [10,11]. In these calculations the interaction between an adsorbed molecule and a substrate atom is considered to be a sum of atom-atom potentials, so that the total molecule-substrate potential can be written as a sum over atom-substrate Fourier expansions. The lowest order term of such a molecule-substrate Fourier expansion only depends on the height of the atoms above the substrate. Sokolowski, in his calculations of second virial coefficients and other properties of adsorbed linear molecules, has expanded this term into spherical harmonics and numerically evaluated the expansion coefficients [12,13]. Further, we remark that the atom-substrate Fourier series has been expanded with respect to atomic displacement coordinates in order to get harmonic force constants.

Another type of expansion which is useful in molecule-molecule scattering calculations and in dynamical calculations of molecular complexes (Van der Waals molecules) and molecular bulk solids, is the so-called spherical expansion [14]. Such an expansion represents explicitly the anisotropy of an intermolecular potential. If the intermolecular potential is given as a sum of atom-atom potentials this spherical expansion can be obtained with the aid of analytical transformation formulas which are known for inverse power law [15] and exponential atom-atom potential types [16]. However, spherical expansions are much more general than atom-atom potential models and they can be used to fit experimental or *ab initio* data directly. They can also be further expanded with respect to translational molecular displacement coordinates [17], which is useful for the calculation of the vibrational states in molecular complexes or solids. Combined spherical and displacement expansions have proved to be valuable for example, in quantummechanical lattice dynamics calculations on solid nitrogen and oxygen [18].

In the present paper we are interested in molecule-substrate interactions and we combine the two ingredients, atom-substrate potentials and molecule-molecule potentials, in order to derive new formulas for molecule-substrate potentials. We combine the advantages of spherical, molecular displacement and Fourier expansions.

In Sec. 6.2 we describe a general method to obtain a molecule-substrate Fourier potential series starting from a spherical expansion for molecule-atom pair potentials. In Sec. 6.3 we derive an alternative method, which is applicable and preferable in the special case that the pair interaction can be approximated by an atom-atom potential model. In Sec. 6.4 we give some quantitative examples.

6.2. General method

6.2.1. Spherical expansion of anisotropic molecule-atom potentials

Consider a molecule interacting with a substrate, that consists of discrete atoms or ions. The total interaction between the molecule and the substrate is assumed to be the sum of molecule-atom pair potentials. Three particle and higher order terms are neglected. In order to represent the anisotropic behaviour, we use a spherical expansion to describe the molecule-atom pair potentials

$$V(\boldsymbol{R},\omega) = \sum_{l=0}^{\infty} \sum_{m'=-l}^{l} v_{lm'}(R) \sum_{m=-l}^{l} (-1)^m C^{(l)}_{-m}(\hat{\boldsymbol{R}}) D^{(l)}_{mm'}(\omega)^*. \qquad (1)$$

This is a special case of the more general expansion for two interacting molecules given by Van der Avoird *et al* [14], which follows easily when one of the molecules is replaced by an atom. In a forthcoming paper we will use the more general spherical expansion in order to derive analytical expressions for the interaction between an electrostatic multipole and a two-dimensional lattice of multipoles. In Eq. (1) $C^{(l)}_m$ is a Racah spherical harmonic and $D^{(l)}_{mm'}$ is a Wigner D function in the active convention [19]. These angle dependent functions are coupled. The result is a scalar, which ensures the invariance of the total expansion with respect to an overall rotation of the system. Furthermore, the vector $\boldsymbol{R} = (R, \hat{\boldsymbol{R}})$ connects both centers of mass, pointing from the atom to the molecule and the molecular orientation is described by the Euler angles $\omega = (\alpha, \beta, \gamma)$. For a linear molecule these angles are the polar angles $\omega = (\varphi, \vartheta, 0)$. In that case the sum over m' must be omitted and the complex conjugated Wigner D functions have to be replaced by Racah spherical harmonics according to Ref. [19]

$$C^{(l)}_m(\vartheta, \varphi) = D^{(l)}_{m0}(\varphi, \vartheta, 0)^*. \qquad (2)$$

In the special case that the molecule consists of a single atom, the expansion of Eq. (1) reduces to an isotropic ($l = 0$) atom-atom potential.

If the molecule possesses a molecular symmetry group G of order n_G, then the total molecule-atom pair potential expansion must be invariant under all operations of this group. It is convenient to exploit this property with the aid of the totally symmetric projection operator [17]

$$\hat{S} = \frac{1}{n_G} \sum_{g \in G} \hat{P}(g). \qquad (3)$$

The molecular symmetry operators $\hat{P}(g)$ act on D functions according to the Wigner convention [20]. It can be shown that the corresponding symmetry adapted functions are linear combinations of D functions,

$$G^{(l)}_{mm'}(\omega) = \hat{S} D^{(l)}_{mm'}(\omega)^* = \sum_n c^{(l)}_{nm'} D^{(l)}_{mn}(\omega)^*. \qquad (4)$$

An example of symmetry adapted functions can be found in Ref. [17], where the tetrahedral rotation functions are listed for $l \leq 10$. Using the symmetry adapted functions from Eq. (4), we can write the spherical expansion of a molecule-atom potential as

$$V(\boldsymbol{R},\omega) = \sum_{l}\sum_{m'} \Phi_{lm'}(R) \sum_{m=-l}^{l} (-1)^m C^{(l)}_{-m}(\hat{\boldsymbol{R}}) G^{(l)}_{mm'}(\omega). \tag{5}$$

There may be more than one symmetric linear combination of D functions for a fixed value of l. In Eq. (5), the summation over m' has to be performed over different combinations only.

It is assumed that the expansion coefficients $\Phi_{lm'}$, occurring in Eq. (5), are (analytical) functions of the intermolecular distance R. These functions are usually obtained by an analytical fit of *ab initio* or experimental data. The simplest and most popular forms are of the inverse power or exponential type, but many other forms have been used [21]. The functions $\Phi_{lm'}$ can also be derived from an atom-atom potential model, with the aid of explicit formulas, as given in for instance Refs. [15] and [16]. This does not imply, however, that a spherical expansion is always equivalent to a sum of atom-atom potentials. On the contrary, it is much more general.

6.2.2. Molecular displacement expansion

In dynamical calculations on adsorbed molecules which perform small oscillations around an equilibrium configuration, one often needs an expansion with respect to molecular displacement coordinates. For this reason we make the following Taylor expansion of the pair potential given by Eq. (5)

$$V(\boldsymbol{R}+\boldsymbol{u},\omega) = \sum_{\alpha=0}^{\infty} \frac{(\boldsymbol{u}\cdot\nabla)^{\alpha}}{\alpha!} V(\boldsymbol{R},\omega), \tag{6}$$

where $\boldsymbol{u}$ denotes a small molecular displacement vector. The substrate is considered to be rigid.

This expansion is most conveniently performed with the aid of the spherical gradient formula [22], as demonstrated by Briels *et al* [17,18]. Since the formulas given in Ref. [17] are very complex, we summarize the result in a compact notation

$$V(\boldsymbol{R}+\boldsymbol{u},\omega) = \sum_{\Lambda} E_{\Lambda}(\boldsymbol{R}) u^{\alpha} C^{(l_1)}_{m_1}(\hat{\boldsymbol{u}}) G^{(l)}_{mm'}(\omega), \tag{7}$$

where the combined index Λ is defined by

$$\Lambda = (l, m, m', \alpha, l_1, m_1) \qquad 0 \leq l_1 \leq \alpha\ ,\ l_1 + \alpha = \text{even}. \tag{8}$$

In Eq. (7), the coefficients $E_{\Lambda}(\boldsymbol{R})$, which depend on the equilibrium intermolecular vector, appear to be given by

$$E_{\Lambda}(\boldsymbol{R}) = E_{lmm'\alpha l_1 m_1}(\boldsymbol{R}) = \frac{1}{\alpha!}\sum_{l_2}\sum_{m_2} \begin{pmatrix} l_1 & l_2 & l \\ m_1 & m_2 & m \end{pmatrix} W^{(\alpha)}_{lm';l_1 l_2}(R) C^{(l_2)}_{m_2}(\hat{\boldsymbol{R}}). \tag{9}$$

Here, the summation over l_2 and m_2 is limited to a few terms because of the selection rules that can be obtained from the Wigner $3j$ symbol. For a fixed combination of l and m' the distance dependent functions $W_{lm';l_1 l_2}$ in Eq. (9) can be calculated by means of the initialization

$$W^{(0)}_{lm';l_1 l_2}(R) = \delta_{l_1 0}\delta_{l_2 l}\sqrt{2l+1}\,\Phi_{lm'}(R) \tag{10}$$

and the recurrence relation

$$\begin{aligned} W^{(\alpha+1)}_{lm';l_1 l_2}(R) = (2l_1+1)(-1)^{l+1}\sum_{j_1}\sum_{j_2}\begin{pmatrix} j_1 & 1 & l_1 \\ 0 & 0 & 0 \end{pmatrix}\begin{Bmatrix} l_2 & l_1 & l \\ j_1 & j_2 & 1 \end{Bmatrix} \\ \times \hat{A}_{j_2 l_2}(R) W^{(\alpha)}_{lm';j_1 j_2}(R) \end{aligned} \tag{11}$$

where the operator $\hat{A}_{j_2 l_2}(R)$ is defined by

$$\begin{aligned} \hat{A}_{j_2 l_2}(R) =& (-1)^{j_2}\left\{\delta_{l_2, j_2-1}\left[\frac{j_2(2j_2-1)}{2j_2+1}\right]^{1/2}\left[\frac{d}{dR}+\frac{j_2+1}{R}\right]\right. \\ & \left. -\delta_{l_2, j_2+1}\left[\frac{(j_2+1)(2j_2+3)}{2j_2+1}\right]^{1/2}\left[\frac{d}{dR}-\frac{j_2}{R}\right]\right\}. \end{aligned} \tag{12}$$

See Ref. [17] for further details.

We have now obtained a useful potential expansion, see Eq. (7), for the interaction between a molecule and an atom. As we have mentioned before, this expansion represents explicitly the anisotropy of the pair potential. Furthermore, it includes an expansion with respect to molecular displacements, that goes beyond the harmonic approximation.

6.2.3. Fourier transformation of the pair potential sum

As a final step, the total molecule-substrate interaction can be obtained as a sum over the expanded molecule-atom pair potentials. In most practical cases the substrate atoms are ordered in lattice planes, so that the molecule-substrate potential shows a two-dimensional periodicity parallel to the substrate surface. This symmetry property can be exploited by transforming the sum over pair potentials into a two-dimensional Fourier series, as will be demonstrated in this subsection.

Assume, for simplicity, that the molecule is interacting with a single two-dimensional lattice of substrate atoms. We choose a global reference frame, so that the xy plane coincides with the lattice plane. Further, it is assumed that there are n_s different substrate sublattice types s, which are translated by a vector $\boldsymbol{\tau}_s$ with respect to the origin. The position of a single substrate atom, of type s, can then be written as

$$\boldsymbol{\tau}_{s k_1 k_2} = \boldsymbol{\tau}_s + k_1 \boldsymbol{a}_1 + k_2 \boldsymbol{a}_2 \qquad (1 \leq s \leq n_s), \tag{13}$$

where $\boldsymbol{a}_1$ and $\boldsymbol{a}_2$ are the two-dimensional lattice vectors and k_1 and k_2 are integers. Let $\boldsymbol{x}$ denote the (equilibrium) position of the molecular center of mass. The total molecule-substrate potential

$$U(\boldsymbol{x}+\boldsymbol{u},\omega)=\sum_{\Lambda}F_{\Lambda}(\boldsymbol{x})u^{\alpha}C^{(l_1)}_{m_1}(\hat{\boldsymbol{u}})G^{(l)}_{mm'}(\omega) \tag{14}$$

is assumed to be the sum of two particle interactions only, so that

$$F_{\Lambda}(\boldsymbol{x})=\sum_{s=1}^{n_s}\sum_{k_1=-\infty}^{+\infty}\sum_{k_2=-\infty}^{+\infty}E_{\Lambda}(\boldsymbol{x}-\boldsymbol{r}_{sk_1k_2}), \tag{15}$$

where we have used Eq. (7). The combined index Λ is defined in Eq. (8). The function F_Λ is invariant under a lattice translation parallel to the substrate surface. For this reason, the following two-dimensional Fourier transformation is possible

$$F_{\Lambda}(\boldsymbol{x})=\sum_{\boldsymbol{g}}\tilde{F}_{\Lambda}(\boldsymbol{g}\mid z)\exp(i\boldsymbol{g}\cdot\boldsymbol{\tau}) \tag{16}$$

with $\boldsymbol{\tau}$ denoting the projection of $\boldsymbol{x}$ on the xy plane, so that $\boldsymbol{x}=\boldsymbol{\tau}+z\boldsymbol{e}_z$. The summation has to be performed over all wave vectors $\boldsymbol{g}$, which are linear combinations of the reciprocal lattice vectors $\boldsymbol{b}_1$ and $\boldsymbol{b}_2$

$$\boldsymbol{g}=n_1\boldsymbol{b}_1+n_2\boldsymbol{b}_2 \qquad (\boldsymbol{a}_i\cdot\boldsymbol{b}_j=2\pi\delta_{ij}), \tag{17}$$

where n_i is an integer.

It appears, in analogy with Ref. [8], that the z-dependent Fourier coefficients are given by means of the Fourier transformation

$$\tilde{F}_{\Lambda}(\boldsymbol{g}\mid z)=\frac{1}{\sigma_c}\left[\sum_{s=1}^{n_s}\exp(-i\boldsymbol{g}\cdot\boldsymbol{r}_s)\right]\int_{\sigma_{xy}}E_{\Lambda}(\boldsymbol{\tau}+z\boldsymbol{e}_z)\exp(-i\boldsymbol{g}\cdot\boldsymbol{\tau})\,d\boldsymbol{\tau}, \tag{18}$$

in which the parameter σ_c equals the substrate unit cell area and where the integration has to be performed over the whole xy plane σ_{xy}. In the following, we will reduce the two-dimensional integral of Eq. (18) to a simpler form. To this end, we separate the integrand into a radial and an angular dependent part, using the following cylindrical expansion of a two-dimensional plane wave

$$\exp(i\boldsymbol{g}\cdot\boldsymbol{\tau})=\sum_{n=-\infty}^{+\infty}i^nJ_n(g\tau)\exp(in\varphi_g)\exp(-in\varphi_\tau) \tag{19}$$

which comprises the Bessel functions J_n of the first kind [23]. The symbols φ_g and φ_τ denote the angles of the vectors $\boldsymbol{g}$ and $\boldsymbol{\tau}$ with respect to the x axis. Further, it can be shown, with the aid of Eq. (9), that

$$E_{\Lambda}(\boldsymbol{\tau}+z\boldsymbol{e}_z)=\Psi_{\Lambda}(\tau,z)\exp\bigl(-i(m+m_1)\varphi_\tau\bigr), \tag{20}$$

with

$$\Psi_\Lambda(\tau,z) = \frac{1}{\alpha!}\sum_{l_2}\sum_{m_2}(-1)^{m_2}\sqrt{\frac{(l_2-m_2)!}{(l_2+m_2)!}}\begin{pmatrix} l_1 & l_2 & l \\ m_1 & m_2 & m \end{pmatrix}$$
$$\times W^{(\alpha)}_{lm';l_1l_2}\left(\sqrt{z^2+\tau^2}\right) P^{m_2}_{l_2}\left(\frac{z}{\sqrt{z^2+\tau^2}}\right). \tag{21}$$

Here, the associated Legendre function $P^{m_2}_{l_2}$ and some of the algebraic factors originate from the following expression for the Racah harmonics [19]

$$C^{(l_2)}_{m_2}\left(\widehat{\boldsymbol{\tau}+z\boldsymbol{e}_z}\right) = (-1)^{m_2}\sqrt{\frac{(l_2-m_2)!}{(l_2+m_2)!}}P^{m_2}_{l_2}\left(\frac{z}{\sqrt{z^2+\tau^2}}\right)\exp(im_2\varphi_\tau). \tag{22}$$

The argument of $P^{m_2}_{l_2}$ equals the cosine of the angle between the vector $\boldsymbol{x}$ and the z axis. Note that the $3j$ symbol in Eq. (21) can only be nonzero if $m_2 = -(m+m_1)$, which explains the argument of the exponential function in Eq. (20). After substitution of Eqs. (19) and (20) into Eq. (18), we obtain the following expression for the total molecule-substrate potential

$$U(\boldsymbol{x}+\boldsymbol{u},\omega) = \sum_\Lambda\left[\sum_{\boldsymbol{g}}\tilde{F}_\Lambda(g\mid z)\exp(i\boldsymbol{g}\cdot\boldsymbol{\tau})\right]u^\alpha C^{(l_1)}_{m_1}(\hat{\boldsymbol{u}})G^{(l)}_{mm'}(\omega). \tag{23}$$

This expansion is a combination of a spherical, a displacement and a Fourier expansion. The Fourier coefficients are given by

$$\tilde{F}_\Lambda(g\mid z) = \frac{2\pi}{\sigma_c}\left[\sum_s\exp(-i\boldsymbol{g}\cdot\boldsymbol{\tau}_s)\right]\tilde{\Psi}_\Lambda(g\mid z)\exp\left(-i(m+m_1)\varphi_g\right), \tag{24}$$

with

$$\tilde{\Psi}_\Lambda(g\mid z) = \frac{1}{\alpha!}\sum_{l_2}\sum_{m_2}i^{m_2}\sqrt{\frac{(l_2-m_2)!}{(l_2+m_2)!}}\begin{pmatrix} l_1 & l_2 & l \\ m_1 & m_2 & m \end{pmatrix}$$
$$\times\int_0^\infty J_{m_2}(g\tau)\,W^{(\alpha)}_{lm';l_1l_2}(\sqrt{z^2+\tau^2})\,P^{m_2}_{l_2}\left(\frac{z}{\sqrt{z^2+\tau^2}}\right)\tau d\tau. \tag{25}$$

We have now transformed the sum over pair potentials, occurring in Eq. (14), into a two-dimensional Fourier series with Fourier coefficients that can be calculated with the aid of Eqs. (24) and (25). Thus, the two-dimensional lattice sum has vanished, but some one-dimensional Fourier integrals, see Eq. (25), remain to be calculated for each wave vector length g. These integrals can be evaluated numerically using a Gauss Legendre quadrature. For special cases, analytical expressions can be given, as shown below.

6.2.4. *Analytical Fourier transforms*

If we want to evaluate the radial Fourier transforms of Eq. (25) analytically, a problem arises because the integrand contains a product of a cylindrical Bessel function J_{m_2} and an associated Legendre function $P_{l_2}^{m_2}$. Unfortunately, integrals with such a combination of functions in the integrand are very difficult. However, there are two special cases in which either J_{m_2} or $P_{l_2}^{m_2}$ is a constant function, so that an analytical solution of the problem exists for some special types of pair potentials. We will give some examples in the following.

In the first case we consider the isotropic ($\Lambda = 0$) Fourier transforms that describe the interaction, without displacement expansion, of a structureless molecule, or an atom, with a substrate. In this case the associated Legendre function vanishes and the integrand can be further reduced with the aid of Eq. (10). So, the isotropic Fourier integrals are given by

$$\tilde{\Psi}_0(g \mid z) = \int_0^\infty J_0(g\tau)\ \Phi_0\left(\sqrt{z^2+\tau^2}\right)\ \tau d\tau. \tag{26}$$

These integrals are known for isotropic inverse power law pair potentials

$$\Phi_{\nu;0}(R) = R^{-\nu}, \qquad \nu \geq 3 \tag{27}$$

as shown by Steele [8]. The corresponding Fourier transforms can be calculated analytically with the aid of [23]

$$\tilde{\Psi}_{\nu;0}(g \mid z) = \begin{cases} \dfrac{1}{\nu-2}\, z^{-\nu+2} & (g=0) \\ \dfrac{1}{\Gamma(\nu/2)} \left(\dfrac{g}{2z}\right)^{(\nu-2)/2} K_{(\nu-2)/2}(gz) & (g>0). \end{cases} \tag{28}$$

Here, K_n is a modified Bessel function and Γ is the ordinary gamma function. An exponential pair potential

$$\Phi_{\exp;0}(R) = \exp(-cR) \qquad (c > 0) \tag{29}$$

is also commonly used [9]. In that case the isotropic Fourier integral equals [24]

$$\tilde{\Psi}_{\exp;0}(g \mid z) = c(c^2+g^2)^{-3/2}\ \left[(c^2+g^2)^{1/2}z+1\right]\ \exp\left(-z(c^2+g^2)^{1/2}\right). \tag{30}$$

The second example concerns the flat ($g = 0$) terms in the Fourier series. These terms describe the interaction of a molecule with a flat surface, in other words the molecule is unaffected by the discrete atomic structure of the substrate layer. For a fixed displacement vector $\boldsymbol{u}$, the flat part of the Fourier series of Eq. (23) must be invariant under a rotation of the molecule around an axis parallel to the global z axis and through the molecular center of mass. This property implies that the index m must be necessarily equal to zero. Further, because of the property [23]

$$J_{m_2}(0) = \delta_{m_2 0} \tag{31}$$

the radial Fourier transform of Eq. (25) reduces to

$$\bar{\Psi}_{\Lambda}(0 \mid z) = \delta_{m0}\,\delta_{m_1 0}\,\frac{1}{\alpha!}\sum_{l_2}\begin{pmatrix} l_1 & l_2 & l \\ 0 & 0 & 0 \end{pmatrix} \times \int_0^\infty W^{(\alpha)}_{lm';l_1 l_2}\left(\sqrt{z^2+\tau^2}\right) P_{l_2}\left(\frac{z}{\sqrt{z^2+\tau^2}}\right) \tau d\tau. \tag{32}$$

We have derived an analytical expression starting with an inverse power law expansion function

$$\Phi_{\nu;lm'}(R) = a_{\nu;lm'}\, R^{-\nu} \qquad (\nu \geq 3) \tag{33}$$

in the pair potential of Eq. (5). In this case the functions $W^{(\alpha)}_{\nu;lm';l_1 l_2}$, occurring in the integrand, are also of the inverse power law type, according to

$$W^{(\alpha)}_{\nu;lm';l_1 l_2}(R) = w^{(\alpha)}_{\nu;lm';l_1 l_2}\, R^{-(\nu+\alpha)}, \tag{34}$$

where the coefficients $w^{(\alpha)}_{\nu;lm';l_1 l_2}$ can be obtained with the aid of the recurrence relation of Eq. (12) together with Eq. (11). After substitution of Eq. (34) in (32), the remaining integrals are all of the type [25]

$$\int_0^1 \rho^\mu\, P_\lambda(\rho)\, d\rho = \frac{\pi^{1/2}\, 2^{-\mu-1}\,\Gamma(\mu+1)}{\Gamma(1+\frac{1}{2}\mu-\frac{1}{2}\lambda)\Gamma(\frac{3}{2}+\frac{1}{2}\mu+\frac{1}{2}\lambda)} \qquad (\mu > -1), \tag{35}$$

where the new integration variable ρ equals the cosine of the angle between the vector $\boldsymbol{x}$ and the z axis, i.e. the argument of the Legendre polynomial in Eq. (32). It can be shown, with the aid of Eq. (35), that the resulting flat Fourier transform equals

$$\bar{\Psi}_{\nu;\Lambda}(0 \mid z) = \delta_{m0}\delta_{m_1 0}\, b^{(\alpha)}_{\nu;lm';l_1}\, z^{-(\nu+\alpha-2)}, \tag{36}$$

where the coefficients $b^{(\alpha)}_{\nu;lm';l_1}$ are given by

$$b^{(\alpha)}_{\nu;lm';l_1} = \frac{\pi^{\frac{1}{2}}\,\Gamma(\nu+\alpha-2)}{2^{\nu+\alpha-2}\,\alpha!}\sum_{l_2}\begin{pmatrix} l_1 & l_2 & l \\ 0 & 0 & 0 \end{pmatrix} \times \frac{w^{(\alpha)}_{\nu;lm';l_1 l_2}}{\Gamma(\frac{1}{2}\nu+\frac{1}{2}\alpha-\frac{1}{2}l_2-\frac{1}{2})\Gamma(\frac{1}{2}\nu+\frac{1}{2}\alpha+\frac{1}{2}l_2)}. \tag{37}$$

We can draw the following conclusion from the examples, described above. For some specific model pair potentials, the isotropic ($\Lambda = 0$) and flat ($g = 0$) Fourier integrals of Eq. (25) can be evaluated analytically. This means that either the molecule or the substrate is considered to be structureless, which is a good approximation for large distances z between the molecule and the substrate. However, for smaller values of z, the anisotropic ($\Lambda \neq 0$) and corrugated ($g \neq 0$) Fourier integrals are not negligible. As we have mentioned before, the latter types of integrals are difficult to handle analytically, because of the occurrence of a cylindrical Bessel function and an associated Legendre function in the integrand. So, in general, the anisotropic and corrugated Fourier transforms can only be calculated numerically. However, it appears that in the special case that the pair potential of Eq. (5) is equivalent to, or derived from, a sum of atom-atom potentials, all Fourier transforms can be tackled analytically with the aid of an alternative method. This will be proven in the next section.

6.3. Alternative method for an atom-atom pair potential model

6.3.1. Atom-atom potential model

In this section we adopt an atom-atom model for the interaction between the molecule and a single substrate atom

$$V(\boldsymbol{R},\omega) = \sum_{a} \phi_a(|\, \boldsymbol{R} + \boldsymbol{r}_a(\omega)\, |), \tag{38}$$

which is of course less general than a spherically expanded molecule-atom potential. The vector $\boldsymbol{R}$ connects the centers of mass of the molecule and the atom and ω describes the orientation of the molecule, as in Sec. 6.2. Further, the vectors $\boldsymbol{r}_a$ denote the relative positions of the atoms a within the molecule with respect to the molecular center of mass. These vectors depend on ω according to the relation

$$\boldsymbol{r}_a(\omega) = \boldsymbol{M}(\omega)\boldsymbol{r}_a^0, \tag{39}$$

where $\boldsymbol{M}(\omega)$ is an active rotation matrix and $\boldsymbol{r}_a^0$ is the position of atom a with respect to a body fixed frame that coincides with the global frame for $\omega = 0$.

In principle, it is possible to transform the sum of atom-atom potentials in Eq. (38) into a spherical expansion [26], given by Eq. (5). Thus, the method of Sec. 6.2 can be applied in order to obtain a Fourier series for the total molecule-substrate potential. The disadvantage of the latter method is that not all Fourier integrals can be calculated analytically, as appears from Sec. 6.2.4. The main reason for this problem is that the spherical expansion of the atom-atom potentials introduces associated Legendre functions which cause problems in the Fourier transformation. On the other hand, if the Fourier transformation is performed first and the spherical expansion afterwards, then only isotropic Fourier integrals are needed. Such integrals can be handled analytically for an inverse power law or an exponential pair potential, as appears from Eqs. (28) and

(30), respectively. So, it seems to be profitable to write the total molecule-substrate potential first as a sum of atom-substrate potentials

$$U(\boldsymbol{x}+\boldsymbol{u},\omega)=\sum_{a} f_a\Big(\boldsymbol{x}+\boldsymbol{r}_a(\omega)+\boldsymbol{u}\Big), \tag{40}$$

where $\boldsymbol{x}$ denotes the equilibrium position of the molecule and $\boldsymbol{u}$ is a small displacement vector, in accordance with Sec. 6.2. The Fourier series

$$f_a(\boldsymbol{x}_a)=\sum_{\boldsymbol{g}} \tilde{f}_a\,(g\mid z_a)\ \exp(i\boldsymbol{g}\cdot\boldsymbol{\tau}_a) \tag{41}$$

describing the interaction between atom a and the substrate, is isotropic. So, it follows from Eqs. (24) and (26) that the Fourier coefficients can be written as

$$\tilde{f}_a\,(g\mid z_a)=\frac{2\pi}{\sigma_o}\left[\sum_{s=1}^{n_s}\exp(-i\boldsymbol{g}\cdot\boldsymbol{\tau}_s)\right]\tilde{\psi}_a(g\mid z_a), \tag{42}$$

with

$$\tilde{\psi}_a(g\mid z_a)=\int_0^\infty J_0(g\tau)\ \phi_a\left(\sqrt{z_a^2+\tau^2}\right)\ \tau\,d\tau, \tag{43}$$

where ϕ_a denotes the atom-atom pair potential, as in Eq. (38).

The main goal of this section is to write Eq. (40) explicitly in terms of the molecular orientation ω and the molecular displacement $\boldsymbol{u}$. Thus we obtain a form similar to Eq. (23), with alternative formulas for the Fourier coefficients $\tilde{F}_\Lambda(g\mid z)$ that will be given analytically. In order to obtain the desired result we have to perform two expansions of the atom-substrate Fourier series, one for the vector(s) $\boldsymbol{r}_a$ and one for $\boldsymbol{u}$, as will be demonstrated in the next two subsections.

6.3.2. Spherical expansion of atom-substrate Fourier series

In first instance, the molecular displacement vector $\boldsymbol{u}$ is considered to be zero, so that we have to make the following expansion of the atom-substrate Fourier series

$$f(\boldsymbol{x}+\boldsymbol{r})=\sum_{\boldsymbol{g}}\tilde{f}(g\mid z+\boldsymbol{r}\cdot\boldsymbol{e}_z)\ \exp(\boldsymbol{g}\cdot\boldsymbol{\tau})\ \exp(i\boldsymbol{g}\cdot\boldsymbol{r}), \tag{44}$$

where we have omitted the label a and the explicit dependence on ω.

Expanding Eq. (42), it follows that

$$\tilde{f}(g\mid z+\boldsymbol{r}\cdot\boldsymbol{e}_z)=\frac{2\pi}{\sigma_o}\left[\sum_{s=1}^{n_s}\exp(-i\boldsymbol{g}\cdot\boldsymbol{\tau}_s)\right]\ \sum_{\beta=0}^{\infty}\frac{(\boldsymbol{r}\cdot\boldsymbol{e}_z)^\beta}{\beta!}\ \tilde{\psi}^{(\beta)}(g\mid z) \tag{45}$$

with

$$\tilde{\psi}^{(\beta)}(g\mid z)=\frac{\partial^\beta}{\partial z^\beta}\ \tilde{\psi}(g\mid z). \tag{46}$$

It appears to be possible to rewrite the expansion of Eq. (44), in combination with (45), in spherical tensor form, as will be shown in the sequel. As a first step we substitute into Eq. (42) the following spherical expansion [27]

$$(\boldsymbol{r}\cdot\boldsymbol{e}_z)^{\beta} = r^{\beta}\sum_{\lambda_1=0}^{\beta}\frac{\beta!(2\lambda_1+1)}{(\beta-\lambda_1)!!(\beta+\lambda_1+1)!!} \times \sum_{\mu_1=-\lambda_1}^{\lambda_1} C^{(\lambda_1)}_{\mu_1}(\hat{\boldsymbol{e}}_z)\, C^{(\lambda_1)}_{\mu_1}(\hat{\boldsymbol{r}})^{*} \qquad (\lambda_1+\beta=\text{even}) \tag{47}$$

and

$$C^{(\lambda_1)}_{\mu_1}(\hat{\boldsymbol{e}}_z) = \delta_{\mu_1 0}. \tag{48}$$

Further, we make use of the well-known spherical expansion of a three-dimensional plane wave [28]

$$\exp(i\boldsymbol{g}\cdot\boldsymbol{r}) = \sum_{\lambda_2}\sum_{\mu_2} i^{\lambda_2}(2\lambda_2+1)\, j_{\lambda_2}(gr)\, C^{(\lambda_2)}_{\mu_2}(\hat{\boldsymbol{g}})\, C^{(\lambda_2)}_{\mu_2}(\hat{\boldsymbol{r}})^{*}, \tag{49}$$

where j_{λ_2} is a spherical Bessel function of the first kind. After substitution of Eqs. (45) and (49) into Eq. (44), the $\hat{\boldsymbol{r}}$-dependent Racah harmonics are recoupled with the aid of Gaunt's rule [22]

$$C^{(\lambda_1)}_{\mu_1}(\hat{\boldsymbol{r}})^{*}\, C^{(\lambda_2)}_{\mu_2}(\hat{\boldsymbol{r}})^{*} = \sum_{l}\sum_{m}(2l+1)\begin{pmatrix}\lambda_1 & \lambda_2 & l\\ \mu_1 & \mu_2 & m\end{pmatrix}\begin{pmatrix}\lambda_1 & \lambda_2 & l\\ 0 & 0 & 0\end{pmatrix} C^{(l)}_{m}(\hat{\boldsymbol{r}}). \tag{50}$$

Finally, the explicit dependence of the expansion on the molecular orientation ω is introduced with the aid of [19]

$$C^{(l)}_{m}(\hat{\boldsymbol{r}}) = \sum_{m'} C^{(l)}_{m'}(\hat{\boldsymbol{r}}^{0})\, D^{(l)}_{mm'}(\omega)^{*}, \tag{51}$$

where $\hat{\boldsymbol{r}}$ and $\hat{\boldsymbol{r}}^{0}$ are related to each other via Eq. (39). As a result we obtain

$$f\,(\boldsymbol{x}+\boldsymbol{r}(\omega)) = \sum_{\Lambda'}\left[\sum_{\boldsymbol{g}}\tilde{S}_{lm}(\boldsymbol{g}\mid z,r)\ \exp(i\boldsymbol{g}\cdot\boldsymbol{r})\right] C^{(l)}_{m'}(\hat{\boldsymbol{r}}^{0})\, D^{(l)}_{mm'}(\omega)^{*}. \tag{52}$$

Here, the summation is performed over the combined index

$$\Lambda' = (l, m, m') \tag{53}$$

which can be considered as a special value of Λ, see Eq. (8), with $\alpha = l_1 = m_1 = 0$. In Eq. (52), the Fourier transforms $\tilde{S}_{lm}$ appear to be

$$\tilde{S}_{lm}(\boldsymbol{g}\mid z,r) = \frac{2\pi}{\sigma_c}\left[\sum_{s=1}^{n_s}\exp(-i\boldsymbol{g}\cdot\boldsymbol{\tau}_s)\right]\sum_{\beta=0}^{\infty}\tilde{\psi}^{(\beta)}(\boldsymbol{g}\mid z)\ \tilde{\chi}^{(\beta)}_{lm}(\boldsymbol{g}\mid r) \tag{54}$$

with

$$\tilde{\chi}_{lm}^{(\beta)}(g \mid r) = (2l+1) r^{\beta} \sum_{\lambda_1=0}^{\beta} \frac{(2\lambda_1+1)}{(\beta-\lambda_1)!!(\beta+\lambda_1+1)!!} \sum_{\lambda_2} i^{\lambda_2}(2\lambda_2+1)\, j_{\lambda_2}(gr) \times \begin{pmatrix} \lambda_1 & \lambda_2 & l \\ 0 & 0 & 0 \end{pmatrix} \begin{pmatrix} \lambda_1 & \lambda_2 & l \\ 0 & -m & m \end{pmatrix} C_{-m}^{(\lambda_2)}(\hat{g}) \qquad (\lambda_1+\beta = \text{even}). \tag{55}$$

After summation over all atoms within the molecule, the total expansion can be written in terms of totally symmetric symmetry adapted functions $G_{mm'}^{(l)}$, with the aid of [17]

$$\sum_{a \in \kappa} \sum_{m'} C_{m'}^{(l)}(\hat{r}_a^0) D_{mm'}^{(l)}(\omega)^* = \sum_{m'} d_{m'\kappa}^{(l)} G_{mm'}^{(l)}(\omega). \tag{56}$$

Here κ denotes a class of symmetry related atoms with the same distance r_κ to the molecular center of mass. In Eq. (56), the Racah harmonics are constant coefficients which must obey the molecular symmetry. As a result, the total molecule-substrate potential expansion becomes

$$U(\boldsymbol{x}, \omega) = \sum_{\Lambda'} \left[\sum_{g} \tilde{F}_{\Lambda'}(g \mid z)\ \exp(i g \cdot \boldsymbol{\tau}) \right] G_{mm'}^{(l)}(\omega) \tag{57}$$

with an alternative formula for the Fourier coefficients

$$\tilde{F}_{\Lambda'}(g \mid z) = \frac{2\pi}{\sigma_c} \left[\sum_{s=1}^{n_s} \exp(-i g \cdot \boldsymbol{\tau}_s) \right] \sum_{\kappa} d_{m'\kappa}^{(l)} \sum_{\beta=0}^{\infty} \tilde{\psi}_{\kappa}^{(\beta)}(g \mid z) \tilde{\chi}_{lm}^{(\beta)}(g \mid r_\kappa) \tag{58}$$

This equation does not contain difficult anisotropic Fourier integrals, which is, from an analytical point of view, a remarkable simplification with respect to Eqs. (24) and (25) for $\Lambda = \Lambda'$.

6.3.3. Molecular displacement expansion

As a final step the Fourier series of the molecule-substrate potential, see Eq. (57), is expanded with respect to molecular displacement coordinates, according to

$$U(\boldsymbol{x} + \boldsymbol{u}, \omega) = \sum_{\alpha=0}^{\infty} \frac{(\boldsymbol{u} \cdot \nabla)^{\alpha}}{\alpha!} U(\boldsymbol{x}, \omega). \tag{59}$$

We will perform the expansion with the aid of the following gradient formula

$$(\boldsymbol{u} \cdot \nabla)\ \tilde{F}_{\Lambda'}(g \mid z)\ \exp(i g \cdot \boldsymbol{\tau}) = u\ \exp(i g \cdot \boldsymbol{\tau}) \sum_{\sigma=-1}^{+1} \left[\hat{A}_{\sigma}(g)\ \tilde{F}_{\Lambda'}(g \mid z) \right] C_{\sigma}^{(1)}(\hat{\boldsymbol{u}}) \tag{60}$$

where the operator $\hat{A}_\sigma(g)$ is defined by

$$\hat{A}_\sigma(g) = \begin{cases} \dfrac{\partial}{\partial z} & \sigma = 0 \\ igC_\sigma^{(1)}(\hat{g})^* & \sigma = -1, 1. \end{cases} \tag{61}$$

It can be proved, with the aid of the recoupling formula (50), that successive application of the gradient formula results in the following expansion for the z- and $\boldsymbol{\tau}$-dependent part of Eqs. (57) and (58)

$$\begin{aligned} \tilde{\psi}^{(\beta)}(g \mid z + \boldsymbol{u} \cdot \boldsymbol{e}_z) \exp(i\boldsymbol{g} \cdot (\boldsymbol{\tau} + \boldsymbol{u})) = & \sum_{\alpha=0}^{\infty} \frac{1}{\alpha!} \sum_{l_1=0}^{\alpha} \sum_{m_1=-l_1}^{l_1} \left[\tilde{W}_{l_1 m_1}^{(\beta;\alpha)}(g \mid z) \ \exp(i\boldsymbol{g} \cdot \boldsymbol{\tau}) \right] \\ & \times u^\alpha \, C_{m_1}^{(l_1)}(\hat{\boldsymbol{u}}) \qquad (\alpha + l_1 = \text{even}) \end{aligned} \tag{62}$$

in which the expansion functions $\tilde{W}_{l_1 m_1}^{(\beta;\alpha)}$ can be calculated by means of the initialisation

$$\tilde{W}_{l_1 m_1}^{(\beta;0)}(g \mid z) = \delta_{l_1 0} \, \delta_{m_1 0} \, \tilde{\psi}^{(\beta)}(g \mid z) \tag{63}$$

and the recurrence relation for fixed β, g and z

$$\begin{aligned} \tilde{W}_{l_2 m_2}^{(\beta;\alpha+1)}(g \mid z) = & (-1)^{m_2}(2l_2 + 1) \sum_{l_1} \sum_{m_1} \sum_{\sigma} \\ & \times \begin{pmatrix} l_1 & 1 & l_2 \\ m_1 & \sigma & -m_2 \end{pmatrix} \begin{pmatrix} l_1 & 1 & l_2 \\ 0 & 0 & 0 \end{pmatrix} \hat{A}_\sigma(g) \, \tilde{W}_{l_1 m_1}^{(\beta;\alpha)}(g \mid z). \end{aligned} \tag{64}$$

Defining, in agreement with Eq. (8),

$$\Lambda = (\Lambda', \alpha, l_1, m_1) = (l, m, m', \alpha, l_1, m_1), \tag{65}$$

we obtain from Eqs. (57), (58) and (62) the final expression for the Fourier series of the molecule-substrate potential

$$U(\boldsymbol{x} + \boldsymbol{u}, \omega) = \sum_{\Lambda} \left[\sum_{g} \tilde{F}_\Lambda(g \mid z) \ \exp(i\boldsymbol{g} \cdot \boldsymbol{\tau}) \right] u^\alpha \, C_{m_1}^{(l_1)}(\hat{\boldsymbol{u}}) \, G_{mm'}^{(l)}(\omega), \tag{66}$$

which is indeed equivalent to Eq. (23) with

$$\tilde{F}_\Lambda(g \mid z) = \frac{2\pi}{\sigma_c} \left[\sum_{s=1}^{n_s} \exp(-i\boldsymbol{g} \cdot \boldsymbol{\tau}_s) \right] \frac{1}{\alpha!} \sum_{\kappa} d_{m'\kappa}^{(l)} \sum_{\beta=0}^{\infty} \tilde{W}_{l_1 m_1;\kappa}^{(\beta;\alpha)}(g \mid z) \, \tilde{\chi}_{lm}^{(\beta)}(g \mid r_\kappa). \tag{67}$$

The results of the alternative method, described above, can be summarized as follows. Starting from an atom-atom potential model, we have derived an alternative formula for the Fourier transforms $\tilde{F}_\Lambda(g \mid z)$, see Eq. (58), which is valid for $\Lambda = \Lambda'$. The extension to $\Lambda \neq \Lambda'$ has been made with the aid of the recurrence relation (64). In the next subsection we will show that the new expressions can be evaluated analytically, for the most commonly used atom-atom potentials.

6.3.4. Analytical derivatives of isotropic Fourier integrals

In order to use the alternative formulas for the Fourier transforms $\tilde{F}_\Lambda(g \mid z)$, we need the derivatives of isotropic atom-substrate Fourier integrals, as appears from Eq. (58) for $\Lambda = \Lambda'$ and from the relations (63) and (64) for $\Lambda \neq \Lambda'$. All other factors in both equations are independent of the atom-atom potential and are easy to calculate. So, the only remaining problem is the evaluation of the derivatives of the isotropic Fourier integrals.

First, we start with an exponential atom-atom potential type

$$\phi_{\exp}(\rho) = \exp(-c\rho) \qquad (c > 0). \tag{68}$$

In this case the isotropic Fourier integral is given by Eq. (30), which is a product of a linear and an exponential function. With the aid of

$$\frac{\partial^\beta}{\partial z^\beta}\left(z \exp(z)\right) = (z + \beta)\exp(z) \tag{69}$$

it is not difficult to prove that the derivatives of the isotropic Fourier integrals are given by

$$\tilde{\psi}^{(\beta)}_{\exp}(g \mid z) = (-1)^\beta \, c(c^2+g^2)^{(\beta-3)/2} \left[(c^2+g^2)^{1/2} z + 1 + \beta\right] \exp\left(-(c^2+g^2)^{1/2} z\right). \tag{70}$$

Secondly, we consider the more difficult case of an inverse power law atom-atom potential

$$\phi_n(\rho) = \rho^{-n}, \qquad n \geq 3 \tag{71}$$

The corresponding isotropic Fourier integrals

$$\tilde{\psi}_n(g \mid z) = \int_0^\infty J_0(g\tau)\,(z^2+\tau^2)^{-n/2}\,\tau\,d\tau \tag{72}$$

are products of inverse power law and modified Bessel functions of z, as appears from Eq. (28). In principle, it is possible to make use of the well-known differentiation formulas for the modified Bessel functions [23], but this results in some tedious algebra. It is easier to use the relation

$$\frac{\partial}{\partial z}\tilde{\psi}_n(g \mid z) \;=\; -nz\,\tilde{\psi}_{n+2}(g \mid z), \tag{73}$$

which can be proved by exchanging the differentiation and the integration. After successive application of Eq. (73), the isotropic Fourier derivatives can be written as a sum over zeroth order integrals

$$\tilde{\psi}^{(\beta)}_n(g \mid z) = \sum_{i=0}^{E(\beta/2)} c_i^{(\beta)}\, z^{\beta-2i}\, \tilde{\psi}_{n+2\beta-2i}(g \mid z), \tag{74}$$

where E denotes the entire function. The coefficients $c_i^{(\beta)}$ can be calculated with the aid of the initialisation

$$c_0^{(0)} = 1 \tag{75}$$

and the recurrence relation

$$c_i^{(\beta+1)} = -(n + 2\beta - 2i)c_i^{(\beta)} \;+\; (\beta + 2 - 2i)c_{i-1}^{(\beta)}, \tag{76}$$

where $c_i^{(\beta)}$ is defined as zero if i is negative or greater than $\beta/2$. Although Eq. (74) is also applicable for $g = 0$, in which case the Fourier integrals are inverse power functions of z, the corresponding derivatives can be better calculated directly with the aid of

$$\tilde{\psi}_n^{(\beta)}(0 \mid z) = (-1)^\beta \frac{(n + \beta - 3)!}{(n-2)!}\, z^{-n-\beta+2}. \tag{77}$$

So we have derived analytical expressions, see Eqs. (70), (74) and (77), for the derivatives of the isotropic Fourier integrals starting from an exponential or an inverse power law atom-atom potential. After substitution of these derivatives into Eq. (63), the Fourier transforms $\tilde{F}_\Lambda(g \mid z)$ can be obtained analytically with the aid of Eq. (67). We conclude that, at least for an exponential and inverse power law atom-atom potential model, all Fourier transforms can be calculated analytically. This is an important improvement with respect to the general method, described in Sec. 6.2.

6.4. A potential expansion for N_2 on graphite

In Secs. 6.2 and 6.3 two methods have been described to obtain a combined spherical, displacement and Fourier expansion for a molecule interacting with a two-dimensional substrate of regularly ordered atoms. In this section we will show some numerical results for N_2 on graphite which illustrate the convergence of the various expansions. As far as the isotropic ($l = 0$) part of the potential expansion is concerned, our results are similar to those of Steele for noble gas atoms on substrates [8]. However, with the aid of the potential expansion terms with $l > 0$ we can visualize the potential anisotropy explicitly. Further, with the aid of the included displacement expansion the importance of anharmonic terms in the molecule-substrate potential can be demonstrated.

Adsorbed monolayers of N_2 molecules on graphite can occur in a rich variety of interesting quasi two-dimensional phases. Neutron scattering experiments [29-31], low-energy electron diffraction [32-34] and heat-capacity measurements [35] have shown that the low temperature ground state of a N_2 adlayer on graphite is an orientationally ordered phase with a commensurate $(\sqrt{3} \times \sqrt{3})R30°$ center of mass structure. This is confirmed by molecular dynamics [10] and Monte Carlo simulations [36,37]. For this ground state structure two classical harmonic lattice dynamics calculations are reported

[38,39], which are valuable for the determination of, as yet unknown, experimental adlayer phonon frequencies. The molecule-substrate force constants, used in these calculations, are derived from a sum of atom-substrate potentials. In a forthcoming paper we will present a quantummechanical lattice dynamics calculation, where the molecule-substrate potential expansion of the present paper will be used.

6.4.1. *Spherical, displacement and Fourier expansion of atom-atom potentials*

Before we show the numerical results for N_2 on graphite we will first derive further analytical expansion formulas for a homonuclear diatomic molecule on a substrate, using a Lennard-Jones 12-6 atom-atom potential model

$$\phi(\rho) = \sum_{n=6,12} \frac{c_n}{\rho^n}. \tag{78}$$

So, the molecule-atom interaction is a special case of Eq. (38), where the sum over atom-atom potentials is restricted to two terms

$$V(\boldsymbol{R},\omega) = \phi(|\, \boldsymbol{R} + \boldsymbol{r}(\omega)\, |) + \phi(|\, \boldsymbol{R} - \boldsymbol{r}(\omega)\, |). \tag{79}$$

As previously defined, the vector $\boldsymbol{R}$ connects the molecular center of mass with a substrate atom and $\omega = (\vartheta, \varphi)$ denotes the molecular orientation in polar angles ϑ and φ. Further, the position of one atom within the molecule with respect to the molecular center of mass is described by the orientation dependent vector $\boldsymbol{r}(\omega)$ with length r.

In the sequel we will first apply the general method of Sec. 6.2 in order to obtain an explicit expression for a combined spherical and displacement expansion of the molecule-atom pair potential. This expression can be used to calculate the total molecule-substrate potential expansion as a sum of pairwise contributions. With the aid of the pair potential expansion formulas we will also derive an explicit analytical expression for the Fourier transform with $g = 0$, describing the interaction with a flat surface. However, as we have explained previously the Fourier transforms with $g \neq 0$ are difficult to evaluate analytically with the method of Sec. 6.2. A solution to this problem is provided by the special method of Sec. 6.3, which can be applied in this case because we have started with an atom-atom potential model. We will show that the method of Sec. 6.3 results, of course, in the same Fourier transform with $g = 0$, as obtained with the method of Sec. 6.2. Although the Fourier transforms with $g \neq 0$ cannot be tackled analytically with the method of Sec. 6.2, the latter method is not useless in this example for it results in formulas for the sum of molecule-atom expansions, that can be used to check the convergence of the Fourier series numerically.

In order to apply the general method of Sec. 6.2, we must first transform the molecule-atom pair potential of Eq. (79) into a spherical expansion similar to Eq. (5). For a linear molecule, the symmetry adapted rotation functions $G^{(l)}_{mm'}$ of Eq. (5) are simple Racah harmonics $C^{(l)}_m$, as follows from Eq. (2). So, Eq. (5) reduces to

$$V(\boldsymbol{R},\omega) = \sum_l \Phi_l(R) \sum_{m=-l}^{l} (-1)^m C^{(l)}_{-m}(\hat{\boldsymbol{R}}) C^{(l)}_m(\omega), \tag{80}$$

where the summation over l is limited to even values because the molecule possesses an inversion center. Further, the radially dependent functions Φ_l, occurring in Eq. (80), can be evaluated analytically with the aid of so called one-center spherical expansion formulas, see for instance Ref. [15], applied to Eq. (79). The result is

$$\Phi_l(R) = \sum_{n=6,12} \sum_{\nu=n+l}^{\infty} \frac{a_{n\nu;l}}{R^\nu} \qquad (\nu = \text{even}) \tag{81}$$

with r-dependent expansion coefficients

$$a_{n\nu;l} = \frac{2c_n(2l+1)\,(\nu-2-l)!\,(\nu-2+l)!!\,r^{\nu-n}}{(n-2)!\,(\nu-n+l+1)!!\,(\nu-n-l)!!\,(\nu-2-l)!!}. \tag{82}$$

Secondly, we expand the molecule-atom pair potential of Eq. (80) with respect to a molecular displacement vector $\boldsymbol{u}$, using Eq. (9) substituted into Eq. (7)

$$V(\boldsymbol{R}+\boldsymbol{u},\omega) = \sum_{\Lambda} \left[\frac{1}{\alpha!} \sum_{l_2} \sum_{m_2} \begin{pmatrix} l_1 & l_2 & l \\ m_1 & m_2 & m \end{pmatrix} W^{(\alpha)}_{l;l_1 l_2}(R) C^{(l_2)}_{m_2}(\hat{\boldsymbol{R}}) \right] u^\alpha C^{(l_1)}_{m_1}(\hat{\boldsymbol{u}}) C^{(l)}_m(\omega). \tag{83}$$

Here, a summation has to be performed over the combined index $\Lambda = (l, m, \alpha, l_1, m_1)$, as defined in Eq. (8). In Eq. (83), the radially dependent functions $W^{(\alpha)}_{l;l_1 l_2}$ determine the potential derivative of order α with respect to the intermolecular vector. These functions are, just as Φ_l in Eq. (81), of the inverse power law type according to

$$W^{(\alpha)}_{l;l_1 l_2}(R) = \sum_{n=6,12} \sum_{\nu=n+l}^{\infty} \frac{w^{(\alpha)}_{n\nu;l;l_1 l_2}}{R^{\nu+\alpha}} \qquad (\nu = \text{even}). \tag{84}$$

The coefficients $w^{(\alpha)}_{n\nu;l;l_1 l_2}$ in this equation can be computed with the aid of the recurrence relation of Eq. (11), starting with the initialisation condition of Eq. (10). However, in this case it is also possible to derive an explicit analytical expression for these coefficients if one considers the combined spherical and displacement expansion of Eq. (83) from another point of view. To this end, we write

$$V(\boldsymbol{R}+\boldsymbol{u},\omega) = \phi(|\,\boldsymbol{R}+\boldsymbol{u}+\boldsymbol{r}(\omega)\,|) + \phi(|\,\boldsymbol{R}+\boldsymbol{u}-\boldsymbol{r}(\omega)\,|) \tag{85}$$

and perform a so called double spherical expansion of the two atom-atom potentials. With the aid of analytical double spherical expansion formulas, see Ref. [17], Eq. (83)

can be obtained almost immediately. After some elementary algebra, we arrive at the desired explicit expression for the expansion coefficients

$$w^{(\alpha)}_{n\nu;l;l_1l_2} = \begin{pmatrix} l_1 & l_2 & l \\ 0 & 0 & 0 \end{pmatrix} \frac{2c_n\,\alpha!\,(-1)^{l_1}\,(2l_1+1)(2l_2+1)(2l+1)\,r^{\nu-n}}{(n-2)!\,(\nu-n+l+1)!!\,(\nu-n-l)!!} \times \frac{(\nu+\alpha-l_2-3)!!\,(\nu+\alpha+l_2-2)!!}{(\alpha+l_1+1)!!\,(\alpha-l_1)!!}. \tag{86}$$

So far, we have obtained explicit analytical expressions for the molecule-atom pair potential expansion. Summation over all pairs results in the following useful combined spherical and displacement expansion for the total molecule-substrate interaction

$$U(\boldsymbol{x}+\boldsymbol{u},\omega) = \sum_{\Lambda} F_\Lambda(\boldsymbol{x})u^\alpha C^{(l_1)}_{m_1}(\hat{\boldsymbol{u}})C^{(l)}_m(\omega) \tag{87}$$

which is a special case of Eq. (14). In Eq. (87), the vector $\boldsymbol{x}$ represents the position of the molecular center of mass with respect to a global frame as defined in Sec. 6.2. Further, the functions F_Λ contain a sum over pair contributions similar to Eq. (15), that can be replaced by a two-dimensional Fourier series, see Eq. (16),

$$F_\Lambda(\boldsymbol{x}) = \sum_{\boldsymbol{g}} \tilde{F}_\Lambda(\boldsymbol{g} \mid z)\exp(i\boldsymbol{g}\cdot\boldsymbol{\tau}) \tag{88}$$

with $\boldsymbol{\tau}$ denoting the projection of $\boldsymbol{x}$ on the xy plane, so that $\boldsymbol{x} = \boldsymbol{\tau} + z\boldsymbol{e}_z$. In Sec. 6.2 it has been demonstrated that the Fourier coefficients with $g = 0$ can be evaluated analytically for the inverse power law pair expansion functions of Eq. (84). Using Eqs. (24), (36) and (37) we obtain

$$\tilde{F}_\Lambda(0 \mid z) = \delta_{m0}\delta_{m_10}\,\frac{2\pi\,n_s}{\sigma_c} \sum_{n=6,12}\sum_{\nu=n+l}^{\infty} \frac{b^{(\alpha)}_{n\nu;l;l_1}}{z^{\nu+\alpha-2}} \tag{89}$$

where n_s is the number of substrate sublattices. Further, the coefficients $b^{(\alpha)}_{n\nu;l;l_1}$ are given by

$$b^{(\alpha)}_{n\nu;l;l_1} = \frac{2c_n\,(-1)^{l_1}\,(2l+1)(2l_1+1)\,(\nu+\alpha-3)!\,r^{\nu-n}}{(n-2)!\,(\nu-n+l+1)!!\,(\nu-n-l)!!\,(\alpha+l_1+1)!!\,(\alpha-l_1)!!}. \tag{90}$$

As we have explained in Sec. 6.2, the higher order Fourier components ($g \neq 0$), are difficult to evaluate analytically because the radial Fourier integral of Eq. (25) contains a product of a cylindrical Bessel function and an associated Legendre function in the integrand. However, in this example we have started with an atom-atom potential model, so that the method of Sec. 6.3 can also be applied. The application of this alternative method is rather straightforward and results in the following expression for the Fourier coefficients

$$\tilde{F}_\Lambda(\boldsymbol{g} \mid z) = \frac{4\pi}{\sigma_c}\left[\sum_{s=1}^{n_s}\exp(-i\boldsymbol{g}\cdot\boldsymbol{\tau}_s)\right]\frac{1}{\alpha!}\sum_{n=6,12}\sum_{\nu=n}^{\infty}\tilde{W}^{(\nu-n;\alpha)}_{l_1m_1}(\boldsymbol{g} \mid z)\,\bar{\chi}^{(\nu-n)}_{lm}(\boldsymbol{g} \mid r), \tag{91}$$

which is a special case of Eq. (67). The coefficients $\tilde{\chi}_{lm}^{(\nu-n)}(g \mid r)$ are defined in Eq. (55) and the functions $\tilde{W}_{l_1m_1}^{(\nu-n;\alpha)}$ can be calculated with the aid of the recurrence relation Eq. (64) together with the initialisation condition of Eq. (63). Of course, the Fourier coefficients of Eq. (89), derived with the general method of Sec. 6.2, must be equivalent to Eq. (91), i.e. the result of the special method of Sec. 6.3. In order to check this equality we use Eq. (55), which reduces to

$$\tilde{\chi}_{lm}^{(\nu-n)}(0 \mid r) = \delta_{m0}\frac{(2l+1)\, r^{\nu-n}}{(\nu-n-l)!!\,(\nu-n+l+1)!!} \qquad (\nu-n=l,l+2,..). \tag{92}$$

From Eqs. (63) and (77) we conclude that

$$\tilde{W}_{l_1m_1}^{(\nu-n;0)}(0 \mid z) = \delta_{l_10}\,\delta_{m_10}\,\frac{c_n\,(\nu-3)!}{(n-2)!\,z^{\nu-2}}. \tag{93}$$

After substitution of Eqs. (92) and (93) in Eq. (91) we obtain Fourier transforms similar to Eq. (89) without molecular displacement expansion ($\alpha = 0$) and with coefficients

$$b_{n\nu;l;l_1}^{(0)} = \delta_{l_10}\,\frac{2c_n\,(2l+1)\,(\nu-3)!\,r^{\nu-n}}{(n-2)!\,(\nu-n+l+1)!!\,(\nu-n-l)!!} \tag{94}$$

in accordance with Eq. (90). The higher order terms with $\alpha > 0$ fulfil the recurrence relation of Eq. (64), which can be simplified to

$$b_{n\nu;l;l_1}^{(\alpha)} = -\frac{(\nu+\alpha-3)}{\alpha}\left[\frac{l_1}{2l_1-1}b_{n\nu;l,l_1-1}^{(\alpha-1)} + \frac{l_1+1}{2l_1+1}b_{n\nu;l;l_1+1}^{(\alpha-1)}\right], \tag{95}$$

where $b_{n\nu;l;l_1}^{(\alpha)}$ equals zero by definition if l_1 is negative or greater than α. It is not difficult to prove that the coefficients of Eq. (90) obey the recurrence relation of Eq. (95). So, the methods of Secs. 6.2 and 6.3 result in the same flat ($g = 0$) Fourier transform. However, the method of Sec. 6.3 is more powerful because with the aid of Eq. (91) the Fourier transforms with $g \neq 0$, which describe the surface corrugation, can also be evaluated analytically.

6.4.2. Numerical results

In the following we present some numerical results for a N_2 molecule interacting with a single graphite layer. In order to obtain a real physical molecule-substrate system, with graphite consisting of several layers, we have to consider a sum of such single-layer contributions. It is instructive to start with one substrate layer, because this illustrates clearly which terms in the total potential expansion can be neglected for the subsequent layers.

The C atoms in one graphite layer are ordered in a two-dimensional two-sublattice structure ($n_s = 2$) with primitive cell vectors a_1 and a_2 of equal length 0.246 nm which make an angle of 60°. We choose the origin of the global frame in the center of a graphite hexagon and orient the x axis along the lattice vector $\boldsymbol{a}_1$. With respect to this reference frame the two substrate atoms within the primitive unit cell are positioned at

$$\boldsymbol{\tau}_s = \frac{s}{3}\boldsymbol{a}_1 + \frac{s}{3}\boldsymbol{a}_2 \qquad (s = 1, 2) \qquad (96)$$

Further, we use the empirically determined atom-atom potential parameters $c_6 = -1.469$ J $\mathrm{mol}^{-1}\mathrm{nm}^6$ and $c_{12} = 2.050$ mJ mol^{-1} nm^{12} corresponding with a minimum $\epsilon = 0.2631$ kJ mol^{-1} of the N-C potential at a distance $\rho = 0.375$ nm [38]. The parameter r, occurring in the expansion formulas, equals half the bond length of the N_2 molecule which is $2r = 0.1094$ nm.

In first instance we neglect the surface corrugation of the molecule-substrate interaction, i.e. we approximate the expansion coefficient $F_\Lambda(\boldsymbol{x})$ in Eq. (87) by the lowest order Fourier transform $\tilde{F}_\Lambda(0 \mid z)$ that can be calculated with the aid of Eqs. (89) and (90). We observe that Sokolowski [12,13] has used similar potential expansion coefficients in his calculations of the second virial coefficient and other statistical thermodynamics properties of N_2 on graphite. Sokolowski, however, did not calculate the expansion coefficients with the aid of analytical formulas, but he evaluated the occurring integrals numerically. In Fig. 1 we have plotted some of the lowest order coefficients $\tilde{F}_{lm}(0 \mid z)$ with $l \leq 12$ and $\alpha = l_1 = m_1 = 0$ as a function of the distance z between the molecule and the substrate layer. In this case the index m is necessarily zero as appears from Eq. (89). From Fig. 1 we conclude that the flat ($g = 0$) isotropic ($l = 0$) coefficient is strongly dominant especially at large distances between the molecule and the substrate plane. Further, it has a relatively deep minimum of -7.2 kJ mol^{-1} at a distance $z = 0.36$ nm. Of course, the higher order terms with $l > 0$ in the potential expansion, including Racah harmonics that describe the anisotropy, have also to be taken into account in order to find the minimum of the flat ($g = 0$) part of the total potential expansion. These higher order terms cause a shift of the flat potential minimum with respect to the isotropic minimum towards the substrate plane ($z = 0.334$ nm, $\vartheta = 90°$). Further, the $l = 2$ flat Fourier transform possesses also a recognizable minimum, although its depth is relatively small (-0.25 kJ mol^{-1}). Another interesting observation is that for all l values the spherical Fourier coefficients become strongly repulsive at short distances.

In order to investigate the influence of the surface corrugation on $F_{lm}(\boldsymbol{x})$, we have included the Fourier terms with $g \neq 0$. The projection of the molecular position $\boldsymbol{x}$ on the substrate plane, the xy plane, is fixed in the center of a graphite hexagon, as is for instance the case in the two-dimensional commensurate $(\sqrt{3} \times \sqrt{3})R30°$ N_2 adlayer [29]. The number of m values for which $F_{lm}(\boldsymbol{x})$ does not vanish is limited because the molecule is positioned at the global z axis, which is a sixfold rotation axis so that m must be a multiple of six. Further, the potential is also invariant under a reflection with respect to the xz plane so that all remaining expansion coefficients $F_{lm}(\boldsymbol{x})$ are real

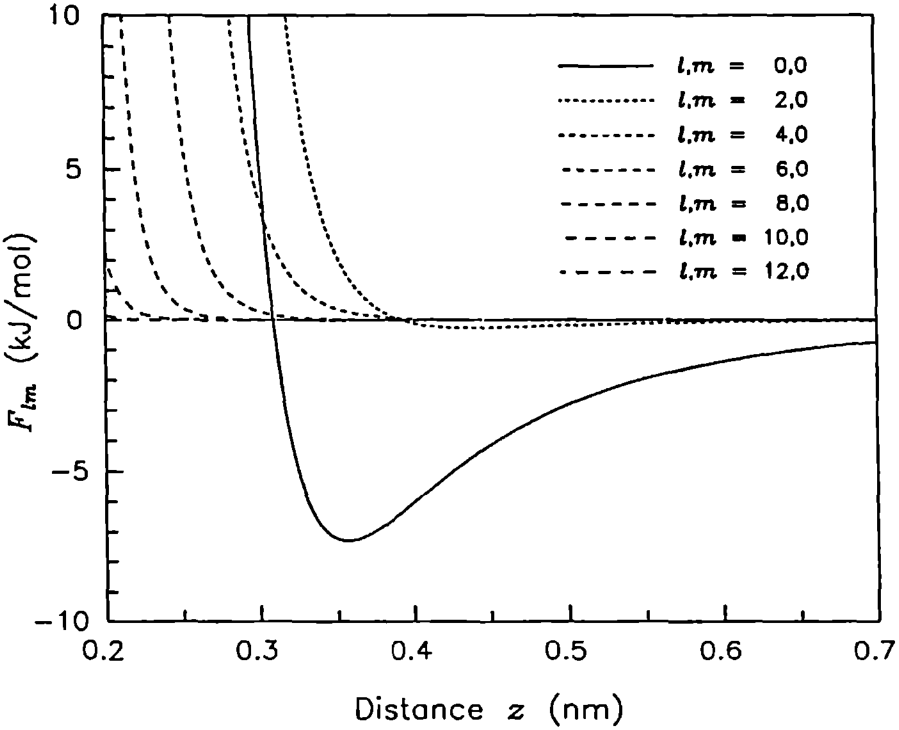

Fig. 1. Potential expansion coefficients F_{lm} with $l \leq 12$, describing the interaction between a N_2 molecule and a single uncorrugated graphite layer, i.e. only the lowest order Fourier coefficients with $g = 0$ are taken into account.

numbers. From Fig. 2, which represents expansion coefficients $F_{lm}(z)$ with $l \leq 12$ and $m = 0$, we observe that the $l = 0$ and $l = 2$ curves strongly resemble the corresponding curves of Fig. 1, apart from a small shift towards the substrate plane at short distances. However, for $l \geq 4$ the higher order Fourier contributions, describing the corrugation, have a great influence, probably caused by nearest neighbor pair interactions. In Fig. 3 all independent expansion functions F_{lm} with $l = 6, 8, 10, 12$ and $m = 0, 6$ are shown. The coefficients with $m = 12$ are omitted, because they are practically zero within the plot domain. From this figure we conclude that the $m \neq 0$ terms, which are responsible for the φ-dependence of the molecule-substrate potential, are negligible at distances greater than 0.3 nm. This is an important conclusion because it implies that if the N_2 molecule is adsorbed beyond this critical distance, then the total molecule-substrate interaction cannot couple in-plane and out-of-plane rotational motions.

So far, we have considered the expansion coefficients $F_{lm}(z)$ describing the interaction between a N_2 molecule and a single graphite layer. For a corrugated surface,

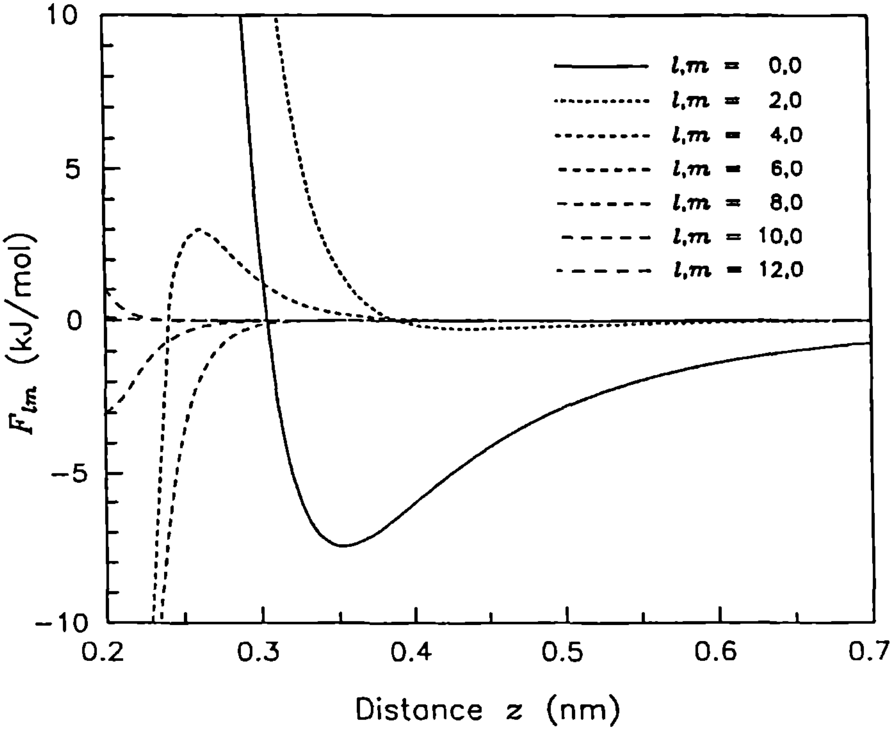

Fig. 2. Potential expansion coefficients F_{lm} with $l \leq 12$ and $m = 0$ for a N_2 molecule interacting with a single corrugated graphite-layer. The molecule is positioned at a distance z above the center of a graphite hexagon.

we have only presented results for the case that the molecule is positioned above the center of a graphite hexagon. As we have mentioned before, the potential expansion coefficients for a real graphite substrate, consisting of several layers with an interlayer distance of 0.337 nm, can be obtained as a sum of single-layer contributions. In this sum the Fourier coefficients with $g \neq 0$ are negligible for the second and lower lying substrate layers, as can be concluded from Figs. 1 and 2, i.e. the lateral positions of the substrate atoms within these layers are of no influence. Further, in order to describe the interaction between a N_2 molecule and a complete graphite substrate it appears to be sufficient to include only one corrugated top layer and ten flat ($g = 0$) layers. Minimizing the total molecule-substrate potential, we find that a single N_2 molecule is adsorbed above the center of a graphite hexagon of the top layer, at a distance z =0.33 nm, with equilibrium angles $\vartheta = 90°$ and $\varphi = 0°$. The only φ dependence of the total potential originates from expansion terms containing coefficients $F_{lm}(z)$ with $m \neq 0$ resulting in a very weak sixfold barrier of 0.5 J mol^{-1} in the φ direction. On the other hand,

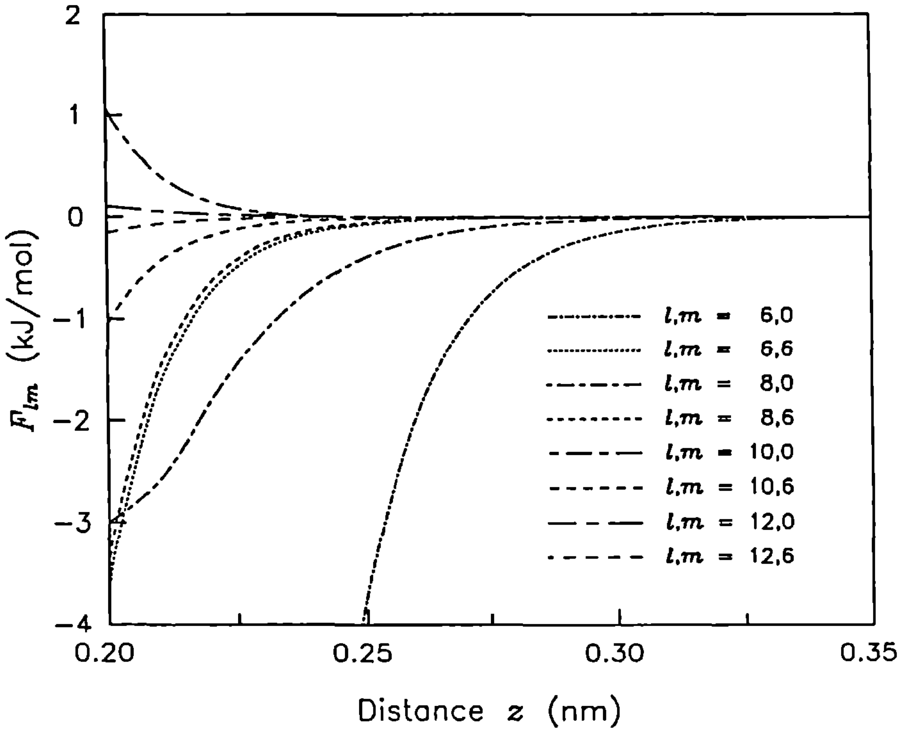

Fig. 3. Potential expansion coefficients F_{lm} with $6 \leq l \leq 12$ and $m = 0, 6$ with the same conditions as in Fig. 2.

the anisotropy in the ϑ direction is relatively strong, as is illustrated by a rotational ϑ barrier of 10 kJ mol^{-1}. So, at an adsorption site the φ anisotropy of the N_2-graphite interaction is negligible compared with the ϑ anisotropy, in agreement with a previous conclusion drawn from Fig. 3.

For quantummechanical lattice dynamics calculations on a commensurate $(\sqrt{3}\times\sqrt{3})$ $R30°$ N_2 adlayer with two-dimensional space group $p2gg$, it is interesting to compare the anisotropy of the N_2-graphite interaction with the anisotropy of the N_2-N_2 interaction. We use the N_2-N_2 potential of Berns and Van der Avoird [40], which is a spherical expansion of an *ab initio* potential surface. Because the molecule-molecule and molecule-substrate interaction are given in the same representation, they can be easily combined in the potential calculation, as well as in the lattice dynamics calculation. Optimization of the adlayer crystal structure, assuming a rigid substrate and fixing the molecular centers of mass at adsorption sites, results in molecular axis orientations parallel to the substrate surface ($\vartheta = 90°$). The equilibrium in-plane orientation for a molecule of the first sublattice becomes $\varphi_1 = 48°$. A molecule of the second sublattice can be obtained

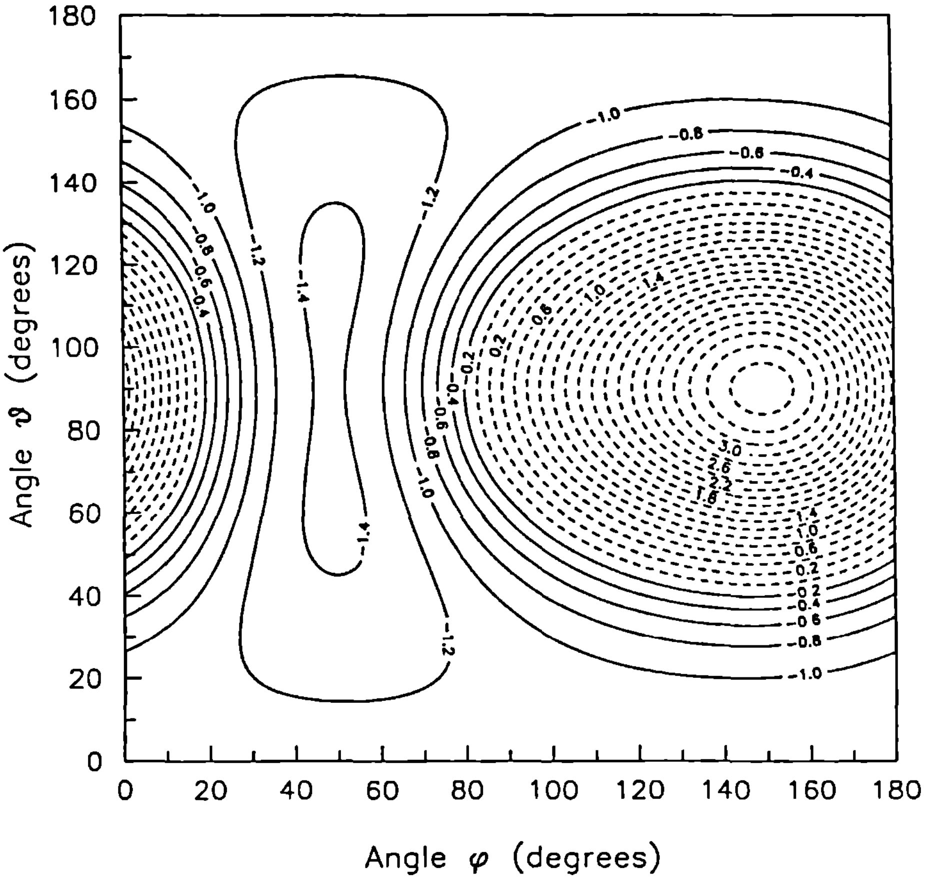

Fig. 4. Anisotropic part of the intralayer crystal field that is experienced by a N_2 molecule within a commensurate $(\sqrt{3} \times \sqrt{3})R30°$ N_2 adlayer as a function of the molecular angles ϑ and φ. The molecule-substrate interaction is omitted and all other N_2 molecules are fixed in their equilibrium positions and orientations, see text.

from the first by means of a glide-reflection, resulting in an equilibrium in-plane angle $\varphi_2 = 132°$.

We will now investigate the anisotropy of the crystal field, with and without N_2-graphite interaction, that is experienced by a molecule of the first sublattice, assuming that all other N_2 molecules are fixed in their equilibrium positions and orientations. In Fig. 4 we have plotted the anisotropic part $(l > 0)$ of the intralayer crystal field, i.e. without substrate, as a function of the angles ϑ and φ. From this contour plot we observe that the intralayer crystal field shows a strong φ anisotropy especially for $\vartheta = 90°$ with a rotational barrier of 5 kJ mol^{-1}. Further, for $\vartheta = 90°$ and $\varphi = 48°$,

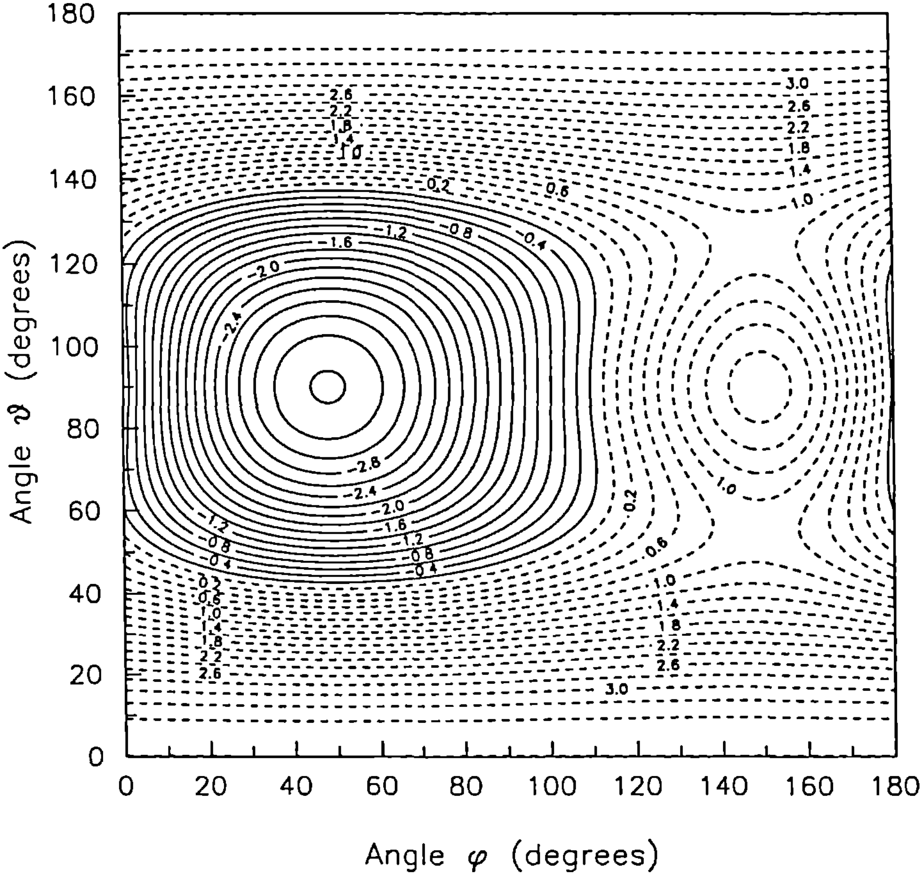

Fig. 5. Superposition of the anisotropic part of the N_2-graphite interaction and the intralayer crystal field of Fig. 4 within a commensurate $(\sqrt{3} \times \sqrt{3})R30°$ N_2 adlayer.

there is a saddle point, so that the planar two-dimensional crystal structure is not stable without molecule-substrate interaction. In the neighborhood of this saddle point the ϑ anisotropy is relatively weak compared with the φ anisotropy, in contrast with the anisotropic behaviour of the N_2-graphite potential as discussed previously.

In Fig. 5 we have added the anisotropic part $(l > 0)$ of the N_2-graphite interaction to the intralayer crystal field of Fig. 4. Comparing these figures, we conclude that because of the strong anisotropy of the N_2-graphite interaction in the ϑ direction, the saddle point in Fig. 4, obtained without substrate, is replaced by a minimum in Fig. 5. However, the φ anisotropy caused by the intralayer interaction is practically not influenced by the molecule-substrate interaction. Summarizing, we expect that in the commensurate $(\sqrt{3} \times \sqrt{3})R30°$ N_2-adlayer the out-of-plane rotational dynamics,

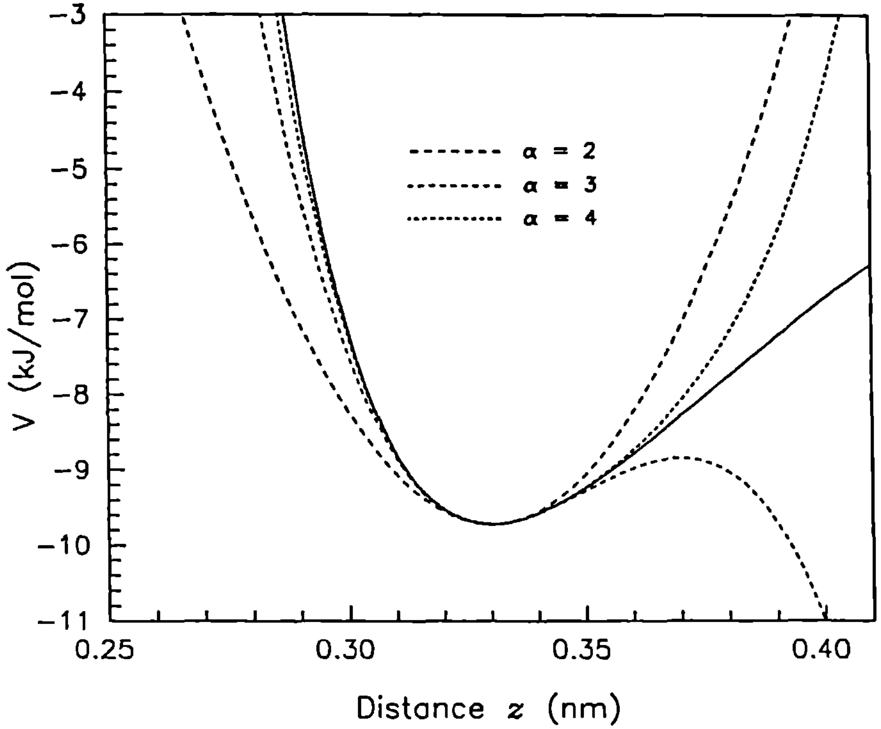

Fig. 6. N_2-graphite interaction as a function of the distance z with respect to the corrugated top layer. The molecule is positioned above the center of a graphite hexagon and the molecular orientation is fixed at angles $\vartheta = 90°$ and $\varphi = 48°$. The dashed curves represent various Taylor approximations up to order $\alpha = 2, 3$ or 4, inclusive.

described by the coordinate ϑ, will be governed by the N_2-graphite interaction and the in-plane dynamical behaviour, corresponding with motions in the φ direction, will be strongly determined by the N_2-N_2 interaction. This does not imply, however, that the φ anisotropy of the molecule-substrate interaction is always negligible. For example, in an incommensurate N_2-adlayer [32], where the molecules are not adsorbed above the centers of graphite hexagons, the corrugated part of the molecule-substrate interaction can cause a φ barrier of 0.5 kJ mol^{-1}, which is 10% of the intralayer value. On the other hand, the ϑ anisotropy appears to be practically independent of the surface corrugation.

So far, we have fixed the molecular centers of mass in their equilibrium positions. In lattice dynamics calculations, including the translational vibrations, the Taylor expansion of Eq. (87) with respect to molecular displacements $\boldsymbol{u}$ is useful. Because the out-of-plane translational motions are, just as the out-of-plane rotations, strongly determined by the molecule-substrate interaction we will investigate the convergence of the Taylor expansion with respect to displacements perpendicular to the substrate surface.

In Fig. 6 the solid curve represents the total N_2-graphite potential as a function of the distance z with respect to the substrate top layer. All other molecular coordinates are set equal to their equilibrium values in the optimized commensurate adlayer, although a variation of φ would not be visible on the energy scale used here. Within the harmonic approximation, represented by the dashed curve with ($\alpha = 2$) in Fig. 6, the bound state energies can be characterized by a fundamental oscillator frequency of 0.4 kJ mol^{-1}. From Fig. 6 we conclude that the harmonic approximation is good if the molecule is in the ground state at -9.5 kJ mol^{-1}, where it oscillates with a translational amplitude of 0.01 nm with respect to the potential minimum. However, for the first excited state at -9.1 kJ mol^{-1}, corresponding with an amplitude of 0.02 nm, the harmonic approximation is not accurate enough. Although the third order Taylor approximation ($\alpha = 3$) is better within a greater domain, it is dangerous to use this approximation because the first excited state is nearly at the same level as the local maximum at $z = 0.36$ nm. This implies that, at finite temperatures, the molecule can easily escape from the surface if the third order Taylor approximation is used. Of course, this is an undesired artifact that is avoided if one only uses Taylor approximations of even order, see for instance the dashed curve corresponding with $\alpha = 4$ in Fig. 6.

6.5. Conclusion

We have elaborated on two methods to obtain an analytical potential expansion for a molecule interacting with a substrate that consists of atoms which are ordered in a two-dimensional lattice.

The most general method, shown in Sec. 6.2, starts with a spherically expanded molecule-atom potential which represents the anisotropy explicitly. This pair potential is expanded with respect to molecular displacements. Finally, because of the two-dimensional translation symmetry parallel to the substrate surface, the lattice sum over the expanded molecule-atom pair potentials is replaced by a two-dimensional Fourier series. We have given analytical expressions for the isotropic ($l = 0$) and flat ($g = 0$) Fourier transforms. As far as the corrugated part of the molecule-substrate potential expansion is concerned, the anisotropic Fourier transforms are difficult to evaluate analytically, however.

In Sec. 6.3 we have presented a special method that is applicable if an atom-atom model is used for the molecule-atom pair potential. This method starts with a Fourier transformation of isotropic atom-substrate potentials. After a spherical expansion of the atom-substrate Fourier series, followed by a translational displacement expansion, the final expression has a similar form as the result of the general method of Sec. 6.2. A great advantage of the special method of Sec. 6.3 is that all expansion coefficients can be evaluated analytically for exponential and inverse power law atom-atom potential types.

As an example, we have applied both methods for a homonuclear diatomic molecule on a substrate, resulting in some simplifications and further analytical formulas. In order to illustrate the convergence of the expansion, some numerical results have been shown for N_2 on graphite. At an adsorption site, the in-plane anisotropy of the N_2-graphite interaction, caused by the corrugation, appears to be negligible compared with the out-of-plane anisotropy. In the commensurate $(\sqrt{3} \times \sqrt{3})R30°$ structure the out-of-plane crystal field anisotropy is strongly determined by the N_2-graphite potential and the in-plane anisotropy is dominated by the N_2-N_2 interaction. The anharmonic terms in the molecular displacement expansion are so important that they will influence the out-of-plane translational vibrations. Truncation of this expansion after the cubic terms should be avoided, since this produces the artifact that an adsorbed molecule can easily escape from the surface.

Finally we observe that the techniques developed in this paper can also be used to obtain general expressions for the interaction between electrostatic multipole moments and a two-dimensional lattice of multipoles. This will be treated in a forthcoming paper.

Acknowledgement

We thank Dr. P.E.S. Wormer and Dr. W.J. Briels for useful discussions. This investigation was supported partly by the Netherlands Foundation for Chemical Research (SON) with financial aid from the Netherlands Organization for Scientific Research (NWO).

References

[1] D. Eichenauer, U. Harten, J.P. Toennies and V. Celli, J. Chem. Phys. **86**, 3693 (1987).
[2] H. Jónsson and J.H. Weare, J. Chem. Phys. **86**, 3711 (1987).
[3] *Ordering in two dimensions*, edited by S.K. Sinha, North Holland, New York (1980).
[4] L.W. Bruch, Surf. Sci. **125**, 194 (1983).
[5] S. Rauber, J.R. Klein, M.W. Cole and L.W. Bruch, Surf. Sci. **123**, 173 (1982).
[6] F.C. Frank and J.H. Van der Merwe, Proc. R. Soc. **198**, 205, 216 (1949).
[7] P. Bak, Rep. Prog. Phys., **45**, 587 (1982).
[8] W.A. Steele, Surf. Sci. **36**, 317 (1973).
[9] J. Belak, K. Kobashi and R.D. Etters, Surf. Sci. **161**, 390 (1985).
[10] J. Talbot, D.J. Tildesley and W.A. Steele, Mol. Phys. **51**, 1331 (1984).
[11] D. Kirin, B. Kuchta and R.D. Etters, J. Chem. Phys. **87**, 2332 (1987).

[12] S. Sokolowski, Phys. Lett. A **117**, 468 (1986).

[13] S. Sokolowski, Z. Phys. Chem. Leipzig **268**, 1111 (1987).

[14] A. van der Avoird, P.E.S. Wormer, F. Mulder and R. Berns, , Top. Curr. Chem. **93**, 1 (1980).

[15] H. Yasuda and T. Yamamoto, Progr. Theor. Phys. **45**, 1458 (1971).

[16] W.J. Briels, J. Chem. Phys. **73**, 1850 (1980).

[17] W.J. Briels, A.P.J. Jansen and A. van der Avoird, Adv. Quant. Chem. **18**, 131 (1986).

[18] W.J. Briels, A.P.J. Jansen and A. van der Avoird, J. Chem. Phys. **81**, 4118 (1984).

[19] D.M. Brink and G.R. Satchler, *Angular Momentum*, Clarendon, Oxford (1975).

[20] E.P. Wigner, *Group Theory*, Academic Press, New York (1965).

[21] H. Pauly in sl Atom-Molecule Collision Theory, edited by R.B. Bernstein, Plenum, New York (1979).

[22] A.R. Edmonds,, *Angular momentum in Quantum Mechanics*, Princeton University Press, Princeton, New Jersey (1957).

[23] M. Abramowitz and I.A. Stegun, *Handbook of Mathematical Functions*, National Bureau of Standards, Washington D.C. (1964).

[24] W. Magnus and F. Oberhettinger, *Formeln und Sätze für die speciellen Funktionen der Mathematische Physik*, Springer Verlag, Berlin (1948).

[25] I.S. Gradshteyn and I.M. Ryzhik,*Table of Integrals, Series, and Products*, Academic Press, New York (1965).

[26] J.M. McKinley and P.P. Schmidt, Chem. Phys. Lett. **110**, 379 (1984).

[27] G. Arfken, *Mathematical methods for physicists*, 2nd ed., Academic Press, New York (1970).

[28] A. Messiah, *Quantum Mechanics*, North-Holland, Amsterdam (1969).

[29] J.K. Kjems, L. Passell, H. Taub, J.G. Dash and A.D. Novaco, Phys. Rev. B **13**, 1446 (1976).

[30] J. Eckert, W.D. Ellenson, J.B. Hastings and L. Passel, Phys. Rev. Lett. **43**, 1329 (1979).

[31] R. Wang, S.K. Wang, H. Taub, J.C. Newton and H. Shechter, Phys. Rev. B **35**, 5841 (1987).

[32] R.D. Diehl and S.C. Fain, Jr., Surf. Sci. **125**, 116 (1983).

[33] R.D. Diehl, M.F. Toney and S.C. Fain, Jr., Phys. Rev. Lett. **48**, 177 (1982).

[34] R.D. Diehl and S.C. Fain, Jr., Phys. Rev. B **26**, 4785 (1982).

[35] T.T. Chung and J.G. Dash, Surf. Sci. **66**, 559 (1977).

[36] B. Kuchta and R.D. Etters, Phys. Rev. B **36**, 3400 (1987).

[37] C. Peters and M.L. Klein, Mol. Phys. **54**, 895 (1985).

[38] C.R. Fuselier, N.S. Gillis and J.C. Raich, Solid State Commun. **25**, 747 (1978).

[39] G. Cardini and S.F. O'Shea, Surf. Sci. **154**, 231 (1985).

[40] R.M. Berns and A. van der Avoird, J. Chem. Phys. **81**, 1192 (1980).

7. Phonons and librons in nitrogen monolayers adsorbed on graphite

T.H.M. van den Berg and A. van der Avoird

Institute of Theoretical Chemistry, University of Nijmegen, Toernooiveld, Nijmegen, The Netherlands

(Submitted to Phys. Rev. B)

Abstract. For the ordered commensurate and incommensurate N_2 monolayers which are formed at low T on the basal plane of graphite we have calculated the structure and lattice dynamics by means of the quantum mechanical Mean Field and Time-Dependent Hartree methods. The potential used is an *ab initio* potential for the N_2-N_2 interactions, with its anisotropy expanded in spherical harmonics, and an empirical atom-atom potential for the N_2-graphite interactions, with variable parameters. The molecular center-of-mass vibrations are expanded in three-dimensional harmonic oscillator functions and the librations in a free rotor basis; translation-rotation coupling is explicitly included. We discuss the anharmonic shifts in the frequencies of the in-plane and out-of-plane phonons and librons, but we find that these shifts, with the exception of the soft out-of-plane libration in the compressed incommensurate herringbone phase, are not larger than in bulk nitrogen in the ordered α and γ phases. For the incommensurate monolayer we find at zero pressure that the planar herringbone ordering, which occurs also in the commensurate phase, is more stable than the pin-wheel structure. At higher pressures, but probably still before bilayer formation, the pin-wheel structure seems to be more stable, however. For the commensurate monolayer we obtain good agreement with the phonon frequencies from inelastic neutron scattering, except for the acoustic phonon gap. Since this gap is directly related to the corrugation in the N_2-graphite potential, we must conclude that this corrugation cannot be correctly reproduced by an atom-atom model, even when the parameters are varied within reasonable limits.

7.1. Introduction

Physically adsorbed layers of N_2 molecules on graphite occur in a variety of quasi-two-dimensional phases. Of basic interest are the stability and dynamics of these phases, the transitions between them and the way in which their behaviour depends on the intermolecular and molecule-substrate interactions. Especially the last few years a number of experimental and theoretical studies have appeared. Structures and phase transitions have been characterized by neutron, X-ray and low energy electron diffraction and by specific heat measurements [1-12]. The adlayer dynamics has been investigated recently by inelastic neutron scattering [13-15] and, in the near future, will be studied probably in more detail by inelastic helium scattering [16-18]. Theoretical investigations have started from empirical model potentials; they involve static potential energy calculations [19] and the use of harmonic [15,20-22] or quasi-harmonic [23] lattice dynamics and classical Monte Carlo [24-28] or Molecular Dynamics (MD) [21,29-31] methods. An excellent review of the results that have been obtained from these studies is given in the recent paper by Roosevelt and Bruch [23].

In the present paper we concentrate on the commensurate $(\sqrt{3} \times \sqrt{3})R\,30°$ monolayer for which the most experimental data are available, and on the incommensurate monolayers. These phases are orientationally ordered and stable at low temperature, for lower and higher coverages, respectively. For the $(\sqrt{3} \times \sqrt{3})R\,30°$ phase a herringbone ordering of the N_2 molecules is well established [6,8,11]. Also the uniaxially incommensurate phase has the herringbone structure, but for the so-called triangular incommensurate phase that occurs at higher pressures both a herringbone and a pin-wheel structure are still considered possible [8,10,32]. We study the dynamics of these phases; the (theoretical) method that we use for this purpose is in several respects complementary to the (quasi-)harmonic and classical MD methods used before [15,20-23,29-31].

The pair potential assumed between the N_2 molecules in the adsorbed layer originates directly from *ab initio* calculations [33]. It is not fitted to a site-site model as used in the other calculations [19-31], but instead its anisotropy is explicitly expressed by a converged expansion in spherical harmonics [34]. In recent work on solid nitrogen [35-39] it has been confirmed that this representation of the orientational dependence of the potential is essential for obtaining accurate librational frequencies. With a site-site model fitted to the same *ab initio* data the librational frequencies in solid α-N_2 and γ-N_2 are 30% too high. The use of this anisotropic expansion of the potential implies that the molecular quadrupole and higher multipole interactions are exactly included, without recourse to a point charge model. For the molecule-substrate interactions we use the same empirical atom-atom potential of Steele [40] that was used in other calculations [19-31]. Because of the uncertainty in these interactions we apply a systematic variation of the parameters in this potential.

The method that we use to perform the lattice dynamics calculations is the Time-Dependent Hartree (TDH) method [37,41]. At zero temperature this method is equivalent to the Random Phase Approximation (RPA). It is also equivalent to the susceptibility approach [42-44] which has been used for the (semi-empirical) description of orientational order/disorder phase transitions. In our group this method has been extended in order to include the anharmonic center-of-mass vibrations of the molecules, which are expanded in a basis of 3-dimensional harmonic oscillator wave functions. The librational wave functions are expanded in spherical harmonics and the effects of rotation-translation coupling are explicitly taken into account. As illustrated by applications to solid α- and γ-nitrogen [35-39] this method is suitable for the calculations of motions with larger amplitudes. The anharmonic effects enter in two ways. First, there is a dilation of the lattice by the averaging over the (zero-point or temperature) vibrations of the molecules in the anharmonic potential wells. This effect, which leads in general to a downward shift of the frequencies, is also included in the quasi-harmonic theory. In commensurate overlayers it cannot occur in the directions parallel to the surface, but in the perpendicular direction it is expected to be rather important [45]. Secondly, there is a direct effect of the (mainly cubic and quartic) anharmonic terms in the potential, which leads to an upward shift of the frequencies in bulk nitrogen [39]. Classical MD calculations [21] indicate that these anharmonic effects are larger for adsorbed layers than they are in bulk solids. On the other hand, our TDH study is complementary to the classical MD treatments [21,29-31] in that it includes the quantum mechanical zero-point vibrations and librations which reduce the cohesion or adsorption energies in these systems [46-48] by about 15%. This is essential in considerations about phase stability.

7.2. Formalism

7.2.1. The Hamiltonian

The center-of-mass positions of the molecules in the adsorbed layer are denoted by $\mathbf{r}_p = \mathbf{R}_p + \mathbf{u}_p$, where $\mathbf{R}_p$ are the equilibrium positions and $\mathbf{u}_p$ the displacements of the molecules p. The orientations of the molecules are described by a set of polar angles ω_p. We assume that the motions of the molecules in the adsorbed layer are separable from the graphite lattice vibrations which have much higher frequencies and small amplitudes. We use a rigid graphite substrate, so that the molecule-substrate potential V_p for a given molecule p depends only on the coordinates $\mathbf{u}_p$ and ω_p of that molecule. The pair potential between the molecules within the adsorbed layer is denoted by $\Phi_{pp'}$. Many-body interactions, as well as substrate-mediated interactions between the adsorbed molecules are neglected. Then, the Hamiltonian for the adsorbed layer is given by

$$H = \sum_p T(\mathbf{u}_p) + \sum_p L(\omega_p) + \sum_p V_p(\mathbf{u}_p, \omega_p) + \tfrac{1}{2} \sum_p \sum_{p' \neq p} \Phi_{pp'}(\mathbf{u}_p, \omega_p, \mathbf{u}_{p'}, \omega_{p'}) \,. \quad (1)$$

It contains the kinetic-energy terms for the translational center-of-mass motions T and the rotational motions L of the molecules, the molecule-substrate potential V_p and the intermolecular potential $\Phi_{pp'}$.

The anisotropic intermolecular potential is written in the form of a spherical expansion [34]

$$\begin{aligned}\Phi_{pp'}(\mathbf{u}_p, \omega_p, \mathbf{u}_{p'}, \omega_{p'}) = \sum_{\mathbf{l}} \varphi_l(r_{pp'}) \sum_{\mathbf{m}} \begin{pmatrix} l_1 & l_2 & l_3 \\ m_1 & m_2 & m_3 \end{pmatrix} \\ \times\, C^{(l_1)}_{m_1}(\omega_p) C^{(l_2)}_{m_2}(\omega_{p'}) C^{(l_3)}_{m_3}(\hat{\mathbf{r}}_{pp'}) \,.\end{aligned} \quad (2)$$

The intermolecular vector is given by $\mathbf{r}_{pp'} = (\mathbf{R}_{p'} + \mathbf{u}_{p'}) - (\mathbf{R}_p + \mathbf{u}_p)$ and $\hat{\mathbf{r}}_{pp'}$ is the unit vector along $\mathbf{r}_{pp'}$. The Racah spherical harmonics $C^{(l)}_m(\omega)$ that describe the orientational dependence of the potential are coupled to a scalar function by the summation over $\boldsymbol{m} = \{m_1, m_2, m_3\}$, with the large parentheses denoting a 3-j symbol [49]. The first summation runs over $\boldsymbol{l} = \{l_1, l_2, l_3\}$ and the factors $\varphi_l(r_{pp'})$ are the expansion coefficients that reflect the anisotropy of the potential. Each expansion coefficient $\varphi_l(r)$ consists of dispersion contributions ($\sim r^{-6}, r^{-8}$ and r^{-10}) and short range contributions, which depend exponentially on r. The quadrupole-quadrupole interaction ($\sim r^{-5}$) appears in the $l_1, l_2, l_3 = 2, 2, 4$ term and the higher multipole interactions ($\sim r^{-l_3-1}$) in the other terms with $l_1 + l_2 = l_3$. The parameters in all these contributions have been directly obtained from *ab initio* calculations on the N_2-N_2 dimer [33]. The expansion appears to be converged for $l_1, l_2 \leq 6$ with $l_1 + l_2 \leq 10$.

The potential as written in Eq. (2) depends on the molecular center-of-mass displacements $\boldsymbol{u}_p$ and $\boldsymbol{u}_{p'}$ through the intermolecular vector $\boldsymbol{r}_{pp'}$. Its dependence on $\boldsymbol{u}_p$ and $\boldsymbol{u}_{p'}$ can be made explicit by a double Taylor expansion [37]. In Appendix A we describe a more efficient expansion in $\boldsymbol{u}_{p'} - \boldsymbol{u}_p$ which leads to essentially the same result

$$\begin{aligned}\Phi_{pp'}(\boldsymbol{u}_p, \boldsymbol{\omega}_p, \boldsymbol{u}_{p'}, \boldsymbol{\omega}_{p'}) = \sum_{\Lambda_1} \sum_{\Lambda_2} &(u_p)^{\alpha_1} C^{(\lambda_1)}_{\mu_1}(\hat{\boldsymbol{u}}_p) C^{(l_1)}_{m_1}(\boldsymbol{\omega}_p) X_{\Lambda_1 \Lambda_2}(\boldsymbol{R}_{pp'}) \\ &\times (u_{p'})^{\alpha_2} C^{(\lambda_2)}_{\mu_2}(\hat{\boldsymbol{u}}_{p'}) C^{(l_2)}_{m_2}(\boldsymbol{\omega}_{p'}) \,,\end{aligned} \tag{3}$$

where $\boldsymbol{u}_p = (u_p, \hat{\boldsymbol{u}}_p)$ are the displacement vectors in polar coordinates and the label Λ stands for the set of indices $\{\alpha, \lambda, \mu, l, m\}$. The expression for $X_{\Lambda_1 \Lambda_2}(\boldsymbol{R}_{pp'})$ which is given in Appendix A is much faster to evaluate than the expression in Ref. [37]. The summation over α_1 and α_2 extends to $\alpha_1 + \alpha_2 \leq \alpha_{max}$, where α_{max} is equal to the order of the Taylor expansion in the displacements. An expansion with $\alpha_{max} = 2$, for instance, yields a potential $\Phi_{pp'}$ which is harmonic in the center-of-mass displacements $\boldsymbol{u}_p$ and $\boldsymbol{u}_{p'}$. In the present calculations we carry this expansion up to $\alpha_{\max} = 4$ inclusive. For the summations over λ and μ holds: $0 \leq \lambda_i \leq \alpha_i$ and $-\lambda_i \leq \mu_i \leq \lambda_i$, where λ_i has the same parity as α_i. After this expansion we have a pair potential which is explicitly dependent on the displacement coordinates of the molecules and thus easy to use in lattice dynamics calculations.

The interaction V_p of a molecule p with the substrate is considered as a sum of pair interactions between the molecule and the individual substrate atoms. The most general form for such molecule-atom interactions is of course a spherical expansion, *i.e.* a special case of Eq. (2). We model this interaction by the atom-atom model

$$V_p(\boldsymbol{u}_p, \boldsymbol{\omega}_p) = \sum_C \left[v\left(\mid \boldsymbol{R}_p + \boldsymbol{u}_p + \boldsymbol{a}(\boldsymbol{\omega}_p) - \boldsymbol{R}_C \mid\right) + v\left(\mid \boldsymbol{R}_p + \boldsymbol{u}_p - \boldsymbol{a}(\boldsymbol{\omega}_p) - \boldsymbol{R}_C \mid\right) \right] , \tag{4}$$

where the vectors $\boldsymbol{R}_C$ denote the positions of the carbon atoms C in the substrate and the orientation dependent vectors $\boldsymbol{a}(\boldsymbol{\omega}_p)$ describe the positions of the nitrogen atoms with respect to the N_2 center-of-mass. Just as the previous calculations [19-31] we choose an atom-atom potential $v(|\boldsymbol{r}|)$ of the Lennard-Jones type as parametrized by Steele [40], but we investigate systematically the effects of the variation of these parameters (see Sec. 7.3).

In Ref. [50] it is shown that the atom-atom interactions can be summed to an atom-substrate interaction with the aid of an analytical Fourier transformation. Next, a spherical expansion of the molecule-substrate interaction can be made to expose its anisotropy explicitly and, finally, a molecular-displacement expansion of the spherical expansion is used to make the molecule-substrate potential explicitly dependent on the displacement coordinates of the molecule [45]. Thus, we have obtained the molecule-substrate potential in the following form

$$V_p(\boldsymbol{u}_p,\omega_p) = \sum_{\Lambda} F_{\Lambda}(\boldsymbol{R}_p)(u_p)^{\alpha} C^{(\lambda)}_{\mu}(\hat{\boldsymbol{u}}_p) C^{(l)}_{m}(\omega_p) \tag{5}$$

where again Λ indicates the set of indices $\{\alpha,\lambda,\mu,l,m\}$. The coefficients $F_{\Lambda}(\boldsymbol{R}_p)$ can be written as a two-dimensional Fourier series

$$F_{\Lambda}(\boldsymbol{R}_p) = \sum_{g} \overline{F}_{\Lambda}(g \mid z_p) \exp(i g \cdot \tau_p) \tag{6}$$

with τ_p denoting the projection of $\boldsymbol{R}_p$ on the graphite basal plane (the xy-plane), so that $\boldsymbol{R}_p = \tau_p + z_p \boldsymbol{e}_z$. The vector g is a vector in the two-dimensional reciprocal lattice of a substrate layer. Analytical expressions for the expansion coefficients $\overline{F}_{\Lambda}(g \mid z_p)$ are given in Ref. [45]. The terms with $g = 0$ describe the flat (but anisotropic and anharmonic) potential which depends only on the height z_p of the molecules above the graphite surface, the terms with $g \neq 0$ contain the effects of the surface corrugation.

In order to summarize the result of these manipulations we introduce the notion of dynamical variables [42,43]. In the harmonic method these are the center-of-mass displacements and the infinitesimal (linearized) angular displacements of the molecules. In our treatment the dynamical variables are

$$Q^{k,\nu}_p = \begin{cases} C^{(l)}_m(\omega_p) & \text{with } \nu = \rho = (l,m) \text{ for the molecular rotations } (k = r) \\ (u_p)^{\alpha} C^{(\lambda)}_{\mu}(\hat{\boldsymbol{u}}_p) & \text{with } \nu = \tau = (\alpha,\lambda,\mu) \text{ for the c.o.m. vibrations } (k = t) \end{cases} \tag{7}$$

and the lattice Hamiltonian for the adsorbed molecular layer can be written as

$$\begin{aligned} H = {} & \sum_{pk} T^k_p + \sum_{p} \sum_{\rho\tau} F_{\rho\tau}(\boldsymbol{R}_p) Q^{r,\rho}_p Q^{t,\tau}_p \\ & + \sum_{p} \sum_{\rho\tau} \sum_{p' \neq p} \sum_{\rho'\tau'} Q^{r,\rho}_p Q^{t,\tau}_p X_{\rho\tau;\rho'\tau'}(\boldsymbol{R}_{pp'}) Q^{r,\rho'}_{p'} Q^{t,\tau'}_{p'} \end{aligned} \tag{8}$$

The kinetic energy T^k_p is either translational, $T^t_p = T(\boldsymbol{u}_p)$, or rotational, $T^r_p = L(\omega_p)$, and the coefficients $F_{\rho\tau}(\boldsymbol{R}_p)$ and $X_{\rho\tau;\rho'\tau'}(\boldsymbol{R}_{pp'})$ are the same as in Eqs. (5) and (3). The complete expressions for these coefficients can be found in Ref. [45] and in Appendix A, respectively.

7.2.2. The Time-Dependent Hartree method

The first step in our treatment is a Mean-Field (MF) calculation. The translational and rotational motions are decoupled at this level so that we obtain two effective particles per molecule [37]. This yields the following MF Hamiltonian

$$H_p^k = T_p^k + \sum_\nu c_p^{k,\nu} Q_p^{k,\nu} \ , \tag{9}$$

with

$$c_p^{k,\nu} = \sum_{\overline{\nu}} \langle Q_p^{\overline{k},\overline{\nu}} \rangle \left[F_{\nu\overline{\nu}}(\boldsymbol{R}_p) + \sum_{p' \neq p} \sum_{\rho' \tau'} X_{\nu\overline{\nu};\rho'\tau'}(\boldsymbol{R}_{pp'}) \langle Q_{p'}^{r,\rho'} \rangle \langle Q_{p'}^{t,\tau'} \rangle \right] , \tag{10}$$

where $\overline{k}$ denotes the complement of the type of the motion k, *i.e.* $\overline{r} = t$ and $\overline{t} = r$. The thermodynamic average of a dynamical variable is defined by

$$\langle Q_p^{k,\nu} \rangle = \mathrm{Tr}^{(pk)} \left\{ d_p^k Q_p^{k,\nu} \right\} \tag{11}$$

i.e. by a single-particle trace with the MF density operator d_p^k. The MF equations

$$H_p^k \left| \psi_p^{k,a} \right\rangle = \varepsilon_p^{k,a} \left| \psi_p^{k,a} \right\rangle \tag{12}$$

are solved self-consistently in a basis of tesseral harmonics (real spherical harmonics) for the rotational states ($k = r$) and three-dimensional harmonic oscillator functions for the translational vibrations ($k = t$). For the case at hand, we have included tesseral harmonics up to $l_{\max} = 12$ or 13, for *ortho* or *para* N_2, respectively, and spherical harmonic oscillator functions up to principal quantum number $n_{\max} = 6$.

The coupling between the molecular motions, neglected at the MF level, is regained with the aid of the Time-Dependent Hartree (TDH) method. This method is briefly summarized in Appendix B. The excitation and de-excitation energies of the adsorbed layer that correspond with the translational phonons, the librons or, in general, with mixed modes of wave vector $\boldsymbol{q}$, are the eigenvalues of the following dynamical matrix

$$\boldsymbol{M}(\boldsymbol{q}) = \boldsymbol{\varepsilon} - \boldsymbol{P}\boldsymbol{Q}\boldsymbol{W}(\boldsymbol{q})\widetilde{\boldsymbol{Q}}^T \ . \tag{13}$$

This matrix comprises the MF excitation energy matrix $\boldsymbol{\varepsilon}$ and the density operator difference matrix $\boldsymbol{P}$ with the elements

$$\varepsilon_{ikab;i'k'a'b'} = \delta_{ii'}\delta_{kk'}\delta_{aa'}\delta_{bb'} \left(\varepsilon_p^{k,a} - \varepsilon_p^{k,b} \right) \tag{14}$$

and

$$P_{ikab;i'k'a'b'} = \delta_{ii'}\delta_{kk'}\delta_{aa'}\delta_{bb'} \left(d_p^{k,a} - d_p^{k,b} \right) \ . \tag{15}$$

The molecules are labelled here by $p = \{\boldsymbol{n}, \boldsymbol{i}\}$, where $\boldsymbol{n}$ labels the unit cells and $\boldsymbol{i}$ the sublattices. Furthermore, Eq. (13) contains transition matrix elements

$$\begin{aligned} Q_{ikab;i'k'\nu} &= \delta_{ii'}\delta_{kk'} \langle \psi_p^{k,a} | Q_p^{k,\nu} | \psi_p^{k,b} \rangle \\ \widetilde{Q}_{ikab;i'k'\nu} &= Q_{ikba;i'k'\nu} \end{aligned} \tag{16}$$

of the dynamical variables. The coupling information is contained in the Fourier transforms

$$W_{ik\nu;i'k'\nu'}(q) = \sum_{n} \exp\left[iq \cdot (R_{p'} - R_p)\right] W_{pp'}^{k\nu;k'\nu'} \tag{17}$$

with $p = \{0, i\}$, $p' = \{n, i'\}$ and

$$\begin{aligned} W_{pp'}^{k\nu;k'\nu'} = &(1 - \delta_{pp'}) \sum_{\bar{\nu}} \sum_{\bar{\nu}'} \langle Q_p^{\bar{k},\bar{\nu}} \rangle X_{\nu\bar{\nu};\nu'\bar{\nu}'}(R_{pp'}) \langle Q_{p'}^{\bar{k}',\bar{\nu}'} \rangle \\ &+ \delta_{pp'} \delta_{k\bar{k}'} \left[F_{\nu\nu'}(R_p) + \sum_{p'' \neq p} \sum_{\rho\tau} X_{\nu\nu';\rho\tau}(R_{pp''}) \langle Q_{p''}^{r,\rho} \rangle \langle Q_{p''}^{t,\tau} \rangle \right] . \end{aligned} \tag{18}$$

The first term in Eq. (18) couples the motions of the molecules at different lattice sites, the other terms are translation-rotation couplings on the same site. Both the molecule-substrate potential and the intermolecular potential are active in the latter.

It is proved in Appendix B that the TDH method is exactly equivalent to the approach that uses generalized susceptibilities [42-44]. The frequency-dependent single-particle susceptibility corresponds with the MF model and it is given in terms of the matrices in Eqs. (13), (14) and (15) by

$$\chi^{(0)}(\omega) = \tilde{Q}^T (\omega - \epsilon)^{-1} P Q . \tag{19}$$

The generalized crystal susceptibility $\chi(q, \omega)$ for wave vector q is related [42] to $\chi^{(0)}(\omega)$ and to the coupling matrix $W(q)$ in Eq. (17) by the Dyson equation

$$\chi(q, \omega)^{-1} = \chi^{(0)}(\omega)^{-1} + W(q) . \tag{20}$$

It is shown in Appendix B that the frequencies of the poles in $\chi(q, \omega)$ are exactly equal to the eigenvalues of the dynamical matrix $M(q)$ in Eq. (13), *i.e.* to the (de-)excitation frequencies of the crystal calculated by the TDH method.

Before we present the results we mention some further computational details. The width parameter A in the three-dimensional harmonic oscillator basis [37] for the center-of-mass vibrations is chosen as $A = (m\omega/\hbar)^{1/2}$, where m is the nitrogen molecular mass and ω is the average of the MF fundamental excitation frequencies. We use 1.42 Å as the nearest neighbor distance between the carbon atoms within the graphite layers and 3.37 Å as the distance between the layers. If not indicated otherwise, we have used Steele's [40] parameters $\sigma = 3.343$ Å and $\varepsilon = 0.2631$ kJ/mol in the atom-atom model for the molecule-substrate potential. Only the top layer of the graphite substrate contributes to the corrugation (*i.e.* the terms with $g \neq 0$) in this potential. It is summed over molecule-atom pairs within a range of 30 Å. The next 10 underlying graphite layers are taken into account in the first Fourier term ($g = 0$) in Eq. (6) by analytic summation [45]. The intermolecular potential in the adsorbed layer is summed over 8.1 Å and the rotational constant of N_2 is taken as $B = 2.013$ cm^{-1}. All calculations are performed at zero temperature.

7.3. Results and discussion

In order to illustrate the effects of the anharmonicity and the corrugation in the potential we compare the results of the full TDH calculations with more approximate treatments. The first approximation consists of limiting the dynamical variables, see Eq. (7), to the terms with $\alpha_1 + \alpha_2 \leq \alpha_{\max} = 2$. This approximation implies that the Hamiltonian in Eq. (8) becomes harmonic in the translational displacements. The anharmonicity in the librations is fully retained through the expansion in spherical harmonics. The next level of approximation is a pure harmonic treatment based on the spherical expansion (SE) of the *ab initio* intermolecular potential [33], cf. Eq. (2). The required first and second derivatives of this potential with respect to the translational and librational displacements are given in Ref. [39]. Finally, we compare also some results obtained with the site-site (SS) model potential [33] that was fitted to the *ab initio* data. In order to study the effects of the surface corrugation we may switch off this corrugation at the various levels, as it has been done previously in (quasi-)harmonic calculations [21,23]. We will not distinguish between *ortho* and *para* N_2 layers, since the MF and TDH calculations with even or odd l free rotor functions in the basis yield practically the same results for the ordered phases considered here.

7.3.1. Commensurate monolayers

First we discuss the results for the commensurate $(\sqrt{3} \times \sqrt{3})R\,30°$ monolayer with the nearest neighbor distance of 4.26 Å fixed by the substrate. It is illustrative to begin with the fundamental excitations at the single-particle level (see Table I). Even in the fully anharmonic TDH treatment it is easy to recognize the normal mode contents of the translational vibrations and librations and to assign the corresponding quantum numbers. Especially for the librations this is striking since their wave functions have been expanded in a free-rotor basis. The frequencies of overtones and combination bands are surprisingly close to the sums of the fundamental frequencies. Also the adsorption energy is close to the harmonic value including the zero-point motions.

Still, one clearly observes the frequency shifts which are due to the anharmonicity. For the out-of-plane translational motions there is already a difference between the harmonic calculations and the MF calculations with $\alpha_{\max} = 2$. This may be unexpected since these calculations use exactly the same potential and the MF scheme with $\alpha_{\max} = 2$ involves a Hamiltonian that is harmonic in the center-of-mass displacements. We have found that the difference is due to the averaging over (anharmonic) librations which is performed in the MF calculations with $\alpha_{\max} = 2$, but not in the harmonic treatment. When the cubic and quartic ($\alpha = 3$ and 4) displacement terms are switched on, we find an upward shift of about 4.5 cm^{-1} for the in-plane vibrations and a downward shift of 5.4 cm^{-1} for the out-of-plane vibration. In order to understand this result we remind the reader that the commensurate adsorbed layer cannot expand in the parallel directions,

Table I. Single-particle excitations in the $(\sqrt{3}\times\sqrt{3})R30^\circ$ monolayer.

	Mean Field		Harmonic	Mode	
	$\alpha_{\max}=4$	$\alpha_{\max}=2$	selfterm	character[a]	
ω_T (cm^{-1})	34.7	30.4	29.7	1 0 0	(in-plane)
	42.0	37.3	36.7	0 1 0	
	55.7	61.1	57.7	0 0 1	(out-of-plane)
	71.3	61.5	59.4	2 0 0	(overtones and combinations)
	77.4	68.0	66.4	1 1 0	
	86.0	74.7	73.4	0 2 0	
	90.4	92.0	87.4	1 0 1	
	96.7	98.7	94.4	0 1 1	
ω_L (cm^{-1})	48.0	52.1	55.3	1 0	(out-of-plane ϑ)
	52.4	52.8	55.9	0 1	(in-plane φ)
	96.6	102.3	110.6	2 0	(overtones and combinations)
	99.0	103.7	111.2	1 1	
	104.8	108.2	111.8	0 2	
z_e (Å)	3.305	3.305	3.305		
$\langle u_z\rangle$ (Å)	0.054	0.025			
$\langle u_x^2\rangle^{1/2}$ (Å)	0.124	0.132			
$\langle u_y^2\rangle^{1/2}$ (Å)	0.128	0.136			
$\langle u_z^2\rangle^{1/2}$ (Å)	0.117	0.103			
φ_e (°)	42[b]	42[b]	42.0		
$\langle\cos^2\vartheta\rangle$	0.040	0.037			
$\langle\sin^2\vartheta\cos 2\varphi\rangle$	0.059	0.060			
$\langle\sin^2\vartheta\sin 2\varphi\rangle$	0.884	0.887			
E (kJ/mol)	−11.143	−11.145	−11.130/−12.537[c]		

[a] Three vibrational quantum numbers are assigned to the translations and two to the librations.

[b] these numbers indicate the maximum in orientational probability.

[c] including/without the zero-point vibrations.

but it can be lifted from the surface by the anharmonicity. It has been observed already [45] that the potential is strongly anharmonic in the z-direction and we find here that the average center-of-mass positions are higher by $\langle u_z\rangle = \langle z\rangle - z_e = 0.054$ Å than the static equilibrium positions. For the librations we find anharmonic shifts of about -3.2 cm^{-1} and a further shift of -4.1 cm^{-1} in the out-of-plane libration when the anharmonic displacement terms are switched on. The latter shift is caused by the lifting of the adsorbed layer.

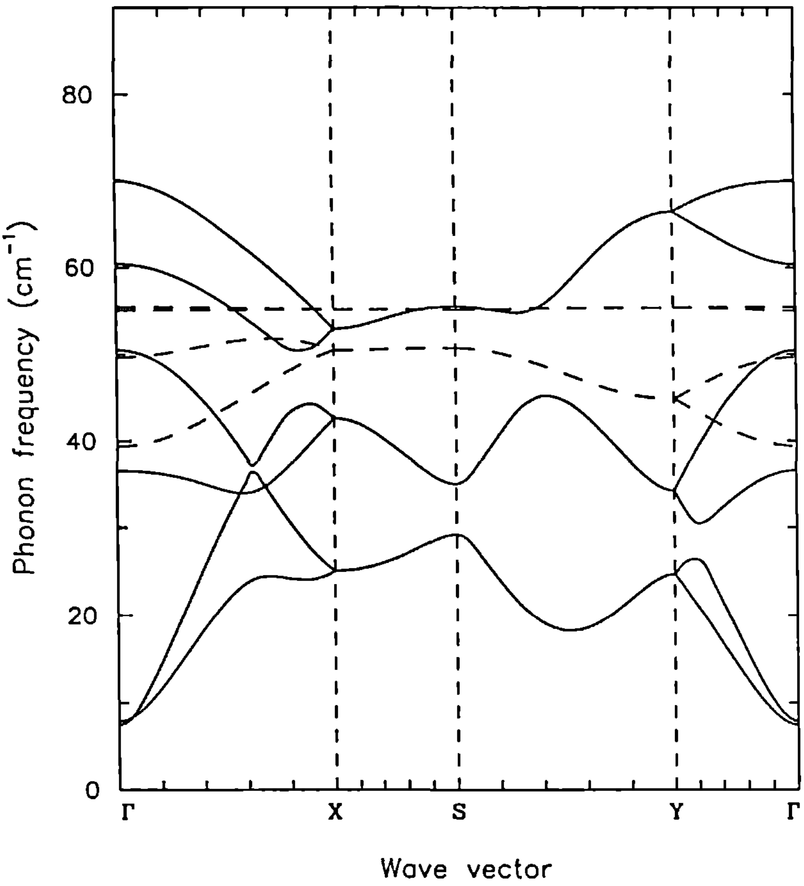

Fig. 1. Phonon/libron dispersion curves for a commensurate $(\sqrt{3} \times \sqrt{3})R\,30°$ N_2 monolayer on graphite from TDH calculations ($\alpha_{max} = 4$). In-plane (solid curves) and out-of-plane (dashed curves) branches have been decoupled by the omission of coupling blocks in the TDH matrix of Eq. (13).

In Figs. 1 and 2 we show the phonon and libron dispersion curves calculated by the TDH method. These curves are similar to the harmonic results [21]. Due to an artificial symmetry which is present only at the harmonic level one can decouple [21] the in-plane motions from the out-of-plane motions by switching off the corrugation in the molecule-substrate potential. At the TDH level only the natural symmetry of the system occurs and we study the effect of the in-plane/out-of-plane (de)coupling by the omission of the corresponding coupling terms in the TDH matrix given by Eq. (13). Even in the decoupled curves in Fig. 1 we have retained the $g \neq 0$ contributions in the molecule-substrate potential, as evident by the presence of the phonon gap. Comparison

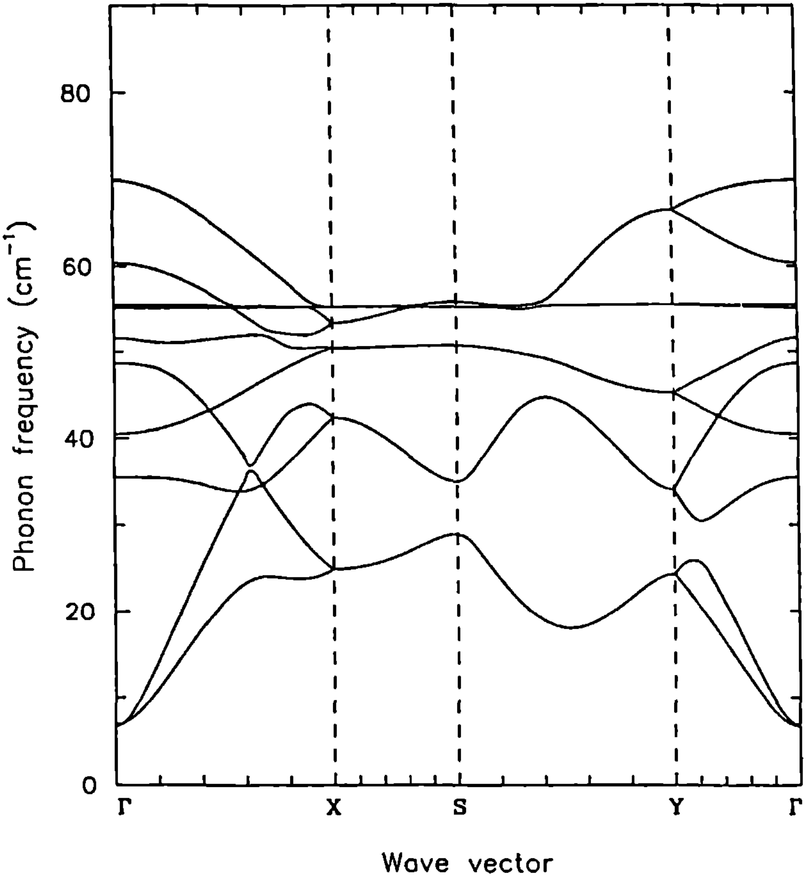

Fig. 2. Phonon/libron dispersion curves for a commensurate $(\sqrt{3}\times\sqrt{3})R\,30^\circ$ N_2 monolayer on graphite from TDH calculations ($\alpha_{\max} = 4$). Symmetry group $p2gg$, Brillouin zone points $\Gamma = (0,0)$, $X = (\pi/a, 0)$, $Y = (0, \pi/b)$ and $S = (\pi/a, \pi/b)$.

of Figs. 1 and 2 shows that also in the full TDH computations there is a near separation between the in-plane and out-of-plane motions. This separation and also the observed near separation between the translational phonons and the librons holds in the entire Brillouin zone, except near the avoided crossings. The in-plane motions are primarily determined by the N_2-N_2 intralayer potential, the out-of-plane motions by the N_2-substrate potential. Yet, we observe in Figs. 1 and 2 that the dispersion of the out-of-plane libron frequencies is substantial. The out-of-plane translational phonon band is very flat indeed.

The $q = 0$ phonon and libron frequencies, as computed at the different levels of approximation, are given in Table II. The lowest two values are the frequencies of

Table II. Lattice frequencies for $q = 0$ (in cm^{-1}) for the commensurate $(\sqrt{3} \times \sqrt{3})R\,30°$ monolayer.

symmetry group		TDH		Harmonic	
p2gg		$\alpha_{max}=4$	$\alpha_{max}=2$	SE[a]	SS[b]
in-plane translations	B_1	6.9	7.4	6.2	6.4
	B_2	7.1	7.7	6.8	6.6
	B_2	35.6	33.0	32.7	35.9
	B_1	48.8	43.2	42.7	43.9
out-of-plane librations	B_2	40.6	44.7	47.6	47.5
	B_1	51.6	54.1	57.1	57.2
out-of-plane translations	A_1	55.9	60.6	57.4	57.4
	A_2	55.5	61.1	57.7	57.7
in-plane librations	A_1	60.4	61.2	63.3	59.7
	A_2	69.9	70.5	75.0	68.9

[a] using the same spherically expanded *ab initio* N_2-N_2 potential as in TDH; equilibrium height $z_e = 3.305$ Å, angle $\varphi_e = 42.0°$ and static adsorption energy $E = -12.537$ kJ/mol.

[b] using the site-site model [33] for the *ab initio* N_2-N_2 potential; equilibrium height $z_e = 3.305$ Å, angle $\varphi_e = 44.0°$ and static adsorption energy $E = -12.618$ kJ/mol.

the acoustic phonon modes which are not equal to zero because of the corrugation in the molecule-substrate potential. These values characterize the so-called phonon gap [13-15]. The translational and librational anharmonicities appear to have very little influence on this gap. The anharmonic shifts in the optical phonon frequencies and in the libron frequencies are strikingly similar to the shifts discussed at the single-particle level. So, these shifts are mainly determined by the anharmonicity in the field experienced by an adsorbed molecule, which is due to the other molecules in the layer as well as to the substrate atoms. The difference between the site-site model of the N_2-N_2 potential and its representation by the spherical expansion is mostly apparent in the frequencies of the in-plane phonons and librons, as might be expected. The effect on the libron frequencies is substantially smaller than in bulk nitrogen, however [39].

Next we compare our results with the data obtained from inelastic neutron scattering [13-15]. The quantities that have been measured are: a phonon gap of 13.4 cm^{-1}, the frequency of the out-of-plane translational phonons $\approx$ 50 cm^{-1}, the width of the in-plane phonon and libron density of states $\approx$ 45 cm^{-1} and the average frequency of this density of states $\approx$ 36 cm^{-1}. The latter two quantities are rather global and they are consistent with the calculations. For the frequency of the out-of-plane phonon band we find a value of 56 cm^{-1}. The corresponding harmonic value is 58 cm^{-1}, both in our

Table III. Lattice frequencies (in cm^{-1}) for the $(\sqrt{3} \times \sqrt{3})R\,30°$ monolayer as a function of the molecule-substrate interaction parameters σ and ϵ (from harmonic calculations with the spherical expansion of the N_2-N_2 potential).

	ϵ (kJ/mol)	0.20	0.20	0.20	0.20	0.25	0.25	0.25	0.25	0.30	0.30	0.30	0.30
	σ (Å)	2.5	3.0	3.5	4.0	2.5	3.0	3.5	4.0	2.5	3.0	3.5	4.0
	z_e (Å)	2.436	2.957	3.463	3.958	2.436	2.957	3.463	3.958	2.436	2.957	3.463	3.958
	φ_e (°)	41.96	41.98	41.99	41.99	41.95	41.98	41.99	41.99	41.94	41.98	41.99	41.99
static energy	E (kJ/mol)	−6.88	−8.68	−11.00	−13.89	−7.87	−10.15	−13.04	−16.66	−8.91	−11.61	−15.09	−19.43
in-plane translations	B_1	5.1	6.1	5.1	3.8	5.5	6.7	5.7	4.2	5.9	7.4	6.2	4.6
	B_2	1.4	6.2	5.5	4.5	4.3	7.2	6.2	4.7	5.5	8.1	6.8	5.1
	B_2	29.9	31.6	32.4	32.4	31.3	32.4	32.6	32.5	32.0	32.7	32.8	32.6
	B_1	41.5	42.4	42.5	42.5	42.2	42.7	42.6	42.4	42.7	42.9	42.7	42.5
out-of-plane librations	B_2	40.8	38.9	39.0	40.2	46.8	45.5	46.2	47.6	52.5	51.6	52.5	54.0
	B_1	50.6	49.7	50.2	51.2	55.8	55.3	56.0	57.2	60.8	60.4	61.3	62.6
out-of-plane translations	A_1	49.2	49.6	50.3	51.2	55.0	55.5	56.3	57.2	60.3	60.7	61.6	62.7
	A_2	49.6	50.0	50.6	51.5	55.3	55.7	56.5	57.5	60.6	61.0	61.9	63.0
in-plane librations	A_1	63.4	63.3	63.3	63.3	63.4	63.3	63.3	63.3	63.5	63.3	63.3	63.3
	A_2	75.1	75.0	75.0	75.0	75.1	75.1	75.0	75.0	75.1	75.1	75.0	75.0

calculations and in Ref. [21]. The calculated phonon gap of 6.9 cm^{-1} is too small by a factor of two, as in the previous harmonic calculations [15,21].

Since the largest uncertainty in the calculations concerns the molecule-substrate potential we have systematically varied the Lennard-Jones parameters σ and ε in the atom-atom model for this potential. The results, which are listed in Table III, can be summarized as follows. As expected, the frequencies of the in-plane optical phonons and librons are rather insensitive to the parameters in the N_2-substrate potential. The out-of-plane frequencies depend only slightly on the parameter σ, although the height of the adsorbed layer and the adsorption energy change considerably with σ. The dependence of the out-of-plane frequencies on the well-depth parameter ε is nearly as $\varepsilon^{1/2}$. The acoustic phonon gap depends on σ and ε, but it does not reach a value that is close to the experimental number. So we must conclude that an atom-atom model as used here and in other calculations [15,19-31] for the molecule-substrate potential cannot represent the correct surface corrugation. This holds even when the parameters in this model are varied, within limits that are reasonable in view of the measured adsorption energy [51] and the out-of-plane phonon frequency of ≈ 50 cm^{-1}.

7.3.2. Incommensurate monolayers

The results for the incommensurate monolayers have been calculated by switching off the corrugation, *i.e.* omitting the $g \neq 0$ contributions, in the molecule-substrate potential. First we have optimized the structure, *i.e.* the two-dimensional lattice parameters and the height of the adsorbed molecules above the substrate. For the herringbone structure with *p2gg* symmetry the lattice parameters a and b have been varied independently; there are two molecules in the unit cell with the same height, which may lie (on the average) within the layer plane or they may be tilted out of the plane. For the pin-wheel structure [23] with *p*6 symmetry there is only one independent lattice parameter and there are four molecules in the unit cell. The height of the pin molecule above the substrate will be different from the height of the three wheel molecules, so these heights have been optimized independently. The wheel molecules may be tilted out of the layer plane.

Minimization of the static energy for the herringbone structure at zero pressure yields $a = 4.224$ Å, $b = 7.124$ Å and the energy $E = -12.486$ kJ/mol. The MF calculations yield $a = 4.36$ Å and $b = 7.21$ Å with energy $E = -11.036$ kJ/mol, so it is essential to include the zero-point motions. The latter value of a is even larger than the corresponding lattice parameter for the commensurate monolayer, but we note here that the incommensurate phases are stable only at higher pressure. For the pin-wheel structure the MF calculations yield nearest neighbor distance $a = 4.14$ Å and $E = -10.895$ kJ/mol with average heights $\langle z \rangle = 3.382$ Å and 3.742 Å for the wheel and pin molecules, respectively. The wheel molecules lie within the layer with $\varphi = 40°$, $160°$ and $280°$ and the pin molecules are indeed localized around the z-direction. The

Table IV. Lattice frequencies for $q = 0$ for the incommensurate herringbone monolayer (lattice constants $a = 4.15$ Å and $b = 6.87$ Å).

symmetry group		TDH		Harmonic	
$p2gg$		$\alpha_{\max}=4$	$\alpha_{\max}=2$	SE[a]	SS[a]
height	z_e (Å)	3.324	3.324	3.324	3.324
	$\langle u_z \rangle$ (Å)	0.064	0.031		
angle	φ_e (°)	40	40	38.9	40.3
energy	E (kJ/mol)	−10.716	−10.705	−12.380[b]	−12.393[b]
Lattice frequencies (cm^{-1})					
in-plane translations	B_1	0.0	0.0	0.0	0.0
	B_2	0.0	0.0	0.0	0.0
	B_2	51.4	48.7	49.2	55.1
	B_1	80.5	74.8	76.3	78.9
out-of-plane librations	B_2	19.5	27.3	25.2	30.3
	B_1	37.5	42.7	44.2	46.9
out-of-plane translations	A_2	53.0	60.0	55.0	54.9
	A_1	56.1	62.1	57.5	57.6
in-plane librations	A_1	78.6	79.6	84.5	79.6
	A_2	88.4	89.9	96.2	88.7

[a] with different N_2-N_2 potentials, as in Table II.

[b] not including zero-point motions.

amplitude in the angle ϑ is substantially larger for the pin molecules (23°) than it is for the wheel molecules (11°) and the fundamental librational frequency is considerably smaller (33.0 cm^{-1}, twofold degenerate, versus 49.7 cm^{-1}, out-of-plane, and 52.3 cm^{-1}, in-plane). All these results for the wheel molecules are similar to the corresponding values for the molecules in the herringbone layer shown in Table I, but the pin molecules behave rather differently.

In order to perform the calculations for non-zero two-dimensional pressures we proceed as follows. For the herringbone structure we choose a grid of three points a and three points b around the values of the lattice parameters which we expect to find for a given pressure. We calculate the MF energies at these grid points and we fit these energies by a second order form in a and b. From this form it is easy to determine the ratio b/a that minimizes the MF energy for constant surface $s = \frac{1}{2}ab$. At zero temperature the MF energy is equal to the Helmholtz free energy A. On the curve of optimized b/a ratios we calculate the two-dimensional pressure $p = -\left(\partial A/\partial s\right)_T$, as well as the chemical potential $\mu = A + ps$. This procedure has been repeated for different grids, *i.e.* different ranges of s and p, in order to obtain the $\mu(s)$, $\mu(p)$ and $p(s)$ curves

Table V. Lattice frequencies for $q = 0$ (in cm^{-1}) for the incommensurate pin-wheel monolayer (nearest neighbor distance $a = 4.057$ Å).

symmetry group $p6$		TDH $\alpha_{max}=4$	
in-plane translations	E_1	0.0	pin+wheel
	B	31.4	wheel
	E_1	38.8	pin+wheel
	E_1	62.4	pin+wheel
	B	73.5	wheel
out-of-plane librations	E_1	24.3	pin+wheel
	B	50.6	wheel
	E_1	52.1	pin+wheel
out-of-plane translations	A	51.7	pin
	E_2	53.1	wheel
	A	54.5	pin+wheel
in-plane librations	E_2	41.7	wheel
	A	68.6	wheel

for the herringbone structure. The corresponding procedure for the pin-wheel structure is trivial, since there is only one independent lattice parameter. Only the optimization of the heights of the pin and the wheel molecules is tedious.

The molecules in the herringbone layer stay within the plane and the optimized b/a ratio is equal to about 1.65 for the whole range of pressures investigated ($p \leq 0.090$ N/m which corresponds to $a \geq 4.15$ Å). For still higher pressures corresponding with $a = 4.05$ Å and $b = 6.68$ Å the herringbone structure becomes unstable; one of the TDH frequencies is imaginary. The ratio $b/a = 1.65$ implies a reduction of 5% with respect to the value of $\sqrt{3}$ that holds for the commensurate monolayer, in good agreement with the experimental observation [52] that the monolayer structure for a range of pressures is uniaxially incommensurate with a reduction in b that ranges from 2 to 5%. For the pin-wheel structure the wheel molecules stay within the layer also. The calculated $\mu(p)$ curves for the herringbone and pin-wheel structures are similar to those in Ref. [23]. At zero pressure we find with the use of the *ab initio* N_2-N_2 potential that the herringbone structure is more stable than the pin-wheel structure by 0.14 kJ/mol. The pin-wheel structure is considerably more compact, however, so it will be favored at higher pressures. Since the $\mu(p)$ curves run nearly parallel it is hard to determine the transition pressure. From the difference in surface per molecule, $s = 15.76$ Å^2 for the herringbone layer and $s = 14.84$ Å^2 for the pin-wheel layer, we estimate that the transition occurs around $p = 0.025$ N/m. The chemical potential $\mu = -8.62$ kJ/mol at this pressure is considerably lower than the bulk value of -5.92 kJ/mol [37] and it is lower also than the value of -7.3 kJ/mol estimated [23] for the beginning of bilayer

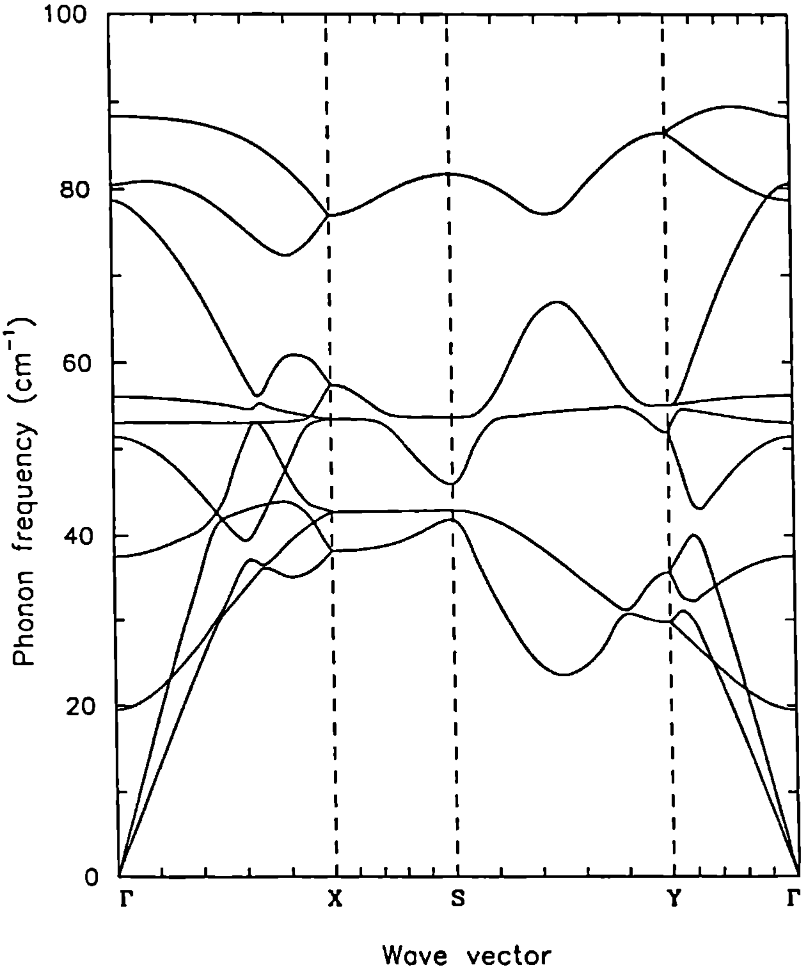

Fig. 3. Phonon/libron dispersion curves for an incommensurate N_2 herringbone monolayer on graphite from TDH calculations ($\alpha_{max} = 4$) with the uncorrugated ($g = 0$) molecule-substrate potential. Lattice constants $a = 4.15$ Å, $b = 6.87$ Å.

formation. So we conclude that the incommensurate monolayer may adopt the pin-wheel ordering at higher pressures.

The phonon and libron dispersion curves for the optimized incommensurate herringbone layer with $a = 4.15$ Å, $b = 6.87$ Å and $s = 14.25$ Å^2 are shown in Fig. 3 and the optical ($q = 0$) frequencies are listed in Table IV. Although some of the avoided crossings occur at different points in the Brillouin zone, Fig. 3 is qualitatively not so different from Fig. 2. The frequencies of the in-plane modes are considerably higher,

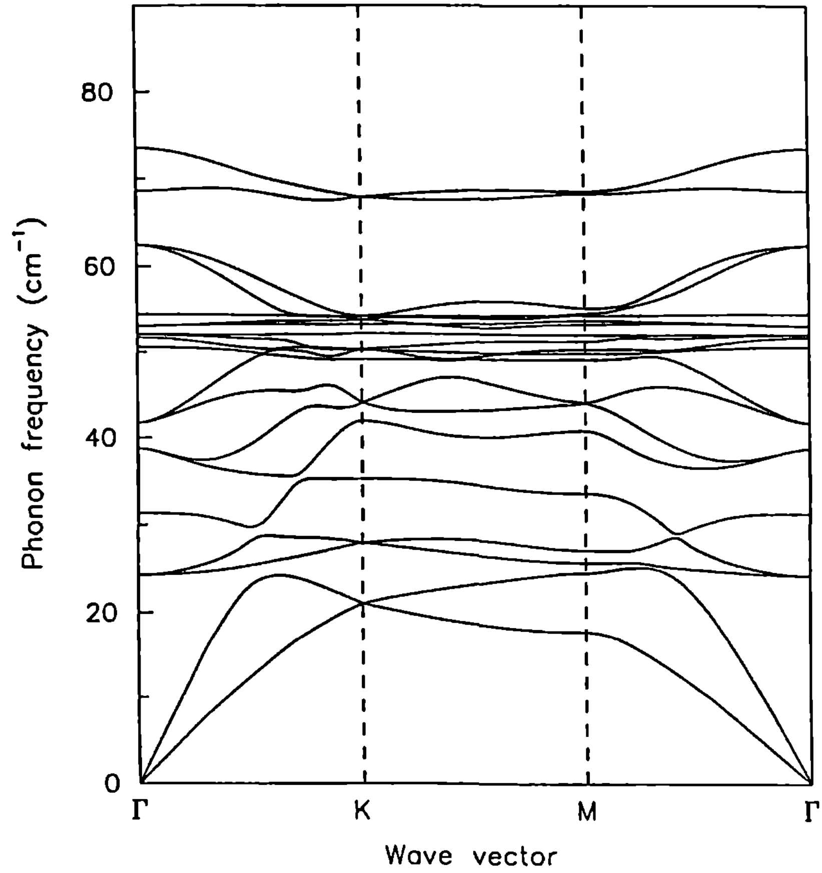

Fig. 4. Phonon/libron dispersion curves for an incommensurate N_2 pin-wheel monolayer on graphite from TDH calculations ($\alpha_{max} = 4$) with the uncorrugated ($g = 0$) molecule-substrate potential. Nearest neighbor distance $a = 4.057$ Å. Symmetry group $p6$, Brillouin zone points $\Gamma = (0,0)$, $K = (2\pi/3a, 0)$ and $M = (\pi/2a, \pi/2a\sqrt{3})$.

however, and their dispersion is larger, due to the compression of the adsorbed layer. Note that there is no phonon gap for $q = 0$, of course, since there is no corrugation in the molecule-substrate potential. The anharmonic frequency shifts are similar to those discussed for the commensurate monolayer, but slightly larger. Especially the large downward shift of the lowest out-of-plane libration is noticeable. The low frequency of this libration and its large anharmonicity are the signs of this mode becoming soft and the molecules wanting to rotate out of the plane at still higher pressures. The phonon and libron curves for the pin-wheel structure are drawn in Fig. 4 and the character of the modes for $q = 0$ is indicated in Table V. Due to the different symmetry and the fact that this structure contains two distinct types of molecules the resulting picture is rather different from the dispersion curves for the herringbone layer. We observe also that the frequencies are much lower, although the calculations leading to Figs. 3 and 4 have been performed for the same surface per molecule ($s = 14.25$ Å^2). This is related to the pressure which is substantially lower for the pin-wheel ordering than for the herringbone structure. To our knowledge the phonon frequencies for the incommensurate monolayers have not been measured yet.

Acknowledgement

We thank Wilfred Janssen, Thijs Bongers and Henri de Bekker for their assistance with the calculations. The investigations were supported in part by the Netherlands Foundation for Chemical Research (SON) with financial aid from the Netherlands Organization for Scientific Research (NWO). Part of this work has been performed as an IBM/ACIS project.

Appendix A

In Ref. [37] the intermolecular potential given by Eq. (2) is written as a double Taylor expansion in the center-of-mass displacements $\boldsymbol{u}_p$ and $\boldsymbol{u}_{p'}$. Here, we derive a similar expansion in a form that is amenable to much faster numerical calculation. First we expand the part of the potential that depends on the displacements as a Taylor series in $\boldsymbol{u}_{pp'} = \boldsymbol{u}_{p'} - \boldsymbol{u}_p$

$$\varphi_l(r_{pp'})C^{(l_3)}_{m_3}(\hat{\boldsymbol{r}}_{pp'}) = \sum_{\alpha=0}^{\infty} \frac{(\boldsymbol{u}_{pp'}\cdot\nabla)^{\alpha}}{\alpha!}\varphi_l(R_{pp'})C^{(l_3)}_{m_3}(\hat{\boldsymbol{R}}_{pp'}). \tag{A1}$$

We can evaluate this expression by means of the gradient formula in spherical tensor form [53]

$$\begin{aligned}\boldsymbol{u}_{pp'}\cdot\nabla\varphi_l(R_{pp'})C^{(l_3)}_{m_3}(\hat{\boldsymbol{R}}_{pp'}) ={}& u_{pp'}\sum_{k_1} A_{l_3k_1}(R_{pp'})\varphi_l(R_{pp'})(-1)^{m_3} \\ &\times\sum_{n_1n_2}\begin{pmatrix}1 & k_1 & l_3\\ n_1 & n_2 & -m_3\end{pmatrix} C^{(1)}_{n_1}(\hat{\boldsymbol{u}}_{pp'})C^{(k_1)}_{n_2}(\hat{\boldsymbol{R}}_{pp'}),\end{aligned} \tag{A2}$$

where the operator $A_{l_3k_1}(R_{pp'})$ is given by

$$\begin{aligned}A_{l_3k_1}(R_{pp'}) ={}&(-1)^{l_3}\left\{\delta_{k_1,l_3-1}\left[\frac{l_3(2l_3-1)}{2l_3+1}\right]^{1/2}\left(\frac{d}{dR_{pp'}}+\frac{l_3+1}{R_{pp'}}\right)\right. \\ &\left.-\,\delta_{k_1,l_3+1}\left[\frac{(l_3+1)(2l_3+3)}{2l_3+1}\right]^{1/2}\left(\frac{d}{dR_{pp'}}-\frac{l_3}{R_{pp'}}\right)\right\}.\end{aligned} \tag{A3}$$

The use of this relation in Eq. (A1) gives

$$\begin{aligned}\varphi_l(r_{pp'})C^{(l_3)}_{m_3}(\hat{\boldsymbol{r}}_{pp'}) =&\sum_{\alpha}\frac{(u_{pp'})^{\alpha}}{\alpha!}\sum_{k_1k_2}{}^{l}W^{(\alpha)}_{k_1k_2}(R_{pp'})\\ &\times\sum_{n_1n_2}(-1)^{m_3}\begin{pmatrix}k_1 & k_2 & l_3\\ n_1 & n_2 & -m_3\end{pmatrix}C^{(k_1)}_{n_1}(\hat{\boldsymbol{u}}_{pp'})C^{(k_2)}_{n_2}(\hat{\boldsymbol{R}}_{pp'}).\end{aligned}\tag{A4}$$

The coefficients ${}^{l}W^{(\alpha)}_{k_1k_2}(R_{pp'})$ can be calculated with the following recursion relation

$$\begin{aligned}{}^{l}W^{(\alpha)}_{k_1k_2}(R_{pp'}) =&(2k_1+1)(-1)^{l_3+1}\sum_{j_1j_2}\begin{pmatrix}j_1 & 1 & k_1\\ 0 & 0 & 0\end{pmatrix}\begin{Bmatrix}k_2 & k_1 & l_3\\ j_1 & j_2 & 1\end{Bmatrix}\\ &\times A_{j_2k_2}(R_{pp'})\,{}^{l}W^{(\alpha-1)}_{j_1j_2}(R_{pp'}),\end{aligned}\tag{A5}$$

with

$${}^{l}W^{(0)}_{k_1k_2}(R_{pp'}) = \delta_{k_1,0}\delta_{k_2,l_3}\sqrt{2l_3+1}\;\varphi_l(R_{pp'})\tag{A6}$$

while the expression in curly braces is a 6-j coefficient.

Now we can split $(u_{pp'})^{\alpha}C^{(k_1)}_{n_1}(\hat{\boldsymbol{u}}_{pp'})$ in factors dependent on the molecular displacements $\boldsymbol{u}_p$ and $\boldsymbol{u}_{p'}$ [54]

$$\begin{aligned}(u_{pp'})^{\alpha}C^{(k_1)}_{n_1}(\hat{\boldsymbol{u}}_{pp'}) =& \sum_{\alpha_1=0}^{\alpha}\sum_{\lambda_1=0}^{\alpha_1}\sum_{\lambda_2=|k_1-\lambda_1|}^{\min(k_1+\lambda_1,\alpha_2)}\sum_{\mu_1}\sum_{\mu_2}B^{\alpha k_1 n_1}_{\alpha_1\lambda_1\mu_1\alpha_2\lambda_2\mu_2}\\ &\times(u_p)^{\alpha_1}C^{(\lambda_1)}_{\mu_1}(\hat{\boldsymbol{u}}_p)(u_{p'})^{\alpha_2}C^{(\lambda_2)}_{\mu_2}(\hat{\boldsymbol{u}}_{p'}),\end{aligned}\tag{A7}$$

where α_2 is given by $\alpha_2 = \alpha - \alpha_1$ and the coefficients are

$$\begin{aligned}B^{\alpha k_1 n_1}_{\alpha_1\lambda_1\mu_1\alpha_2\lambda_2\mu_2} =&(-1)^{\lambda_1+n_1}\frac{(\alpha+k_1+1)!!(\alpha-k_1)!!(2\lambda_1+1)(2\lambda_2+1)}{(\alpha_1+\lambda_1+1)!!(\alpha_1-\lambda_1)!!(\alpha_2+\lambda_2+1)!!(\alpha_2-\lambda_2)!!}\\ &\times\begin{pmatrix}k_1 & \lambda_1 & \lambda_2\\ 0 & 0 & 0\end{pmatrix}\begin{pmatrix}k_1 & \lambda_1 & \lambda_2\\ -n_1 & \mu_1 & \mu_2\end{pmatrix}.\end{aligned}\tag{A8}$$

Introducing this into Eq. (2) and Eq. (A4), the intermolecular potential reads

$$\begin{aligned}\Phi_{pp'}(\boldsymbol{u}_p,\omega_p,\boldsymbol{u}_{p'},\omega_{p'}) =&\sum_{\Lambda_1}\sum_{\Lambda_2}(u_p)^{\alpha_1}C^{(\lambda_1)}_{\mu_1}(\hat{\boldsymbol{u}}_p)C^{(l_1)}_{m_1}(\omega_p)X_{\Lambda_1\Lambda_2}(\boldsymbol{R}_{pp'})\\ &\times(u_{p'})^{\alpha_2}C^{(\lambda_2)}_{\mu_2}(\hat{\boldsymbol{u}}_{p'})C^{(l_2)}_{m_2}(\omega_{p'}),\end{aligned}\tag{A9}$$

where Λ stands for the set of indices $\{\alpha,\lambda,\mu,l,m\}$, and $X_{\Lambda_1\Lambda_2}$ is given by

$$\begin{aligned}X_{\Lambda_1\Lambda_2}(\boldsymbol{R}_{pp'}) =& \sum_{l_3m_3}\begin{pmatrix}l_1 & l_2 & l_3\\ m_1 & m_2 & m_3\end{pmatrix}\sum_{k_1k_2}{}^{l}W^{(\alpha_1+\alpha_2)}_{k_1k_2}(R_{pp'})\sum_{n_1}\sum_{n_2}(-1)^{m_3}\\ &\times\begin{pmatrix}k_1 & k_2 & l_3\\ n_1 & n_2 & -m_3\end{pmatrix}C^{(k_2)}_{n_2}(\hat{\boldsymbol{R}}_{pp'})B^{\alpha_1+\alpha_2 k_1 n_1}_{\alpha_1\lambda_1\mu_1\alpha_2\lambda_2\mu_2}.\end{aligned}\tag{A10}$$

This expansion is considerably simpler than that given in Ref. [37] because only one recurrence relation is needed for the coefficients ${}^{l}W^{(\alpha)}_{k_1k_2}(R_{pp'})$, instead of two.

Appendix B

The TDH method can be derived [37,41] by looking at the response of a system to a time-dependent perturbation. It is assumed that this perturbation can be represented by a sum of single-particle operators $h_p^k(t)$ and that the perturbed density operator is a product of single-particle density operators $d_p^k(t) = d_p^k + \delta_p^k(t)$. The density operators d_p^k correspond to the unperturbed MF model and the operators $\delta_p^k(t)$ describe the response of the system to the perturbation. The column vectors $\boldsymbol{h}(\boldsymbol{q},\omega)$ and $\boldsymbol{\delta}(\boldsymbol{q},\omega)$ contain the space-time Fourier transforms of the transition matrix elements of the single-particle operators $h_p^k(t)$ and $\delta_p^k(t)$ in a (finite) basis of MF states $\psi_p^{k,a}$

$$h_{ikab}(\boldsymbol{q},\omega) = (2\pi N)^{-1/2} \int dt \exp(i\omega t) \sum_n \exp(i\boldsymbol{q}\cdot\boldsymbol{R}_p)\langle \psi_p^{k,a} | h_p^k(t) | \psi_p^{k,b}\rangle \tag{B1}$$

and

$$\delta_{ikab}(\boldsymbol{q},\omega) = (2\pi N)^{-1/2} \int dt \exp(i\omega t) \sum_n \exp(i\boldsymbol{q}\cdot\boldsymbol{R}_p)\langle \psi_p^{k,a} | \delta_p^k(t) | \psi_p^{k,b}\rangle \ . \tag{B2}$$

As shown in Ref. [37] the Liouville equation, which describes the time evolution of the density operator, reduces in first order to the linear response equation

$$[\omega - \boldsymbol{M}(\boldsymbol{q})]\boldsymbol{\delta}(\boldsymbol{q},\omega) = -\boldsymbol{P}\boldsymbol{h}(\boldsymbol{q},\omega) \ . \tag{B3}$$

The density operator difference matrix $\boldsymbol{P}$ is given by Eq. (15) and the matrix $\boldsymbol{M}(\boldsymbol{q})$ by Eq. (13). The TDH (de-)excitation energies are the eigenvalues of the matrix $\boldsymbol{M}(\boldsymbol{q})$.

The response properties of the system as given by Eq. (B3) can also be expressed by the generalized susceptibility $\chi(\boldsymbol{q},\omega)$. To that end, we define the perturbation $h_p^k(t)$ as the action of an external field with components $E_p^{k,\nu}(t)$ on the dynamical variables $Q_p^{k,\nu}$, see Eq. (7). For the Fourier component with frequency ω and wave vector $\boldsymbol{q}$ this yields, in matrix form

$$\boldsymbol{h}(\boldsymbol{q},\omega) = -\boldsymbol{Q}\boldsymbol{E}(\boldsymbol{q},\omega) \ , \tag{B4}$$

where the matrix $\boldsymbol{Q}$ is given by Eq. (16). When the response of the system is also expressed in terms of the dynamical variables

$$\boldsymbol{Y}(\boldsymbol{q},\omega) = \tilde{\boldsymbol{Q}}^{\mathrm{T}}\boldsymbol{\delta}(\boldsymbol{q},\omega) \tag{B5}$$

and the generalized susceptibility $\chi(\boldsymbol{q},\omega)$ is defined by

$$\boldsymbol{Y}(\boldsymbol{q},\omega) = \chi(\boldsymbol{q},\omega)\boldsymbol{E}(\boldsymbol{q},\omega) \tag{B6}$$

then it follows from Eq. (B3) that

$$\chi(\boldsymbol{q},\omega) = \tilde{\boldsymbol{Q}}^{\mathrm{T}}[\omega - \boldsymbol{M}(\boldsymbol{q})]^{-1}\boldsymbol{P}\boldsymbol{Q} \ . \tag{B7}$$

The TDH (de-)excitation energies of the system, *i.e.* the eigenvalues of the matrix $\boldsymbol{M}(\boldsymbol{q})$, correspond with the poles of the susceptibility $\chi(\boldsymbol{q},\omega)$. Analogously, we define the MF single-particle susceptibility by

$$\chi^{(0)}(\omega) = \tilde{\boldsymbol{Q}}^{\mathrm{T}}\left[\omega - \boldsymbol{\epsilon}\right]^{-1}\boldsymbol{P}\boldsymbol{Q}\ , \tag{B8}$$

where the matrix $\boldsymbol{\epsilon}$ contains the MF (de-)excitation energies, see Eq. (14). If we insert Eq. (13) for $\boldsymbol{M}(\boldsymbol{q})$ into the linear response equation (B3), multiply the latter by $\tilde{\boldsymbol{Q}}^{\mathrm{T}}(\omega - \boldsymbol{\epsilon})^{-1}$ and substitute Eqs. (B4), (B5) and (B8) we obtain

$$[\boldsymbol{I} + \chi^{(0)}(\omega)\boldsymbol{W}(\boldsymbol{q})]\boldsymbol{Y}(\boldsymbol{q},\omega) = \chi^{(0)}(\omega)\boldsymbol{E}(\boldsymbol{q},\omega)\ . \tag{B9}$$

Comparing this result with Eq. (B6) we find that the relation between the collective TDH susceptibility $\chi(\boldsymbol{q},\omega)$ and the single-particle MF susceptibility $\chi^{(0)}(\omega)$ is given by the Dyson equation, Eq. (20).

In considerations about orientational order/disorder phase transitions [42,43] the rotational MF Hamiltonians are replaced by free rotor Hamiltonians, with well-known eigenstates. The rotational single-particle susceptibility $\chi^{(0)}(\omega)$ can then be evaluated relatively simply, in some models even analytically. The translational susceptibility is usually approximated by the analytical formula for harmonic oscillators. At higher temperatures, these susceptibilities are sometimes calculated within the classical approximation [42]. Cubic and quartic terms in the lattice Hamiltonian, Eq. (8), are neglected and only the lowest order dynamical variables for the rotations, see Eq. (7), are retained. This yields a simplified coupling matrix $\boldsymbol{W}(\boldsymbol{q})$ which does not depend on averaged dynamical variables as occurring in Eq. (18). In our calculations we avoid such approximations. The accuracy to which Eq. (20) is equivalent to TDH is only limited by the use of a finite basis.

References

[1] T.T. Chung and J.G. Dash, Surf. Sci. **66**, 559 (1977).

[2] A.D. Migone, H.K. Kim, M.H.W. Chan, J. Talbot, D.J. Tildesley and W.A. Steele, Phys. Rev. Lett. **51**, 192 (1983).

[3] Q.M. Zhang, H.K. Kim and M.H.W. Chan, Phys. Rev. **B33**, 413 (1986).

[4] Q.M. Zhang, H.K. Kim and M.H.W. Chan, Phys. Rev. **B32**, 1820 (1985).

[5] Y. Larher, J. Chem. Phys. **68**, 2257 (1978).

[6] R.D. Diehl and S.C. Fain, Surf. Sci. **125**, 116 (1983).

[7] J.K. Kjems, L. Passell, H. Taub, J.G. Dash and A.D. Novaco, Phys. Rev. **B13**, 1446 (1976).

[8] J. Eckert, W.D. Ellenson, J.B. Hastings and L. Passell, Phys. Rev. Lett. **43**, 1329 (1979).

[9] R. Wang, S.K. Wang, H. Taub, J.C. Newton and H. Schechter, Phys. Rev. **B35**, 5841 (1987).

[10] S.K. Wang, J.C. Newton, R. Wang, H. Taub, J.R. Dennison and H. Schechter, Phys. Rev. **B39**, 10331 (1989).

[11] K. Morishige, C. Mowforth and R.K. Thomas, Surf. Sci. **151**, 289 (1985).

[12] M. Nielsen, K. Kjaer, J. Bohr and J.P. McTague, J. Electron Spectrosc. Relat. Phenom. **30**, 111 (1983).

[13] V.L.P. Frank, H.J. Lauter and P. Leiderer, in *Phonons 89*, Eds. S. Hunklinger *et al.*, World Scientific, Singapore (1990), p. 913.

[14] V.L.P. Frank, H.J. Lauter, F.Y. Hansen, H. Taub, L.W. Bruch and J.R. Dennison, in *Phonons 89*, Eds. S. Hunklinger *et al.*, World Scientific, Singapore (1990), p. 922.

[15] F.Y. Hansen, V.L.P. Frank, H. Taub, L.W. Bruch, H.J. Lauter and J.R. Dennison, Phys. Rev. Lett. **64**, 764 (1990).

[16] K.B. Gibson, S.J. Sibener, B.M. Hall, D.L. Mills and J.E. Black, J. Chem. Phys. **83**, 4256 (1985).

[17] D. Eichenauer, U. Harten, J.P. Toennies and V. Celli, J. Chem. Phys. **86**, 3693 (1987).

[18] K. Kern and G. Comsa, Advan. Chem. Phys. **76**, 211 (1989).

[19] L.W. Bruch, J. Chem. Phys. **79**, 3148 (1983).

[20] C.R. Fuselier, N.S. Gillis and J.C. Raich, Solid State Commun. **25**, 747 (1978).

[21] G. Cardini and S.F. O'Shea, Surf. Sci. **154**, 231 (1985).

[22] D.J. Tildesley and R.M. Lynden-Bel!, J. Chem. Soc. Faraday Trans. (II) **82**, 1605 (1986).

[23] S.E. Roosevelt and L.W. Bruch, Phys. Rev. **B41** 12236 (1990).

[24] B. Kuchta and R.D. Etters, Phys. Rev. **B36**, 3400 (1987).

[25] B. Kuchta and R.D. Etters, Phys. Rev. **B36**, 3407 (1987).

[26] B. Kuchta and R.D. Etters, J. Chem Phys. **88**, 2793 (1988).

[27] C. Peters and M.L. Klein, Phys. Rev. **B32**, 6077 (1985).

[28] C. Peters and M.L. Klein, Mol. Phys. **54**, 895 (1985).

[29] Y.P. Yoshi and D.J. Tildesley, Mol. Phys. **55**, 999 (1985).

[30] J. Talbot, D.J. Tildesley and W.A. Steele, Mol. Phys. **51**, 1331 (1984).

[31] J. Talbot, D.J. Tildesley and W.A. Steele, Surf. Sci. **169**, 71 (1986).

[32] H. You and S.C. Fain, Faraday Discuss. Chem. Soc. (London) **80**, 159 (1985).

[33] R.M. Berns and A. van der Avoird, J. Chem. Phys. **72**, 6107 (1980).

[34] A. van der Avoird, P.E.S. Wormer, F. Mulder and R. Berns, Topics Curr. Chem. **93**, 1 (1980).

[35] A.P.J. Jansen, W.J. Briels and A. van der Avoird, J. Chem. Phys. **81**, 3648 (1984).

[36] A. van der Avoird, W.J. Briels and A.P.J. Jansen, J. Chem. Phys. **81**, 3658 (1984).

[37] W.J. Briels, A.P.J. Jansen and A. van der Avoird, J. Chem. Phys. **81**, 4118 (1984).

[38] A.P.J. Jansen and R. Schoorl, Phys. Rev. **B38**, 11711 (1988).

[39] T.H.M. van den Berg, M.M.G. Bongers and A. van der Avoird, J. Phys.: Condens. Matter **2**, 8015 (1990).

[40] W.A. Steele, J. Phys. (Paris) **38**, C4-61 (1978).

[41] D.R. Fredkin and N.R. Werthamer, Phys. Rev. **A138**, 1527 (1965).

[42] J.C. Raich, H. Yasuda and E.R. Bernstein, J. Chem. Phys. **78**, 6209 (1983).

[43] B. de Raedt and K.H. Michel, Phys. Rev. **B19**, 767 (1979).

[44] D.N. Zubarev, *Nonequilibrium Statistical Thermodynamics*, Consultants Bureau, New York (1974).

[45] T.H.M. van den Berg and A. van der Avoird, Phys. Rev. **B40**, 1932 (1989).

[46] D.A. Goodings and H. Henkelman, Can. J. Phys. **49**, 2898 (1971).

[47] J.K. Kjems and G. Dolling, Phys. Rev. **B11**, 1639 (1975).

[48] B.C. Kohin, J. Chem. Phys. **33**, 882 (1960).

[49] D.M. Brink and G.R. Satchler, *Angular Momentum*, Clarendon, Oxford (1975).

[50] W.A. Steele, Surf. Sci. **36**, 317 (1973).

[51] R.D. Diehl and S.C. Fain, J. Chem. Phys. **77**, 5065 (1982).

[52] R.D. Diehl and S.C. Fain, Phys. Rev. **B26**, 4785 (1982).

[53] A.R. Edmonds, *Angular Momentum in Quantum Mechanics*, Princeton University Press, Princeton, New Jersey (1957).

[54] K.G. Kay, H.D. Todd and H.J. Silverstone, J. Chem. Phys. **51**, 2359 (1969).

8. Phonons and rotons in commensurate p-H_2 and o-D_2 monolayers on graphite

W.B.J.M. Janssen, T.H.M. van den Berg and A. van der Avoird

Institute of Theoretical Chemistry, University of Nijmegen, Toernooiveld, Nijmegen, The Netherlands

(Accepted for publication in Phys. Rev. B (1991))

Abstract. For the commensurate $(\sqrt{3} \times \sqrt{3})\, R\, 30°$ phase of p-H_2 and o-D_2 on graphite we have calculated the phonon and roton band structure by the time-dependent Hartree method. A basis of three-dimensional harmonic-oscillator functions (up to $n = 8$ inclusive) is used for the translational vibrations and a basis of spherical harmonics for the weakly hindered rotations. The anisotropic potential between the molecules in the adsorbed layer is taken from *ab initio* calculations. An anisotropic molecule-substrate potential is modelled semi-empirically. Both potentials are explicitly expanded with respect to the molecular displacements, with the inclusion of high anharmonic terms, and with respect to their anisotropy. Moreover, the molecule-substrate potential is Fourier expanded to expose the effects of the surface corrugation. The structure of the in-plane phonon band agrees well with the data available from inelastic neutron scattering. For the peak which has been ascribed previously to the out-of-plane phonon band we suggest an alternative assignment. For the rotons we have derived, both numerically and analytically, the dependence of the band structure on the (unknown) anisotropy of the molecule-substrate potential.

8.1. Introduction

A subject that has aroused interest recently is the structure and dynamics of H_2 and D_2 layers physisorbed on the basal plane of graphite. A variety of adsorbed phases and transitions between these phases have been identified by means of low energy electron diffraction (LEED), neutron diffraction and specific heat measurements [1-9]. For the commensurate $(\sqrt{3} \times \sqrt{3})\, R\, 30°$ phase, which occurs up to 1.08 monolayer coverage for H_2 and up to 1.05 monolayer coverage for D_2, at temperatures below 20 K, also the dynamics has been investigated by inelastic neutron scattering (INS) [10-15]. Although it was not possible to study single crystals and thus to measure directly the full two-dimensional phonon dispersion curves, an elegant experimental setup and interpretation allowed the determination of phonon frequencies for different points in the two-dimensional Brillouin zone.

The motions and stability of these H_2 and D_2 overlayers on graphite are determined by an interplay between the intermolecular interactions in the adsorbed layers and the interactions of the adsorbed molecules with the periodic substrate. The $(\sqrt{3} \times \sqrt{3})\, R\, 30°$

phase can be considered as a two-dimensional molecular crystal with a nearest neighbor distance of 4.26 Å (which is substantially larger than the nearest neighbor distances of 3.79 Å and 3.61 Å in bulk hydrogen and deuterium). Because of this large lattice spacing and the small masses of H_2 and D_2 the molecules exert large, and probably strongly anharmonic, zero-point motions. The quantum nature of these systems is most evident from the molecular rotations, however. One expects to find nearly free rotations of the molecules in the layers, characterized by quantum numbers j and m. Even values of j occur for p-H_2 and o-D_2, odd j values for o-H_2 and p-D_2. Due to the large rotational energy splittings between different j states the molecular rotations are just weakly perturbed by the anisotropic environment and weakly coupled by anisotropic intermolecular interactions. So the ground state of p-H_2 and o-D_2 is orientationally disordered with nearly spherical ($j = 0$) molecules and collective rotational excitations to a $j = 2$ roton band. Also o-H_2 and p-D_2 are orientationally disordered, except at very low temperatures [16,17] where the $j = 1$ ground state is split into states with $m = 0$ and $m = \pm 1$. Most experimental studies [1-15] concern these orientationally disordered phases of *para*, *ortho* or mixed (normal) hydrogen and deuterium layers.

It will be obvious from these considerations that the standard (harmonic) lattice dynamics method and the classical molecular dynamics (MD) method which are usually applied to the ordered and disordered phases of molecular crystals and, more recently, also to adsorbed layers, cannot be applied here. Gotlieb and Bruch [18,19] have calculated the vibrational ground state of H_2 and D_2 layers adsorbed on graphite by a variational Quantum Monte Carlo method. Their vibrational wave function was a product of single-molecule functions for the center-of-mass vibrations, multiplied by a Jastrow function to account for the correlation between these vibrations. The molecules were assumed to be effectively spherical and, thus, to interact via an isotropic pair-potential. The center-of-mass vibrations were restricted to be planar, *i.e.* parallel to the graphite surface. Novaco [20] has shown that it is essential to include also the displacements of the molecules perpendicular to the surface, even if one is primarily interested in their vibrations in the parallel directions. He has calculated the dispersion relations for the in-plane phonons in commensurate H_2 and D_2 layers on graphite by means of the self-consistent phonon (SCP) method and found the results to be in good agreement with the available INS data [10-15]. Also in this calculation it was assumed that the H_2 and D_2 molecules are effectively spherical and interact via isotropic potentials. This assumption was verified by Novaco and Wroblewski [21] who calculated the single-molecule rotational states in H_2, HD and D_2 layers on graphite in the anisotropic field originating from the substrate. The anisotropic interactions between the adsorbed molecules were neglected, however.

In the present calculations for commensurate $(\sqrt{3} \times \sqrt{3})\,R\,30°$ layers of H_2 and D_2 on the basal plane of graphite we compute both the in-plane and the out-of-plane phonon states, as well as the collective rotational (roton) states and their coupling to the phonon states (which appears to be small indeed). We use the full anisotropic intermolecular potential for hydrogen from *ab initio* calculations [22,23]. For the molecule-substrate interaction we construct an anisotropic model potential which generalizes the isotropic H_2-graphite potential obtained from selective adsorption measurements [24,25] (in the same way as Novaco and Wroclewski did [21]). Phonon-, roton-, and possibly mixed, states are calculated by means of the time-dependent Hartree (TDH) method. Basis functions at the first (mean-field) level of this calculation are the free rotor functions of H_2 or D_2 (spherical harmonics) and three-dimensional harmonic oscillator functions for the center-of-mass vibrations of the molecules. This TDH method with the same *ab initio* H_2-H_2 potential has been applied previously to H_2 and D_2 solids [26]. It was found, even for the smaller nearest neighbor separations that occur in these bulk solids, that the use of Jastrow functions for the correlation between the center-of-mass vibrations could be avoided if the full anharmonicity of the intermolecular potential was included and the harmonic oscillator basis for these center-of-mass vibrations was sufficiently large, so that the wave functions at the mean-field level could adapt to this anharmonicity. Results are presented for commensurate p-H_2 and o-D_2 layers on graphite; in a forthcoming paper we will discuss results for o-H_2 and p-D_2 overlayers.

8.2. Theory

8.2.1. The Hamiltonian

The center-of-mass positions of the molecules in the adsorbed layer are denoted by $\boldsymbol{r}_p = \boldsymbol{R}_p + \boldsymbol{u}_p$, where $\boldsymbol{R}_p$ are the equilibrium positions and $\boldsymbol{u}_p$ the displacements of the molecules p. The orientations of the molecules are described by a set of polar angles $\boldsymbol{\omega}_p$. We assume that the motions of the molecules in the adsorbed layer are separable from the graphite lattice vibrations which have much higher frequencies and small amplitudes. We use a rigid graphite substrate, so that the molecule-substrate potential V_p for a given molecule p depends only on the coordinates $\boldsymbol{u}_p$ and $\boldsymbol{\omega}_p$ of that molecule. The pair potential between the molecules within the adsorbed layer is denoted by $\Phi_{pp'}$. Many-body interactions, as well as substrate-mediated interactions between the adsorbed molecules are neglected. Then, the Hamiltonian for the adsorbed layer is given by

$$H = \sum_p T(\boldsymbol{u}_p) + \sum_p L(\boldsymbol{\omega}_p) + \sum_p V_p(\boldsymbol{u}_p, \boldsymbol{\omega}_p) + \tfrac{1}{2} \sum_p \sum_{p' \neq p} \Phi_{pp'}(\boldsymbol{u}_p, \boldsymbol{\omega}_p, \boldsymbol{u}_{p'}, \boldsymbol{\omega}_{p'}) \ . \quad (1)$$

It contains the kinetic-energy terms for the translational center-of-mass motions T and the rotational motions L of the molecules, the molecule-substrate potential and the intermolecular potential.

In the mean-field formalism the translational and rotational Hamiltonians are given by

$$H_p^T(\boldsymbol{u}_p) = T(\boldsymbol{u}_p) + \langle V_p(\boldsymbol{u}_p, \boldsymbol{\omega}_p) \rangle^{L_p} + \sum_{p' \neq p} \langle \Phi_{pp'}(\boldsymbol{u}_p, \boldsymbol{\omega}_p, \boldsymbol{u}_{p'}, \boldsymbol{\omega}_{p'}) \rangle^{L_p L_{p'} T_{p'}} \quad (2a)$$

$$H_p^L(\omega_p) = L(\omega_p) + \langle V_p(u_p, \omega_p)\rangle^{T_p} + \sum_{p' \neq p} \langle \Phi_{pp'}(u_p, \omega_p, u_{p'}, \omega_{p'})\rangle^{L_{p'}T_pT_{p'}} \tag{2b}$$

where $\langle X\rangle^{K_p}$ means the thermodynamic average of an operator X over the eigenstates of H_p^K with $K = T$ or L. From these equations it follows that the translational and rotational Hamiltonians are coupled and we have to solve the problem in an iterative way. The translational Hamiltonian is diagonalized in a basis of three-dimensional spherical harmonic-oscillator functions [27]. The basis for the rotational Hamiltonian consists of tesseral harmonics (real combinations of spherical harmonics).

The single-molecule eigenstates for the translations and rotations can then be used to calculate the collective excitations of the adsorbed layer. For this purpose we use the time-dependent Hartree (TDH) method [27,28], which at zero temperature is equivalent to the random-phase approximation (RPA). In the TDH method the excitation energies are the eigenvalues of the matrix

$$M(q) = \begin{pmatrix} \chi - P\Phi(q) & -P\Phi(q) \\ P\Phi(q) & -\chi + P\Phi(q) \end{pmatrix} . \tag{3}$$

The diagonal matrices χ and P contain the mean-field excitation energies and the mean-field population differences

$$\chi_{abiK;a'b'i'K'} = \delta_{aa'}\delta_{bb'}\delta_{ii'}\delta_{KK'}(\varepsilon_{iK}^{(a)} - \varepsilon_{iK}^{(b)}) \tag{4}$$

$$P_{abiK;a'b'i'K'} = \delta_{aa'}\delta_{bb'}\delta_{ii'}\delta_{KK'}(P_{iK}^{(a)} - P_{iK}^{(b)}) \tag{5}$$

$\varepsilon_{iK}^{(a)}$ is the mean-field energy of excitation level a of a molecule of sublattice i and $K = T$ or L. The population of this excitation level is given by

$$P_{iK}^{(a)} = \frac{\exp(-\beta\varepsilon_{iK}^{(a)})}{\sum_b \exp(-\beta\varepsilon_{iK}^{(b)})} \tag{6}$$

with $\beta = (kT)^{-1}$.

The matrix $\Phi(q)$ describes the coupling between the mean-field excitations on different molecules, as well as translation-rotation coupling

$$\begin{aligned} \Phi_{abiK;a'b'i'K'}(q) = & \sum_n \exp(iq \cdot R_n) \left\langle \psi_{iK}^{(a)}\psi_{i'K'}^{(b')} \middle| \langle \Phi_{\{0,i\}\{n,i'\}}\rangle^{iK_c;i'K'_c} \middle| \psi_{iK}^{(b)}\psi_{i'K'}^{(a')} \right\rangle \\ & + \delta_{ii'}\delta_{KK'_c} \sum_{n''}\sum_{i''} \left\langle \psi_{iK}^{(a)}\psi_{iK_c}^{(b')} \middle| \langle \Phi_{\{0,i\}\{n'',i''\}}\rangle^{i''K;i''K_c} \middle| \psi_{iK}^{(b)}\psi_{iK_c}^{(a')} \right\rangle \\ & + \delta_{ii'}\delta_{KK'_c} \left\langle \psi_{iK}^{(a)}\psi_{iK_c}^{(b')} \middle| V_{\{0,i\}} \middle| \psi_{iK}^{(b)}\psi_{iK_c}^{(a')} \right\rangle \end{aligned} \tag{7}$$

where $\psi_{iK}^{(a)}$ is the mean-field wave function corresponding with $\varepsilon_{iK}^{(a)}$; q is the wave vector of the collective excitation, n and n'' label the unit cells and K_c is the complement of K. The TDH matrix contains elements with $K \neq K'$. These elements mix the translations and rotations so that the translation-rotation coupling which was neglected in the mean-field treatment is restored by the TDH method.

8.2.2. The intermolecular potential

The intermolecular potential is written in the form of a spherical expansion

$$\begin{aligned}\Phi_{pp'}(\boldsymbol{u}_p,\omega_p,\boldsymbol{u}_{p'},\omega_{p'}) = &\sum_{\boldsymbol{l}} \varphi_{\boldsymbol{l}}(r_{pp'}) \sum_{\boldsymbol{m}} \begin{pmatrix} l_1 & l_2 & l_3 \\ m_1 & m_2 & m_3 \end{pmatrix} \\ &\times C^{(l_1)}_{m_1}(\omega_p) C^{(l_2)}_{m_2}(\omega_{p'}) C^{(l_3)}_{m_3}(\hat{\boldsymbol{r}}_{pp'}) \, .\end{aligned} \tag{8}$$

The intermolecular vector is given by $\boldsymbol{r}_{pp'} = (\boldsymbol{R}_{p'} + \boldsymbol{u}_{p'}) - (\boldsymbol{R}_p + \boldsymbol{u}_p)$ and $\hat{\boldsymbol{r}}_{pp'}$ is the unit vector along $\boldsymbol{r}_{pp'}$. The Racah spherical harmonics $C^{(l)}_m(\omega)$ that describe the orientational dependence of the potential are coupled to a scalar function by the summation over $\boldsymbol{m} = \{m_1, m_2, m_3\}$, with the large parentheses denoting a 3-j symbol [29]. The first summation runs over $\boldsymbol{l} = \{l_1, l_2, l_3\}$ and the factors $\varphi_{\boldsymbol{l}}(r_{pp'})$ are the expansion coefficients that reflect the anisotropy of the potential. They will be specified in Sec. 8.3.

A Taylor expansion of the potential can be made in both the molecular displacements $\boldsymbol{u}_p$ and $\boldsymbol{u}_{p'}$, so that the potential becomes explicitly dependent on these displacements. This expansion is amply described in Refs. [26,27] and the resulting form of the potential looks as follows

$$\begin{aligned}\Phi_{pp'}(\boldsymbol{u}_p,\omega_p,\boldsymbol{u}_{p'},\omega_{p'}) = &\sum_{\Lambda_1} \sum_{\Lambda_2} (u_p)^{\alpha_1} C^{(\lambda_1)}_{\mu_1}(\hat{\boldsymbol{u}}_p) C^{(l_1)}_{m_1}(\omega_p) X_{\Lambda_1 \Lambda_2}(\boldsymbol{R}_{pp'}) \\ &\times (u_{p'})^{\alpha_2} C^{(\lambda_2)}_{\mu_2}(\hat{\boldsymbol{u}}_{p'}) C^{(l_2)}_{m_2}(\omega_{p'}) \, ,\end{aligned} \tag{9}$$

where Λ stands for the set of indices $\{\alpha, \lambda, \mu, l, m\}$ and the expression for $X_{\Lambda_1 \Lambda_2}(\boldsymbol{R}_{pp'})$ is given in Ref. [26]. The summation over α_1 and α_2 extends to $\alpha_1 + \alpha_2 \leq \alpha_{max}$, where α_{max} is equal to the order of the Taylor expansion in the displacements. An expansion with $\alpha_{max} = 2$, for instance, yields a potential $\Phi_{pp'}$ which is harmonic in the center-of-mass displacements $\boldsymbol{u}_p$ and $\boldsymbol{u}_{p'}$. In the present calculations we carry this expansion much further, see Sec. 8.3. For the summations over λ and μ holds: $0 \leq \lambda_i \leq \alpha_i$ and $-\lambda_i \leq \mu_i \leq \lambda_i$, where λ_i has the same parity as α_i. After this expansion we have a potential which is explicitly dependent on the displacement coordinates of the molecules and thus easy to use in lattice dynamics calculations.

8.2.3. The molecule-substrate potential

Following previous calculations [20,21], we consider the interaction V_p of a molecule p with the substrate as a sum of pair interactions between the molecule and the individual substrate atoms. The most general form for such molecule-atom interactions is of course a spherical expansion, *i.e.* a special case of Eq. (8). From selective adsorption measurements [24] only the first, isotropic, term in such an expansion is known, however. As we wish to investigate also the effects of the anisotropy in the molecule-substrate interaction, we model this interaction by the atom-atom model, which contains this anisotropy implicitly. So, we write

$$V_p(\boldsymbol{u}_p,\omega_p) = \sum_{C} \left[v\left(\mid \boldsymbol{R}_p + \boldsymbol{u}_p + \boldsymbol{a}(\omega_p) - \boldsymbol{R}_C \mid\right) + v\left(\mid \boldsymbol{R}_p + \boldsymbol{u}_p - \boldsymbol{a}(\omega_p) - \boldsymbol{R}_C \mid\right) \right] . \tag{10}$$

where the vectors $\boldsymbol{R}_C$ denote the positions of the carbon atoms C in the substrate and the orientation dependent vectors $\boldsymbol{a}(\omega_p)$ describe the positions of the hydrogen atoms with respect to the H_2 center-of-mass. Just as Novaco and Wroblewski [21] we choose an atom-atom potential $v(|\boldsymbol{r}|)$ of the Lennard-Jones type, which is parametrized in such a manner that the isotropic component of the resulting molecule-atom potential agrees with the isotropic potential from the selective adsorption measurements (see Sec. 8.3).

In Ref. [30] it is shown that the atom-atom interactions can be summed to an atom-substrate interaction with the aid of an analytical Fourier transformation. Next, a spherical expansion of the molecule-substrate interaction can be made to expose its anisotropy explicitly and, finally, a molecular-displacement expansion of the spherical expansion is used to make the molecule-substrate potential explicitly dependent on the displacement coordinates of the molecule [31]. The molecule-substrate potential can then be written in the following form

$$V_p(\boldsymbol{u}_p,\omega_p) = \sum_{\Lambda} F_\Lambda(\boldsymbol{R}_p)(u_p)^\alpha C_\mu^{(\lambda)}(\hat{\boldsymbol{u}}_p) C_m^{(l)}(\omega_p) \tag{11}$$

where again Λ indicates the set of indices $\{\alpha,\lambda,\mu,l,m\}$. The coefficients $F_\Lambda(\boldsymbol{R}_p)$ can be written as a two-dimensional Fourier series

$$F_\Lambda(\boldsymbol{R}_p) = \sum_{\boldsymbol{g}} \overline{F}_\Lambda(\boldsymbol{g} \mid z_p) \exp(i\boldsymbol{g}\cdot\boldsymbol{\tau}_p) \tag{12}$$

with $\boldsymbol{\tau}_p$ denoting the projection of $\boldsymbol{R}_p$ on the graphite basal plane (the xy-plane), so that $\boldsymbol{R}_p = \boldsymbol{\tau}_p + z_p\boldsymbol{e}_z$. The vector $\boldsymbol{g}$ is a vector in the two-dimensional reciprocal lattice of a substrate layer.

Analytical expressions for the expansion coefficients $\overline{F}_\Lambda(\boldsymbol{g} \mid z_p)$ are given in Ref. [31]. The terms with $\boldsymbol{g} = 0$ describe the flat (but anisotropic and anharmonic) potential which depends only on the height z_p of the molecules above the graphite surface, the terms with $\boldsymbol{g} \neq \boldsymbol{0}$ contain the effects of the surface corrugation.

8.2.4. Analytical model for the roton bands

Due to the large rotational constants of H_2 and D_2 the rotational excitation (roton) energies are rather large (≈ 360 cm^{-1} for p-H_2 and ≈ 180 cm^{-1} for o-D_2). Since the typical excitation energies for the translational vibrations (phonons) are much lower (see Sec. 8.4), one expects little mixing between the rotons and the phonons. The dependence of the roton band structure on the anisotropy of the intermolecular potential and of the molecule-substrate potential may be derived analytically. Since the latter anisotropy is not known this will be very useful in the interpretation of (future) experimental data.

After substitution of Eq. (9) for the intermolecular potential and Eq. (11) for the molecule-substrate potential into Eq. (2b), we can write the rotational mean-field Hamiltonian as

$$\begin{aligned} H_p^L(\omega_p) = L(\omega_p) &+ \sum_{lm} \widetilde{F}_{lm}(\boldsymbol{R}_p) C_m^{(l)}(\omega_p) \\ &+ \sum_{p'\neq p} \sum_{l_1 l_2} \sum_{m_1 m_2} \widetilde{X}_{l_1 m_1; l_2 m_2}(\boldsymbol{R}_{pp'}) C_{m_1}^{(l_1)}(\omega_p) \left\langle C_{m_2}^{(l_2)}(\omega_{p'}) \right\rangle^{L_{p'}} , \end{aligned} \tag{13}$$

with

$$\widetilde{F}_{lm}(\boldsymbol{R}_p) = \sum_{\alpha\lambda\mu} F_{\Lambda}(\boldsymbol{R}_p) \left\langle (u_p)^{\alpha} C_{\mu}^{(\lambda)}(\hat{\boldsymbol{u}}_p) \right\rangle^{T_p} \tag{14}$$

and

$$\begin{aligned} \widetilde{X}_{l_1 m_1; l_2 m_2}(\boldsymbol{R}_{pp'}) = &\sum_{\alpha_1\lambda_1\mu_1} \sum_{\alpha_2\lambda_2\mu_2} \left\langle (u_p)^{\alpha_1} C_{\mu_1}^{(\lambda_1)}(\hat{\boldsymbol{u}}_p) \right\rangle^{T_p} \\ &\times X_{\Lambda_1\Lambda_2}(\boldsymbol{R}_{pp'}) \left\langle (u_{p'})^{\alpha_2} C_{\mu_2}^{(\lambda_2)}(\hat{\boldsymbol{u}}_{p'}) \right\rangle^{T_{p'}} . \end{aligned} \tag{15}$$

For the systems under consideration one can make several approximations. The only significant terms in the intermolecular potential and in the molecule-substrate potential are the terms with $l_1, l_2 \leq 2$ and $l \leq 2$ (see Sec. 8.3). The terms that are relevant for the roton frequencies are the anisotropic interactions with l_1, l_2 or $l \neq 0$. Because of the sixfold symmetry at the adsorption sites the terms with $m \neq 0$ vanish. In the ground state of p-H$_2$ and o-D$_2$ the molecules are very nearly in a pure $j = 0$ state. So, the expectation values $\langle C_m^{(l)}(\omega_p)\rangle^{L_p}$ are practically zero, except for $l = m = 0$. Using all these simplifications we are left with the following rotational mean-field Hamiltonian

$$H^L(\omega_p) = BJ^2(\omega_p) + v_2\, C_0^{(2)}(\omega_p) , \tag{16}$$

where B is the rotational constant of H$_2$ or D$_2$, J^2 is the molecular total angular momentum operator and v_2 is the strength of the anisotropic crystal-field at the adsorption sites

$$v_2 = \widetilde{F}_{2,0}(\boldsymbol{R}_p) + \sum_{p'\neq p} \widetilde{X}_{2,0;0,0}(\boldsymbol{R}_{pp'}) . \tag{17}$$

The first contribution to this crystal-field originates from the molecule-substrate interactions, the second term from the anisotropic interactions between the molecules in the adsorbed layer. Diagonalizing this Hamiltonian in a basis of spherical harmonics $Y_m^{(j)}(\omega_p)$ with $j = 0$ and $j = 2$, we find that only the states with $m = 0$ are mixed

$$\begin{aligned} \psi^{(0)} &= Y_0^{(0)} - \delta Y_0^{(2)} \\ \psi^{(1)} &= Y_0^{(2)} + \delta Y_0^{(0)} \end{aligned} \tag{18}$$

with the mixing coefficient δ given by

$$\delta \approx \frac{9\sqrt{5}}{245}\,\frac{v_2}{B}\,. \tag{19}$$

The corresponding mean-field energies are

$$\begin{aligned} \varepsilon^{(0)} &\approx -\frac{9}{245}\,\frac{v_2^2}{B} \\ \varepsilon^{(1)} &\approx 6B + \frac{2}{7}v_2 + \frac{9}{245}\,\frac{v_2^2}{B}\,. \end{aligned} \tag{20}$$

The eigenstates $\psi^{(2)}$, $\psi^{(3)}$, $\psi^{(4)}$ and $\psi^{(5)}$ with $m \neq 0$ are the pure basis functions $Y_m^{(2)}$ with $m = \pm 1$ and $m = \pm 2$ and the corresponding eigenvalues are

$$\begin{aligned} \varepsilon^{(2,3)} &= 6B + \frac{1}{7}\,v_2 \\ \varepsilon^{(4,5)} &= 6B - \frac{2}{7}\,v_2\,. \end{aligned} \tag{21}$$

The roton frequencies are the eigenvalues of the TDH matrix in Eq. (3), restricted to the pure rotational excitations (0) → (1), (2), (3), (4), (5). We take $T = 0$ K so that the matrix $\boldsymbol{P}$ becomes minus the unit matrix and we rewrite the eigenvalue problem for the matrix in Eq. (3) into the following eigenvalue equations

$$\boldsymbol{\chi}^{1/2}\Big[\boldsymbol{\chi} + 2\boldsymbol{\Phi}(\boldsymbol{q})\Big]\boldsymbol{\chi}^{1/2}\boldsymbol{x}(\boldsymbol{q}) = \boldsymbol{x}(\boldsymbol{q})\boldsymbol{\Omega}^2(\boldsymbol{q})\,. \tag{22}$$

The diagonal matrix $\boldsymbol{\chi}$ is now defined as

$$\chi_{aa'} = \delta_{aa'}\left(\varepsilon^{(a)} - \varepsilon^{(0)}\right)\,, \tag{23}$$

and the Fourier transformed anisotropic coupling matrix can be written as

$$\begin{aligned} \Phi_{aa'}(\boldsymbol{q}) = 3Q^2\sqrt{70} &\sum_{m_1 m_2 m_3} \begin{pmatrix} 2 & 2 & 4 \\ m_1 & m_2 & m_3 \end{pmatrix} \left\langle \psi^{(a)} \middle| C^{(2)}_{m_1} \middle| \psi^{(0)} \right\rangle \left\langle \psi^{(0)} \middle| C^{(2)}_{m_2} \middle| \psi^{(a')} \right\rangle \\ &\times \sum_{\boldsymbol{n}} \exp(i\boldsymbol{q}\cdot\boldsymbol{R_n}) \left\langle r_{0\boldsymbol{n}}^{-5} C^{(4)}_{m_3}(\hat{\boldsymbol{r}}_{0\boldsymbol{n}}) \right\rangle^{T_0 T_{\boldsymbol{n}}}\,. \end{aligned} \tag{24}$$

Here, we have used the fact that all the adsorbed molecules are equivalent. Moreover, we have observed that the anisotropic intermolecular interactions with $l_1 = l_2 = 2$ are dominated by the quadrupole-quadrupole interactions (Q is the molecular quadrupole moment of H_2). The eigenvalue matrix $\boldsymbol{\Omega}^2(\boldsymbol{q})$ obtained by solving Eq. (22) contains the squares of the roton frequencies $\omega_a(\boldsymbol{q})$ on the diagonal.

It follows from Eq. (24) that for $\boldsymbol{q} = 0$ the matrix $\boldsymbol{\Phi}(\boldsymbol{q})$ is diagonal. This is related to the sixfold symmetry of the adsorption sites which causes only the terms with $m_3 = 0$ to survive. This leads to $m_1 = -m_2$ and, since the mean-field states $\psi^{(a)}$

are characterized by quantum numbers m, we find immediately that $\Phi(0)$ is diagonal with elements

$$\begin{aligned} \Phi_{1,1}(0) &= \frac{6}{5}S \\ \Phi_{2,2}(0) = \Phi_{3,3}(0) &= -\frac{4}{5}S \\ \Phi_{4,4}(0) = \Phi_{5,5}(0) &= \frac{1}{5}S, \end{aligned} \tag{25}$$

where S is the two-dimensional quadrupole-quadrupole lattice sum

$$S = Q^2 \sum_n \left\langle r_{0n}^{-5} C_0^{(4)}(\hat{r}_{0n}) \right\rangle^{T_0 T_n} . \tag{26}$$

For the optical roton frequencies we obtain from Eq. (22)

$$\omega_a(0) = \left[\left(\varepsilon^{(a)} - \varepsilon^{(0)} \right) \left(\varepsilon^{(a)} - \varepsilon^{(0)} + 2\Phi_{aa}(0) \right) \right]^{1/2} . \tag{27}$$

The crystal-field strength v_2 from Eq. (17) and the quadrupole-quadrupole coupling S are much smaller than the rotational energy splitting $6B$. In very good approximation we find that the roton frequencies are given by

$$\begin{aligned} \omega_1(0) &= 6B + \frac{6}{5}S + \frac{2}{7}v_2 + \frac{18}{245}\frac{v_2^2}{B} && \text{for } m = 0 \\ \omega_{2,3}(0) &= 6B - \frac{4}{5}S + \frac{1}{7}v_2 + \frac{9}{245}\frac{v_2^2}{B} && \text{for } m = \pm 1 \\ \omega_{4,5}(0) &= 6B + \frac{1}{5}S - \frac{2}{7}v_2 + \frac{9}{245}\frac{v_2^2}{B} && \text{for } m = \pm 2. \end{aligned} \tag{28}$$

In this approximation the splittings between the roton frequencies for $q = 0$ are additively determined by two contributions: the quadrupole-quadrupole lattice sum S and the effects caused by the crystal-field v_2. For general wave vectors the quadrupole-quadrupole interaction matrix $\Phi(q)$ is no longer diagonal but, essentially, we obtain the same additivity. The crystal-field leads to splittings between the roton subbands of different $|m|$, the quadrupole-quadrupole coupling leads to dispersion of these subbands. Degeneracies between the different branches cause avoided crossings. Roton bands calculated for different v_2 will be discussed in Sec. 8.4. According to Eq. (28) we can directly obtain the strength of the anisotropic crystal-field v_2 and, in particular, the unknown contribution $\widetilde{F}_{2,0}(\boldsymbol{R}_p)$ of the molecule-substrate interaction from the splittings between the subbands.

8.3. Computational aspects

The intermolecular potential used in our calculations is an *ab initio* calculated H_2-H_2 potential of Schäfer and Meyer [22] improved by Schäfer and Köhler [23] through a multiproperty analysis. This potential is represented by a spherical expansion, Eq. (8), with all the anisotropic contributions for $l_1, l_2 \leq 2$. Each expansion coefficient $\varphi_l(r)$ consists of dispersion contributions ($\sim r^{-6}$, r^{-8} and r^{-10}) and a short-range contribution which depends exponentially on r. The quadrupole-quadrupole interaction ($\sim r^{-5}$) appears in the $l_1, l_2, l_3 = 2, 2, 4$ term. This potential has been used in lattice dynamics calculations on solid H_2 and D_2 [26] and has proved to yield satisfactory results.

The modelling of the anisotropic molecule-substrate potential is described in Section 8.2.3. Our atom-atom model parameters are fitted to the empirical isotropic C-H_2 potential determined by selective adsorption measurements [24]. The Lennard-Jones parameters that were derived from these measurements are $\sigma_{C-H_2} = 2.89$ Å and $\varepsilon_{C-H_2} = 0.3753$ kJ/mol. We choose the Lennard-Jones parameters for the atom-atom C-H potential so that the isotropic term of the expansion in Eq. (11) (when restricted to only one carbon atom) matches the empirical isotropic C-H_2 potential. Thus, the anisotropic part of the molecule-substrate potential is determined by the separation of the two hydrogen atoms. If we use the experimental bond length of the hydrogen molecule (0.7417 Å) the Lennard-Jones parameters for the C-H interaction are $\sigma_{C-H} = 2.76$ Å and $\varepsilon_{C-H} = 0.2184$ kJ/mol. By changing the apparent bond length we can scale the anisotropy, just as done in Ref. [21]. With these parameters we find that the isotropic term of the molecule-substrate potential has a minimum above the centers of the carbon-rings at $z = 2.785$ Å.

In previous lattice dynamics calculations on bulk hydrogen it was shown that due to the large zero-point motions of the hydrogen molecules the displacement expansion of the potential should not be truncated before the sixth-order terms [26]. Both for the intermolecular and for the molecule-substrate potential we have therefore extended the displacement expansion to $\alpha_{max} = 6$. The spherical expansion of the molecule-substrate potential is only extended to $l_{max} = 2$, because of the weak anisotropy of the hydrogen molecules.

The two-dimensional character of the adsorbed layer causes the translational motions of the molecules to be strongly anisotropic. The amplitude of the in-plane vibrations turns out to be very different from that of the out-of-plane vibration. Therefore, a large basis of spherical harmonic oscillator functions is needed for the translational motions. With harmonic oscillator functions up to $n_{max} = 8$, which results in a basis of 165 functions, the results are well converged. In these spherical harmonic oscillator functions occurs a scaling parameter A which is used to optimize the basis [27]. For a three-dimensional isotropic oscillator $A = (M\omega/\hbar)^{1/2}$, where M is the molecular mass and ω the harmonic-oscillator frequency. In the case of an adsorbed layer, with the in-plane frequencies very different from the out-of-plane frequency, we average over the three fundamental excitations

$$A = \left[M \frac{\{(\varepsilon^{(1)} - \varepsilon^{(0)}) + (\varepsilon^{(2)} - \varepsilon^{(0)}) + (\varepsilon^{(3)} - \varepsilon^{(0)})\}}{3\hbar^2} \right]^{1/2} , \tag{29}$$

which yields better convergence with the same number of basis functions. Because of the weakly anisotropic interactions a small basis of tesseral harmonics up to $j_{max} = 2$ is sufficient for the calculation of the rotational mean-field states.

In all calculations we use 1.42 Å as the nearest neighbor distance between the carbon atoms within a graphite layer and 3.37 Å as the distance between the graphite layers. The nearest neighbor spacing between the adsorbed molecules in the $(\sqrt{3} \times \sqrt{3})\,R\,30°$ overlayer then equals 4.26 Å. The range of the two-dimensional lattice summation over the intermolecular potential is set at 8.0 Å. From Ref. [31] it is clear that only for the interaction of an adsorbed molecule with the top layer of the graphite substrate the corrugation has to be considered. This is achieved by summation over the molecule-atom pair potentials within a range of 30 Å. The rest of the graphite crystal is taken into account by including in Eqs. (11) and (12) the first Fourier term ($g = 0$) of the interaction with the next 10 layers. For the rotational constant of hydrogen we take $B = 59.06$ cm^{-1} and for deuterium $B = 29.83$ cm^{-1}. All calculations are performed at zero temperature.

8.4. Results and discussion

From the single-particle states of the molecules calculated at the mean-field level one can derive various quantities, such as the total Helmholtz free energy, the translational and rotational energy and the expectation values of the displacements of the molecules. These are listed in Table I.

Our first observation is that the vibrationally averaged height $\langle z \rangle$ of the molecules above the graphite surface is substantially greater than the height $z_0 = 2.785$ Å of the equilibrium positions of the molecules. These equilibrium positions are calculated from the isotropic term in the molecule-substrate potential and they lie above the centers of the sixfold carbon-rings. For p-H$_2$ and o-D$_2$ we find that $\langle u_z \rangle = \langle z \rangle - z_0$ equals 0.178 Å and 0.122 Å, respectively. This reflects the strong anharmonicity of the out-of-plane vibrations. Although the choice of origin should be irrelevant for a complete basis, we have located the basis functions for the translational vibrations at height $\langle z \rangle$, since this appears to yield the best converged results for a fixed number of basis functions.

We observe further a strong anisotropy in the translational vibrations. The root-mean-square amplitude of the in-plane vibrations is almost twice as large as the amplitude of the out-of-plane vibrations, both for p-H$_2$ and for o-D$_2$. We find good agreement

Table I. Helmholtz free energy (F), translational kinetic energy (E_T) and average displacements (at $T = 0$ K) for commensurate p-H_2 and o-D_2 layers on graphite.

	This work	Ref.[20]	Ref.[21]	Ref.[19]	Exper.[9]
			p-H_2		
F (kJ/mol)	−3.963	−4.247			
E_T (kJ/mol)	0.776				
$\langle z\rangle$ (Å)	2.963	3.0	2.92		
$\langle u_z^2\rangle - \langle u_z\rangle^2$ (Å^2)	0.053	0.04	0.042		
$\langle u_x^2 + u_y^2\rangle$ (Å^2)	0.345		0.353	0.436	
			o-D_2		
F (kJ/mol)	−4.438	−4.717			
E_T (kJ/mol)	0.531				
$\langle z\rangle$ (Å)	2.907	2.9	2.88		
$\langle u_z^2\rangle - \langle u_z\rangle^2$ (Å^2)	0.037	0.04	0.029		
$\langle u_x^2 + u_y^2\rangle$ (Å^2)	0.270		0.268	0.328	0.25

with the amplitude of the in-plane vibrations in o-D_2 which has been determined from neutron diffraction intensities [9].

The TDH calculations yield the phonon and roton band structure, as well as possible mixing between these bands. Since the roton frequencies in p-H_2 and o-D_2 are considerably higher than the phonon frequencies there is very little mixing, however, and we discuss the phonons and the rotons separately. In the calculations of the phonon bands we have included 5 excited center-of-mass vibrations of each molecule: the two fundamental in-plane vibrations, the fundamental out-of-plane vibration and the two lowest in-plane overtones. The latter were taken into account because they appear to be nearly degenerate with the fundamental out-of-plane mode. Thus, one might expect Fermi-resonances between these modes which will affect the phonon band structure, except in those points of the two-dimensional Brillouin zone where such resonances are forbidden by symmetry (e.g. the Γ-point). The following characteristics of the in-plane phonon band structure have been determined by INS [10-15]: the lowest phonon frequency at the Γ-point (ω_0), the total width of the in-plane phonon band ($\Delta\omega$), the frequency of the transverse phonon at the M-point (ω_T) and the frequency of the longitudinal phonon near the K-point (ω_L). The mode with frequency ω_0 is an acoustical phonon mode (an overall translation of the entire adsorbed layer).

The value of ω_0 (often called the phonon gap) is a direct measure for the corrugation in the substrate-adsorbed layer potential. The results which we have obtained for these quantities are shown in Table II, together with the experimental data and the results available from calculations by Novaco *et al.* [20,21] and by Gottlieb *et al.* [18,19]. Phonon dispersion curves are displayed in Figs. 1 and 2.

Table II. Phonon frequencies[a] (in cm^{-1}).

	This work	Ref.[20]	Ref.[19]	Exper.[11,15]
		p-H_2		
$\omega_0(E_1)$	34.1	32.4	27.2	32.9
$\Delta\omega$	25.5	29.3		19.1
ω_T	45.7	45.1		40.2
ω_L	56.0	58.2		49.6
$\omega(E_2)$	107.6			
$\omega(A_1)$	115.3			(157)
		o-D_2		
$\omega_0(E_1)$	25.3	25.6	21.7	27.8
$\Delta\omega$	10.5	10.3		6.6
ω_T	30.8	30.7		30.8
ω_L	34.4	35.0		33.4
$\omega(E_2)$	67.7			
$\omega(A_1)$	71.3			

a) $\omega_0(E_1)$ is the phonon gap, *i.e.* the frequency of the E_1 mode at the Γ-point (space group $p6mm$).
$\Delta\omega$ is the band width of the in-plane phonon band.
ω_T is the frequency of the transversal phonon mode at the M-point.
ω_L is the frequency of the longitudinal phonon mode near the K-point.
$\omega(E_2)$ is the frequency of the in-plane two-phonon excitation at the Γ-point.
$\omega(A_1)$ is the frequency of the out-of-plane mode at the Γ-point.

The results from our TDH calculations lie very close to the in-plane phonon frequencies from the SCP calculations by Novaco [20].

Apparently these phonon frequencies are determined mainly by the isotropic potential. The isotropic term in the molecule-substrate potential is derived from selective adsorption measurements [24], both in our calculations and in those of Novaco [20]. For the H_2-H_2 interactions he applies a semi-empirical isotropic potential of Silvera and Goldman [32], whereas we use an anisotropic *ab initio* potential [22,23]. Moreover, we include the out-of-plane phonons and the rotons, which we find to be well separated from the in-plane phonons, however. Our results are in good agreement with the experimental data [11]; the dispersion of the in-plane phonons is just slightly overestimated. We have also modelled the H_2-graphite interactions with empirical atom-atom potentials derived from solid hydrocarbons [33], but the results appeared to be substantially worse.

From Figs. 1 and 2 it is obvious that the out-of-plane phonons mix with in-plane

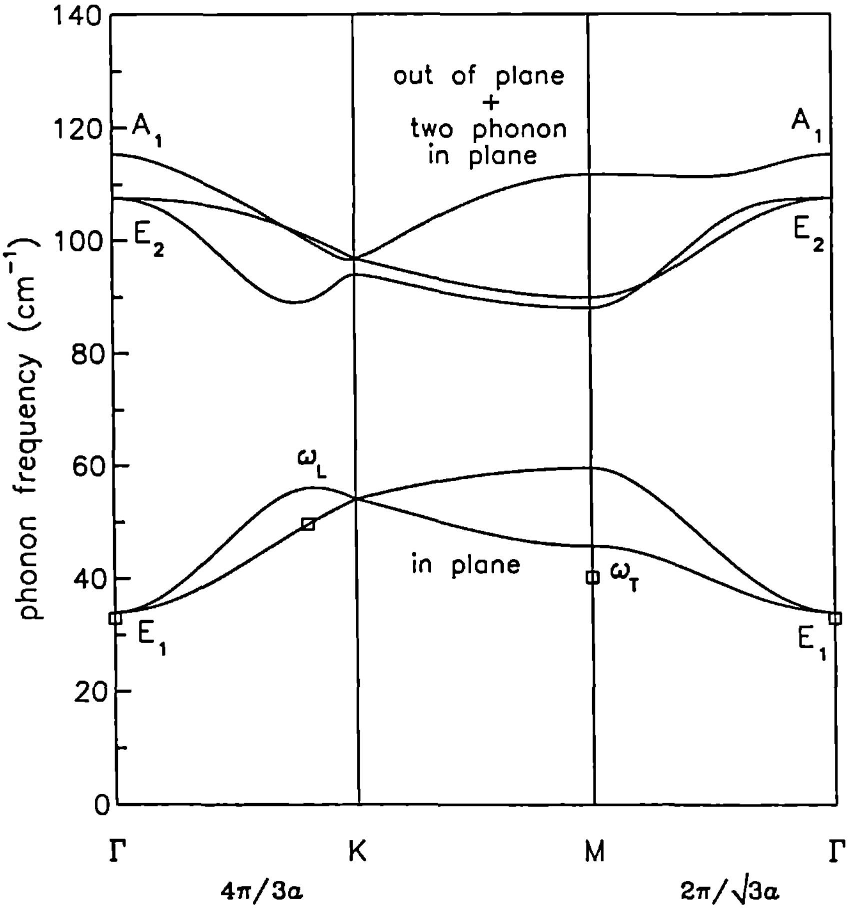

Fig. 1. Phonon dispersion curves for a p-H_2 monolayer on graphite, from TDH calculations at $T = 0$ K, compared with the experimental values of ω_0, ω_L and ω_T (□) from refs. [11,12] ($a = 4.26$ Å is the nearest neighbor distance in the adsorbed layer).

two-phonon states. The frequencies of the out-of-plane phonons are close to the out-of-plane vibrational frequency (122.4 cm^{-1}) of a single H_2 molecule obtained from selective adsorption measurements [24]. The frequency for the out-of-plane mode which was deduced from the INS spectrum of p-H_2 on graphite [15] is substantially higher, however (157 cm^{-1}). An alternative assignment of the INS spectrum [15] might be suggested. This spectrum contains a strong peak at 118 cm^{-1} which is due to the $j = 0 \rightarrow 1$ rotational transition. This transition is optically forbidden, but it is induced by neutron scattering. We think that the out-of-plane phonons (calculated at 115.3 cm^{-1} for $q = 0$) might be hidden under this peak. (Actually a side peak is observed

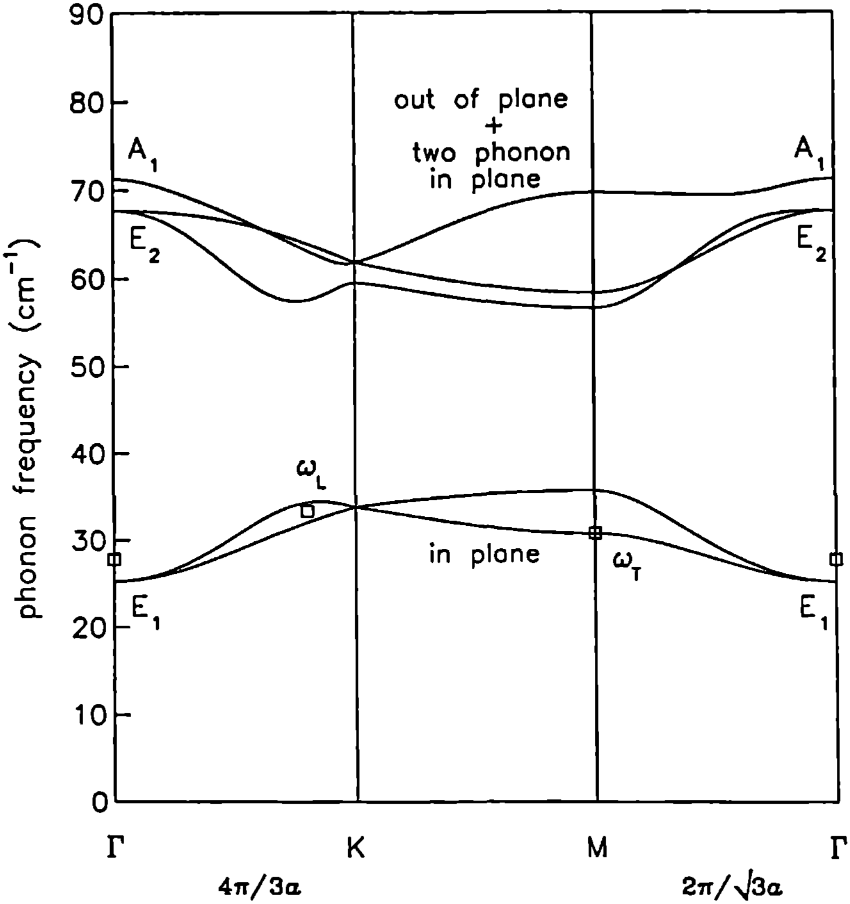

Fig. 2. Phonon dispersion curves for an o-D_2 monolayer on graphite, compared with the experimental values of ω_0, ω_L and ω_T (□) from refs. [11,12].

at 114 cm^{-1}.) The broad peak around 157 cm^{-1} should then be assigned, probably, to a combination band of the $j = 0 \rightarrow 1$ rotational transitions or the out-of-plane phonons with the in-plane phonon modes. Such a combination band may range from 151 to 170 cm^{-1} (4.53 to 5.08 THz) which is consistent with the broad peak in the experimental spectrum. If this alternative assignment is not correct, then we would have to conclude that the shift in the out-of-plane vibrational frequency from 122 cm^{-1} for a single H_2 molecule to 157 cm^{-1} for a full H_2 monolayer is caused by substrate-mediated interactions between the molecules in the adsorbed layer. In our calculations these interactions have been ignored. It would be surprising, however, if they affect so strongly the out-of-plane vibrations, while the in-plane modes are in good agreement

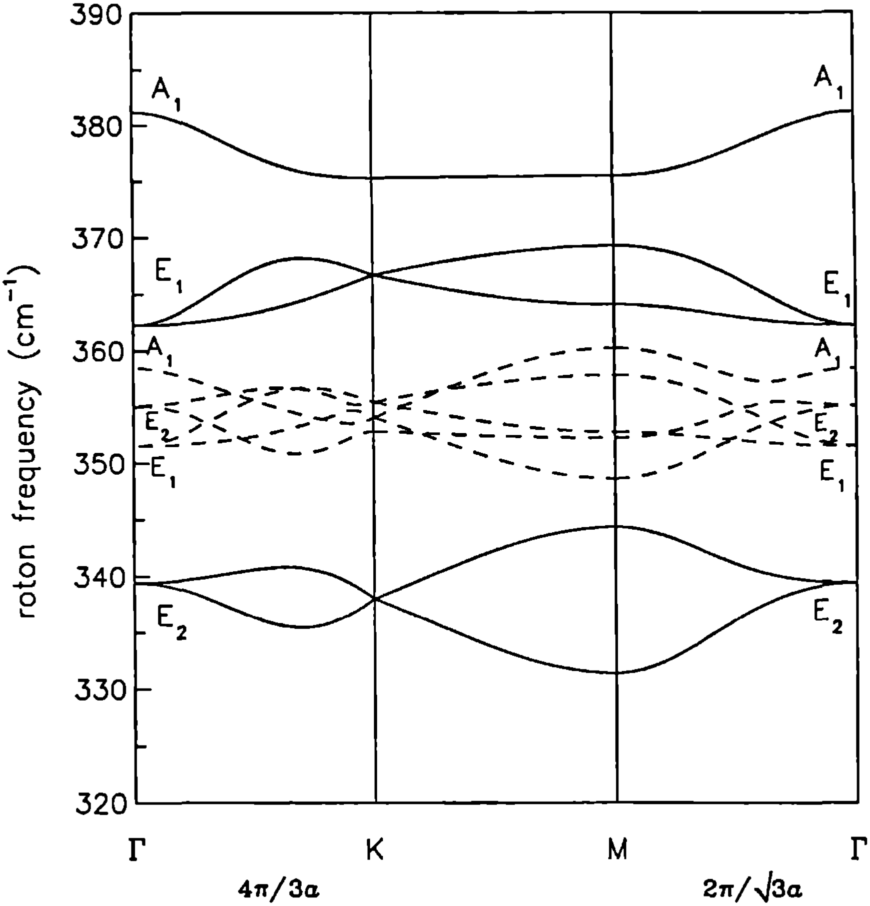

Fig. 3. Roton dispersion curves for a p-H_2 monolayer on graphite, from TDH calculations at $T = 0$ K. Solid curves: with v_2 from Eq. (17). Dashed curves: with $v_2 = 0$.

with experiment. Therefore, we prefer the first explanation.

The structure of the roton bands for p-H_2 and o-D_2 layers on graphite is shown in Figs. 3 and 4. Since the anisotropy of the molecule-substrate potential is entirely unknown (see Sec.8.2.3 and 8.2.4), we have varied the strength of this anisotropy by changing the anisotropy parameter v_2 in the crystal-field, see Eqs. (16) and (17).

The dashed curves are obtained for $v_2 = 0$, the solid curves are calculated with the values of v_2 (65.1 cm^{-1} for p-H_2 and 69.9 cm^{-1} for o-D_2) that are obtained from the anisotropic H_2-H_2 potential within the layer, in combination with the atom-atom model for the H_2-substrate interaction (see Sec. 8.2.3). The latter values of v_2 are almost certainly overestimated as it is known that the atom-atom model overrates the

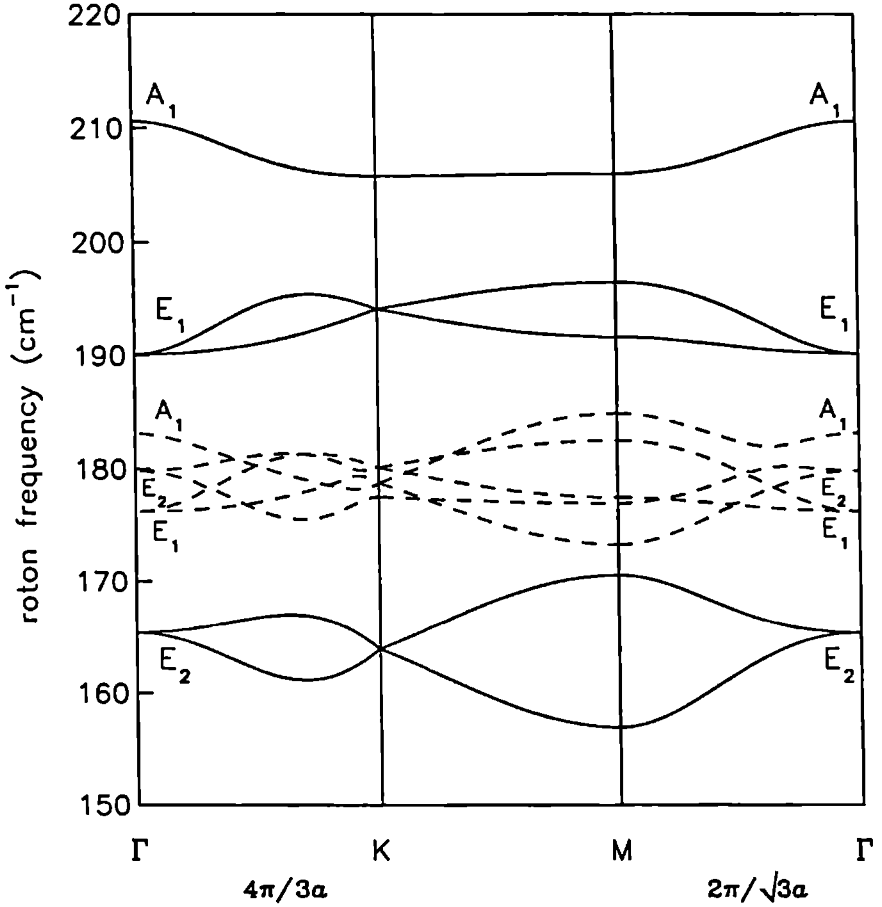

Fig. 4. Roton dispersion curves for an o-D_2 monolayer on graphite. Solid curves: with v_2 from Eq. (17). Dashed curves: with $v_2 = 0$.

asphericity of the H_2 molecule and it appears from NMR measurements [17] for o-H_2 and p-D_2 on graphite that v_2 is probably rather small. It is obvious that the value of v_2, which is dominated by the anisotropy $\tilde{F}_{2,0}$ in the molecule-substrate interaction, see Eq. (17), has an enormous effect on the roton dispersion curves. This effect can be completely understood from the derivation in Sec. 8.2.4 which leads to Eq. (28).

One observes nearly parallel shifts of the roton subbands when v_2 is changed. The shape of these subbands, which is primarily determined by the quadrupole-quadrupole interactions within the adsorbed layer, is practically not altered, except for avoided crossings. From Table III it appears that the simple formula given by Eq. (28) is indeed capable of yielding rather accurate roton frequencies. This will be very valuable when

Table III. Optical ($q = 0$) roton frequencies (in cm^{-1}), obtained from the full TDH calculations including phonons, and obtained from Eq. (28) with v_2 calculated from Eq. (17) and S from Eq. (26), see text.

$p6mm$	p-H_2		o-D_2	
symmetry	Eq. (28)	TDH	Eq. (28)	TDH
E_2	339.0	339.5	165.7	165.4
E_1	363.7	362.3	192.5	190.1
A_1	382.1	381.2	214.9	210.6

these frequencies will be measured, because Eq. (28) allows the direct calculation of v_2 from the splittings between the (optical) roton frequencies. Experimental data for p-H_2 on graphite are available [34] from electron energy loss spectroscopy (EELS). A peak has been observed at 379 ± 16 cm^{-1}, which agrees in particular with the frequency of the calculated optical roton with polarization perpendicular to the surface (symmetry A_1). The resolution of these measurements was too low to observe any splittings. Moreover, the selection rules effective in EELS might prevent the observation of rotons polarized parallel to the surface.

Acknowledgement

We thank drs. V.L.P. Frank, H.J. Lauter and H. Wiechert for communicating their results prior to publication. The investigations were supported in part by the Netherlands Foundation for Chemical Research (SON) with financial aid from the Netherlands Organization for Scientific Research (NWO).

Note

This chapter will also be included in the Ph.D. thesis of W.B.J.M. Janssen.

References

[1] J. Cui and S.C. Fain Jr., Phys. Rev. B 39, 8628 (1989).

[2] J. Cui, S.C. Fain Jr., H. Freimuth, H. Wiechert, H.P. Schildberg and H.J. Lauter, Phys. Rev. Lett. 60, 1848 (1988).

[3] H.P. Schildberg, H.J. Lauter, H. Freimuth, H. Wiechert and R. Haensel, Jpn. J. Appl. Phys. 26, Suppl. 3, 345 (1987).

[4] H. Freimuth, H. Wiechert and H.J. Lauter, Surf. Sci. **189/190**, 548 (1987).

[5] H.J. Lauter, H.P. Schildberg, H. Godfrin, H. Wiechert and R. Haensel, Can. J. Phys. **65**, 1435 (1987).

[6] M. Nielsen, J.P. McTague and L. Passell, in *Phase Transitions in Surface Films*, edited by J.G. Dash and J. Ruvalds (Plenum, New York, 1980), p. 127.

[7] H. Freimuth and H. Wiechert, Surf. Sci. **178**, 716 (1986).

[8] H. Freimuth and H. Wiechert, Surf. Sci. **162**, 432 (1985).

[9] H. Freimuth, H. Wiechert, H.P. Schildberg and H.J. Lauter, unpublished, cited in Refs. [12,19].

[10] M. Nielsen, J.P. McTague and W. Ellenson, J. Phys. (Paris) Colloq. **38**, C4-10 (1977).

[11] H.J. Lauter, V.L.P. Frank, P. Leiderer and H. Wiechert, Physica B **156/157**, 280 (1989).

[12] V.L.P. Frank, H.J. Lauter and P. Leiderer, Phys. Rev. Lett. **61**, 436 (1988).

[13] H.J. Lauter, in *Phonons 89*, edited by S. Hunklinger *et al.* (World Scientific, Singapore, 1990), p. 871.

[14] V.L.P. Frank, H.J. Lauter and P. Leiderer, in *Phonons 89*, edited by S. Hunklinger *et al.* (World Scientific, Singapore, 1990), p. 913.

[15] J.L. Armony, V.L.P. Frank, H.J. Lauter and P. Leiderer, in *Phonons 89*, edited by S. Hunklinger *et al.* (World Scientific, Singapore, 1990), p. 916.

[16] A.B. Harris and A.J. Berlinski, Can. J. Phys. **57**, 1852 (1979).

[17] P.R. Kubik, W.N. Hardy and H. Glattli, Can. J. Phys. **63**, 605 (1985).

[18] J.M. Gottlieb and L.W. Bruch, Phys. Rev. B **40**, 148 (1989).

[19] J.M. Gottlieb and L.W. Bruch, Phys. Rev. B **41**, 7195 (1990).

[20] A.D. Novaco, Phys. Rev. Lett. **60**, 2058 (1988).

[21] A.D. Novaco and J.P. Wroblewski, Phys. Rev. B **39**, 11364 (1989).

[22] J. Schäfer and W. Meyer, J. Chem. Phys. **70**, 344 (1979).

[23] J. Schäfer and W. Köhler, Z. Physik D **13**, 217 (1989).

[24] L. Mattera, F. Rosatelli, C. Salvo, F. Tommasini, U. Valbusa and G. Vidali, Surf. Sci. **93**, 515 (1980).

[25] M. Karimi and G. Vidali, Surf. Sci. **208**, L73 (1989).

[26] W.B.J.M. Janssen and A. van der Avoird, Phys. Rev. B **42**, 838 (1990).

[27] W.J. Briels, A.P.J. Jansen and A. van der Avoird, J. Chem. Phys. **81**, 4118 (1984).

[28] D.R. Fredkin and N.R. Werthamer, Phys. Rev. A **138**, 1527 (1965).

[29] D.M. Brink and G.R. Satchler, *Angular Momentum* (Clarendon, Oxford, 1975).

[30] W.A. Steele, Surf. Sci. **36**, 317 (1973).

[31] T.H.M. van den Berg and A. van der Avoird, Phys. Rev. B **40**, 1932 (1989).

[32] I.F. Silvera and V.V. Goldman, J. Chem. Phys. **69**, 4209 (1978).

[33] D.E. Williams and T.L. Starr, Comput. Chem. **1**, 173 (1977).

[34] R.E. Palmer and R.F. Willis, Surf. Sci. **179**, L1 (1987).

Summary

The subject of this thesis is: lattice dynamics calculations on molecular crystals and physically adsorbed molecular layers. The methods used are the standard harmonic method for the solids with larger molecules (chlorinated benzenes and tetracyano-ethene) and the Time-Dependent Hartree (TDH) method for N_2, H_2 and D_2 crystals and overlayers. The harmonic method is extended to include the coupled intramolecular vibrations (vibrons). In the quantum mechanical TDH method the translational vibrations of the molecules (phonons) are expanded in a basis of three-dimensional harmonic oscillator wave functions and their collective librations (librons) or hindered rotations (rotons) in a free rotor basis. For the larger molecules we have used semi-empirical atom-atom potentials, for H_2, D_2 and N_2 we have based ourselves on *ab initio* intermolecular potentials, with their anisotropy given explicitly in spherical harmonics.

Chapters 1 and 2 describe a combined spectroscopic and computational study of chlorinated benzene crystals. The calculations appeared to be indispensable to understand the vibron band structure in the various crystal modifications, as well as the effects of the random $^{35}Cl/^{37}Cl$ isotopic disorder. Chapter 3 deals with the phonon/libron and vibron dispersion in tetracyano-ethene as observed by inelastic neutron scattering. It is found that the anomalous dispersion measured in one of the vibron branches is caused by the long range electrostatic coupling between strong vibrational transition-dipole moments. Near the center of the Brillouin zone, the shape of the dispersion curve for the mode involved appears to be sensitive to the size and shape of the macroscopic crystal domains. Chapter 4 is a methodological study. On the well-studied case of solid nitrogen we compare different lattice dynamics methods and different expansions of the *ab initio* potential and we calculate the anharmonic effects.

Chapters 5 and 6 contain the theory that was required before we could apply the TDH lattice dynamics method to the study of adsorbed layers. We had to derive explicitly the anisotropy and the displacement dependence of the molecule-substrate potential and to perform two- and three-dimensional lattice sums. For these sums we have derived the two-dimensional Fourier components which describe the corrugation of the periodic substrate. The resulting formulas have been coded and included in a (modified) two-dimensional lattice dynamics program package. In Chapters 7 and 8 we have used this package for computations on N_2, H_2 and D_2 monolayers on graphite. For N_2 on graphite we have treated both the commensurate and incommensurate monolayers, their thermodynamic stability and the (anharmonic) phonon and libron frequencies. For p-H_2 and o-D_2 layers the use of a quantum mechanical method is essential. We have calculated the phonon and roton dispersion curves and compared the results with the scarce experimental data. More detailed summaries of the work and the conclusions can be found in the individual chapters.

Samenvatting

Het onderwerp van dit proefschrift is: roosterdynamica berekeningen aan moleculaire kristallen en geadsorbeerde moleculaire lagen. De gebruikte methoden zijn de standaard harmonische methode voor vaste stoffen met grotere moleculen (gechloreerde benzenen en tetracyano-etheen) en de Time-Dependent Hartree (TDH) methode voor N_2, H_2 en D_2 kristallen en geadsorbeerde lagen. De harmonische methode is uitgebreid voor gekoppelde intramoleculaire vibraties (vibronen). In de quantummechanische TDH methode worden de translationele moleculaire vibraties (fononen) geëxpandeerd in een basis van drie-dimensionale harmonische oscillator golffuncties. De collectieve libraties (libronen) of gehinderde rotaties (rotonen) worden ontwikkeld in een vrije rotor basis. Voor de grotere moleculen hebben we gebruik gemaakt van semi-empirische atoom-atoom potentialen. Voor N_2, H_2 en D_2 hebben we ons gebaseerd op *ab initio* intermoleculaire potentialen, waarbij de anisotropie expliciet gegeven wordt in termen van sferisch harmonischen.

In hoofdstuk 1 en 2 wordt een gecombineerd experimenteel en theoretisch onderzoek aan gechloreerde benzeen kristallen beschreven. De berekeningen bleken onmisbaar te zijn voor de interpretatie van de vibron bandstructuur en van $^{35}Cl/^{37}Cl$ isotoop effecten in de diverse kristalmodificaties. Hoofdstuk 3 behandelt de fonon/libron en vibron dispersie in tetracyano-etheen zoals gemeten m.b.v. inelastische neutronenverstrooiing. De gemeten anomale dispersie van een van de vibronbanden blijkt veroorzaakt te worden door de elektrostatische koppeling tussen sterke overgangsdipoolmomenten. De vorm van de betreffende dispersiecurve is gevoelig voor de grootte en vorm van de macroscopische kristaldomeinen. Hoofdstuk 4 beschrijft een methodologische studie. Voor het veel bestudeerde vast stikstof vergelijken we verschillende roosterdynamica methoden en verschillende expansies van de *ab initio* potentiaal en berekenen we anharmonische effecten.

Hoofdstuk 5 en 6 bevatten de theorie die nodig is om de TDH roosterdynamica methode te kunnen toepassen op geadsorbeerde lagen. De anisotropie van de molecuul-substraat potentiaal en de afhankelijkheid van translationele uitwijkingen hebben we expliciet afgeleid. Voor de in deze potentiaal optredende twee- en drie-dimensionale roostersommen zijn twee-dimensionale Fourier componenten afgeleid, die de corrugatie van het periodieke substraat beschrijven. De resulterende formules zijn geprogrammeerd en toegevoegd aan een (gemodificeerd) twee-dimensionaal roosterdynamica programma. In hoofdstuk 7 en 8 hebben we dit programma gebruikt voor berekeningen aan N_2, H_2 en D_2 monolagen op grafiet. Voor N_2 op grafiet hebben we zowel de commensurable als de incommensurabele monolagen onderzocht. Met name is gekeken naar hun thermodynamische stabiliteit en naar de (anharmonische) fonon en libron frequenties. Voor p-H_2 en o-D_2 lagen is het gebruik van een quantummechanische methode essentieel. De fonon en roton dispersiecurven zijn berekend en vergeleken met de eerste experimentele resultaten. Meer gedetailleerde samenvattingen en conclusies zijn te vinden in de afzonderlijke hoofdstukken.

Curriculum vitae

van Tom van den Berg (geboren op 18 april te Schijndel).

Mei 1979

Eindexamen Atheneum B aan het Maaslandcollege te Oss.

September 1979

Aanvang studie Technische Natuurkunde aan de Technische Universiteit Eindhoven.

November 1985

Ingenieursexamen Technische Natuurkunde.
Afstudeerrichting: Theoretische Natuurkunde (bij prof.dr. B.J. Verhaar).
Eerste graads onderwijsbevoegdheden: Wiskunde, Natuurkunde en Mechanica.

Januari 1986

Aanvang promotieonderzoek in de vakgroep Theoretische Chemie aan de Universiteit Nijmegen onder leiding van prof. dr. ir. A. van der Avoird.